EXPERIMENTAL AND THEORETICAL INVESTIGATION OF EFFECT OF FIN GEOMETRY ON FROST FORMATION ON MICROCHANNEL HEAT EXCHANGERS

By

EHSAN MOALLEM

Bachelor of Science in Mechanical Engineering
University of Tehran
Tehran, IRAN
2004

Master of Science in Mechanical Engineering
University of Tehran
Tehran, IRAN
2007

Submitted to the Faculty of the
Graduate College of the
Oklahoma State University
in partial fulfillment of
the requirements for
the Degree of
DOCTOR OF PHILOSOPHY
July, 2012

EXPERIMENTAL AND THEORETICAL INVESTIGATION

OF EFFECT OF FIN GEOMETRY ON FROST FORMATION

ON MICROCHANNEL EVAPORATORS

Dissertation Approved:

Dr. Lorenzo Cremaschi

Dissertation Adviser

Dr. Daniel E. Fisher

Dr. Jeffrey D. Spitler

Dr. A. J. Johannes

Outside Committee Member

Dr. Sheryl A. Tucker

Dean of the Graduate College

TABLE OF CONTENTS

Chapter Page

Chapter Page

Chapter Page

LIST OF TABLES

Table Page

LIST OF FIGURES

Figure Page

NOMENCLATURE[1]

A: Area (m^2)

Ch_d *or* C_d: Channel depth (air side) or Coil depth (mm)

Ch_h: Channel height (air side) (free space between two adjacent fins) (mm)

Ch_w: Channel width (air side) (free apace between two adjacent vertical tube walls) (mm)

c_p: Specific heat (J/kgC)

d: distance (mm)

D_{ab}= binary diffusion coefficient of water to air (2.28E-5) (m^2/s)

D_h: Hydraulic diameter of air passage (channel) free flow area bounded between two adjacent fins and walls of two adjacent tubes

$D_{h,frost}$: Hydraulic diameter of air passage (channel) free flow area bounded between growing layers of frosts on fins and tube walls (decreasing as frost thickness increases)

ERT: Entering Refrigerant (coolant) Temperature (°C)

Fo or Fo_m: mass transfer Fourier number $Fo_m = \frac{D_{ab}t_t}{Ch_h^2}$

Fs: Frost number or supersaturation level of air Fs= $\frac{P_{air}-P_{surf}}{P_{surf}}$

[1] The present nomenclature is valid through the entire dissertation except specifically defined terms for some equations in which a different nomenclature is offered below the equation.

h: Heat transfer coefficient (W/m^2C)

j or J: Colburn j-factor ( )

k: thermal conductivity (W/mC)

L: Coil Length (mm)

l_l: Louver length (mm)

l_p or L_p: Louver pitch (mm)

$\dot{m}$: mass flow rate (kg/s)

Nu: Nusselt number

P: Perimeter (m^2)

P_{air}: Pressure of water vapor pressure in the air stream (Pa)

P_{surf}: Pressure of water vapor pressure in the air at surface temperature (Pa)

Pr: Prandtl number

$\dot{Q}$: Heat transfer (W)

Re: Reynolds number ( )

Re_{D_h}: Reynolds number based on hydraulic diameter of the air passage free flow area (bounded between two adjacent fins and walls of two adjacent tubes)

Re_{D_hfrost}: Reynolds number based on hydraulic diameter of the current air passage free flow area during frost growth (decreasing as frost thickness on fins increases)

R.H.: Relative Humidity ( )

St: Stanton number

t: (Frost) thickness (m) or (mm)

t_{fin}: fin thickness (m)

t_t: time (sec)

T: Temperature (°C)

T_t: Tube thickness (mm)

V: Velocity (m/s)

Greek letters

δ : dimensionless thickness ( )

ΔT_{LM}: Mean logarithmic temperature difference (°C)

η: Fin efficiency ( )

μ: viscosity (kg/ms)

ρ: Density (kg/m^3)

ω: Absolute humidity (kg water vapor / kg dry air) ( )

Subscripts

0 : at initial time (t=0)

avg: average

c: cross section

corr: correlaion

ent.: entering, entrance

exp.: experimental

f: frost

fin: fin

s: surface

surf: surface

t: at time t

T: Temperature (°C)

CHAPTER I

INTRODUCTION

1.1 ABSTRACT

This dissertation focuses on various aspects of frost growth on louvered folded fins in outdoor microchannel heat exchangers used in air source heat pump systems. In this research, the effects of surface temperature, fin geometries, surface coatings and environmental parameters such as air humidity and velocity on the thermal and hydraulic performance of the microchannel heat exchangers under frosting condition were investigated. The overall aim was to provide some guidelines about frost behavior of microchannel heat exchangers and isolate and quantify the effect of geometry, surface coatings and surface temperature. A set of empirical correlations were developed to predict frost thickness, air face velocity drop and heat transfer coefficients for various fin geometries. The approach taken was to perform laboratory experiments on small scale coils and sample fins that were cut out from commercially available heat exchangers and to replicate their operating conditions in laboratory.

A good estimation of the fin surface temperature was achieved with the methodology developed in the present study. Experimental data of frost weight, local frost thickness, air pressure drop across the coils, time of frost-defrost cycles and heat transfer rates were recorded for heat exchangers operating in actual transient frosting conditions. Data showed that the frosting time and the frost growth rates depend mainly on the local fin surface temperature while water retention and surface coatings could have secondary and minor effects. Some geometries performed better in frosting condition than others such as geometries with lower fin density that delayed the blockage of the air flow. The fin length and fin depth had minor effects on frosting performance. It was found that air humidity has a significant effect on rate of frost formation while air velocity seemed to have a small effect on frost formation.

1.2 BACKGROUND

Air source heat pump systems are used for heating and cooling of residential and commercial buildings all year around. They are energy efficient, compact, and have low installation costs. An air source heat pump exchanges heat directly from the indoor environment to the outdoor ambient air, and during winter operation, the outdoor coil might accumulate frost on its surface. Frost forms on the surface of the outdoor coils when humid air comes in contact with the coil surface which has a temperature below the dew point temperature of entering air and also below freezing point of water (0ºC). Frost on the surface acts as an insulation, obstructs air flow, reduces the heat transfer rate and increases the air pressure drop of air passing through the coil. Defrost cycles are periodically executed in between the heating times to melt the ice, drain the water from the outdoor coil, and free its surface from accumulated frost before the heating service is initiated again. Microchannel coils have been employed recently in heat pump applications to replace conventional fin and tube coils due to their compactness, lower coil weight and less refrigerant charge which could lower the direct contribution to global warming due to potential refrigerant leakage (Garimella, 2003; Kim and Groll, 2003a; Kim and Bullard, 2002; Park and Hrnjak, 2007). These heat exchangers are usually made of Aluminum and because of the low conductive thermal resistance of the microchannel tubes, the fin base temperature is closer to the local saturation temperature of the refrigerant in comparison to conventional fin and tube type heat exchangers. While in cooling mode microchannel heat exchangers increase the energy efficiency compared to spine fin or plate fin-and-tube coils with similar face area, during heating mode the energy performance of heat pump systems with microchannel outdoor coils are generally low due to a higher frequency of defrost cycles (Kim and Groll, 2003a; Padhmanabhan et al., 2008). Because frequent defrost cycles penalize the heating seasonal energy efficiency, it is crucial to understand the characteristics of frost growth on outdoor coils and develop heat exchangers that would minimize, if not eliminate, defrost cycles.

There are several parameters that affect frost formation on outdoor coils, such as air velocity, air humidity, air temperature, cold surface temperature (Kondepudi and O'Neal, 1989; Lee et al., 1997) surface energy and fin-base surface microscopic characteristics (include coatings and roughness or brazing fluxes) (Na and Webb, 2003; Shin et al., 2003), fin geometry and coil water retention after defrost cycles (Xia et al., 2006).

Results from a previous work (Padhmanabhan et al., 2008) and preliminary results of this study (Moallem et al., 2010a; Moallem et al., 2012b) showed that water retention, which was assumed to be one of the main reasons of faster frost growth on microchannels, was not the dominant factor affecting the frost, even though it seemed to have some effects on the air side pressure drop. The key parameters that affect frost nucleation and growth were observed to be fin surface temperature and the fin geometry. Air face velocity also affected frost formation but, in the range of heat pump applications, the effect of air velocity was minor. The effects of outdoor air temperature and air humidity were also studied. However they are the environmental conditions and are independent form system during the actual service of the heat pump unit. Between the main factors that affect the frost, surface temperature increase is a parameter that depends on evaporating refrigerant temperature and is mostly controlled by the system designers to provide good heating capacity. The effect of fin surface temperature was partly analyzed in the literature by changing the refrigerant saturation temperature. The challenge was the various coil geometries were not directly comparable to each other with this approach. Each coil had a different internal geometry that made different flow regime and different hydraulic and thermal entry lengths inside tubes and ports. Even with the same entering refrigerant temperature, the surface temperature of various coils has a considerable difference, not only between different coils, but also in different locations of a single coil between inlet and outlet header. This was also the challenge in the present study. In our initial work (Moallem et al., 2010b), experimental data showed that the frost in fin and tube coils grows non-uniformly from inlet to outlet header. Even for microchannel coil, this effect was less noticeable but still existed and frost accumulates more near

inlet header rather than outlet even in for 0.3m by 0.3m (1ft by 1ft) coil custom made for laboratory testing. The preliminary data of the present study, showed that testing various coils with different geometries could not lead to a conclusive theory of a suitable geometry because the isolated effect of fin on frost formation could not be achieved (Moallem et al., 2012b). Also in previous microchannel studies in the literature, the geometries were changed to search for the best option for thermal performance but surface temperature was not investigated nor independently controlled (Xia et al., 2006). As a result, the effect of geometry modification was coupled with the effect of surface temperature change. To overcome this difficulty a new methodology was developed to measure and control the fin surface temperature independently which will be described in detail in this thesis.

There are correlations in the literature that can predict the heat transfer coefficient and pressure drop for various micrchannel geometries in steady-state dry and steady-state wet conditions but there has been no correlations to predict the performance of microchannel coils under frosting condition. The previous researchers instead developed models for frost growth which might be difficult to implement, had convergence issues, required advanced skills for troubleshooting, long hours of computational time and extensive experimental validation of the model. In addition, the predicted results from the current models available in the public domain are sometimes contradicting or inconsistent with each other. For this reason, I chose a different approach. Since there are some well-known heat transfer and pressure drop correlations for dry microchannel coils, developing the same type of correlation for coils under frosting condition seems a very appealing and useful idea.

The scientific merit of this research is a fundamental understanding of frost nucleation and growth on folded louvered fins with microchannel tubes. The approach is to extend the existing correlations for dry or wet microchannel coils to a new correlation to predict the performance of the coils under frosting condition by an empirical approach. The other goals of this dissertation are to investigate the effect of fin geometry on the frosting performance of different microchannel coils and to determine

the geometry that could minimize the frost formation. Also drop-in microchannel coils with new fins might be able to replace the conventional fin and tubes coils in heat pump applications.

1.3 OBJECTIVES OF THE DISSERTATION

The overarching goal of this study was to investigate the thermal hydraulic characteristics of folded louvered fin microchannel heat exchangers operating under frosting conditions. The present thesis focuses on evaporator applications for air source heat pump systems. The specific objectives of the current work were as follow:

1) To search for the most recent information on frost formation on outdoor heat exchangers and connect the works in the literature in order to develop a fundamental understanding of frost formation on microchannel heat exchangers.
2) To perform an experimental investigation of frost growth on microchannel coils with different fin geometries in a controlled environment in laboratory and provide data of frost mass, frost thickness, air side pressure drop, heat transfer coefficients and capacity degradation and effects of different coatings and water retention on the coil performance.
3) To experimentally characterize, isolate and quantify the main factors that affect the frost formation.
4) To develop a set of empirical correlations that predicts the aspects of transient frost formation on microchannel heat exchangers, that is, frost thickness, air face velocity drop, and heat transfer coefficients.
5) To develop a set of empirical correlations that predicts the aspects of transient frost formation on microchannel heat exchangers, that is, frost thickness, air face velocity drop, and heat transfer coefficients.

In addition, several frost, defrost and re-frost tests were performed and completed to provide some information about water droplets effects on the fins performance during frosting. These tests were limited and should not be used as comparison. They serve as basis for future research in this topic.

1.4 PROGRAM TO MEET THE OBJECTIVES

To address the challenges of the frost problem, theoretical and experimental work is needed. On the experimental side, two approaches were taken. A series of initial frost tests was performed on real heat pumps (Padhmanabhan et al., 2008) and custom made 0.3m by 0.3m (1ft by 1ft) microchannels with a geometry similar to the ones of full scale microchannel heat exchangers adopted in the most recent heat pump system prototypes under research and development in this field (Moallem et al., 2012b). The second approach was to prepare a special small scale test facility to be able to test each individual one-row sample of fins, which is cut out from the commercially available coils. While the first approach allowed replicating air flow similarity and regular minor non uniformities in air side or refrigerant side of full scale microchannels, the fin samples approach allowed eliminating the non uniformities from the experiments to focus on pure effect of surface temperature and various geometries. The complex thermal hydraulic coupled effects due to non uniformity in surface temperature, non uniform approaching air velocity, and variation of the local heat transfer coefficients, which typically occur in real microchannel evaporators, were minimized with the proposed set up of second approach. Second approach had also another advantage that explained earlier. In the second approach by cutting small samples and measuring and controlling their surface temperature, it was possible to investigate the effect of fin temperature and fin geometry independently from each other and quantifying their impact on the frosts growth. It is worth noting that measuring and controlling the fin surface temperature is not a trivial process. It is quite

impractical to obtain the correct accurate surface temperature by simply attaching a thermocouple on the surface. If insulation is used to cover the thermocouple contact point, the local fin temperature is altered; if insulation is not used, the probe measures an average temperature of air and the surface. All attempts were made in this study to attach a thermocouple to read a true value of the surface temperature, have failed. Other solutions that were tried were using infrared cameras, but the emissivity, view angle, and resolution of the fin surface due to coil rough surface were problematic. The approach was to measure the surface temperature by attaching thermocouples outside the air flow in the back side of one single fin in the second approach as will be described later in detail. In this configuration, it was possible to control the surface temperature of the sample fin and virtually eliminate any local perturbation in the air stream around the fins. This method is a new methodology and was never used before. 3 different fin surface temperature (-5, -8,-11°C) and 9 different fin geometries were investigated to study the effects of fin density, fin depth, fin length, and existing of louvers. Three different fin density of 10, 14 and 20 fin per inch, three different fin depths of 19, 26 and 30 mm and three fin lengths of 8, 10 and 13mm were tested. One fin design without louver and one design without using brazing flux to attach the fins to the tubes were also employed. In both approaches, 0.3m by 0.3m (1ft by 1ft) coils (Moallem et al., 2012b; Moallem et al., 2012c) and small samples (present dissertation) were tested with different hydrophilic and hydrophobic coatings to investigate the effect of coating on their water retention performance.

CHAPTER II

LITERATURE REVIEW

2.1 INTRODUCTION

Frost growth on heat exchangers has been subject to study for researchers since 1960's. Most of these studies have been performed on heat exchangers for refrigeration applications. Some researchers have developed analytical models by employing basic differential equations for heat and mass transfer and corrected their models with factors from the experiments. Some characteristics of frost have been determined experimentally such as frost density, frost conductivity and frost porosity. Other characteristics such as frost grow rate, frost thickness, frost weight and frost visual shape were modelled either numerically or semi-empirically with the support of experimental data generated from ad-hoc set ups in laboratories. Some studies were performed to identify the basic properties of frost and some others investigated frost propagation on different geometries. Some other studies focused on developing models for frost growth on various geometries.

Each study implicitly contained the effect of its own geometry, and dividing them into groups was not possible since each study had multiple relevant findings that belong to two or more groups. I decided to sort the literature review in a chronological order. The older frost studies will be mentioned first which mainly focus on obtaining the frost properties such as frost density and conductivity. Then gradually the tone of studies shifts toward studying frost formation rate on simple geometries like flat plate or cylinders. Finally the recent frost studies were conducted on fin and tube geometries and some models have been developed too. Earlier studies about properties of frost are useful to interpret the data obtained from coils in the present study such as pressure drop etc. that showed various behaviours at different surface temperatures. Other modeling studies are related to the present work because studying them in detail lead this study to take an empirical approach vs a modeling approach due to difficulties that each model were facing such as validation, skills needed for troubleshooting and convergence issues. Some other studies have been mentioned here to show sometimes there is no a common consent between various researchers about effect of each individual factor affecting the frost maybe because of complexity of transient heat and mass transfer problem of frost propagation. This even means that still some parametric study could help finding evidences to support one idea rather than the others. The other studies mentioned in this chapter contain those who investigated parameters affecting the frost experimentally on different geometries and fin and tube heat exchangers or simple geometries such as bank of flat plates or cylinders. These studies are relevant to the present dissertation because they provide a fundamental understanding of frost growth and describe the dominant factors or measuring techniques that control and measures frost formation for different geometries. At last a few studies that have focused on microchannels will be discussed too. A separate chapter was also assigned to fundamental investigation of frost formation and theories of formation in molecular scale and visual categorizing of frost types to provide a deeper fundamental understanding of the phenomena.

2.2 LITERATURE SURVEY OF FROST FORMATION IN CHRONOLOGICAL ORDER

Formation of frost generally has been subject to study for a long time since 1724 when Fahrenheit (1724) noticed that cold water can form flakes of ice on the surface (Hobbs, 1974). However, formation of frost on heat exchangers started to draw attention after 1950's. One of the earliest studies of frost on heat exchangers was done by Stoecker (1957) about how frost can affect the performance of coils. Stoecker (1960) added another series resistance to approximate that decrease overall conductivity due to frost.

Chen and Rohsenow (1964) studied the frost roughness for the geometry of inside tubes using a photographic approach with comparison to standard sand. Frost roughness was estimated to be between 0.25 to 0.50 mm.

Yonko and Sepsy (1967) developed an empirical correlation to obtain frost conductivity as a function of frost density using the geometry of a flat horizontal plate. They found that frost thickness grow rate is most affected by surface temperature and air humidity while air velocity does not have a significant influence on it. They found that although air velocity does not have a noticeable effect on frost thickness grow rate but it affects the frost density. Their results showed that frost conductivity increased with increased surface temperature, air humidity and air velocity. As they showed according to all previous studies, frost density was a positive function of frost conductivity. That means that with increasing frost density, frost conductivity increases too and vice versa. So it is resulted that frost density also increases with increased surface temperature, air humidity and air velocity. A table summarizing their general qualitative results and comparison to other studies is offered at the end of this section on Table 1. They developed a model to predict the frost conductivity by setting up energy and mass diffusion equations of water vapor inside frost layer. They assumed a spherical shape for frost particles with air pockets surrounding them

forming a simple structure such as a group of balls equally spaced in 3 dimensions. The results of the model for thermal conductivity had considerable deviation from measured experimental data but authors explained that it could be because of melting and seeping water into the frost layer which changes the microscopic frost structure from assumed idealized homogenous structure.

Hosoda and Uzuhashi (1967) by using an experimental setup, obtained equations for density and conductivity of frost on a fin and tube heat exchanger. They found that surface temperature and air velocity are major factors affecting frost but since their correlations were dimensional, it might not be applicable to other geometries and operating conditions other than the ones for which the correlation were originally developed. Their result showed that with lower surface temperature and lower air velocity frost grows with lower density while in higher surface temperature and higher air velocity frost is more ice-like with high density.

Brian et al. (1969) and Brian et al. (1970) developed a model to predict density, thickness and heat transfer rate of frost growth process on a copper flat plate. They assumed that frost density is uniform along the depth of frost layer and they used finite difference to solve the mass, energy and diffusion equations. They proposed empirical correlations for frost density as a function of air humidity, air stream Reynolds number and time based on experimental data in their previous work (Shah, 1969). For frost conductivity experimental data, they used the experimental data which was a function of temperature and frost density from their previous work (Brazinsky, 1967). Heat transfer decreased quickly with frost growth in first hour of the test but it reached asymptotically to a constant value after about 90 minutes after starting the test. Frost thickness was found to grow faster in higher humidity but grew slightly faster in lower Re number.

Biguria and Wenzel (1970) developed an empirical correlation for frost density and frost conductivity on a geometry of flat plate in forced convection flow in a wind tunnel. The plate temperature was varied between -98 to -29°C that lead to frost surface temperature from -20 to -

7°C for different air velocity from 3 to 12m/s. They used an optical thermometer to estimate the frost surface temperature and stated the accuracy of this measurement was ±1°F (0.6°C). They employed a cathetometer to measure the frost thickness. Details of their experimental work was described in Biguria (1968). They found that frost thickness growth rate slightly decreases with increasing air velocity. Frost density increased by increasing plate temperature, increasing air velocity, decreasing air humidity and decreasing distance from plate leading edge. Frost conductivity variation was consistent with frost density except that for increasing air humidity which increased the frost thermal conductivity. They stated that their correlation could predict the frost density within ±7% and frost conductivity within ±25% accuracy.

Yamakawa et al. (1971) and Yamakawa et al. (1972) conducted a series of frost growth test on flat plate and a bank of parallel stainless steel flat plates. They used an infrared thermometer to determine the frost surface temperature and claimed that the attaching thermocouples to measure the frost surface temperature as was used in previous works does not lead to an accurate results. They stated that the accuracy of their thermometer was 0.2°C in 0°C and they conducted tests to determine frost emissivity too. According to their results, frost thickness, mass, density and conductivity all increased with increasing air humidity or increasing air velocity. They found that heat transfer coefficient is almost independent of time during frost formation and it depends on amount of mass transfer to the plate based on different conditions. The heat transfer coefficient was slightly higher than what Lewis and Chilton-Colburn analogy suggests but mass transfer coefficient was found to be lower than what the analogy predicts. They stated that as time goes by, the heat and mass transfer rates decrease because of the frost thickness growth and increased resistance.

Kennedy and Goodman (1974) investigated frost formation on a vertical copper flat plate in natural convection air flow regime. An interferometer was used to determine the air temperature adjacent to frost surface. Authors stated that they have been able to measure frost surface

temperature, frost density, frost thickness and frost mass as well. The temperature of the plate was -12°C and ambient air temperature was 24°C. The ambient air water vapor mass fraction was in the range of 0.01 to 0.015 which corresponded to relative humidities of 45% to 75%. The details of experimental setup were referred back to another work by the same authors (Goodman and Kennedy, 1972) and (Goodman, 1972). They found that relation between heat and mass transfer coefficient is greater than what predicted by Lewis analogy.

Jones and Parker (1975) developed a relation to predict the frost density and frost thickness in time by starting with initial values and following the rates of changes of these variables. They compared their results with experimental data obtained by Yonko and Sepsy (1967). They stated that their model could predict the frost growth even with varying air velocity, temperature and humidity during the frost growth rate within 30% however only thickness verifications were introduced.

Hayashi et al. (1977a; 1977b) used a photographic observation approach to classify frost types based on plate temperature and water vapor concentration for as geometry of a flat plate. They divided the frost growth period into three phases which will be discussed further in details with images in next chapter, "Fundamental understanding of frost formation". The thickness was measured using a cathetometer and after each run a sample of frost was cut out and weighted. Frost surface temperature was measured by placing thermocouples into the frost layer surface. They proposed a model to predict frost thickness and weight based on assumed geometry of vertical columns of frost in the air stream in the beginning of frost formation process. They also found increasing surface temperature and air velocity increase the frost density and conductivity while air velocity does not have a significant effect on frost thickness consistent with what Yonko and Sepsy (1967) have found before.

Schneider (1978) proposed a simplified frost model with a relation for frost thickness growth on cylindrical tubes that was claimed to be independent of Re number and vapor pressure but instead depending on ratio of super-saturation defined in their work and frost conductivity.

Schulte and Howell (1982) studied the effect of air turbulence on frost growth on a flat horizontal plate. They changed the air turbulence intensity between 1 and 22% and found it did not have any significant effect on frost growth. They measured the thickness in various locations of the flat plate and found that air velocity and air temperature will slightly affect the frost thickness growth pattern on their geometry.

Dietenberger (1982) Proposed a model for frost growth on flat plates dividing the frost growth procedure into three phases and used previous models in the literature, with some additions for each phase, to match the simulation results with previous experimental data from the literature. (O'neal, 1982; O'neal and Tree, 1982) studied the frost formation extensively on a bank of parallel plates in temperature ranges of -5 to -12°C for different air velocity and humidity. They found that frost height increases with decreasing plate temperature and increasing air humidity. The effect of air temperature was negligible. Higher air velocities caused slightly higher frost thickness growth rate but it was true until a critical Reynolds number was reached. Higher Reynolds number had reverse effect. They also found that frost density increases as plate temperature and air humidity and Reynolds number increase.

Barrow (1985) stated that a reduction in capacity of frosted coil is mostly due to blockage effects of frost and reduced air flow rate. The insulation resistance effect of frost has small effect on the heat transfer and could be neglected. The influence of temporarily increased local velocity and heat transfer coefficients and surface roughness due to frost could not overcome the effect of reduced air mass flow rates at last. It should be noted that some researchers believe that the total

capacity reduction is more because of air flow reduction than insulation effects of frost such as Barrow (1985) while other researchers believe otherwise (Yamakawa et al., 1971).

Chepurnoi et al. (1985) experimentally investigated frost growth on fin and tube coil by measuring the thickness and comparing to other available data from the literature. Authors suggested a correlation to predict the thickness on similar geometries.

Satio et al. (1984) used experimental microscopic observation to study early frost growth stages (less than 2 minutes) on a vertical cold polished copper plate and on horizontal cylinders in an array (to simulate a geometry similar to fin and tube coil) under forced convection. Air temperature was 20°C and surface temperature was varied in the range of -5 to -15°C. They performed their experiments with three different air relative humidity level of 50, 65 and 80% and air velocity of 2, 6 and 13 m/s. They found that in early frost deposition stage water vapor condenses on the cold surface as an unstable supercooled liquid for a short time and then these droplets freeze immediately. They found that frost density is affected by number and density of the formation of these frozen droplets on the surface. This short time was called "freezing time" was found to be reduced by a number of affecting factors such as lower surface temperature, higher air humidity, higher air velocity, shorter distance from the leading edges and smaller contact angel (hydrophilic surfaces). Freezing time was different for different test conditions but as an example for air velocity of 2m/s and relative humidity of 80% in the location of 5mm from the leading edge, freezing time for surface temperatures of -5, -7, -10 and -13 was 35, 25, 15 and 20 seconds respectively. For other conditions, the freezing time was different and it varied from 5 to 90 seconds but the majority of the data points lied between 10 to 30 seconds. They observed that after freezing of these small droplets, micro-ice crystals start to grow on them one dimensionally perpendicular to the surface in early stages. They offered dimensionless correlations for density and thickness of frost using a dimensional analysis.

A model of frost with considering all heat transfer mechanisms was developed by Auracher (1987). From the convection, conduction, radiation and diffusion terms it was shown that convection and radiation inside the frost layer have less than 1% effect and can be neglected and only diffusion and conduction should be considered inside frost layer.

Zakrzewski (1984) developed a computer model that calculated optimal cycle duration for frost and defrost based on different assumed values for heat exchanger area, frost density and temperature differences. As frost cycle progressed in time, the capacity dropped gradually. When defrost kicked in, the capacity of unit was somehow accounted to be negative because it consumed energy and provides no useful heating. The decision about how long frost and defrost cycle duration should last could be a parameter to be optimized. This was achieved by their computer model. The final results were highly dependent on assumed heat transfer coefficients and temperature differences and other heat exchanger characteristics which are not the same for all heat exchangers. For the range of parameters they assumed, the optimum frost cycle time was varying between 1 to 4 hours. This result is typically higher than conventional time of defrost on industrial microchannel heat exchangers which is equal or less than 45 minutes for most cases.

Aihara et al. (1989) showed that if a heat exchanger is being placed in a fluidized bed so that a flow of liquid fluid pass on the tubes there will be frost outside tubes but if there are particles of glass beads of roughly 1mm diameter in this stream, then frost can not be formed on the tube surface. In other words, glass beads remove frost particles that are deposited on the tube surface. This finding is interesting because if the same concept could be employed in air stream then the problem of frost formation on heat exchanger could be able to be solved.

Sami and Duong (1988; 1989) introduced a numerical model of frost growth on flat plate based on molecular diffusion of water vapor. The results of model were compared against previous experimental data and the models of Jones and Parker (1975), Yonko and Sepsy (1967) and Shah

(1969). The new model seemed to be able to predict the experimental data better than previous models.

Emery and Siegel (1990) experimentally studied the effect of frost formation on a sample of fin and tube coil placed in the cold air stream by measuring heat transfer and pressure drop. They found that heat transfer degradation is a function of time and air humidity while pressure drop is a function of frost thickness and surface roughness. They also found that for an approximate frost layer thickness of 2mm on their specific geometry, the capacity has reduced 50%.

Kondepudi (1988), in his Ph.D. dissertation performed a thorough experimental study on fin and tube heat exchangers with 1)louvered, 2)wavy, 3)corrugated, and 4)flat plate fins and also spine fin types under frosting condition. The effects of change in air and surface temperature, air humidity, air velocity and fin density were studied and mass of frost, heat transfer coefficient, enthalpy change and air pressure drop across the coil were measured. It was found that frost grow increases when any of the air humidity, air velocity, air temperature or fin density increases, while the most influential factor was determined to be air humidity. After air humidity, higher fin density leaded to faster frost growth and higher air pressure drop because of the air flow blockage effect. Higher air velocities leaded to faster frost grow rate too but the differences were small. A model was also developed for flat fin type and claimed to be able to predict the experimental data within 15 to 20% error. Similar results of their findings were published in Kondepudi and O'Neal (1989) and Kondepudi and O'Neal (1991). In their study, frost mass was not measured directly with a scale; but it was measured using difference between air humidity before and after the coil and finally it was checked against weight of condensate melted frost. In another follow up work (Kondepudi and O'Neal, 1993) a fin and tube frost model was presented using quasi steady state assumption and uniform frost growth all over the heat exchanger. However, the validation results compared with experimental data was not presented.

(Ostin and Andersson) (1991) with an experimental approach, stated that frost thickness is depending significantly on temperature and air humidity but not on air velocity. Air temperature was 21°C while three surface temperatures of -7, -11 and -20°C and three air relative humidity of 32, 52 and 75% and air velocities of 3 and 6 m/s were tested. Their geometry was a bank of parallel horizontal plates under forced convection. Their result showed that if air humidity increases, thickness and mass of frost growth rate increase too but if surface temperature increases, frost thickness growth rate decreases as expected but frost mass growth rate change just slightly. This last result about effect of surface temperature was drawn from 30% air relative humidity test that rate of frost deposition is very slow there so that after 5 hours, only 1.5 gram of frost was accumulated on the plates. It is possible that the frost mass gradient was not very apparent from their experience because of extreme low air humidity and slow frost rate and the difficulties to measure such a small weight. Especially they used a mechanical arm and bearing to make contact with weighing machine that had friction according to authors. They measured a frost density based on their measured thickness and mass and found frost thermal conductivity using previous correlations of Auracher (1987) and Dietenberger (1983). The density of frost found to be higher when air velocity was higher consistent with what Yonko and Sepsy (1967) had found before. They proposed a correlation to obtain frost effective thermal conductivity as a function of frost density based on their density measurements that was slightly lower from other previous studies. They stated that some part of frost melt and seep into the previous layer of frost and they called it cyclic frost growth. They found that after four hours of this cyclic frost growth, frost density increases from around 100kg/m^3 to 300kg/m^3 and frost thermal conductivity increased to about three times its initial value too. They explained that this increase is because of densification of frost layer that happens as a result of melting and refreezing. In another work, Ostin and Johannesson (1991) found that one particular hydrophilic coating (a polyurethane composition) delays the frost formation on the flat plate surfaces in comparison to bare aluminium to a significant amount of more than 1,2 and 3 hours for different coating thicknesses

of 0.2, 0.4 and 0.7mm respectively but this effect will be lost after a few frost/defrost cycles. The used coating contained the famous antifreeze solution, Ethylene Glycol, to prevent frost and ice formation and during the water absorption, the coating formed a flexible and soft hydrogel with a slippery surface. This polyurethane resin used to absorb water several times its original weight but solubility of Ethylene Glycol in water and resin eventual detachment from the plate surface might have been the reason that this coating lost its performance after a few frosting cycles.

Shinagawa et al. (1992) investigated nucleation of water vapor on a cold copper surface to determine the circumstances in which whether liquid or solid nucleation happens. There was only water vapor used in an evacuated test chamber that was in contact with cold surface and there was no air present there. They found that partial pressure of vapor has a key role to determine which type of deposition happens on the surface. In their experiment, water vapour partial pressure and surface temperature were not changed independent of each other and results are only available for a certain range of conditions. Visual observation was used to determine the type of frost deposition. They found that for the surface temperature of -16°C and below and for the water vapour pressure of 50 to 200 Pa, only ablimation frosting which is direct formation of solid condensate from water vapor (direct solidification) occurs. From the surface temperature of -11°C and water vapor of 350 Pa to surface temperature of -16°C and 200 Pa, formation of liquid condensate happens on the surface that is followed by freezing of the droplets immediately. The experiment was setup so that the surface temperature used to decrease in a slow rate and water vapor pressure used to decrease too at the same time because of deposition of water vapor on the surface. They concluded that the condensation frosting which is formation of liquid condensate followed by freezing happens when the water vapor pressure is above 200 Pa. But the maximum temperature they had in their experiment was -8°C and 350 Pa so there was no experimental point to verify this hypothesis for temperature between 0°C and -8°C especially for water vapor partial pressure of 500 to 650 Pa which is near frost test conditions of heat exchangers. Their

conclusions might need to be used with care in heat exchanger frosting conditions. In another study, Shinagawa et al. (1994) studied nucleation of a mixture of water vapor and p-xylene on a cold surface with an experimental technique identical to previous study which approximately ranged the same pressure and temperature conditions. In another study, Shinagawa et al. (1995) used cyclohexane substance to study the phase transition from vapor into crystals on a cold surface keeping the surface temperature constant at -22, -33 and -40°C and increased the vapor pressure gradually. They found the critical vapor pressure that cyclohexane starts to nucleate on cold surface happens at 950, 450 and 270 Pa for the three mentioned temperature respectively. They developed a model using molecular kinetic theory to predict this behaviour that finally compared with their experimental data with good agreement.

Sherif et al. (1993) presented a model of frost growth on a flat plate using a numerical approach to find the temperature and thickness of the frost taking advantage of previous correlations for frost density and conductivity. The results were compared successfully to previous experimental data of Yonko and Sepsy (1967) and to other models (Jones and Parker, 1975; Sami and T. Duong, 1989).

Tao et al. (1993a) proposed a 1-D model for flat plate to predict frost density and frost thickness by using an effective mass diffusivity that accounts for a deviation of actual mass transport (which was several times higher) from the Fick's diffusion law as they explained. In another study Tao et al. (1993b; 1994) investigated the frost growth on a single straight fin of Aluminum, Brass, Plastic and Teflon experimentally. This straight fin was actually a flat plate that connects to the surface from the bottom edge side and frost grew on both side of the flat plate while the temperature of fin root was changed from -6°C to -20°C. The air temperature was constant at 21°C and relative humidity was in the ranged between 30 to 60%. The frost grew in higher thicknesses and density on leading edges of the fin than the trailing edges. The middle part of the fin seemed to have large fragile crystals growing directionally biased toward the direction of air

flow. The trailing edge crystals were similar to the leading edges but in lower density and thickness. The frost thickness at the trailing edge was roughly half of thickness on the leading edge and in the midpoint it was something between these two values however it was very non-uniform. The frost grow on the aluminium fin was found to be slower than the brass fin. They observed the early frost formation process with a microscope and divided the frost growth period into three phases. In the first phase, subcooled liquid droplets appear on the surface. In second phase, which happens after a short time after first phase, all of these droplets turn into ice and solid crystals appear on the surface. And in the third phase, crystals begin to grow into many branches like trees and fill the free spaces. They found that for the Aluminum surface, subcooled liquid droplets turned into ice in less than one second so the duration of the first phase is very short. In another numerical model Tao and Besant (1992) proposed a model to predict frost thickness, density and rate of ablimation in two directions of normal and parallel to the flat plate numerically. They validated their results against Mao et al. (1992) results. The only limitation was model could work only for 5 to 10cm after the leading edge. At nearer distance to the leading edge the model seemed to deviate from experimental data and moreover there were no experimental data in Mao et al. (1992) measurements closer than 5cm to the plate leading edge. This makes usage of this data and model for heat exchanger applications difficult because most of regular heat pump heat exchangers has a one row or two row coils that mostly have coils with less than 5cm depth. Mao et al. (1992) did an extensive set of measurements on frost thickness, mass and heat flux on an Aluminum flat plate with average roughness of 0.36μm under forced convection as function of distance from leading edge, air humidity, air velocity and surface temperature. The air temperature varied between 15 to 23°C and cold plate temperature ranged from -5 to -15°C. Air absolute humidity ratio varied between 0.004 to 0.01 kg/kg and air velocity range from 1.2 to 2.7 m/s which corresponds to Re of 3000 to 7000. The data showed that thickness increased linearly in the beginning (approximately first 60 min) and started to flatten out later in the tests (between 60 to 120min). The other interesting observation was the thickness

was almost uniform in different depth of the plate and although it had some variations along the plate but there was not a significant excess accumulation of frost on the leading edges. This seemed to be true for different air humidity and different air velocities that were tested. Air velocity had a small effect on thickness increase too and an increase of 30% in air velocity caused a 15% increase in thickness measurements. Surface temperature decrease had a distinct effect on thickness and increased it significantly. Frost mass concentration that was defined the mass of frost per local unit area of the plate (kg/m^2) used to drop quickly by increasing the distance from leading edge. The areas near the leading edges had a considerable higher mass concentration and this effect was magnified in higher air humidity. On the contrary, the surface temperature had small effect on mass concentration. Heat flux which was defined heat transfer rate per plate surface area (W/m^2) had higher amount at leading edge and decreased after that point regardless of time all during the test. They finally offered an empirical correlation for frost thickness, mass, dimensionless frost density and conductivity, heat and mass transfer coefficients and compared their correlations with other experimental results from previous studies which were in a fair agreement. The dimensionless form of their equation for some variables such as temperature contained both air temperature and surface temperature and caution should be used to interpret the data based on increase or decrease of such variables. With considering these points, their findings were consistent with previous findings in other studies. Mao et al. (1993) repeated the same measurements but for lower air velocity in laminar[2] region i.e air velocity of 0.4 to 0.9 m/s (Re: 1000~2100). A similar correlation with different coefficients for mentioned parameters were proposed. They found that in laminar air flow, the frost thickness is much less than in the turbulent air flow with other identical parameters. Also in laminar air flow frost thickness decreased from leading edge to trailing edges more significantly than in turbulent air flow

[2] The criteria for laminar and turbulent flow for a undisturbed flat plate in the free stream which is considered as an external flow regime is Re(critical)=500,000 but as long as all the discussion about heat exchangers deal with channel flow between parallel fins or plates, the definition of Reynolds number is based on internal flows and hydraulic diameters of the channel flow. So the critical Reynolds number is Re(critical)=2300.

however frost thickness at trailing edge was never less than 65% of leading edge thickness. Heat transfer coefficient had a slight increase in time for turbulent flow but it had a slight decrease in time for laminar flow. Heat transfer coefficient had a significant decrease with increasing surface temperature for both laminar and turbulent flows. Mass transfer coefficients decreased in time for both turbulent and laminar flow. Mass transfer coefficient however decrease slightly with decreasing surface temperature in turbulent flow but increased with surface temperature decrease for laminar flow. They pointed out the offered correlations are engineering estimations and could not capture the complexities of leading edges (x less than 50mm) and early frost growth stages. The other limitation was the large fluctuation of air absolute humidity using hot steam spray in tests ranging from $\Delta\omega$ =0.0005 to 0.001 kg/kg for the air humidity of ω=0.004 kg/kg which affected directly the mass transfer coefficient measurements (in comparison to the present study which is $\Delta\omega = \pm 0.0002$kg/kg). In another study similar to what was explained, Mao et al. (1999) did an experimental study of frost growth on the flat plate in the air and temperature conditions applicable for commercial freezers. The surface temperature was between -20 to -40°C and air temperature ranged from -10 to -26°C. Finally empirical correlations for these conditions were proposed. They found smoother frost layer which was thinner and denser formed in higher cold surface temperature and lower relative humidity. In these set of data, measurements were conducted 25mm beyond leading edges and farther so there was no information for frost formation behaviour near leading edge which might be important in frost formation on the microchannel heat exchangers.

Ameen (1993) investigated frost growth on fin and tube heat exchanger using previously developed correlation to set up a model, which under-predicted the mass of frost and the evaporator temperature but the model predicted well the overall capacity.

Le Gall et al. (1997) proposed another 1-D model for frost deposition on a cold flat plate. By accounting temperature and density variation inside frost layer, they proposed a diffusion

correction factor to account for deviation of increased mass transfer coefficient from the Fick's diffusion law.

Chang and Wang (1997) developed a generalized heat transfer correlation for 91 different samples of louvered fin michrochannel heat exchangers in dry condition collected from previous studies. The correlation could predict Colburn j factors of 89% of the data bank within 15% error. Their correlation will be used as a comparison to the correlation developed in the present study in the following chapters.

Martinez-Frias and Aceves (1999) introduced a model for frost formation on fin and tube evaporator to predict COP, frost thickness and pressure drop. Author claimed that model has been verified with experimental data in their previous work (Martinez-Frias et al., 1996). Authors explained that their frost model has been implemented into an existing heat pump model (Rice, 1991) and effect of frost on heat pump performance has been obtained and plotted.

Storey and Jacobi (1999) investigated the effect of air vortices on the frost growth in a laminar channel flow between two parallel flat plates with an experimental approach. They showed that dimensionless frost thickness grows linearly with square root of environmental time with slope of one. The dimensionless frost thickness was frost thickness divided by space between plates and environmental time was defined as a combination of Fourier, Biot and Lewis number. They developed a scaling relation for frost growth rate and they found that generating air vortices in the airflow using a special type of vortex generator increases local frost growth rate by 7%. They found that air Re number ($500<Re<2500$) and location in the channel (not distance from leading edge along the flow in depth of the plate but it was the horizontal distance left or right side of the vortex generator on the plate) does not have significant effects on frost thickness. Details of their experimental setup was explained in Storey (1997). An interesting fact also was reported by Storey (1997) and Storey and Jacobi (1999) about usage of an incorrect form of a relation to

obtain frost thermal conductivity by a number of previous studies. The original equation was developed by Woodside (1958) and it had a incorrect form in its original printing on their work. A 1/2 multiplier was typographically missing in an integral calculation and even the Woodside (1958) numerical data only matched with correct form of this equation. Other researchers (Biguria and Wenzel, 1970; Hayashi et al., 1977b; Yonko and Sepsy, 1967) reported and used somehow the original incorrect form of this equation in their models. Finally, A follow up work by Robinson and Jacobi (2001) corrected the assumption of constant mass deposition on frost layer.

Ismail and Salinas (1999) developed a one dimensional transient model for frost formation between two cold flat plates and compared with experimental data from the literature. It was shown that results from the model for frost thickness and density, except the initial points, matched well with experimental data.

Thomas et al. (1999) and Chen et al. (1999b; 2000a; 2000b) investigated the frost growth on a bank of fins placed in the air flow and mass and thickness of frost and heat transfer rates were measured. Weight of frost was measured after the test by placing the fins on a scale. A model was developed upon their findings and compared to experimental data. The model was able to predict the frost characteristics well except the pressure drops which were found to be very sensitive to thickness and could not be predicted very well. In another work by the same authors (Chen et al., 2003), the effect of fan was added to the model and a sensitivity analysis was performed to help optimizing the design of heat exchanger. Thomas et al. (1999) showed that on a flat plate with a depth of 100mm the maximum frost thickness happens very near the leading edges at 14mm from the leading edge. The value of thickness at this point was around 40% higher than trailing edge and was decreasing linearly from leading edge to trailing edge.

Sahin (2000) developed a model to predict effective frost conductivity for the early crystal growth period based on assumption that frost layer could be divided into two parts of cylindrical ice columns and air gaps. A parameter (β) was introduced defined as the ratio of volume of ice to volume of empty space (air) in frost layer. Consistent with other studies he found that frost density and conductivity are lower at lower surface temperatures. Frost conductivity and density increased with increasing air temperature, decreasing air humidity and increasing air velocities. A one dimensional mass diffusion and heat transfer process was assumed in his equations. The details of the experimental setup to measure effect of various parameters on frost density, thickness and mass deposition rate was described in Sahin (1994) and Sahin (1988) where the geometry of flat plate was used. In addition to mentioned results he also showed there that with decreasing surface temperature or air temperature frost thickness increases faster but the effect of surface temperature was much more significant. With increasing air humidity frost thickness increased significantly but with increasing air velocity frost thickness increased slightly. Instead of measuring mass of frost, he measured the deposition rate of frost mass on the plate per unit area (kg/m^2s) and he showed that this rate is fairly constant during the test and only drops slightly after one hour from the beginning of frost deposition. It means that frost mass increases linearly in the first one hour of the experiment. It was shown that the surface temperature and air temperature change could not affect the frost mass deposition rate for two surface temperatures of -15 and -25°C and two air temperatures of 13 and 20°C. Air humidity increase from absolute humidity of 0.004 to 0.007 kg/kg resulted in significant increase of mass deposition rate however increasing air velocity from Re=2400 to 3700 increased mass deposition rate somewhat. They stated that higher air velocities increase both the mass deposition rate and frost density so that they offset the effect of each other and there is no much difference in frost thickness growth. They observed that at the beginning of frost growth, first a thin smooth layer of frost covers the surface. Then frost crystals that are relatively far from each other begin to grow on this layer in

vertical direction in about the same rate. This fact was previously observed by Hayashi et al. (1977b) and Kamath (1985).

Okoroafor and Newborough (2000) experimentally investigated the frost growth on aluminium flat plates coated with 3 hydrophilic coatings. They found that the purely hydrophilic polymer coated plate had a frost thickness about 10-30% lower than uncoated plate but no contact angle was reported in their work. They reported that frost density and frost mass deposition rate were higher in higher air relative humidity (RH of 70% vs. 40%).

Dyer et al. (2000) experimentally studied the effect of 5 different substrate surfaces on frost growth which were flat plates with the surfaces of bare aluminum plate (53°<CA<92°), coated aluminum plate (38°<CA<55°), Kapton tape (32°<CA<67°), PTFE on steel (74°<CA<106°) and PTFE tape (84°<CA<103°). They found that frost thickness grows 13% faster in hydrophilic coated surface in comparison to bare aluminum plate. Using microscopic observations, they also found that there are significant differences in liquid coverage of the surface between hydrophobic and hydrophilic surface in the very beginning of the frost formation process.

Luer and Beer (2000) experimentally investigated the frost deposition between parallel cold plates in air side laminar flow condition. The authors formulated a theoretical expression for frost growth, employing numerical iterations to find a correct temperature and density distribution inside frost layer. The results were compared against their experimental data and a fairly good agreement was observed except for very low surface temperatures of -16°C. Air velocity, air humidity and surface temperature were varied and authors found that an increase in air velocity results in more dense frost formation. The higher humidity resulted in faster frost thickness growth and higher frost density. Only exception was in lower humidity range: the frost density decreased initially and then started increasing afterwards. Decreased plate temperature resulted in faster and more porous frost layer grow while changing the air temperature at constant absolute

humidity, did not make a significant change on frost thickness growth. They also found that in the first 60 minutes of the frost test, frost thickness is about 3 times higher in leading edge in comparison to trailing edges.

Zhao et al. (2001) investigated experimentally the performance of a number of heat pump microchannel evaporators using CO_2 as refrigerant and a semi-empirical model was developed. But the study focused more on refrigerant side of the heat exchanger and did not consider frost formation on the air side for evaluation of microchannels heat exchangers. Actually the air side condition was chosen in low relative humidity region to minimize frost deposition on the surface.

Wu and Webb (2001) experimentally investigated possibility of causing frost to be released from cold surfaces of hydrophobic and hydrophilic coated flat aluminium plates by mechanical vibrations. The pattern of frost on hydrophilic surface was observed to be uniform while this pattern on hydrophobic surface was non-uniform and rough. After defrost, hydrophilic surface was totally wetted while on hydrophobic surface, there was individual droplets. They found frost could not be released from the surface by mechanical vibration and they observed similar frost grow rate on both hydrophilic and hydrophobic surfaces.

Cheng and Cheng (2001) developed a model for frost growth on flat plate which was based on surface temperature, air velocity and air humidity. The results of model were compared to previous experimental data of Yonko and Sepsy (1967) and to previous models of Jones and Parker (1975) and Sherif et al. (1993). A good agreement was found.

Huang (2002) addressed the frost growth shape prediction on a cylinder using conjugate gradient method. The author found that this method was able to predict the shape of frost except for initial and final times, which seemed to be singularity points.

Yun et al. (2002) proposed another approach of obtaining frost density and conductivity based on frost surface roughness. The roughness correlations contained 20% error and it was based on locations of peaks and valleys of frost layer for the specific geometry of a flat plate.

Jhee et al. (2002) investigated effect of surface treatment on frost and defrost performance of fin and tube heat exchangers experimentally. It was found that although the amount of residual water is less on hydrophobic treated coil, but three different hydrophilic or hydrophobic surface treatment with 3 different contact angles of 12, 74 and 124° generally had a small influence on coil thermal performance improvement. In their study 74° was referred to as the contact angle of bare aluminum while 12 and 124° were contact angles of chrome-based and PTFE (polytetrafluoroethylene) based coatings respectively. They claimed that lower density frost grows on the hydrophobic surface and the coil frost blockage ratio increases slightly faster for this surface treatment.

Mei et al. (2002) investigated frost formation on a 7kW heat pump system and experimentally observed that by adding a 1kW electrical heater to suction line accumulator, the frost formation on the evaporator could be postponed by a considerable time. The reason was that the heater increase both evaporator and condenser working temperature and the evaporator frosted less than before. Some of this heat was recovered in the condenser which was useful to heat up the conditioned space. Although the time of each frosting cycle, before it needs a defrost cycle, seemed to be doubled, the authors did not discuss whether 1kW electrical heater would consume more or less energy than the one required for additional defrost cycles. They measured the energy consumption required for defrosting a standard heat pump by using a 10kW electrical heater for melting the formed frost directly. Then they compared this result with their new heat pump adopting a 1kW heater in suction line accumulator which does not seem to be a fair comparison.

Lee and Ro (2002) investigated frost formation on a vertical plate experimentally by varying air temperature, humidity, velocity and surface temperature and frost thickness, mass and density were measured. They found that air humidity and surface temperature are the dominant factors affecting the frost formation. In higher humidity and colder surface temperature frost grew significantly faster, thicker and coarser. For lower air temperature and higher air velocities frost grows slightly in a thicker layer. Frost thickness was measured using a CCD camera while frost surface temperature was measured using an infrared thermometer. The common inaccuracy using infrared thermometer due to unknown surface emissivity was not discussed. The mass of frost was measured by mechanically scraping the frost off the plate at the end of experiment. In another work, Lee and Ro (2005) found that frost growth formulation for a simple model with super-saturation assumption results in better prediction of experimental data than the saturation assumption. They also found that initial density of frost significantly affects the results.

Song et al. (2002) experimentally investigated performance of a microchannel coil using CO2 as refrigerant in a split system in heating mode. In their study, instead of common horizontal refrigerant headers, vertical headers were used and authors tried to explain that non uniform refrigerant distribution causes non uniform frost growth and eventually results in non uniform air flow.

Cheng and Shiu (2002) experimentally studied the pattern and thickness of frost on a flat plate in two dimensions (frost thickness and depth) and good macroscopic and microscopic visualisation was performed by taking various pictures of frost growth at different time instants and conditions. Air temperature, humidity and velocity, and the cold surface temperature were varied to study the effect of them on frost growth. They found that frost grows not only in normal direction to the flat plate but also in opposite direction of air flow in the leading edge as well making a round tip head on the beginning of flat plate. However with increased air temperature or air velocity, the round tip edge becomes thinner and sharper. They also found that with higher air velocities more

crystals grow on the surface and this increases the thickness and density of the frost layer. Because more than one variable was varied at a time, the sole effect of each factor was hard to be quantified in their experiments.

Shin et al. (2003) investigated experimentally the effect of surface hydrophilicity on frost formation rate for three contact angles of 23, 55 and 88° on a flat horizontal plate. They coated aluminium plates with lacquer for 88° contact angle surface and plasma polymerization coating for other two surfaces. The air was at 12°C and plate was kept constantly at temperature of -22°C. Frost mass, thickness and heat flux were measured and fine thermocouples were placed in depth of the frost layer to measure the thermal conductivity of frost. They found that frost density and conductivity were slightly higher in hydrophilic surface (i.e. lower contact angles). Frost thickness was found to grow slightly slower in hydrophilic surface while frost mass was equal for all the samples. They proposed empirical correlations for thickness and mass growth, density (as a function of time and contact angle) and thermal conductivity (as a function of contact angle and density) and compared with previously available correlations literature. They claimed that thermal conductivity of frost layer in the depth of frost layer is 2 or 3 times lower than conductivity close to frost-air interface or at the plate surface all through the test.

Shimomura et al. (2003) investigated a 1-D frost growth model on a flat plate using non uniform frost properties i.e. density and thickness, and eventually compared results with experimental data of previous works. In other words, while previous models considered density variations through time, their model considered different densities at various frost depths and the density changed through time as well. The authors compared the results with previous uniform-property models and showed that their new model was able to predict the previous experimental data much better than previous models. They also concluded that for higher air velocities frost depth (thickness) growth rate decreases.

Kim and Groll (2003a; 2002; 2003b) compared frost/defrost time and heating performance of a conventional fin and tube coil with a microchannel coil in a unitary split system. They also compared effect of fin spacing for two 15 and 20 fin per inch coils and slope of the slanted coil in vertical and 15 degrees sloped. The vertical 15 FPI had the best heating performance and frosted in lower frequencies. It seemed that slanted coil did not help better water drainage and did not improve frosting performance. The angular installation, in 20 FPI, improved the heating capacity and system performance while in the 15 FPI it was the opposite. Any angular installation leads to more frequent defrost cycles. The effect of fin density was observed to vary. In vertical installations, 15 FPI performed better that 20 but in angular installations, both had equal performances. Coarser FPI leads to lower defrost frequencies. The authors noticed that the frequency of defrost cycles was proportional to how fast the accumulated frost blocks the air passage in the coil.

Cho et al. (2003) did some experiments on microchannels and compared regular microchannel with another type that has some cross link connections between tubes. Crosslink means that fluid in one tube can flow into the flow of other tubes depending on type of the cross link. Temperature and capacity were measured and authors observed that cross-link microchannel type showed slightly better performance in some special cases.

He et al. (2003) experimentally investigated frost growth on a fin and tube evaporator of a heat pump and claimed that there is a critical frost thickness below which the heat pump performance does not show noticeable changes. The heat transfer and air flow rate started dropping beyond this critical thickness (0.24mm). No wind tunnel or psychometric chamber was used in their experiments and authors performed their experiments during a specific winter night, for which ambient air dry bulb and humidity fluctuation were in an acceptable range.

Seker et al. (2004a) proposed a 1-D mathematical model to predict frost thickness, UA values of coil and air pressure drop for a specific geometry of a fin and tube coil. Frost distribution was assumed to be uniform over the heat exchanger. In another work of the same authors (Seker et al., 2004b), an experimental setup was introduced and the results of the previous model were compared against experimental data. A fair match was reported.

Lee et al. (2004) experimentally investigated the effect of hydrophilicity on frost formation on a flat plate for two different contact angles of 23 and 88°. The operating conditions were somehow different from what commonly being used in HVAC and it was in fact for household refrigerator application. The plate temperature was between -12 to -28°C and the air temperature was between 10 to 20°C. They found frost structure to be similar between two different contact angles. The lower contact angle surface (Hydrophilic) had slightly lower thickness and higher density but differences between results of two different contact angles were very small. Only in very low air humidity it was found that the frost density on hydrophilic surface increased 20 to 30% of frost density in hydrophobic surface. They found frost structure is a main function of air humidity and plate temperature while air velocity has minor effect on it; however air velocity had an effect on frost density. They divided the frost crystal shapes into three main groups of feather, grass and plate type that generally formed under high, medium and low air humidity respectively. Frost thickness increases with increase of air humidity or decrease of plate temperature but slightly affected by air velocity.

Kulkarni et al. (2004) used a previously developed simulation model to improve the designs of microchannel headers for better refrigerant distribution. A new radial shape for headers was proposed and analyzed. Iragorry and Tao (2004; 2005) proposed that a frost temperature and density measurement techniques could be employed to control defrosts of evaporators. They proposed that defrost initiation could be decided by measuring the thickness and density while defrost termination could be decided upon sudden change in frost surface temperature. Frost

surface temperature and its variation measured using an infrared thermometer and thickness was measured by a custom made set of strain gauges in a flexible beam element.

Na and Webb (2004a) adopted a super-saturation[3] assumption for water vapor near the frost layer and cold wall surface due to temperature gradient and proposed a new model, a new correction factor and new correlations for local frost density and conductivity on flat plate and a bank of parallel flat plates (Na and Webb, 2004b). Frost thickness was measured using a micrometer but the measurements, their uncertainty and potential interference with frost nucleation sites were not sufficiently discussed in detail in their main study (Na, 2003). The authors pointed out that that their attempt to measure the thickness by laser beam method, as originally proposed by Sanders (1974) and Mao et al. (1999), was not successful due to high roughness of the frost surface. The mechanical micrometer option was found to be more suitable in their experiments. The thickness was measured every 10 minutes to every 30 minutes. Even though this might be quite a large interval it seemed that it was able to show the trend of the data. The authors also showed that if previous saturation assumption is used, frost grow rate in their new model will be over predicted by 30%. In the other study, Na and Webb (2003) investigated the effect of surface energy and surface roughness on frost formation on a flat plate. It was found that lower energy surfaces (high contact angle for water droplets or hydrophobic surface) will delay the frost formation. The authors observed that water vapor near the cold surface changed its phase either by direct de-sublimation on the surface or by freezing immediately after condensation. Good microscopic

[3] Air is referred to as supersaturated when the water vapor pressure in the air near the surface is higher than saturated water vapor pressure at that specific air temperature which is in proximity of the surface. This happens because when air comes to contact with the surface, initially its temperature decreases quickly and then the water saturation pressure will change to a new lower value consequently. However the previous amount of water content or existing water vapor pressure in that part of the air is more than this new saturation pressure at the new colder temperature. So the excessive water content should condense and get out of the mixture. This is an unstable state (thermodynamically meta-stable) and water vapor will ultimately condensate or sublimate quickly on the cold surface. The level of supersaturation defined by Sanders (1974) is $\frac{P_{vapor}-P_{vapor,sat.suf.}}{P_{vapor,sat.surf.}}$ in which P_{vapor} is the water vapor pressure in the air (the same as the water vapor saturation pressure at the dew point temperature) and $P_{vapor,\ sat.}$ is the saturate water vapor pressure at the surface temperature.

pictures from frost formation in initial and later stages were reported. The authors found that inhomogeneity in surface energy caused a heterogeneous frosting pattern and surface roughness yielded to faster frost nucleation.

Hoke et al. (2004) studied experimentally the effects of surface hydrophilicity on frost formation structure by growing frost on two different flat plates made of glass (CA<10°) and PTFE (PolyTetraFluoroEthylene) (84°<CA<103°) under forced convection. They found that frost deposition on some surfaces are “condensation frosting” (water vapor forms liquid droplets that freeze immediately and grow and coalesce with neighbouring droplets) rather than “ablimation frosting” (direct deposition of water vapor on the cold surface as a solid frost) although surface temperature is well below zero Celsius or triple point of water (Hoke, 2000). The study showed that in mature frost growth, frost grows faster in thickness and lower in density on hydrophilic surfaces in comparison to hydrophobic surfaces while for the early frost growth period (a few minutes), totally the opposite is true (Hoke et al., 2004). However the differences were not significantly large. Frost density varied 40% between hydrophobic and hydrophilic surface in early frost growth periods and only 15% different in mature frost growth. Although the frost conductivity has always been a function of frost density, but in the frost growth on hydrophobic and hydrophilic surfaces there were other factors affecting conductivity like orientation of frost spires within the layer. This generally leaded to this effect that a slightly higher conductive frost layer always formed on the hydrophilic surfaces (Hoke et al., 2004). Their results about frost density however were somehow in contradiction with previous findings of Shin et al. (2003) who have found that frost density and thermal conductivity both are slightly higher on hydrophilic surfaces. They suggested hydrophobic coated surface for compact evaporators where fin spacing is low because hydrophilic surface in general create a thicker frost layer that reduces the air flow more quickly than hydrophobic surface (Hoke, 2000).

Wang and Liu (2005) suggested desiccant plates to be placed before evaporator to prevent frost and used Zeolite plates with an electrical power consumption of 50W for each Zeolite plate, to cover 0.08m² area of a coil. The authors concluded that this option might solve the frosting problem. But no experimental data were showed and initial cost of desiccant plates, comparison of additional electrical energy consumption for desorption of plates and comparison to conventional defrost method were not addressed. Authors only presented the air pressure drop air temperature and humidity change through desiccant plates using a simulation with basic equations.

Tian et al. (2005) investigated frosting on a fin and tube evaporator coil in automotive industry experimentally and developed a model that was able to predict the performance. The details of the model, which was curve fit based, were referred back to the literature and were not directly revealed in their paper. Since the scope of the paper was not to study the frost growth itself, they concluded that the reasons of frost formation were mainly compressor low performance and valve control strategies that needed to be improved.

Cleland (2005) discussed some coil frosting conditions and proposed some methods to delay frost growth by controlling the temperature difference between air and cold surface.

Xia and Jacobi (2005) proposed a method to calculate the heat and mass transfer coefficients on flat tube heat exchangers in wet and frosted surfaces. The results of their solution were compared with other work done by the same authors (Xia and Jacobi, 2004) and a 3% deviation was reported. In the 2004 work, the authors presented an analytical solution for fin efficiency and conduction in a one dimensional fin and proposed that this analytical infinite series solution can be replaced by first term approximation with a good accuracy. In another study (Xia et al., 2005; Xia et al., 2006), heat transfer coefficients, pressure drop, weight and other frost grow parameters were experimentally investigated on flat tubes heat exchangers with five different louvered fin

geometries and authors made recommendations for fin designs. The effects of fin design and heat exchanger depths were not carefully isolated. Flat tube microchannel heat exchangers are similar to standard microchannel coils from air side point of view but different from refrigerant side point of view because flat tubes do not have any internal ports. The main reasons of different in frost results of first dry cycle and next re-frost wet cycles was introduced to be water retention and frozen droplets from previous defrost cycle, which significantly affects the pressure drop and heat transfer on next cycles. In another report on the work (Jacobi et al., 2005), all the results found on flat tube and round tube heat exchangers were summarized again and more detailed explanation was provided about results, the effect of fin geometries on the performance, the characteristics of the water drainage and how to model it, and an attempt to calculate the air pressure drop on wet coils.

Zhong et al. (2005) experimentally investigated off cycle water drainage behaviour of various geometries of microchannel (flat tube) and fin and tube heat exchangers using dynamic dip testing. They stated although the amount of condensate might be different between real coil operation conditions and dip tests, results from this test method is still able to provide repeatable data to predict the general relative behaviour of experimental data of real time drainage. Near 25 different coils samples (0.2m by 0.2m) were hung from a digital balance to measure their weight history in time as they used to come out of water reservoir. A model was also developed to predict the water drainage behaviour based on gravity, surface tension and air drag effects and verified against their experimental data. They found that fin and tube geometry has a quick drainage while louvered geometry of microchannel (flat tube) heat exchangers has a slower drainage. Inclination of the coil had a small influence on drainage and offset strip fin (one type of fin in their work) drained better than louvered fin geometry. In a follow up work Joardar et al. (2006) used the same method and setup to study the effect of coatings and coil inclination in a broader extent. For coils with fins without louver, inclination helps drainage significantly but in

louvered fin inclination had minor effect on drainage due to competing effects of gravity and surface tension. Hydrophilic coated coil in any inclination angle retained less water than hydrophobic coated coils. They found that a geometrical change by adding special strips on the bottom of heat exchanger can improve water drainage up to 20%. In a follow up work, Liu and Jacobi (2008) addressed the issues about reliability of dip testing method and they found that for fin and tube heat exchangers, hydrophilic coating could increase the amount of water retention while in microchannel coils hydrophilic coated coils retains less water. They also found that the speed of drawing the coil out of water reservoir affects the results and sometimes spraying or droplet injection methods should be employed to simulate a closer condition to what really happens in the real frost/defrost cycling.

Zhong et al. (2006) proposed a new method to make super hydrophobic surface with contact angle of 148° by cutting special pattern of micro grooves into metal surface. In a similar work, Sommers and Jacobi (2006) made a hydrophobic surface by cutting micro scale (30μm wide by 10μm depth) grooves into plain aluminium surface without using any chemical coating. They found that with this method, surface contact angle could be increased about 54° in comparison to plain aluminium surface and a lower inclination angle of the plate is needed to let the droplet slide down. They also found the critical volume of the droplets (the volume of droplet that above which the droplet starts sliding down the surface) reduced about 50%. In a follow up work Sommers and Jacobi (2008) developed a simple mechanistic model to predict the critical droplet size on the micro grooved surface. A complementary work was done by Liu et al. (2009) and revealed more details of shapes of droplets and effect of groove depth on contact angles and drainage enhancement.

Yang et al. (2006b) proposed a mathematical model that predicted frost thickness and frost density on fin and tube coils. The model was applied to two different geometries of 2 rows and 8 rows sample coils placed in air stream. Experimental data were compared with the numerical model results and a perfect match was reported. The model discretized the geometry into small cells and then heat and mass balance were written for each cell and solve them numerically using a Fortran code. The model assumed a uniform frost thickness for a fin and a uniform frost thickness for a tube in each cell. The author did not provide information about size of each cell but it seemed that each fin, plus the length of the tube pertained to it, has been assumed to be in one cell. Fin spacing was changed between 5 to 20mm while this is far from the conventional fin and tube coils that have fin spacing between 1 to 2mm. In another study by the same authors, Yang et al. (2006a) optimized the fin spacing in different rows of an 8 rows fin and tube coil. They showed that if fin spacing is larger in the first row (10mm) and smaller in the next rows (7.5mm 4th row and 5mm for 8th row), the average heat transfer could be increased by 6% and frost time for each cycle could be increased by 13%. The details of various experimental tests were referred back to their previous work (Yang et al., 2006b); however, in that work also various experiments that could support the result of this optimization were not presented. In their previous work published by almost the same authors (Lee et al., 1997; Lee et al., 2003), a mathematical model was presented to predict frost growth on a flat plate and successfully compared with experimental data obtained from a test setup. It was shown that the developed model was able to calculate the frost thickness, density and frost surface temperature within the 10% of experimental data, except at early stages of frost growth. A new correlation between heat and mass transfer coefficients was also proposed $(\mathrm{Le}^{1-\mathrm{n}} = 0.9)(\mathrm{Le}: \mathrm{Lewis\ number})$. It was found that thickness and density have their largest amount in the fins leading edges and decrease with distance from the leading edge. Frost thickness was measured using digital micrometers and frost surface temperature was measured by infrared thermometers. The details of thickness

measurements so that it does not affect the frost growth or the common problems of surface emissivity in using infrared thermometers were not discussed.

Tso et al. (2006) developed a model for frost growth on fin and tube coils considering uneven temperature distribution on the coil surface and matched the model results with experimental data of Kondepudi and O'Neal (1993). The mass of frost and air pressure drop was compared to experimental data but the thickness variation, which was introduced to be a result of non uniform surface temperature, was not verified against experimental data.

Wu et al. (2007a) experimentally investigated early stages of frost formation on horizontal flat copper plates using microscopic observations. The plate temperature range was between -20 to 0°C and air relative humidity varied between 15 to 85% in constant dry bulb temperature of 22°C. They observed that frost formation starts with formation of small supercooled liquid droplets that freeze quickly. Then initial frost crystals forms and grows on the frozen droplets while some of crystals collapse on the existing crystals and finally frost layer continues to grow. They found that formation of droplets happens for all temperatures and humidity range tested. The droplets freeze sooner in lower surface temperatures and higher air relative humidity while droplets are smaller at lower surface temperature and lower air relative humidity. They found that the freezing time for these supercooled droplets is mainly a function of surface temperature while air humidity had smaller effects on it. The freezing time varied between 2 or 3 minutes to 17 minutes in various conditions. More detail analysis of their data with pictures of their work showing different forms of frost crystals are discussed in the next chapter. The contact angle of the bare copper was reported 84° in their work. Using the same setup, Wu et al. (2007b) investigated early stages of frost formation tested a bare and a hydrophobic coated copper surface with contact angles of 56° and 110° respectively. They found that compare to bare copper surface, hydrophobic surface has sparser distribution but larger size of supercooled droplets and also delayed freezing of droplets and frost formation. They observed a lower frost thickness on hydrophobic surface. They tried to

explain that the reason for formation of supercooled droplets on the surface is simply because Gibbs free energy barrier of water nuclei is smaller than of ice nuclei so that droplets always form on the surface. They explained that because hydrophobic surface has a higher energy barrier than the bare surface, the droplets form more on the bare surface. More explanation about discussion of free energy of the surfaces is provided in the next chapter. Reader should note that in both of their works, they used a relatively high air dry bulb temperature for their experiments maybe because their application has been different from HVAC applications. In their experiments, the air had a lot of moisture content in comparison to air conditions that HVAC standards require for testing heat pump units (AHRI). To give a quantitative criteria, their air condition with air dry bulb equal to 22°C and the plotted relative humidity of 35, 50 and 85% in their figures, is equivalent to absolute humidity ratio of 0.0058, 0.0083and 0.0140 kg vapor/kg air respectively while HVAC standards require frost test to be done in air dry bulb temperature of 1.67°C and relative humidity of 82% which is equivalent to absolute humidity ratio of 0.0035 kg vapor/kg air. If we want to simulate the same absolute humidity ratio of 0.0035 in their work, the relative humidity should be around 20% for the air dry bulb of 22°C. Their graphs shown in their work then should be extrapolated somehow to this lower relative humidity and caution should be used to apply their result to HVAC applications such as the present study.

Huang et al. (2007) investigated experimentally the non uniform air distribution on a fin and tube evaporator coil of an air to water heat pump under frosting condition. The research focused on air distribution and its effect on the malfunctioning of thermal expansion valve. In another study, Huang et al. (2004) found that with a pre-start fan strategy in a defrost cycle the unnecessary high discharge pressure could be avoided.

Wang et al. (2007) proposed a new super hydrophobic coating for surface that could achieve a very high contact angle of 155° to avoid frost formation on the surface. The pictures showed that frost grows differently between bare copper surface (needle type) and the super hydrophobic

coated surface which was braches on the top of frozen supercooled droplets. Authors tried to conclude only from visual observations that thickness on this new super hydrophobic surface is less than bare surface but no quantitative comparison was offered.

Park and Hrnjak (2007) investigated study of a microchannel capacity as a gas cooler not an evaporator. The temperature of tubes was not constant in each pass and because of the special circuiting, some tubes had higher temperatures than others. Authors offered that if they can insulate the effect of heat conduction between hot tubes and cold tubes, by cutting some fins that connect those tubes, the capacity of the microchannel could be increased around 4% with uncertainty of 2.5%.

Kim et al. (2008) investigated frost formation on a cylinder experimentally and proposed empirical dimensionless correlations for frost properties. In these correlations, frost thickness, density, surface temperature and heat transfer coefficient were derived as functions of Reynolds number, Fourier number, absolute humidity, dimensionless air temperature and dimensionless cold surface temperature which were within the 15% deviation of the experimental data recorded by authors.

Padhmanabhan et al. (2008) experimentally investigated a comparison of frost and defrost cycling performance between a microchannel heat exchanger with louvered fin and a fin-and-tube heat exchanger with straight fins on a 4-ton (48,000 Btu/hr) heat pump system. Load cells were used to measure the mass of frost accumulation on the coil of the unit during heating tests. Data showed that the frosting time of the microchannel heat exchanger is more than 50% shorter than for the fin and tube heat exchanger. The average heating capacity and system performance were also lower for the system with microchannel heat exchangers. Higher frost growth rate in microchannel heat exchangers were concluded to be due to residual water in the coil after defrost, augmented temperature difference between air and the surface of the heat exchanger, and

preferential frost nucleation sites on the louvered fins and microchannel tubes. Blowing nitrogen on the microchannel coil removed any visible water retained in the coil after the defrost cycle but the cycle time increased only by 4% with respect to wet and frost conditions. The cycle time of the same microchannel starting with dry condition was about 60% longer than the cycle time in wet and frost conditions.

Park and Jacobi (2009) developed a generalized air side heat transfer and pressure drop correlation for the data of 121 different louvered fin microchannel samples in dry working condition collected from the literature. The correlations could predict the Colburn j-factor and Fanning f-factor could predict within 12 and 16% error respectively which was stated to have improved accuracy and broader generality to predict the bank of data in comparison to previous correlations.

Zhang and Hrnjak (2009) experimentally investigated performance of two different flat tube heat exchangers and a plate fin and tube heat exchanger in frosting condition. Air pressure drop and heat transfer coefficients of coils were measured and it was shown that flat tubes had a higher capacity than plate fin and tube coil. The water drainage, which was assumed to be a major factor in frosting time, was considered and it was found that one of the flat tubes coils with parallel fin design has a significantly better water drainage than the other flat tube coil with serpentine fins.

Huang et al. (2009) experimentally investigated effect of a new hydrophobic anti-frosting paint on fin and tube heat exchanger to increase the time of frost cycle. Although coated coil could extend the frosting time to about 3 times as of uncoated coil for the first dry start cycle, but for the second and third wet start cycles it performed similar or even worse than uncoated coil. Authors stated that further research is required to come up with a solution to dry the coil after each defrost cycle and take the absorbed water out of this coating, so that the new coating could extend the frosting cycle time significantly in practical use.

Lenic et al. (2009) investigated a 2-D modelling of frost growth on the fin and tube heat exchangers and verified with their experimental data. The real fin and tube coil was not used in the air stream and instead the study focused on frost growth on a flat plate in 2 dimensions. One dimension was the frost thickness itself and the other one was distance from the fin leading edge in depth of the plate along the air stream. The model discretized the equation and solved them numerically using finite volume approach. Effect of different air humidity, air temperatures and air velocities was investigated. Although a very good approach was proposed to solve the problem, more attention was paid to accurate prediction of air side behavior of the phenomenon and frost formation complexity itself was somehow neglected. For example only frost thickness in the middle of the plate and air temperature, which was passing over the plate were compared and validated with experimental data. The authors did not mention about how to consider tubes in their model.

Kim et al. (2009) developed a model to predict the frost growth on a flat vertical plate and compared their results with their experimental setup data. They found that thickness of frost is only slightly higher on leading edges compare to frost thickness at the trailing edge.

Shao et al. (2010) focused on overall performance difference of two systems with microchannel and fin and tube evaporators under frosting condition for a single frosting cycle by developing a model for each case and comparing against their experimental tests. Although a good modelling approach was taken, the model did not try to validate each model component like evaporator or condenser separately with experiments and tried to predict the total capacity and COP of the whole cycle. The details of evaporator model equations about sensible and latent heat balance, the frost thermal resistance and properties, segmentation of the model especially for microchannel along the air direction and implementation of louvered fins in the model were not revealed in details and mostly referred back to the literature. For example, the model assumed a constant frost resistance for the whole evaporator model while the images in the paper showed a non uniform

distribution of frost on the evaporator coil so that in some locations, there was no frost at all. The results of the simulation matched the experimental data if, as authors explained, refrigerant and air distribution patterns are applied to the model but the details of mal-distribution, which was the key point to match the experimental data with results of the model, were not sufficiently explained. The authors pointed out that the effect of fan speed and the effect of fin density on the performance could be studied by using their developed model but the experimental data were not adequate to support this conclusion.

Fossa and Tanda (2010) investigated frost growth on vertical channels (flat plates) under natural convection. Various plate dimensions with different relative humidity (30 to 85%) and various plate temperature (-4ºC to -40ºC) and frost mass, thickness and density were measured. Authors used thermocouples to measure surface temperature with uncertainty of 0.1ºC and infrared camera to measure frost surface temperature with uncertainty of 0.8ºC. For frost thickness measurements, two approaches were used. First, a nylon tip fin attached to a micrometer was visually moved to the frost surface and second, an optical sensor was used to emit a pulsed light and measure the intensity of reflected beam to measure the frost thickness. The details of the installation of the temperature sensor were not presented and potential interferences with the frost growth were not discussed. The authors investigated frost growth under natural convection and the process took few hours. Thus, it is likely that their results cannot be applied to forced convection frost growth on heat exchangers, in which the air flow regime is quite different and the frosting mechanism is significantly more rapid.

A recent experimental study on frosting performance of parallel-flow parallel-fin (PF^2) flat tube microchannel heat exchangers with horizontally installed tubes was presented by Zhang and Hrnjak (2010). They found that the time of the first frost cycle was 21% longer than the second frost cycle and considerably longer (92%) than the time of the 15th consecutive frost cycle for PF^2 heat exchanger. Results showed that 10% decrease in air relative humidity from 80 to 70%

caused the frosting time to increase 42%. They observed an improvement in frosting performance over a conventional serpentine fin which they attributed to better drainage capability of the PF^2 heat exchanger.

The affecting parameters on frost formation from previous studies have been summarized in the Table 1. This is just a qualitative approach to make a better understanding about how each parameter generally affect the frost growth process in an increasing or decreasing way.

Table 1: Summary of affecting parameters on the frost formation characteristics in different studies

Affecting factor	Study	Geometry	Frost Thickness	Frost Mass (Weight)	Frost Density	Frost Conductivity
Increasing Surface Temperature	Yonko & Sepsy (1967)	Flat plate (horizontal)	Decrease	-	Increase	Increase
	Brian et al. (1969, 1970) & (Shah 1969)	Flat plate (horizontal)	-	-	Increase	Increase
	Biguria and Wenzel (1970)	Flat plate (horizontal)	-	-	Increase	Increase
	Hayashi et al. (1977)	Flat plate (horizontal)	-	-	Increase	Increase
	O'neal (1982)	Parallel flat plates	Decrease	-	Increase	-
	Ostin & Andersson (1991)	Parallel flat plates (hor.)	Decrease	No effect	Increase	Increase
	Mao et al. (1992)(1993)	Flat plate (horizontal)	Decrease	Slight decr	Increase	Increase
	Sahin (2000)(1994)	Parallel flat plates (horiz	Decrease	No effect	Increase	Increase
	Lüer and Beer (2000)	Parallel flat plates (horiz	Decrease	-	Increase	-
Increasing Air Humidity	Yonko & Sepsy (1967)	Flat Plate (horizontal)	Increase	-	Increase	Increase
	Brian et al. (1969, 1970) & (Shah 1969)	Flat plate (horizontal)	Increase	Increase	Slight incre	Slight incre
	Biguria and Wenzel (1970)	Flat plate (horizontal)	-	-	Decrease	Increase
	Yamakawa et al. (1971)(1972)	Flat plate (horizontal)	Increase	Increase	Increase	Slight incre
	O'neal (1982)	Parallel flat plates	Increase	-	Increase	-
	Ostin & Andersson (1991)	Parallel flat plates (hor.)	Increase	Increase	Increase	Increase
	Mao et al. (1992)(1993)	Flat plate (horizontal)	Increase	Increase	Increase	Increase
	Sahin (2000)(1994)	Parallel flat plates (horiz	Increase	Increase	Slight decr	Decrease
	Lüer and Beer (2000)	Parallel flat plates (horiz	Increase	-	Increase	-
Increasing Air Velocity	Yonko & Sepsy (1967)	Flat Plate (horizontal)	No effect	-	Increase	Increase
	Brian et al. (1969, 1970) & (Shah 1969)	Flat Plate (horizontal)	Slight decr	Increase	Increase	Increase
	Biguria and Wenzel (1970)	Flat Plate (horizontal)	Slight decr	-	Increase	Increase
	Yamakawa et al. (1971)(1972)	Flat Plate (horizontal)	Increase	Increase	Increase	Increase
	Hayashi et al. (1977)	Flat plate (horizontal)	No effect	Increase	Increase	Increase
	O'neal (1982)	Parallel flat plates	Slight incre	-	Increase	-
	Ostin & Andersson (1991)	Parallel flat plates (hor.)	No effect	Increase	Increase	Increase
	Mao et al. (1992)(1993)	Flat plate (horizontal)	Slight incre	Increase	Increase	Increase
	Storey (1997)	Flat Plate (Horizontal)	No effect	-	-	-
	Sahin (2000)(1994)	Parallel flat plates (horiz	Slight incre	Increase	Increase	Slight Incre
	Lüer and Beer (2000)	Parallel flat plates (horiz	Increase	-	-	-
Increasing Air Temperature	Brian et al. (1969, 1970) & (Shah 1969) (Tair>0℃)	Flat Plate (horizontal)	Decrease	No effect	Increase	Increase
	O'neal (1982)	Parallel flat plates	Slight decr	-	-	-
	Mao et al. (1992)(1993) (Tair>0℃)	Flat plate (horizontal)	Decrease	Slight decr	Increase	Slight decr
	Tao et al. (1994) (Tair<0℃)	Flat plate (horizontal)	Increase	-	Increase	-
	Sahin (2000)(1994) (Tair>0℃)	Parallel flat plates (horiz	Decrease	No effect	Increase	Increase
	Lüer and Beer (2000)	Parallel flat plates (horiz	No effect	-	-	-
Increasing distance from leading edge	Biguria and Wenzel (1970)	Flat plate (horizontal)	-	-	Decrease	Decrease
	O'neal (1982)	Parallel flat plates	No effect	-	Slight decr	-
	Mao et al. (1992)(1993)	Flat plate (horizontal)	Slight decr	Decrease	No effect	Slight decr
	Tao et al. (1994)	Flat plate (horizontal)	Decrease	-	Decrease	-
	Lüer and Beer (2000)	Parallel flat plates (horiz	Decrease	-	-	-
Increasing ...*	Hoke et al. (2004) & Hoke (2000)	Flat plate (horizontal)	Increase	Various	Decrease	Increase
Increasing...**	Jhee et al. (2002)	Fin and Tube	Slight incre	Increase	Decrease	-
	Hoke et al. (2004) & Hoke (2000)	Flat plate (horizontal)	Decrease	Various	Increase	Decrease
	Dyer et al. (2000)	Flat plate (horizontal)	Decrease	-	-	-

* Increasing surface contact angle (make it more hydrophobic) in early frost growth (first few minutes)

** Increasing surface contact angle (make it more hydrophobic) in mature frost growth

The summary of what have been found in the present study was consistent with the majority of data presented in Table 1. The details will be discussed later in the following chapters and exceptions will be addressed in detail.

A part of the present initial study was published before on frost formation on fin and tube coils with a comparison to microchannels (Moallem et al., 2010b). Another paper focused on microchannel and influence of each factor on its frosting performance (Moallem et al., 2010a). More detailed analysis of effect of different parameters on frost formation was published in International journal of refrigeration (Moallem et al., 2012b). Effect of coatings on frost and defrost behaviour of microchannel was presented on another conference paper (Moallem et al., 2011). More detail data analysis and comparisons and suggesting solutions about effect of coatings were published in journal of Experimental Thermal and Fluid Science (Moallem et al., 2012c). The main part of construction phase of the device and measurement techniques of small microchannel samples were published in another work on ASHRAE Transactions (Hong et al., 2012) in which I was the second author. The experimental result of the present research were also used in a modelling work (Padhmanabhan et al., 2011) in which I was the last author. A couple of other studies about the effect of geometry and coatings on small scale microchannels are under review in two relevant journals (Moallem et al., 2012a; Moallem et al., 2012d).

2.3 SUMMARY AND CONCLUSION FROM THE LITERATURE REVIEW

From the literature survey, it appears that there is a lack of information about the specific isolated effect of fin geometrical dimensions on the performance of the microchannel heat exchangers under frosting operating conditions. The complexity of the phenomena makes the theoretical analysis problematic and most of the results are based on a limited range of experimental tests in which the effects from the operating parameters such as surface temperature and geometry are difficult to isolate and quantify (Kim and Groll, 2003a; Xia et al., 2006). Other results are based on fin and tube geometry (Yang et al., 2006b) or bank of parallel fins or simple geometries such as flat plates (Lenic et al., 2009; Lüer and Beer, 2000; Na and Webb, 2004a) and they are not directly applicable to air flow in between louvered folded fins in microchannel heat exchangers.

To address this challenge, a special custom made small scale test facility was prepared to be able to test one individual sample column of folded fins used in microchannel heat exchangers. The sample bank is cut out from commercially available coils and mounted on a cooling module that replicates the working conditions. The set up eliminates the complexity due to non uniformity effects in the fin surface temperature. The refrigerant side is completely decoupled from the air side and the fins are attached to aluminium plates with controlled wall boundary temperatures. Preliminary data of previous studies, showed that there are still some degree of non-uniformities in frost thickness and properties even in results of a 0.3m by 0.3m (1ft by 1ft) microchannel coils (Moallem et al., 2010a; Moallem et al., 2012b). First, the internal refrigerant heat transfer coefficient changes along a single tube due to thermal entry length of the refrigerant. This results in non-uniform surface temperature distribution on outside surface of a single tube. Second, all the tubes do not receive the same amount of refrigerant due to non uniformities in header distributions and this cause different frost thickness on each part of the coil. These thermal entry lengths and header non-uniformities totally change again when a new coil is inserted for test due

to its different internal geometry. This results in different outside surface temperature for the new coil and this makes comparison of two different coils even more difficult. The last part of non uniformity is non uniform frost growth in different locations on a single fin. The bases of the fins which are attached to the tube have a colder surface temperature than other ends (center) that are far from the tube. However, because microchannel coils have a relatively shorter tube spacing (around half inch) in comparison to fin and tube coils (around 1 inch) the fin efficiency in microchannel coils are closer to 1. There are also other geometrical aspects other than tube spacing which increase the fin efficiency of microchannels such as fin total area, etc. For the geometries of the present study the fin efficiency varied from 0.91 to 0.97 and this indicates that the temperature of the center of the fin is not significantly different from the fin root temperature.

These shortcomings and non uniformities were eliminated with the experimental apparatus described here and only last insignificant part of frost formation, non uniformity, remains. Isolating one row of a coil as a sample fin in a controlled surface temperature is an effective approach to isolate the effect of surface temperature and study the impact on frost formation due to fin design modifications. Moreover, in a real coil, it is quite impractical to obtain a true value of the fin surface temperature because attaching a thermocouple on the surface without insulation will show an average temperature of air and the surface and with insulation, it blocks the heat transfer between air and refrigerant at that small area and surface temperature will be lower than other non disturbed part of the coil. All attempts made to attach a thermocouple to read the correct fin surface temperature have failed. Other solutions of infrared cameras and infrared thermometers also failed because of highly rough surface of the heat exchanger and unknown various emissivity of the surface in different convex and concave points that affects the results significantly. With the proposed experimental apparatus the surface temperature was controlled to the range of accuracy of thermocouples of ±0.5°C.

To study the effects of fin density and fin depth and existing of louvers, different type of fin samples were prepared. Three different fin density of 10, 14 and 20 fin per inch, three different fin width 8, 10 and 13mm and three different fin depths of 19, 26 and 30 mm are going to be tested. One fin design without louver was also included in the samples. 5 samples with the same geometry and different hydrophilic and hydrophobic coatings were also investigated to evaluate their frost and defrost behaviour and water drainage characteristics.

A set of three correlations for frost thickness, air face velocity drop, and heat transfer coefficient that properly account for frosting operating conditions of 7 different geometry of microchannel heat exchangers each working under three different surface temperature frosting conditions is going to be developed and verified against experimental data. The benefit in using these correlations are they do not need a model approach and a code to converge and finds the values of frost thickness or heat transfer coefficients. They can be used in a simple excel sheet and finds the values of frost thickness, air face velocity and heat transfer coefficient at each desired moment of the frost test for any geometry in the range of present study.

CHAPTER III

FUNDAMENTAL UNDERSTANDING OF FROST FORMATION

3.1 INTRODUCTION

Ice may form either by deposition of water vapor from the air on the surface or by freezing of liquid water. In both cases, the initiation of ice on the surface occurs by the nucleation of a small ice embryo. Then this crystal structure begins to grow either from the surrounding liquid or vapor phase (Hobbs, 1974). In the present study, the growth begins from the water vapor in the air. This growing crystal structure is called frost. The surface that frost grows on it is called substrate in this context. Frost forms on a surface when humid air comes in contact with the surface which has a temperature below the dew point temperature of entering air and also below freezing point of water (0ºC). There are several classifications for frost (ice crystals) formation process among different researchers. Hobbs (1974) and Fletcher (1962) divide the general process into two main phases:

1) Nucleation Phase,

2) Growth Phase

3.2 NUCLEATION PHASE

In the process of frost or ice formation generally we are concerned with three phase change processes – the condensation of water vapor to form droplets, the freezing of water droplets to form ice-crystal and the direct formation of ice-crystal from the vapor by ablimation. These phase changes typically do not begin in a continuous manner, but require nucleation (Fletcher, 1962). Nucleation process in general is divided into two different categories; homogenous nucleation and heterogeneous nucleation. If there is no surface or other material than water (and air) present during freezing process, then ice phase must be initiated by water molecules combining together to form an ice embryo which can grow spontaneously. This initiation process is called homogeneous or spontaneous nucleation. Although it is not possible to cool large quantities of liquid water far below 0ºC, without initiating freezing, small droplets of water can be cooled well below 0ºC and yet still remain in liquid state. This liquid water below 0ºC is called supercooled or undercooled water (Hobbs, 1974). Similarly, if we have pure water vapor, we can make it reach the supersaturation level either by cooling it or by compressing it isothermally. To attain the state of lowest energy, the vapor should now condense, but this condensation must start with the formation of small water droplets, and these are unstable under the fluctuations of thermal agitation. The vapor thus remains in its metastable gaseous state and temporarily no condensation takes place. As supersaturation increases, small droplets become more stable and the probability of their survival increases, until at a certain critical supersaturation the survival rates become appreciable and condensation to a fog take place. Such nucleation that occurs within the bulk of a pure substance, as mentioned before, is referred to as homogenous nucleation (Fletcher, 1962). In the other hand, if nucleation of ice phase occurs on a surface or even on a foreign particle in the air or water with particle acting as a nuclei, this ice embryo is said to form by heterogeneous nucleation (Hobbs, 1974). In the present study, at the beginning of frost tests, frost forms on the surface of heat exchangers which is a heterogeneous nucleation while after the surface was

covered with frost, frost deposits on the existing structure. This deposition might not be in nucleation phase anymore and it is actually in Growth phase. But as long as both homogeneous and heterogeneous nucleation happens at least in some special cases of our tests, both of them are discussed here.

3.2.1 Homogeneous Nucleation

Homogeneous nucleation is important from that point of view that almost every study of heterogeneous nucleation uses the same concept or result of homogenous nucleation with minor modifications (Fletcher, 1962). So it is worthwhile to explain a little about the homogeneous nucleation first. In homogeneous nucleation, nucleation may start by freezing of a part of a supercooled liquid droplet or by direct depositing of water vapor from the air on the existing ice embryo (Hobbs, 1974). In supercooled water, some fluctuations in structure result in rapid microscopic variations in local temperature, pressure and density or in the structure of an existing phase (Frenkel, 1946). These variations are caused by continuous transient formation and disintegration of ice embryos within the liquid water. When an ice embryo is larger than a critical size, it might be thermodynamically advantageous for it to continue to increase its size (Hobbs, 1974). In this case it grows into a larger microscopic ice crystal. Expressions for number of ice embryos which can grow in a unit volume of supercooled liquid in a unit time is offered by Turnbull and Fisher (1949). In homogeneous nucleation of ice by deposition from vapor, supercooled or supersaturated vapor starts to deposit on an existing ice embryo that has a critical microscopic radius size. In this case, the rate of deposition depends on number of ice embryos that can get to critical radius size so that they can grow larger after that point. The rate of formation of these ice embryos in this theory depends on the difference between water vapor pressure in the environment and the saturated vapor pressure on the ice surface, the internal free energy between ice and water vapor, a shape factor of ice embryo, the temperature of ice surface

and a numerical constant. We do not tend to get involved into explanation the series of expressions that gives the quantitative approximation value of rate of formation for microscopic ice embryos. The reason is, beside the fact that it is not very informative for the reader, it needs explanation of a large number of different quantities and parameters. For more details please refer to Hobbs (1974). At this stage, nucleation can continue in two competing processes; by direct deposition of vapor on ice embryo or condensation of vapor as a supercooled liquid droplet followed by freezing. To determine which mechanism is dominant, Fletcher (1962) did a theoretical analysis and showed domination of either mechanism depends on values of pressures (water vapor pressure in the environment and saturate water vapor pressure at ice surface temperature) and ice temperature and he suggested a calculation process to determine which side will be dominant at each condition. Assuming the numerical values for parameters used in equations, Krastanow (1940) calculated that the deposition of ice crystals from vapor by homogeneous nucleation should be predominant over the condensation of water droplets for temperatures below -65°C if the saturation ratio with respect to water were about 14. This calculation was repeated by Dufour and Defay (1963) with different assumptions for parameters. They stated that homogeneous nucleation of ice by deposition from vapor is unlikely above -100°C (reproduced from Hobbs (1974)). So there is still not a commonly accepted theory that all researchers agree up on and this is mainly because of high uncertainties that one can have in choosing the influential parameters which are initial shape of ice embryo (cubic vs. hexagonal prism), interfacial energy between ice and water vapor and other parameters. But relying on either of these studies, the conclusion is in temperature above -65°C which is the case of the present study, the homogeneous nucleation phase after formation of ice embryos continues with condensation of water droplets followed by freezing (The direct ablimation of water vapor from the air on the current structure is the subject of 'Growth phase' - not nucleation phase- which will be explained in the following sections). There are many experimental studies in the literature that determined the nucleation point temperature. Because one of the questions about homogeneous

nucleation is how low the temperature of a water droplet could be while it still stays in liquid state. To determine this nucleation point, the water droplet should be extremely pure in order to avoid heterogeneous nucleation. This leads to working experimentally with very small droplets in a size of micrometers since in this case the probability of a particular droplet being nucleated by a foreign particle is small (Hobbs, 1974). Rumpf and Geigl (1938) noted that water droplets of radius 2 to 3 μm could be easily supercooled to -35°C which was the lowest temperature limit of their experiments. Other researchers found this limit for small droplets of roughly the mentioned size up to 20 μm to be -40°C, -38.5°C and -40.5°C (Cwilong, 1947; Fournier, 1949; Lafargue, 1950; Mossop, 1955; Schaefer, 1952; Weickmann, 1949). In attempting to supercool larger droplets of water, Mossop (1955) found that droplets of about 1mm diameter can be cooled down to -34°C before nucleation starts. Bayardelle (1955) found the same result for a droplet of 4.6mm diameter. For more detail information please refer to Hobbs (1974).

3.2.2 Heterogeneous Nucleation

3.2.2.1 Heterogeneous Nucleation General Description

Heterogeneous nucleation of ice on a surface has been subject to study for a long time since 1724 when Fahrenheit (1724) noticed that cold water can form flakes of ice on the surface (Hobbs, 1974). Since then, there have been many studies that experimentally or theoretically investigated ice nucleation from different perspectives that we are going to review some of them briefly here. As in case of homogeneous nucleation two types of heterogeneous nucleation could be considered: direct deposition of water vapor on a surface or freezing of supercooled liquid water on the surface. The presence of foreign particle or surface in both types of heterogeneous nucleation, increases the temperature that nucleation starts. In other words, presence of foreign

particle either in forms of solid particle in the water or presence of a surface with different material, results in reduction in required supersaturation in comparison to case of homogeneous nucleation (Fletcher, 1962; Hobbs, 1974). The first general equation for theoretical macroscopic heterogeneous nucleation was developed by Fletcher (1960). The surface free energy of ice embryo will be generally minimum if the shape of ice embryo is some polyhedron[4]. Again like homogeneous nucleation, some fluctuations in structure and variations in local temperature, pressure and density happens that are caused by continuous formation and disintegration of ice embryos. When an ice embryo is larger than a critical size, it can grow freely producing a decrease in the free energy function of the system. The critical size of ice embryo and number of critical embryos per unit area are functions of number of parameters such as surface tension between water vapor (or supercooled water which one is the parent phase) and ice embryo, free energy difference between water vapor and ice embryo, temperature, number of water molecules and other factors like geometry and contact angle of the substrate. We do not tend to get into detail of these calculations because beyond the fact that it is only a theoretical model, it is also not very informative for the reader. For more detailed information please refer to Hobbs (1974). Based on this theory, Fletcher (1958) calculated the temperature at which deposition happens on a particle of small radius (10^{-8} to 10^{-4}m) from water vapor. This spherical particle can be a simplified shape of a bump of the surface in the surface roughness discussion. The calculation was performed for contact angles (between ice embryo or water and surface of the particle) of 0, 18 and 26°. For the particle sizes between 10^{-6} and 10^{-4}m, the temperature that deposition starts on the particle was found to be around 0, -12 and -28°C for the contact angles of 0, 18 and 26° respectively. For particle sizes below 10^{-4}m, the temperature of deposition decreased rapidly about 10 to 20 degrees Celsius. In general, we are interested to know that roughly which

[4] Polyhedron is a geometric solid in three dimensions with flat faces and straight edges. So any 3 dimensional object with flat face and straight edges could be accounted as polyhedron such as pyramid or tetrahedron, cube or hexahedron, octahedron, dodecahedron or any other combination or complex union of these objects.

mechanism is dominant between two competing processes; by direct deposition of vapor as an ice embryo or condensation of vapor as a supercooled liquid droplet followed by freezing as discussed in homogeneous nucleation. Fletcher (1959b) showed that if heterogeneous nucleation occurs on spherical particles of radius 0.1μm to 100μm (0.0001mm to 0.1mm), then in the range of [surface] temperature around 0°C, condensation happens if saturation ratio[5] is more than 1.2 and ablimation happens below this value. In the range of temperature around -10°C, condensation happens if saturation ratio is more than 1.05 and ablimation happens below this value. Between 0°C and -10°C, the result was linear so one can interpolate to find the desired saturation ratio below which ablimation dominant in comparison to condensation. As a general criteria condensation is preferred at small subcoolings (related to surface temperature) and large (air side) supersaturations while ablimation is preferred at large supercoolings (low surface temperatures) and small supersaturation (Fletcher, 1962)[6]. For more detail about these theoretical models and calculations please refer to Fletcher (1962). These calculation was based entirely on thermodynamic considerations and it had some limitations such as it needed some assumptions about unknown chemical bonding and crystallographic factors to calculate interfacial energies (Hobbs, 1974).

The other factors that makes theoretical analysis difficult is sometime there are some lattice misfits in interfacial surfaces of ice embryo and other objects. This results in concentration of dislocations across the interface between ice embryo and ice nucleus (the growing part on the

[5] The Saturation Ratio or level of supersaturation is mostly defined as the pressure of water vapor near the surface but at bulk temperature over the pressure of water vapor at the surface temperature. In the present study the air approaches the coils at 1.67/0.56°C (DB/WB) (35/33°F) (AHRI H2 condition). The water vapor pressure then would be around 560Pa while the water vapor pressure at the different surface temperatures between -4 to -9°C would be between 440 to 280Pa respectively. So the supersaturation ratio for air when it comes to contact with cold surface would be between 1.3 to 2 (130% to 200%).

[6] In the present study, we are generally dealing with small supercoolings and small supersaturations so basically both could happen however if we consider the results of Fletcher (1959b) for particles in the air and we assume that the roughness of the aluminum surface is exactly spherical shapes as he assumed in his model, then in the range of supersaturation of 1.3 to 2 nucleation of ice should start with condensation on aluminum surface. In practice, it may be very difficult to distinguish between condensation and ablimation since freezing may not involve macroscopic droplets but merely a thin layer of water or microscopic droplets in size of 1μm or even smaller that freeze in a few seconds (Hobbs, 1974).

substrate). These dislocations cause a certain elastic strain in ice or frost structure. In theory explained above, these effects will be accounted for with parameters used in model to adjust free energy between two phases. Turnbull and Vonnegut (1952) estimated these dislocations lower the temperature of nucleation in theoretical calculation about 1.5 degrees Celsius for a misfit of 1 per cent on the basal plane (Hobbs, 1974).

Other affecting factors such as surface imperfections effects will be discussed in the followings.

The other factor that influences the nucleation of ice on a surface is called the surface energy. Since the water molecules are polar, the binding between these molecules and molecules of the surface is principally an electrostatic bond. It might be expected that water molecules attaches better to materials which have a fairly intense ionic field. If ice crystal nucleates on an ionic material, the binding between two faces in contact is due to interaction of one of OH dipoles of each water molecule and the electric field of other material molecules (Boer, 1950). The energy of this interface will be therefore minimized if the dipole of water molecule orients parallel to the direction of electric field in its vicinity. This configuration of dipoles produces a lower entropy and therefore a higher free energy in the bulk of the ice away from the interface. Fletcher (1959a) analyzed this interfacial energy and bulk entropy and their effect on the nucleating ability and concluded that any substance that orients the ice dipoles parallel to one another at its surface, will be a poor nucleating agent. This theory predicts that in hexagonal molecule structures which have lattice dimensions close to ice, basal planes are poor ice nucleating surfaces and nucleating should be confined to prism faces. Prism faces exist in large steps on basal planes and they might provide good nucleating sites (Hobbs, 1974).

3.2.2.2 Effect of Dislocations, Steps, Corners of the Surface on Ice Nucleation

The nucleation of ice on the surface can be affected by the geometrical shape of the surface. The substrate is not always a perfect smooth flat plane. Huge roughness of the surface, surface dislocations, steps, edges, conical cavities, corners and in general the surface imperfections in a crystalline substrate affect the ice nucleus that forms on the surface and generally make nucleation occur at a lower supersaturation than required for a perfect plane surface (Fletcher, 1962). In the present study, the louvered geometry of the fins used in coils might cause some deviations from flat plate approximations used in the previous studies not only because of the different air flow pattern but also from nucleation sites point of view. Fletcher (1960; 1969) considered the effect of surface imperfections that we are summarizing it here as below (Hobbs, 1974): Steps and corners on a crystalline substrate are likely sites for nucleation. It was shown that critical free energy barrier which should be overcome to form a stable embryo is reverse proportional to the number of surfaces that embryo has contact with the surface. As an example if ice embryo is assumed to be a cubic shape, it could have 3 contact planes in a corner and 2 contact planes in a step that have lower critical free energy barrier than of flat surface. Then it is more likely that embryo forms on the corners and steps rather than upon the plane surface. Fletcher (1960) provided the shape factors for plane surface, steps and corners to estimate the free energy of ice nucleation. The shape factors were also a function of the orientation that base or prism plane of hexagonal prism crystal takes to attach the surface. However, in the above analysis, the elastic strain in ice embryo has not been included in the argument yet that might have large effect on results (Hobbs, 1974). Fletcher (1969), assuming a model of nucleation for a nucleating particle as a sphere, calculated the free energy of formation of the ice embryos on the surface in the radius ranges between 0.001μm to 10μm (Hobbs, 1974).

3.2.2.3 Freezing of Droplets on the Surface

As mentioned before, the supercooled droplets are unstable form of liquid that tends to freeze based on a number of factors such as degree of supercooling, volume of the droplet etc. The freezing discussion of the supercooled droplets is actually a discussion of a probability function that depends on the factors mentioned above. There have been models developed by researchers based on statistically or stochastically controlled manners to predict this probability of freezing. Existing "Statistic" and "Singular" models both predict that the probability of freezing increase exponentially with decreasing of temperature. However, in statistic models, the probability depends on rate of freezing whereas in singular models it is independent of this variable (Hobbs, 1974). There are also experimental studies to measure the temperature at which pure (totally free from gross impurities) water droplets freeze on the surface based on surface temperature, droplet size and rate of cooling. Heverly (1949) studied freezing of water droplets on the tip of a thermocouple or on a small piece of wax paper with diameter between 0.05 to 1mm, with cooling rates from 1 to 20°C per minute and with air pressure varied between 1 to 0.01 bar. He observed that the temperature at which droplets start to freeze was somehow independent of cooling rate and the air pressure (Hobbs, 1974). Heverly (1949) also found that for droplets of diameter between 0.4 to 1mm, the nucleation temperature was about -16°C but for droplets below 0.4mm, the nucleation temperature decreased as the size of droplets decreased so that droplets with diameter of 0.06mm nucleated at about -30°C (Hobbs, 1974). His finding was somehow consistent with later finding of Dorsch and Hacker (1950) and Holster (1951). In comparison of experimental data and prediction of existing Singular or Statistic models, even with more sets of data that obtained experimentally in broader range later in 1960's, models still could not predict the whole set of data correctly (Hobbs, 1974).

3.2.2.4 Effect of Electrical Field

There are other investigations in ice nucleation such as study the effect of strong electrical fields on nucleation of supercooled water droplets. Rau (1951) showed that the droplets can be remained liquid in supercooled temperatures but immediately freeze as soon as a negative charge applies to them. There were other studies similar to Rau (1951) and all of them found that applying electrical charge or electrical field will cause the droplets to freeze between 8 to 15°C in a higher temperatures than in absence of electrical charge. However, all of those studies are open to criticism that the observed nucleation might have been due to impurities produced by the electrical charge. Further experiments of Smith et al. (1971) with bulk of supercooled water revealed that nucleation was initiated by cavitation. Production and collapse of cavity bubbles occurred in the water disrupted by electrical field of around 1200kV/m, and freezing initiated from the site of these bubbles as they collapsed (Hobbs, 1974). From the current study point of view, which is interested in preventing frost formation or its nucleation on a surface, presence of electrical fields seem to be a disadvantage that eases the process of ice nucleation. So based on previous studies, presence of strong electrical field around the nucleating surface is not recommended.

3.2.2.5 Effect of Surface Microscopic Characteristics or Surface Energy

In the present study, surface characteristics are important in two different ways. First, it is valuable in heterogeneous nucleation discussion, to find surface characteristics which postpone or delay the formation of frost initially on the surface. The second one is after a defrost cycle, when frost melts, different surface characteristics (hydrophilic versus hydrophobic coatings) can result in different levels of water retention in the coil and might affect the next frosting cycle. Here in this chapter, we only talk about the first aspect and we will investigate the second aspect in other

chapters by comparing to experimental data obtained in this study. After formation of a thin layer of frost on the surface, the frost grows not in form of nucleation but in a "growth phase" which new crystals form on the existing crystal structure and probably the surface characteristic could not affect the frost growth anymore. The best surface characteristic is then one that prevents or delays nucleation. Formation of supercooled liquid droplets is even preferred to formation of ice crystals on the surface because water droplets could partially drain through louvers of the coil and reduce the frost formation on the surface. In the heterogeneous nucleation discussion of ice on the surface, it is believed that ice nucleates well on the materials with crystal properties similar to that of ice (Hobbs, 1974). Vonnegut (1947) investigated data for inorganic materials which has similar cell dimensions and crystal symmetries as close as possible to ice using X-ray crystallographic. He found that materials such as Silver Iodine (AgI) and lead iodine (PbI_2) both have hexagonal crystal forms and their cell dimensions differs only a few percents from those of ice and so are closest to ice. Experiments eventually showed that both of them were good nuclei for ice nucleation. The interesting fact is when water molecules wants to join an existing structure such as ice, there will be no misfit in new growing structure because the new joining molecules are the same size as (ice) molecules that exist in the mesh. In the other hand, when molecules of water wants to join a existing structure of AgI or PbI_2, this joining will cause a small percentage of misfit in the interface of their surfaces with ice due to different size of atoms between AgI and water or PbI_2 and water molecules. This misfit is very small about 1.6% in prism plane and 1.4% in basal plane for AgI. This percentage for PbI_2 is 3.6% and 0.5% in prism and basal planes respectively (Hobbs, 1974). The fact that ice is not an efficient nuclei itself but AgI and PbI_2 are shows that this small lattice misfit is a key role for an effective ice nucleus. This fact makes the effects of imperfections, edged, steps and dislocations of a surface more important than before. Hosler (1951) investigated a large number of materials and found (AgI) and ($AgNO_3$) are the best nuclei and deposition of water vapor starts on them at temperatue around -3 to -4°C and ($CuSO_4$) and (HgO) are worst materials for ice nucleation with starting deposition temperature of around -

20°C (Hobbs, 1974). Mossop (1956a) found that ice nucleation starts on AgI and PbI_2 at temperature of -6 and -7°C respectively while this nucleation temperature for materials such as MgO and CdS are -30 and -36°C respectively (Hobbs, 1974)[7]. Other studies (Pruppacher and Sanger, 1955a; Pruppacher and Sanger, 1955b) investigated the effect of different materials as nuclei for ice and found that (AgI) and (CuS) were the best nuclei and (Ag_2O) and ($AgNO_3$) were the weakest. They pointed out that materials that have a large difference in polarizability of their anions and cations were generally good ice nuclei (Hobbs, 1974). In another study, Fukuta (1958) investigated a large number of different materials and 78 material was found to be effective ice nuclei. He concluded that no water-soluble salt is effective as ice nuclei at temperature above -11°C but water insoluble components with crystallographic structure similar to that of ice, are highly effective as ice nuclei. He also found that for these highly effective ice nuclei, he stronger the ionic nature of the material the more effective it is as an ice nucleus (Hobbs, 1974).

There were also other studies that showed the effect of material on ice nucleation changes if the initial condition of material is dry or wet because of remaining water in microscopic cavities in the particle or the surface (Hobbs, 1974). Some materials are very sensitive to this initially being wet and some others show negligible difference such as Silver Iodine (AgI). Edwards and Zipper (1970) using some experimental evidences to support their theory, suggested that this difference

[7] It should be noted that when ice nucleation starts on one kind of salt as mentioned above at very low temperatures such as -36°C, it does not necessarily mean that they can be used as a coating on the surface of heat exchanger to postpone the ice formation on the surface. There are two reasons for that: First reason is most of these salt are soluble in water and they will be removed from the surface of the coil during frost and defrost and second reason is at 1950's and 1960's most of these researches were aimed to find a good nucleus material for ice nucleation to be able to seed clouds. Basically the way that most of the researchers did their experiments were to spray powders of aqueous solution of such a salt in a cloud chamber that have saturated or supersaturated air and then continue to lower the temperature of the chamber until the nucleation on foreign particles appear. In this case, the temperature of the salt particle is equal to the temperature of the water vapor, so the water vapor is sort of free to either deposit on this foreign material or stay in supersaturated state or condense as a rain drop. However, in heat exchanger, the water vapor in the air comes into contact with a surface which has a much lower temperature than the air. The air locally gets very cold and can not hold the previous amount of water content anymore and so it deposits the excess water content on the surface. It could be somehow regardless of surface tendency to actively participate in accepting water molecules into its molecular structure. In a common sense, it is somehow like dropping a rain drop or snow flake on the surface which tendency of the surface has negligible effects on it. The whole purpose of these discussions about inorganic salts here is to have more understanding about fundamentals of heterogeneous nucleation and how it starts.

in sensitivity of the surface toward being initially wet or dry depends on ability of adsorption and depth of layer in which material can hold an adsorbed water layer into the molecular structure of the surface (Hobbs, 1974).

In previous periods of study of ice formation, the focus of the studies were on generally on finding good nuclei for ice formation to be used as powders to seed the clouds and help condensation or ice formation. Thus, ice-nucleating behavior of these materials such as Silver Iodine (AgI) was studied extensively in the past fundamental studies. In the present study we might be more interested in materials which are not good ice nuclei but because these studies help us understand the general process and affecting parameters of ice formation, it is useful to take a brief look to those studies as well.

Previously we talked about Fletcher (1959b; 1962) theory about nucleation of ice on a foreign object surface and used it to predict which of the competing process of ablimation and condensation will be dominant. This theory actually is being used to predict the condition under which a particle acts as a freezing (after condensation) nucleus or as a direct deposition (ablimation) nucleus. In the case of Silver Iodine, this problem has been investigated experimentally by many workers but with contradictory results. Cwilong (1949), Schaefer (1954) and Birstein (1955) reported that ice ablimates on the surface and Silver Iodine is a deposition nuclei while D'Albe (1949) and Mossop (1956b), on the other hand, claimed that it was not possible to distinguish whether it is a freezing or deposition nuclei. In a more accurate observation, Edwards and Evans (1960) by controlling temperature and humidity and Silver Iodine particle diameters, stated that AgI is much more active as a freezing nuclei than deposition nuclei (about 100 times). Sulakvelidze et al. (1965) found that apart from the temperature of Silver Iodine, the initial temperature of the water that comes into contact with Silver Iodine is also affecting the result considerably (Hobbs, 1974). It is clear that because of numerous numbers of factors involved in the crystal growth and nucleation process, the result of one observer might

be totally different from another observer. This might help us to understand better that why some studies that we are going to talk about in the followings report condensation phase prior to frost formation (Hoke et al., 2004) while other studies observe no condensation or supercooled droplets and their observation shows only direct ablimation from gas phase into ice crystals (Hayashi et al., 1977b). There are other studies that investigated other possible reasons for these contradiction of results but because working with AgI is somehow out of scope of this study, we ask reader to follow more detail discussion about this in Hobbs (1974). For closure, just to demonstrate how even small insignificant factors might have significant effects on final results of nucleation, it is worth to mention a couple of more studies that investigated the effect of exposure to light and purity of material. Reynolds et al. (1951) found that Silver Iodine (AgI) nuclei behavior changes considerably as it exposes to sunlight. Other studies later approved the effect of ultraviolet lights on behavior of (AgI) as an ice nuclei (Hobbs, 1974). In another study, Burley (1964) showed that the shape of ice crystals that forms on the surface of a material such as Silver Iodine (AgI) is different before and after Silver Iodine has been exposed to ultraviolet light. The ice crystals were mainly thin hexagonal plates with few rectangular plates when freshly prepared Silver Iodine was used as the nuclei. However, after Silver Iodine was exposed to ultraviolet light, the fraction of rectangular plated increased. The rate of increase was proportional to the exposure time to the light (Hobbs, 1974). Other researchers found that some of these sensitive and strange behaviors of nucleus materials such as Silver Iodine are because of small impurities in the process of their production. Corrin and Storm (1963) showed that (AgI) obtained from different production methods, contains different small amounts of hygroscopic foreign materials which markedly affect the nature of water adsorption isotherms. Later, Steele and Kerbs (1965) found that nucleation efficiency of absolutely pure AgI is much less and in fact is one-hundredth that of conventional AgI that contained impurities (Hobbs, 1974).

We observe that there are a lot of details and complexities in defining a surface as a good nuclei or weak one because of complex nature of mass deposition and crystal formation which is affected by many other factors. There are still more detailed works about affecting parameters on nucleating efficiency of AgI that we do not tend to get into it more. Reader can refer to Hobbs (1974) to read more about this subject. It is worth noting that some of them even have interesting contradictory results and this is even a heavily investigated material such as (AgI) which many different researchers were working on it for decades. The same discussion will apply when we want to investigate the surfaces that have hydrophobic and hydrophilic characteristics with their different rates of frost deposition in terms of frost thickness, mass, density and thermal conductivity. In other words, we somehow should expect that we are not dealing with a sort of simple one-variable straight phenomena that we could predict in every case with details, how the results should be. We will talk about this later when we get more into the details of experimental data in the future chapters.

There are other studies that showed that some organic materials such as Phloroglucinol (Langer et al., 1963), substitute Fluorenes (Head, 1961; Head, 1962), 1-leucine (Power and Power, 1962) and metaldehyde (Fukuta, 1963) have a good nucleating characteristics and the ice starts to form on them at temperatures similar to AgI although their molecular structure are not similar to that of ice (Hobbs, 1974). In organic behavior of materials (similar to inconsistency of inorganic material discussion) researchers also report different or sometimes contradictory results for the temperature and efficiency of ice nucleation for each material. For more information please see Hobbs (1974).

3.2.2.6 The visual shape of first initial microscopic layer of ice crystals on a foreign surface

It is worth noting that when we are talking about visual shapes of ice crystals, mostly we are talking about "growth phase" rather than nucleation phase because nucleation just happens for a first thin layer of crystals very adjacent to the surface. After that point, ice crystals forms on the top of the existing crystals which fall into category of growth phase. We talked about number of previous studies mentioned above that investigated somehow the growth phase in terms of visual observations. In the other hand, they are other studies that just focus on the first layer of ice crystals on a foreign surface which is the heterogeneous nucleation. One approach for this kind of investigation is choosing a material that has a similar molecular structure to ice and observe the shape of ice crystals forming on a well-defined face of a single-crystalline substrate of these materials (Hobbs, 1974). The similarity of foreign material structure to ice creates a tendency for ice crystals to form on surface more easily. The substrate then, is not a huge surface but it is indeed a crystal itself with a hexagonal shape approximately in the same order of magnitude as size of the ice crystals or only few times larger. In this case, the crystal of a material such as AgI or PbI_2 is exposed to water or water vapor so that ice crystals form at outside boundaries of AgI crystal. These studies might be important to us because it can give insight into the shape of the first thin layer of ice crystals from on a foreign surface. Montmory (1956) and Jaffray and Montmory (1957a; 1957b) observed that at the temperature of -10°C the ice crystals form on the basal faces of AgI and PbI_2 and they are in the forms of hexagonal plates. Kleber and Weis (1958) later found similar results for AgI, PbI_2 and a couple of more substances (Hobbs, 1974). Bryant et al. (1959) performed a more accurate condition control for their experiments and found that for the AgI, if the temperature is between -8 and -25°C, the ice crystals preferentially from on the prism planes of AgI in the shapes of thin plates. If the temperature is between -4 and -8°C and also below -25°C, the growth was greater along basal planes of AgI in the shapes of hexagonal prisms. They also found that for PbI_2 as a substrate, for temperatures above -6°C, the initial

deposition is in a form of liquid droplets and as the temperature is lowered, the droplets freeze and turn into ice crystals with prism planes parallel to prism planes of PbI_2. Bryant et al. (1959) observed that for AgI, at temperatures above -4°C, only water droplets appeared, but as temperatures was lowered from -4 to -12°C, number of formed ice crystals increased. They stated that at temperatures between -4 to -12°C, the initial deposition are in forms of droplets that freeze afterwards while below -12°C, the ice may have formed by direct deposition from vapor phase. Other studies revealed the influence of other factors such as ultraviolet light on the shapes and growth of ice crystals on a sample material such as AgI. Burley (1964) found that for a large crystal of Silver Iodine (AgI), the growth of ice crystal is more rapidly on the prism faces while after exposing AgI to ultraviolet light for 1 to 4 hours, basal planes become more active nucleation sites (Hobbs, 1974). There are other studies that later revealed more details about the effects of impurities and microscopic decomposition due to ultraviolet light exposure in AgI that we do not get more into details of these studies. The reader could refer to Hobbs (1974) for more details.

3.2.2.7 Summary on Heterogeneous Nucleation and the Complementary Theory

The previous studies on a sample material such as Silver Iodine (AgI) which was assumed to be a good ice nuclei revealed that effectiveness of a material as a good or poor ice nuclei does not depend only on environmental parameter such as temperature and water vapor pressure but also on the molecular structure of the material, its surface imperfections, misfits and even impurities in its structure. We pointed out that for the materials that have a molecular structure similar to of water or ice such as AgI, a small misfit that forms in the interface between ice and AgI makes AgI a very effective nuclei. However, there are theories that states other factors are playing significant roles in this process as well. Karasz et al. (1956) pointed out that AgI is a hydrophobic

material in nature and the surfaces of AgI and ice are probably energetically incompatible (Hobbs, 1974). This view was supported later by measurements of Zettlemoyer et al. (1961). They postulated that ice first develops on the few isolated impurity sites of AgI which are hydrophilic in character (Hobbs, 1974). Corrin et al. (1964) stated that although impurity sites in AgI are hydrophilic and they increase the adsorption of water, there is not a corresponding increase in ice nucleating. They believed that ice initiates on hydrophobic sites which are the last sites to absorb water as the water vapor pressure is increased (The increased water vapor pressure reaches this sites sooner than hydrophilic sites) (Hobbs, 1974). To check this hypothesis that ice nucleates better on hydrophobic surfaces with a few numbers of isolated hydrophilic sites on it Zettlemoyer and Hosler (1963) made several types of silica and measured their ice nucleation capabilities. They found these silica surfaces can change into an effective ice nuclei similar to AgI. Hamilton et al. (1968) found that a balance between hydrophilic and hydrophobic surface groups, together with a proper distribution of sites, is important for the heterogeneous nucleation of ice (Hobbs, 1974). If this theory is correct then the inefficiency of pure AgI as ice nucleus mentioned before could be attributed to the lack of enough impurity sites on which ice can form (Hobbs, 1974). The variation in nucleation ability of AgI exposed to ultra violet light could be also explicable in terms of this theory. Ultra violet lights decomposes the molecular structure of AgI to free Iodine and metallic silver that in presence of air result in formation of patches of silver oxide on the surface. This condition is favorable for nucleation of the ice (Hobbs, 1974).

Edwards and Evans (1962) suggested that an efficient ice nucleus has to satisfy three conditions, have a small lattice misfit with ice, a low net surface (electrical) charge (polarizability[8] such as the molecules of water itself), and a slight degree of hydrophobic characteristics (Hobbs, 1974). In order to have a surface with slight degrees of hydrophobic characteristics, surface atoms should have somehow a slight charge and they are likely to have polarizable atoms (Weyl, 1949).

[8] A polarized or polarizable molecule is molecule who's electrons can easily move within it's atomic levels. As an example, water molecules can be polarized under an electric field.

This can explain the results of Hosler (1951) and Pruppacher and Sanger (1955a; 1955b) that most of the good ice nuclei's contain highly polarizable atoms (Hobbs, 1974).

While a lot of aspects of heterogeneous ice nucleation have been explored by numerous studies, it should not be assumed that the mechanism of heterogeneous nucleation is fully understood by now. It seems that different materials show very different behavior in ice nucleation process in comparison to their normal well-known characteristics. So caution should be used to generalize the behavior of a specific material or characteristic to general ice nucleation process.

3.3 GROWTH PHASE

3.3.1 Introduction

After nucleation of ice embryos, this crystal structure begins to grow in different ways in different directions. The growth phase in the present study (which happens after a few first minutes of heterogeneous nucleation on the metal surface) and other early studies on formation of ice crystals in the nature as a form of snow has some similarities such as in both of them growth phase happens by joining of water molecules in the air to the existing structure of crystals. This makes it beneficial to review some of the relevant previous fundamental studies on the crystal growth process. On the other hand, one of differences between the frost in current study and free formation of crystals is in the frost formation is some crystal structures collapse into existing crystals (Wu et al., 2007a) based on air drag force, melting of surface of frost adjacent to the air stream or other factors and this makes the analysis more complicated. To study growth phase, first we divide our study of growth phase into three sections: Theoretical models, Available experimental data and External visual shapes of crystals.

3.3.2 Theoretical Models

There have been many efforts to model the growth phase of ice crystals from water vapor since early work of Jeffreys (1918) who used an electric potential analogy between the vapor field and a conductor and proposed a relation for rate of crystal growth (Fletcher, 1962). Also there were many efforts after this study to correct the assumption of electrostatic capacity of ice crystals used in those relations, they were not very good approximations of real ice-crystal growth since

process of crystal growth is much more complex than simple electrostatic analogy mentioned above (Fletcher, 1962). In addition to difficulties to estimate surface free energy between interfacial participating surfaces in molecular scale, the process of deposition of water vapor molecules on ice crystal will also be affected by dislocations and irregularities in the growing crystal surface. The surface of crystal mostly has some steps, edges, dents, kinks and disorientations of other water molecules. In addition to that adsorption of water vapor molecules on the crystal surface, is followed by migration of this molecule over the surface until it reaches a position where it can be fitted into crystal structure with a net decrease in the free energy of the system (Fletcher, 1962). Even in the case of existing of an undistorted flat crystal surface, any further growth to form new crystal layers requires clustering together of adsorbed molecules to form islands upon the perfect faces (Fletcher, 1962). There are some studies that have investigated the formations of dislocations and disorientations which depend on temperature and air supersaturation level (Burton et al., 1951; Frank, 1949; Verma, 1953). We do not tend to get involved into details of these discussions again because dislocations and disorientations are somehow out of scope of our study. The general idea is we must expect that rather than a few single dislocations here and there, there will be a whole group of dislocations emerging on most crystal faces than even interact with one another (Fletcher, 1962).

3.3.3 Available Experimental Data

One of the experiments performed to determine the growth rate of ice crystals, was Shaw and Mason (1955). They studied the growth rate of a single ice crystal growing on a cooled copper rod with a microscope. They found that if we define the dimensions of a single ice crystal with diameter (d) and height (h), then d^2 and h^2 grow linearly in time and they provided the slopes of these lines as constants. These slopes depend highly on temperature of formation and slightly on

supersaturation level and still slopes were found to vary from crystal to crystal (Fletcher, 1962). The other experimental data on frost formation in the growth phase are the same as studies mentioned and reviewed in the chapter 2, Literature Review because almost all of the regular frost studies investigate frost growth rate and characteristics in the growth phase.

3.3.4 Visual Shape of Ice (Frost) Crystals

In growth of an ice crystal, one theory is based on equilibrium process for new joining molecules of water using Wulff (1901) theorem which states equilibrium state is when the distance of any crystal face from the center of the crystal is proportional to the free energy per unit area of that face (Fletcher, 1962). Although no exact values of such energies are known for ice, yet approximate values could be found by assuming that every molecule interacts only with its nearest neighbors and counting the concentration of nearest neighbor pairs linked across any crystal plane. Because ice has hexagonal structure, then the planes with lower energy would be basal planes and prism planes[9]. Using this crystal structure model, lattice parameters and the assumption of nearest neighborhood pairs, it can be shown that the energy of a prism face is about 6% greater than of a basal face. The Wulff (1901) theorem then shows that the equilibrium should be a hexagonal prism (Fletcher, 1962). The ratio of axial length to hexagonal diameter is 0.82 according to Krastanow (1943). Although ice crystals formed in the nature in the forms of snow or in the laboratory has generally the shape of hexagonal prism, but dimensional ratio may vary from 0.1 to 10. Moreover so many other more complicated shapes like stars, hollow prisms, scrolls and dendritic planes may occur. In these cases it would be quite impossible to explain these complicated forms on basis of any equilibrium theory. We therefore might conclude that the different forms of ice crystals are not only equilibrium structures but they can be affected by

[9] Assume a hexagon in x-y plane. If this shape is dragged along z axis, it makes a 3 dimensional hexagonal prism. Both top and bottom hexagon shapes are called basal planes and 6 rectangular shapes formed on each side is called prism planes.

kinetic effects due to thermal or diffusion gradients, surface accommodations coefficients or other similar mechanisms. They become then frozen before attaining equilibrium (Fletcher, 1962).

Several attempts have been made in previous studies to identify the crystal shapes based on influencing parameters such as formation temperature and water vapor pressure and air velocity during growth of the crystal. It is also possible that foreign particles or surface energy characteristics have influence on this process too (Fletcher, 1962). Early studies on the crystal shapes were examination of forms of snow crystals and the temperature that they were formed. A study of influence of temperature and supersaturation level of air on the visual shape of crystal formation was carried out by Hanajima (1944; 1949) (reproduced from Hobbs (1974)). The Figure 1 shows the relation between crystal formation temperature and air supersaturation level and the shape of crystals that they found in the environmental conditioned snow making apparatus. Vertical axis shows the saturated vapor pressure with respect to ice (supersaturation level). The curve W in the Figure 1 shows the saturated vapor pressure with respect to supercooled water at the corresponding temperature. For the purpose of the present study (temperature is between -4 to -12°C), it seems that according to their study findings, the shape of frost crystals on microchannels should be a combination of needles, irregular needles and occasionally columns or cups. The pictures of these types of crystals will be shown in the followings. Nakaya (1954) did an extensive study on the visual shapes of snowflakes both in natural snow and artificial snow crystals which were the results of individual ice crystal grow in the laboratory. Snowflakes are interesting in studying the ice crystal growth because they are individual growing crystals that are isolated from the effect of every other foreign surface effects and collision and penetration of adjacent frost crystals. Thus, clear and correct shape of growing frost or ice crystal could be investigated. In frost formation on heat exchangers or on any other surface, the fundamental of frost crystal growth is the same as snowflakes formation however because of penetration of frost crystals into each other, melting of the surface and seeping the

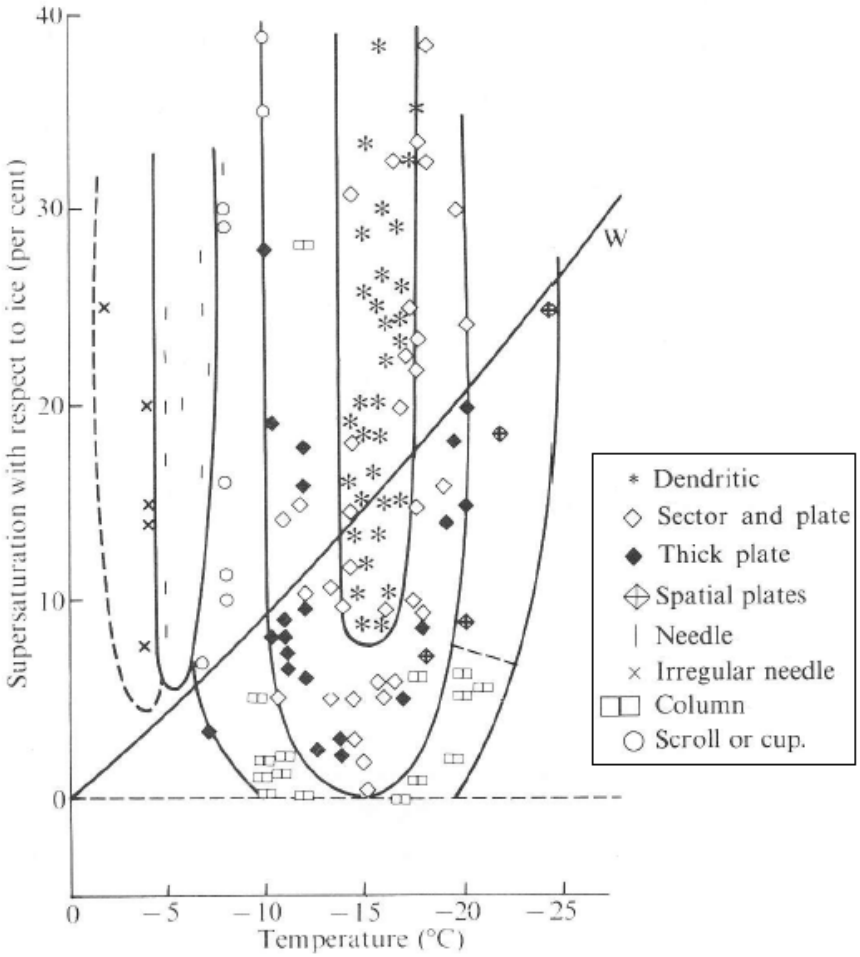

Figure 1: Relationship between the visual shape of an ice crystal and temperature and air supersaturation level observed by (Hanajima, 1949).

water into deeper layers and refreezing again and other mechanisms, there are more complexity in visual shape of frost. Snowflake study will provide a fundamental base to gather valuable information about the type and shape of frost crystal growth in every particular temperature and environmental condition. It is also worth noting that the shapes of ice crystals are not bounded to few definite shapes that are mentioned in this dissertation and what is presented here is only a very general category of frost crystals that have been offered to approximate the general behavior of ice crystal growth. Nakaya (1954) showed more than around 1000 different visual shapes of snow crystals and previous studies such as Bentley and Humphers (1931) showed more than 3000

different pictures of snow crystals. This shows the difficulty of categorizing the ice crystals into a limited number of certain visual shapes. Nakaya (1954) found that basic habit of ice crystals (plate, prism or other shapes) is determined mainly by temperature of formation while the rate of growth and some more complicated secondary features of deposition (such as dendritic growth) are controlled by supersaturation of the water vapor in the air (Hobbs, 1974). Figure 2 shows a schematic demonstration of a very general classification of snow flakes suggested by Nakaya (1954).

A few examples of actual pictures of different crystal shapes of Nakaya (1954) bank are demonstrated in the following figures. For other types please see Nakaya (1954).

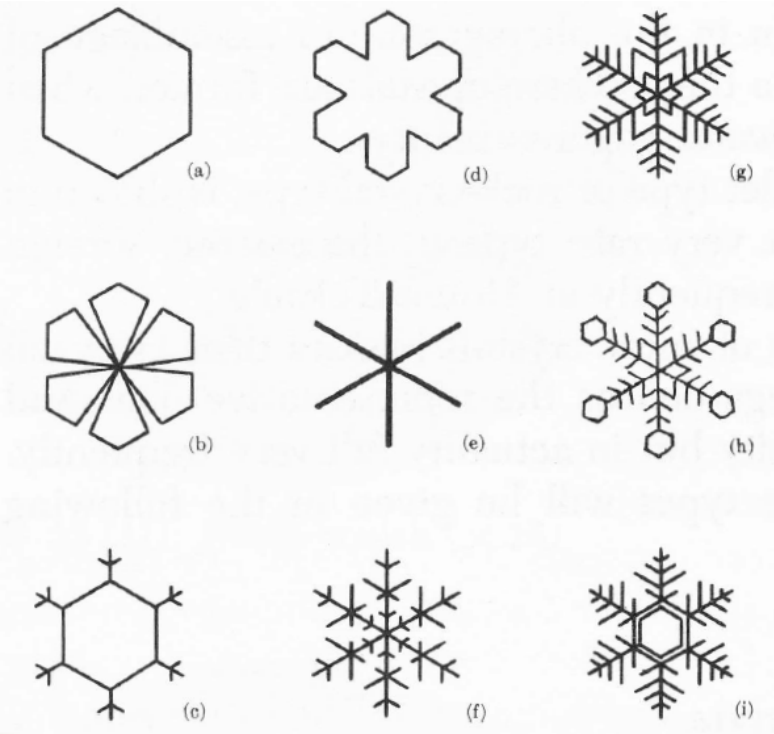

Figure 2: Schematic classification of regular plane crystals: (a) simple plate; (b) branches in sector form; (c) plate with twings; (d) broad branches; (e) simple stellar form; (f) dendritic form; (g) fernlike form; (h) dendritic form with plate; (i) plate with dendritic extensions. Figure reproduced from Nakaya (1954).

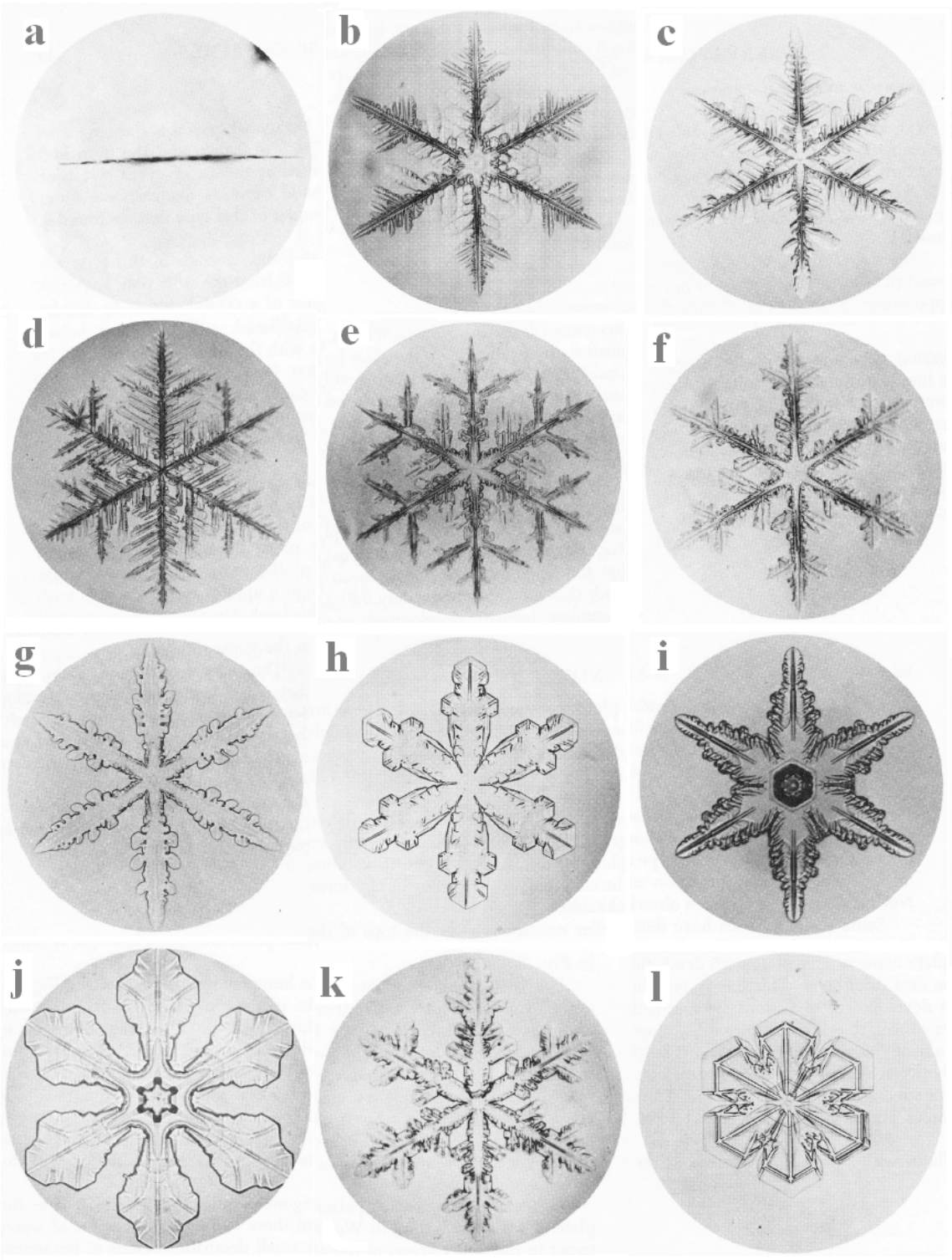

Figure 3: Actual images of a few forms of snow crystals; (a) side view of a fern crystal (×17); (b) fernlike crystal (×17); (c) slightly sublimed crystal; (d) crystal showing partial asymmetry (×21); (e) ordinary dendritic crystal (×19); (f) ordinary dendritic crystal (×19); (g) ordinary dendritic crystal partially sublimed; (h) broad branches (×26); (i) broad branches (×39); (j) Intermediate type of broad branch and plate (×49); (k) intermediate type of dendritic and broad branch (×25); (l) sector form (×37). Images reproduced form Nakaya (1954).

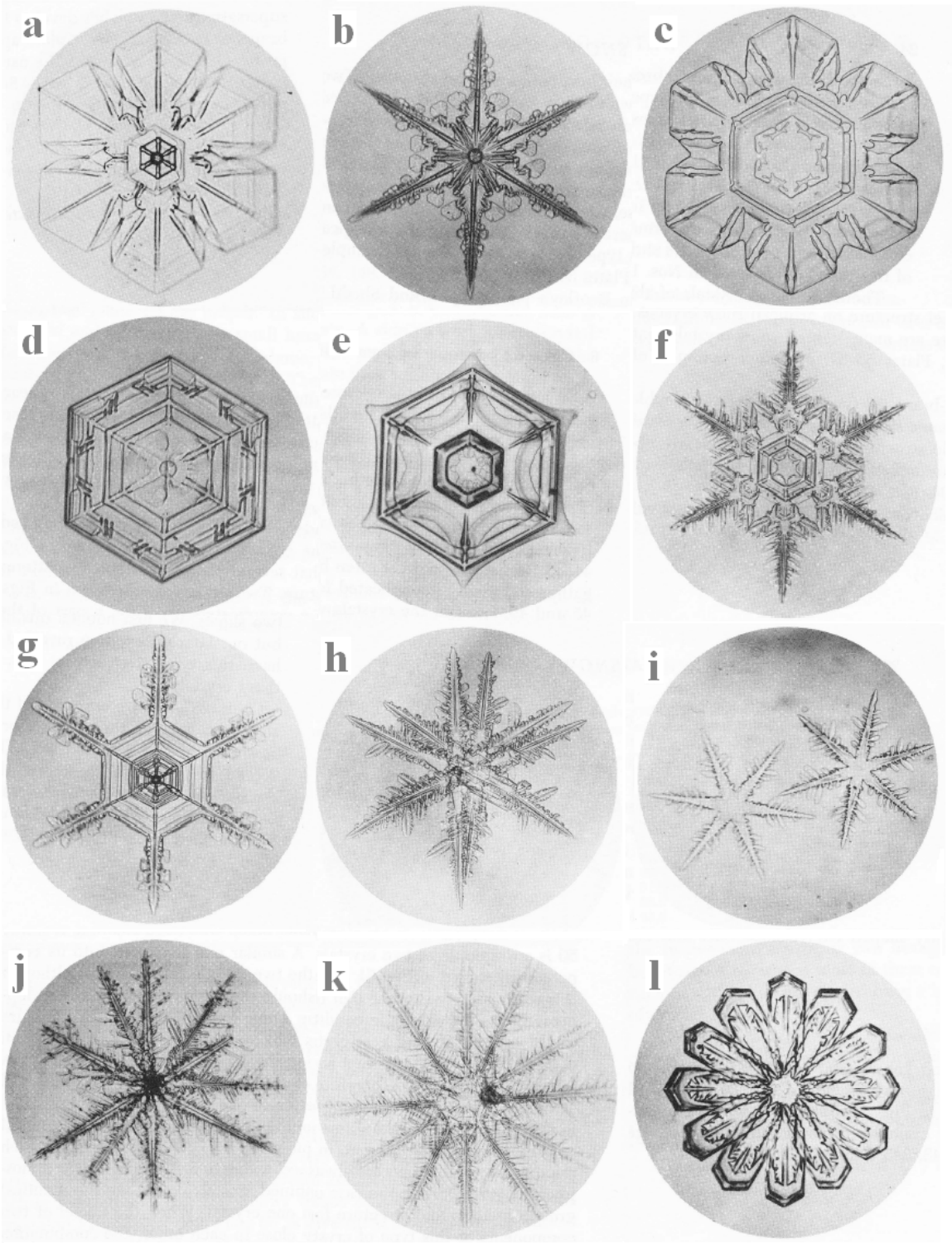

Figure 4: Actual images of a few forms of snow crystals; (a) sector form (×37); (b) sector form with dendritic extension (×36); (c) plate with sector extensions; (d) hexagonal plate (×39); (e) hexagonal plate with a trace of extensions (×45); (f) plate with fernlike extensions (×24); (g) plate with simple dendritic extensions (×20); (h) combination of two dendritic crystals (×21); (i) combination similar to figure (h) separated into components (×18); (j) irregular twelve-branched crystal (×18); (k) twelve-branched crystal fernlike branches (×16); (l) twelve-branched crystal broad branches (×29). Images reproduced form Nakaya (1954).

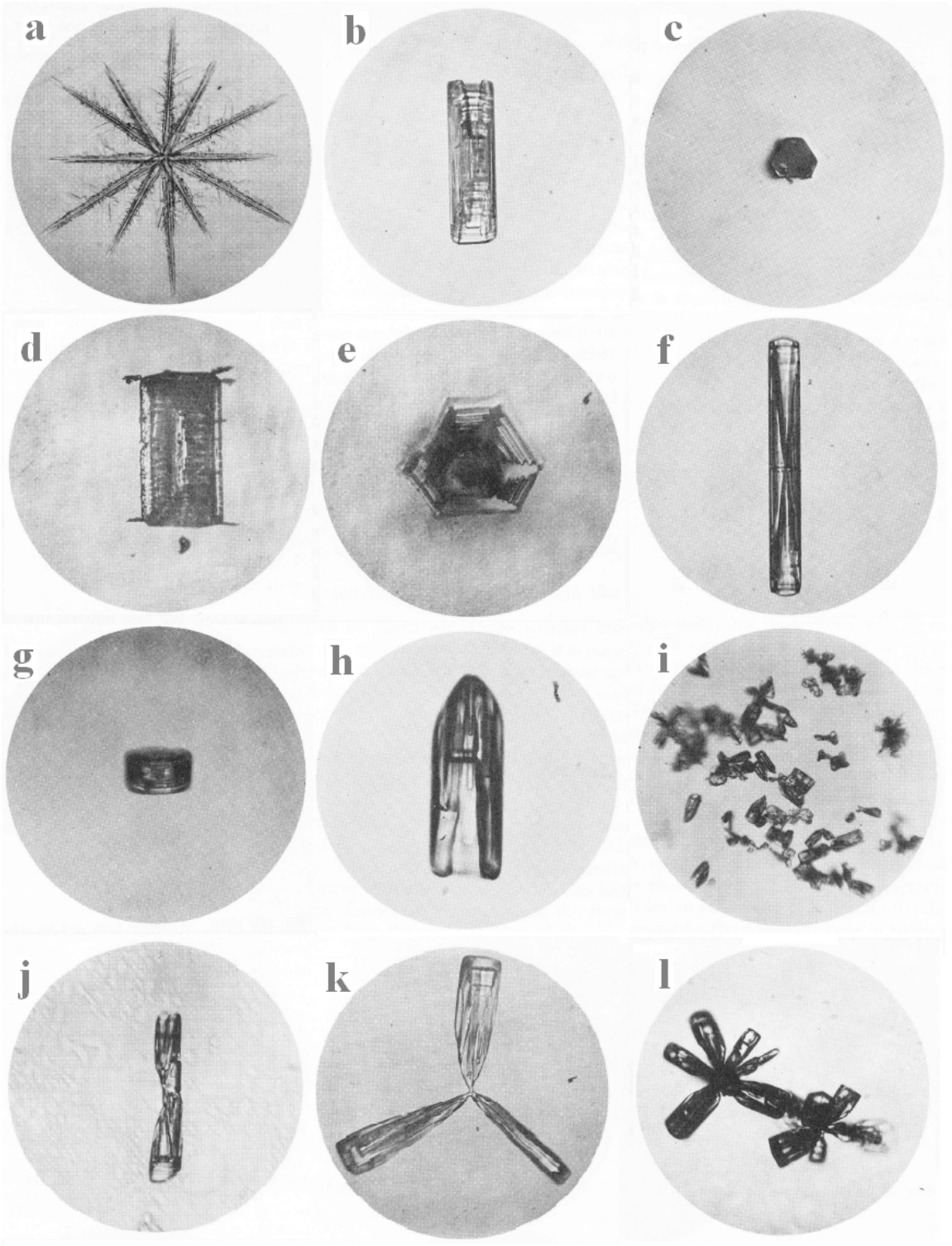

Figure 5: Actual images of a few forms of snow crystals; (a) twelve-branched crystal long and short branches (×21); (b) column with one side rolled up, side view (×35); (c) top view of figure (b); (d) columns showing skeleton structure (×39); (e) side view of figure (d) (×54); (f) slender column (×42); (g) short column (×54); (h) bullet-type crystal (×86); (i) combination of bullets (×17); (j) combination of two bullets (×51); (k) combination of three bullets (×43); (l) combination of several bullets (×37). Images reproduced form Nakaya (1954).

According to images shown above, there are all combinations of the previous form of crystals that can join and make a new shape such as combination of bullets with dendritic shape and so forth. There are also some malformed crystals and peculiar shape crystals. Getting into more details of this discussion is out of scope of this dissertation and for more information please refer to Nakaya (1954). The conclusion is though, in a very general and probably inaccurate category, the shape of crystals can be divided into few general categories as described in Figure 2.

There have been studies on artificial production of snow in the lab with especial chambers or apparatus. The shapes of artificial snow are more or less similar to the images of natural snow and we do not repeat them here. Most of the times, the shapes are still similar but not perfectly similar to natural snow. Occasionally there are some new shapes such as cubic or sheath-like crystals form too that are rarely seen in natural snow. When water vapor comes in contact with a cold object so that ablimation happens, malformation and irregular shapes are even more common and most of the times the shapes are not as perfect and symmetric as the natural or artificial snow. For more details please refer to Nakaya (1954).

From the images of Figure 3 to Figure 5 it is apparent that the visual shape of crystal formation even in the simplest non-disturbed free formation status is so extensive to be hardly categorized into few specific classifications let alone when other complexities such as melting, penetration of other layers, formation under different surface temperature in different depth of frost layers etc. are present in actual frost formation on the surface of heat exchangers. Therefore, always caution should be applied to define a clear boundary between different shapes of crystal and oversimplification and rigid general categorization should be avoided.

Mason (1957) categorized the crystal shapes from previous data gathered from snow investigations and found that in crystal formation temperature between -3 to -8^{o}C, the crystals are

more needle type shape, in temperature between -8 to -25ºC, they are more in shapes of plates and sector stars. Also in the temperature range of -10 to -20ºC stellar dendrites could form. In temperatures below -20ºC the shapes are mostly prisms, single crystals, twins or prismatic clusters (Fletcher, 1962). There are also other laboratory tests that replicate the atmospheric condition which crystals formed in the lab in the form of snow like ice crystals. Similar results were reported by different studies. The summary was the crystals were "plates" type in the range of temperature between 0 to -5ºC, "prism" type when temperature is between -5ºC to -10ºC, "plates" in temperatures between -10ºC to -25ºC and "prism" in temperatures below -25ºC (Mason, 1953) (reproduced from Fletcher (1962)). In another experimental study, Shaw and Mason (1955) grew single ice crystals on a cold metal plate under controlled conditions for temperature and level of air supersaturation. They concluded that crystal type is a primary function of temperature and air level of supersaturation has a small, non-systematic effect on it. The transition temperature were those found by Mason (1953).

Using another technique, Kobayashi (1957) grew ice crystals on a fine thread or rabbit hair using a thermal gradient chamber and studied them photomicrographically (Fletcher, 1962). Kobayashi (1957) found similar results to Hanajima (1944; 1949) in Figure 1 with minor differences. As an example of differences, Kobayashi (1957) found thin hexagonal plates at temperature between 0 to -4°C while Hanajima (1944; 1949) found irregular needles in this condition. Later Hallett and Mason (1958) did a similar set of experiments in a cloud chamber using thin nylon wire and glass fibers to grow ice crystals and confirmed the results obtained by Kobayashi (1957) that shapes of crystals depend mostly on temperature. The diagram found by Hallett and Mason (1958) is shown in Figure 6. It should be noticed that it seems with increasing of supersaturation level, the plates in temperatures between 0 to -4°C change to dendrites. That might explain the difference between observations of Hanajima (1944; 1949) that called the frost shape in this region irregular needles versus Kobayashi (1957) that found them more plate type.

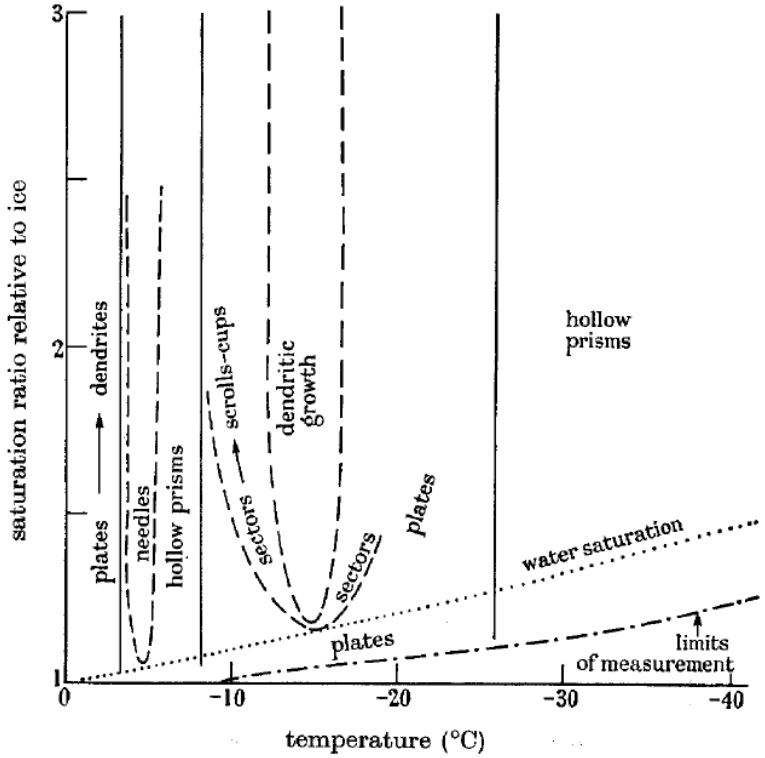

Figure 6: Diagram of ice crystal shapes in different temperatures and different level of air supersaturation (Hallett and Mason, 1958).

As shown in Figure 6, ice or frost crystals form in conditions of the present study will be mostly in form of plates and needles. The surface temperature (fin root temperature) in the present study varies between -11 and -5ºC but the actual frost surface temperature that crystals form there might be approximately between 0 to -9ºC. Except than initial moments of frost growth for coldest temperature tests of -11ºC, for the rest of the -11ºC test and all other temperature tests, frost surface temperature will be higher than -11ºC. In the present study, hollow prisms or dendrites (branching like a tree) might form too but mainly in the conditions of this study we expect mostly plates and needle type frost crystals.

Later Kobayashi (1958) investigated again frost crystal shapes that grows on fine filaments in the snow making chamber and found that if the level of supersaturation is very low (~0.1%), then

crystals grow in a near equilibrium state as the theoretical model predicts but with increased vapor excess which is the common case of most of normal crystal formation processes, the temperature is the dominant factor determines the type of crystal shapes. The diagram proposed by Kobayashi (1958) is shown in Figure 7. In this diagram, the horizontal axis is the formation temperature in the ambient air and vertical axis is the excessive water vapor concentration (or density) relative to saturation concentration.

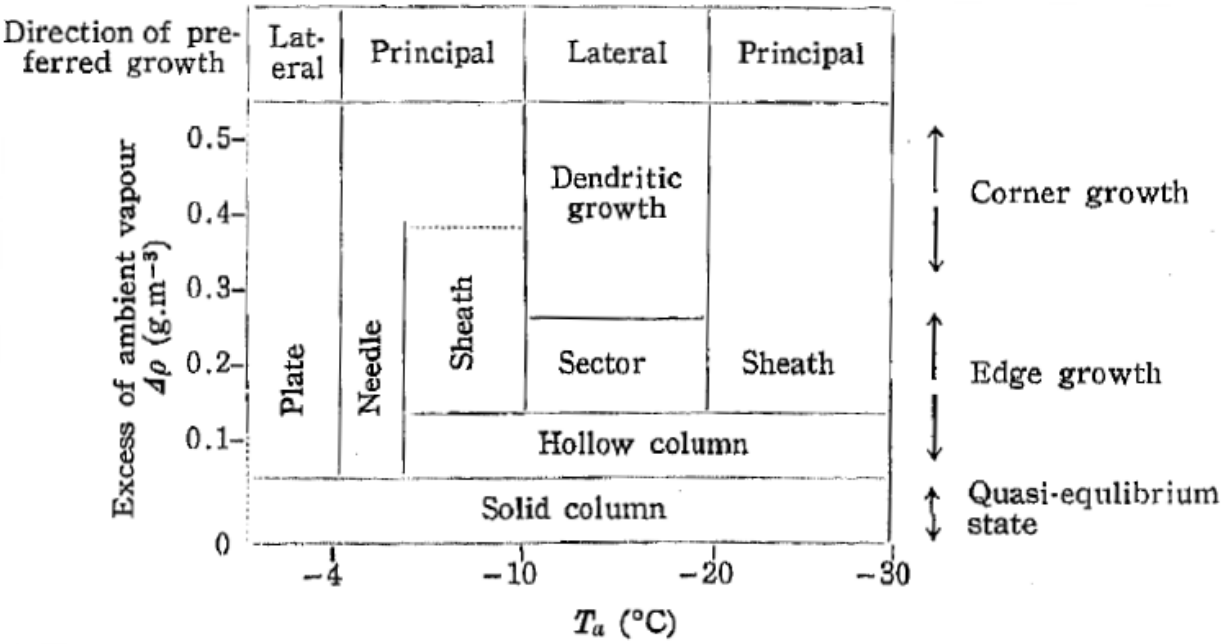

Figure 7: Ice crystal shapes as a function of their formation temperature and vapor density excess over ice (Kobayashi, 1958).

In the present study, the excessive water vapor density is approximately between 0.7 to 1.5g/m^3 so only if we assume that Kobayashi (1958) results are still temperature dominated for higher excessive vapor concentrations then we can expect frost crystals to be plate and needle type.

Hayashi et al. (1977a; 1977b) used a photographic observation approach to classify frost types based on plate temperature and water vapor concentration for a geometry of a flat plate. It was the first study that divided the frost growth period into three phases which is shown in Figure 8:

a) Crystal growth period
b) Frost layer growth period
c) Frost layer full growth period

In crystal growth period, first a thin layer of frost covers all over the surface (Figure 8a). Then frost crystals that are relatively far apart from each other grow perpendicular to the surface at about the same rate. Then the frost becomes like a forest of trees with many branches but it is still not homogeneous layer (Figure 8b,c). Then in the frost layer growth period, a rough frost layer which is a combination of cluster of rod type crystals, grows by generating branches on the top of the previous existing crystals or by the interaction of each crystal (Figure 8d,e). Then frost grows into a uniform mesh until the frost surface becomes nearly flat (Figure 8f). In frost layer full growth period, the frost layer shape remains unchanged until the frost surface temperature reaches or exceeds 0ºC due to increased thermal resistance. Then Hayashi et al. (1977b) state that a part of frost in the surface melts and water droplets seep into the frost layer and freeze there. This will lead to increased thermal conductivity of frost and then frost surface temperature decreases which results in frost deposition again. This process of melting, refreezing and deposition continues periodically until an equilibrium state in heat and mass transfer is maintained (Figure 8g,h,i). This condition might happen due to increased thickness of the frost layer which results in a large thermal resistance. The frost surface temperature will eventually reach air dew point or 0ºC whichever closer and then frost thickness does not grow significantly anymore. The concept of melting and refreezing in frost layer was considered by other researchers before too (Yonko and Sepsy, 1967). Finally, in frost layer full growth period frost layer becomes a dense tight layer which can be called aged frost (Hayashi et al., 1977b). They observed that crystal growth period

might take shorter or longer to finish based on surface temperature. As an example for surface temperature of -15°C, crystal growth period takes about 10 minutes while at surface temperature of -5°C, it takes up to 30 minutes.

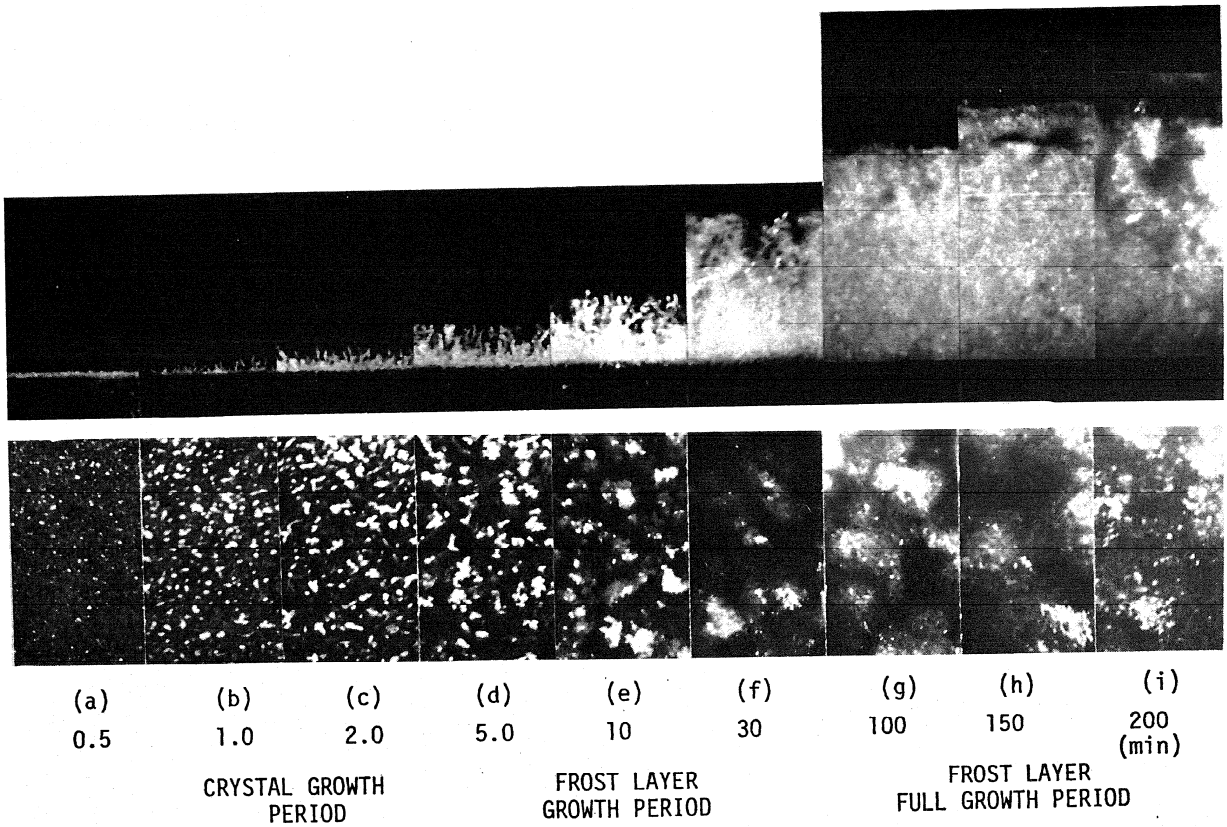

vection, graphical face= -12.4 °C; ures show the top

There are other photographic observations of frost nucleation and growth process in the literature. Na and Webb (2003) investigated the frost formation on flat plates and their observation of the formation process are shown in Figure 9 which has somehow similarities with what Hayashi et al (1977b) explained.

(a) (b) (c)

Figure 9: Different frost shapes on the cold surface ($T_{surface}$ = -20ºC): (a) initiation of frost, beginning of nucleation; (b) growth of frost and (c) covering the surface (Na and Webb, 2003)

There are other categories for frost formation process in literature which is very similar to Hayashi et al. (1977b) study. For example, Kamath (1985) assumes the same three different frost regimes for frost formation:

a) Nucleation

b) Dry Frost growth

c) Wet Frost growth

Nucleation phase of frost happens as soon as air - that always has a certain content of water moisture except for absolutely dry air – touches a cold surface. In this case, small dotted ice crystals first appear on the surface. It seems that they grow perpendicular to the surface initially for a short period of time, depending on temperatures and conditions of deposition, and afterwards a mesh of crystals in a smooth layer covers the whole surface. The initial period before that smooth mesh layer covers the surface is referred to as Nucleation phase. The formed layer continues to grow in either in Dry growth or Wet growth depending on temperature of the frost surface. The layer continues to grow in both thickness and density and the frost surface temperature varies in response to these changes. If the frost surface temperature reaches or exceeds the melting point (0ºC), while it is still below air dew point temperature, then the vapor

content of the air condenses on the frost surface. Liquid droplets then seep into the frost layer and freeze inside frost layer that has a lower temperature causing the frost layer to become denser. This would increase the thermal conductivity of the frost and might cause the frost surface temperature to drop below melting point. Then frost deposition on the frost surface starts again which results in thickness increase. Again with increasing frost thickness the frost surface temperature might reach the melting point and this cyclic process continues. This process is referred to as wet frost growth. On the other hand, if surface temperature is so low that frost surface temperature remains below melting point and below air dew point temperature, then air moisture content would deposit continuously on the surface directly into solid crystals from gas phase without condensation. This process is referred to as Dry frost growth (Kamath, 1985). Actually Wet frost growth happens when part of the frost layer is below melting point (deep parts) and other surface parts are above or equal to melting point. But all the frost layer temperature is below air dew point temperature otherwise evaporation or sublimation happens on that particular location and air starts to remove crystals changing them directly into gas phase from that location. In another word, if frost surface temperature is above air dew point temperature, no frost deposition occurs (except for that part of air that moves into the porous frost layer and is adjacent to the colder frost layers). If frost surface temperature is below air dew point temperature, then two cases may occur: 1- Frost surface temperature is below melting point (0ºC) (Dry frost growth) 2- Frost surface temperature is above melting point (Wet frost growth). It is obvious that in the case of Wet frost growth, the original cold surface temperature, where the thickness of frost is zero, is below melting point but frost surface temperature is above melting point.

It is worth noting that that at any time during the test or frost formation process, because of air temperature fluctuations and changes in dew point temperature, if the dew point temperature reaches below the frost surface temperature for a while, frost formation would stop for that period

of time. Sometimes even it is possible and actually it happened during the current study that frost would be removed from the surface by air by turning the crystals directly into vapor due to sudden decrease in air dew point temperature far below the frost surface temperature. In this case air that reaches the frost surface has relatively lower moisture content and it can still take more moisture from frost layer.

In cases when surface temperature are much lower than air dew point temperature (about 60ºC lower) there is mist or fog formation in the air adjacent to the surface (Rosner and Epstein, 1968).

For conditions of the present study however, the entering air was kept in a constant dry bulb temperature of 1.67ºC ±0.56 ºC and constant wet bulb temperature of 0.56ºC ±0.28ºC. These conditions lead to a constant dew point temperature of -1.02 ºC±0.65ºC. In all the tests of this study, dew point temperature was lower than melting point and all the frost formation process in this study is assumed to be in Dry frost growth regime.

There are other studies that divided the frost growth period into totally different stages. One of these studies is Hoke (2000) and Hoke et al. (2004) that divide the frost growth period into two distinct scenarios: The first is "condensation frosting" which happens when water vapor forms liquid droplets that freeze immediately and grow and coalesce with neighbouring droplets although surface temperature is well below zero Celsius or triple point of water. The second is “ablimation frosting” which is direct deposition of water vapor on the cold surface as a solid frost. Hoke et al. (2004) believed that every frosting process starts initially with condensation frosting and then after some time water vapor ablimates on the frozen droplets and since then frost process continues through ablimation. Condensation frosting period was divided into three regimes: a) "condensation period" which is a short time that takes to condensate to be frozen b) "early frost growth" period which is frost increases in thickness in an almost constant growth rate. c) "mature frost growth" that thickness increases proportional to square root of time. The duration

of first regime, condensation period, was found to decrease with decreasing surface temperature, decreasing surface contact angle (moving to hydrophilic surfaces) and increasing mass transfer driving potential but it could hardly last beyond 10 minutes for any case. Hoke et al. (2004) also mentions that the transition from early frost growth to mature frost growth is gradual and it is difficult to identify and demarcate. They found that initial frost structure is different in hydrophilic and hydrophobic surfaces. On a hydrophobic surface a protrusion (a thin vertical spire that comes out of the top of water droplet which is freezing) formed on the top of each droplet at the end of freezing process which acted as a site for further frost deposition while on the hydrophilic surfaces there was no protrusion observed. The spires could be more than one for each droplet and after some time branches appeared on spires to form a more uniform frost layer.

There are other previous studies than observed somehow condensation frosting as well. Shinagawa et al. (1992) investigated nucleation of water vapor on a cold copper surface to determine the circumstances in which whether liquid or solid nucleation happens. There was only water vapor used in an evacuated test chamber that was in contact with cold surface and there was no air present there. They found that partial pressure of vapor has a key role to determine which type of deposition happens on the surface. In their experiment, water vapour partial pressure and surface temperature were not changed independent of each other and results are only available for a certain range of conditions. Visual observation was used to determine the type of frost deposition. They found that for the temperature of -16°C and below and for the water vapour pressure of 50 to 200 Pa, only ablimation frosting (direct solidification) occurs. From the surface temperature of -11°C with water vapor of 350 Pa to surface temperature of -16°C and 200 Pa, formation of liquid condensate happens on the surface that is followed by freezing of the droplets immediately. The experiment was setup so that the surface temperature used to decrease in a slow rate and water vapor pressure used to decrease too at the same time because of deposition of water vapor on the surface. They concluded that the condensation frosting happens when the

water vapor pressure is above 200 Pa. But the maximum temperature they had in their experiment was -8°C and 350 Pa and there was no experimental point to verify this hypothesis for temperature between 0°C and -8°C especially for water vapor partial pressure of 500 to 650 Pa which is near frost test conditions of heat exchangers. Their conclusions might need to be used with caution in heat exchanger frosting conditions.

The other study that talked about "condensation frosting" is Tao et al. (1994) which with microscopic observation claimed that there is a short time in the beginning of frost formation (around one minute for aluminium surfaces) that subcooled liquid droplets form on the surface. Then quickly all of them turn into solid crystals although cold plate temperature is well below zero in the range of -6°C to -20°C. The air temperature was constant at 21°C and relative humidity was in the ranged between 30 to 60%.

There is another study that assumed condensation frosting which is Satio et al. (1984). They used experimental microscopic observation to study early frost growth stages on a polished copper cold vertical plate and on horizontal cylinders in an array (to simulate a geometry similar to fin and tube coil) under forced convection using microscopic observation. Air temperature was 20°C and surface temperature was varied in the range of -5 to -15°C. They performed their experiments with three different air relative humidity level of 50, 65 and 80% and air velocity of 2, 6 and 13 m/s. They found that in early frost deposition stage water vapor condenses on the cold surface as an unstable supercooled liquid for a short time and then these droplets freeze immediately. They found that frost density is affected by number and density of the formation of these frozen droplets. This short time was called "freezing time" was found to be reduced by a number of affecting factors like lower surface temperature, higher air humidity, higher air velocity, shorter distance from the leading edges and smaller contact angel (hydrophilic surfaces). Freezing time was different for different test conditions but as an example for air velocity of 2m/s and relative humidity of 80% in the location of 5mm from the leading edge, freezing time for surface

temperatures of -5, -7, -10 and -13 was 35, 25, 15 and 20 seconds respectively. For other conditions, the freezing time was different and it varied from 5 to 90 seconds but the majority of the data points lied between 10 to 30 seconds. They observed that after freezing of these small droplets, micro-ice crystals start to grow on them one dimensionally perpendicular to the surface in early stages. The reason that their freezing time observation was much longer than Tao et al. (1994) study, which was less than one second, is not known. Although Satio et al. (1984) testing surface was copper and Tao et al. (1994) surface was aluminium and relative humidity was slightly different author does not think that these reasons alone could explain this large difference between two observations.

Other study that stated condensation frosting happens in all frost growth processes is Wu et al. (2007a) that experimentally investigated frost formation on horizontal flat copper plates using microscopic observations. The plate temperature range was between -20 to 0°C and air relative humidity varied between 15 to 85% in constant dry bulb temperature of 22°C. They observed that frost formation starts with formation of small supercooled liquid droplets that freeze afterwards as shown in Figure 10. Then initial frost crystals forms and grows on the frozen droplets while some of crystals collapse on the existing crystals and finally frost layer continues to grow.

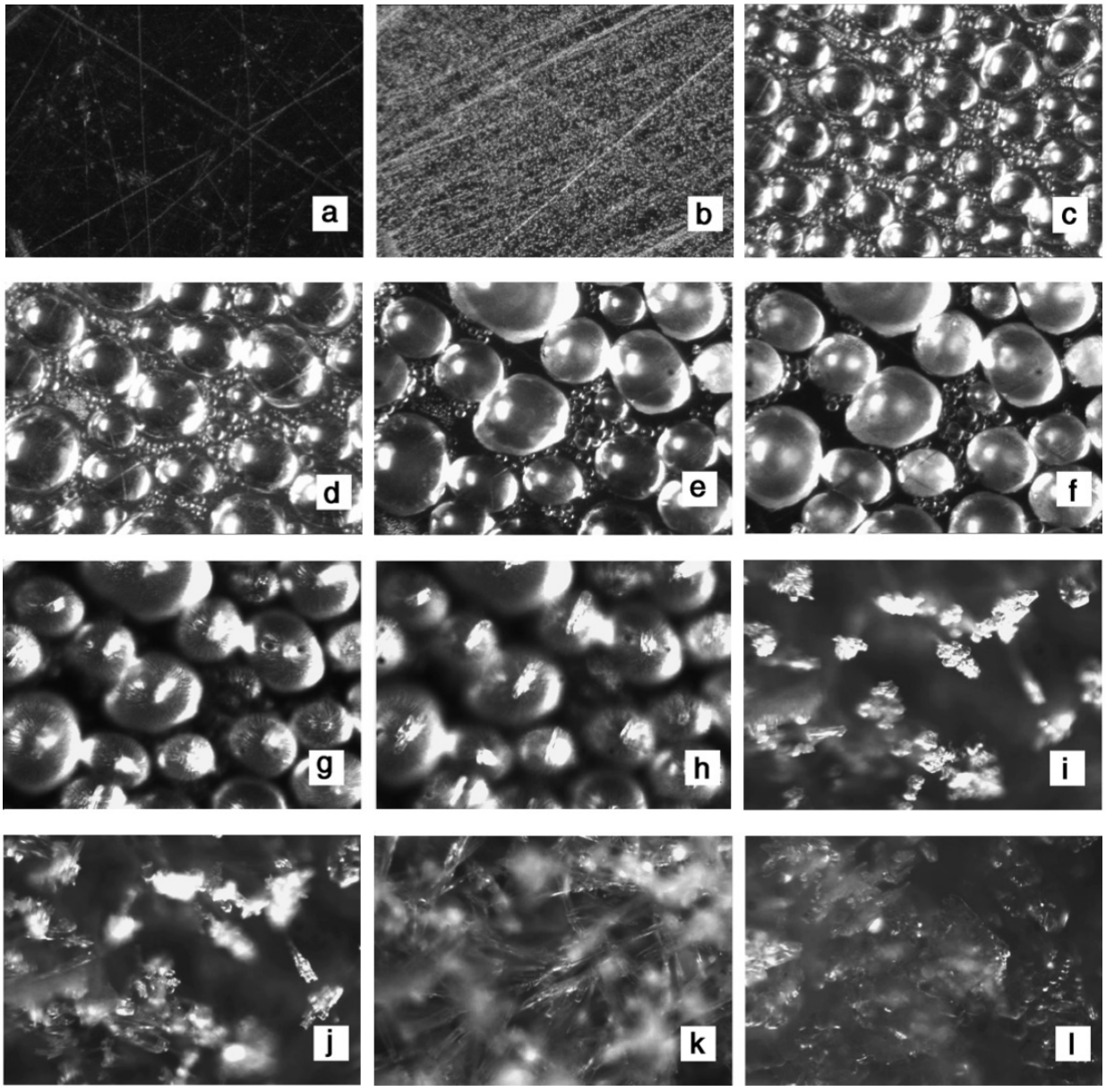

Figure 10: Initial stages of frost formation on a copper flat plate (CA=84°) at surface temperature of -12°C with air dry bulb temperature of 22°C and 50% relative humidity. The pictures are taken by a microscopic camera every 2.5 second from the beginning of frost growth (Wu et al., 2007a).

They found that formation of droplets happens for all temperatures and humidity range tested however droplets freezes sooner in lower surface temperatures and higher air relative humidity while droplets were smaller at lower surface temperature and lower air relative humidity. They

found that the freezing time for these supercooled droplets is mainly a function of surface temperature while air humidity had smaller effects on it as shown in Figure 11. The freezing time for air relative humidity of 85% was found to be around 3 minutes for surface temperature between -20 and -10°C. For surface temperature between -8 and -10°C, this time was about 3t to 10 minutes and for temperatures between -6 and -8°C, it was found to be between 3 to 25 minutes as shown in Figure 11[10]. Supercooled droplets sizes were found to be a function of surface temperature and relative humidity too. The average diameter of droplets for the surface temperature between -20 and -8°C was about 0.1mm but as surface temperature was varied from -8°C to -6°C, the droplet diameter grew up to 0.5mm. By microscopic observation they categorized initial crystal shapes into five main types of 1-supercooled water droplet structure 2-irregular crystals 3-flake crystals 4-needle and pole crystals 5-feather (dendrite) crystals. They found that the initial shape of crystal depends mainly on surface temperature and slightly depends on excessive vapor concentration between the bulk air and air adjacent to plate surface as shown in Figure 12 and Figure 13. In the excessive vapor concentration between 0.001 to 0.002 kg vapor/kg air (close to the present study range) their result showed that the shape of crystals would be frozen supercooled water droplet structure at surface temperature between 0 and -7°C and would be irregular crystals at surface temperature range between -7 and -10°C. If surface temperature gets lower between -10 and -13°C, then it will enter the region of flake crystals. According to their results, the initial frost crystals will not be needle or dendritic type in the above ranges which is close to present study range of experiments. Their findings somehow seems to be contradictory to previous findings of Hallett and Mason (1958) and Kobayashi (1958) shown in Figure 6 and Figure 7 about shape of crystals that found plates, needles and dendritic type of frost in those range of surface temperature and air humidity. Wu et al. (2007a) states that these are

[10] Based on their results it seems that if a coil designer could keep the surface temperature of the coil above -6°C, then the freezing time is so long (more than 15 minutes) that supercooled water might be able to drip down and drain from the coil based on gravity. So frost formation on the coil might significantly decrease for surface temperature above -6°C. We will discuss frost formation on surface temperatures below or above -6°C in the next chapters with our experimental results.

initial frost crystal shapes and they assumed that the frost surface temperature (temperature of frost formation) to be equal to the surface temperature. It is possible that real temperature of frost formation in Wu et al. (2007a) work which has to be in thermal equilibrium with air stream adjacent to the surface, are indeed higher than plate surface temperature. Especially because air temperature in Wu et al. (2007a) experiments was very high and was kept constant at 22°C. If this is true, then the data of Wu et al. (2007a) with a shift in temperature should somehow should match the previous findings of Hallett and Mason (1958) and Kobayashi (1958). Reanalyzing the data of Wu et al. (2007a) with a shift in temperature is consistent with this assumptions and actually with such a shift, the needle type and feather (dendritic) type crystals in Wu et al. (2007a) study could have formed in the higher temperatures as Hallett and Mason (1958) and Kobayashi (1958) found in their results. This interpretation of shifting the data of course needs further investigation and author of this dissertation does not intend to underestimate or neglect the other necessary cautions or complexities involved in these sorts of data interpretation. Getting further into the detail discussion of this topic is somehow out of scope of the present study. As a closure, author wants to point out that assuming the frost crystal types to be needle and dendritic type (in the range of surface temperature between 0 and -10°C and excessive water vapor concentration between 0.001 to 0.002 kg vapor/kg air) is more consistent with the findings of other previous researchers (Hayashi et al., 1977b) and also recent findings of Wang et al. (2007) who found the frost type to be needle type at surface temperature of -7°C which is going to be discussed in more details in the followings. Later, using the same previous experimental setup, Wu et al. (2007b) in another work, investigated early stages of frost formation and tested a bare and a hydrophobic coated copper surface with contact angles of 56° and 110° respectively. Their images at surface temperature of -10°C from frost for bare copper surface showed somehow that the visual shape of frost is more needle type and a type of "forest of trees" as Hayashi et al. (1977b) stated before. Images of frost on the hydrophobic surface were somehow more similar to feather (dendritic) type, however higher resolution pictures are needed to precisely confirm this

observation. Anyway, their later findings were somehow more consistent with observations of other studies.

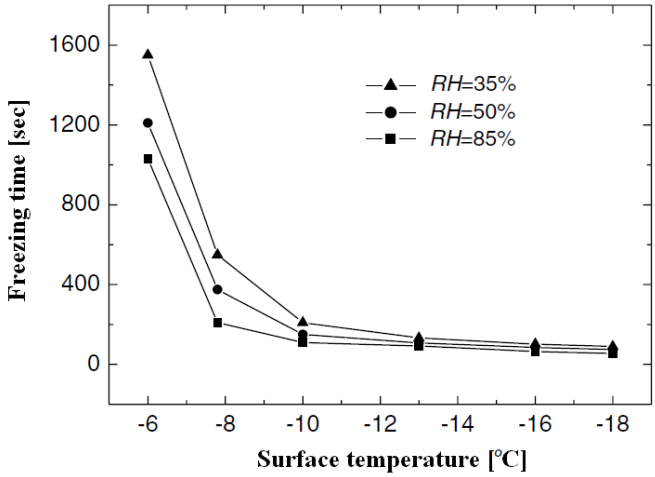

Figure 11: Different freezing times of supercooled droplets as a function of surface temperature and air relative humidity for a copper plate (Wu et al., 2007a).

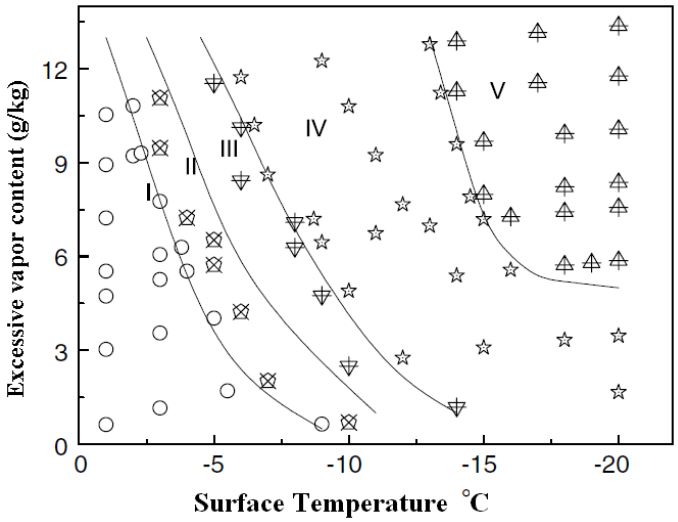

Figure 12 – Types initial frost crystals shapes as a function of surface temperature and excessive water vapor content between bulk air and air adjacent to the surface. I: super-cooled water droplets, II: irregular crystals, III: flake crystals, IV: needle and pole crystals, V: feather crystals (Wu et al., 2007a)

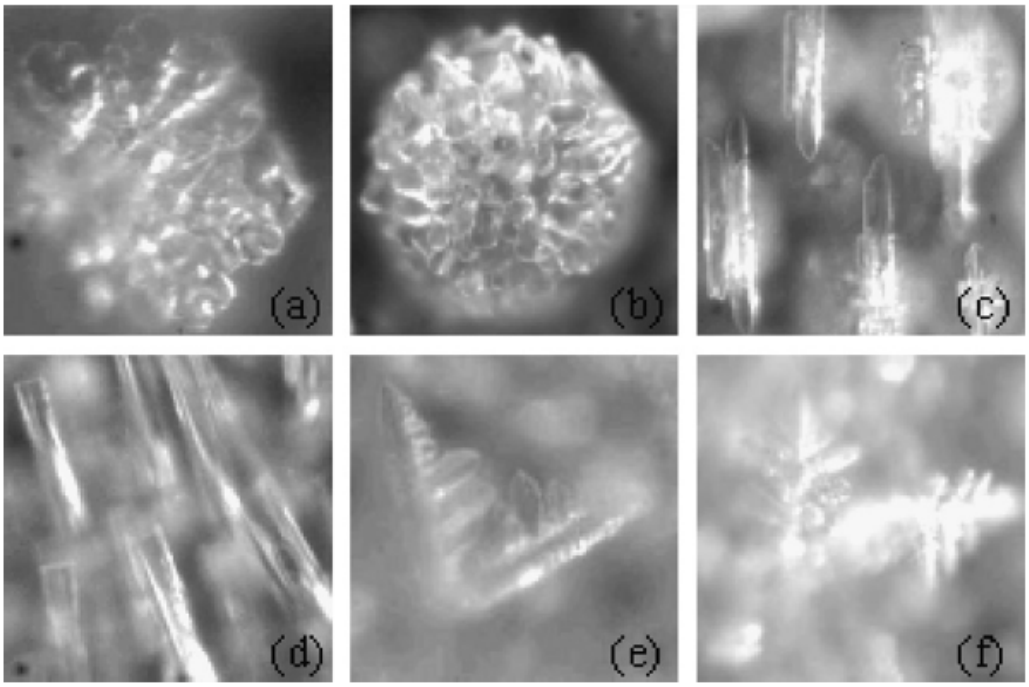

Figure 13 - Four typical shapes of initial frost crystals (a) irregular crystals (b) flake crystals (c, d) needle and pole crystals (e, f) feather crystal (Wu et al., 2007a).

One of the studies that focused more on visual differences that surface coatings make on the shape of frost was Wang et al. (2007). They experimentally studied frost formation on a new developed super hydrophobic surface with contact angle of 155° using microscopic observations. They found that for a bare copper surface the shape of frost at surface temperature of -7°C and 55% air relative humidity was more needle type that grows into a grass structure or forest soon as shown in Figure 14. For other two hydrophobic surfaces with contact angles of 120° and 155°, first liquid droplets started to form and froze on the surface and then frost started to grow on top of the frozen droplets. For super hydrophobic (155°) surface the thickness seemed less than regular hydrophobic surface (120°). The pictures from their work on frost growth for 3 different surfaces are shown in Figure 14. Wang et al. (2007) also found that the supercooled droplets forms on the bare surface too but the size of droplets are much smaller than in hydrophobic surface as shown in Figure 15.

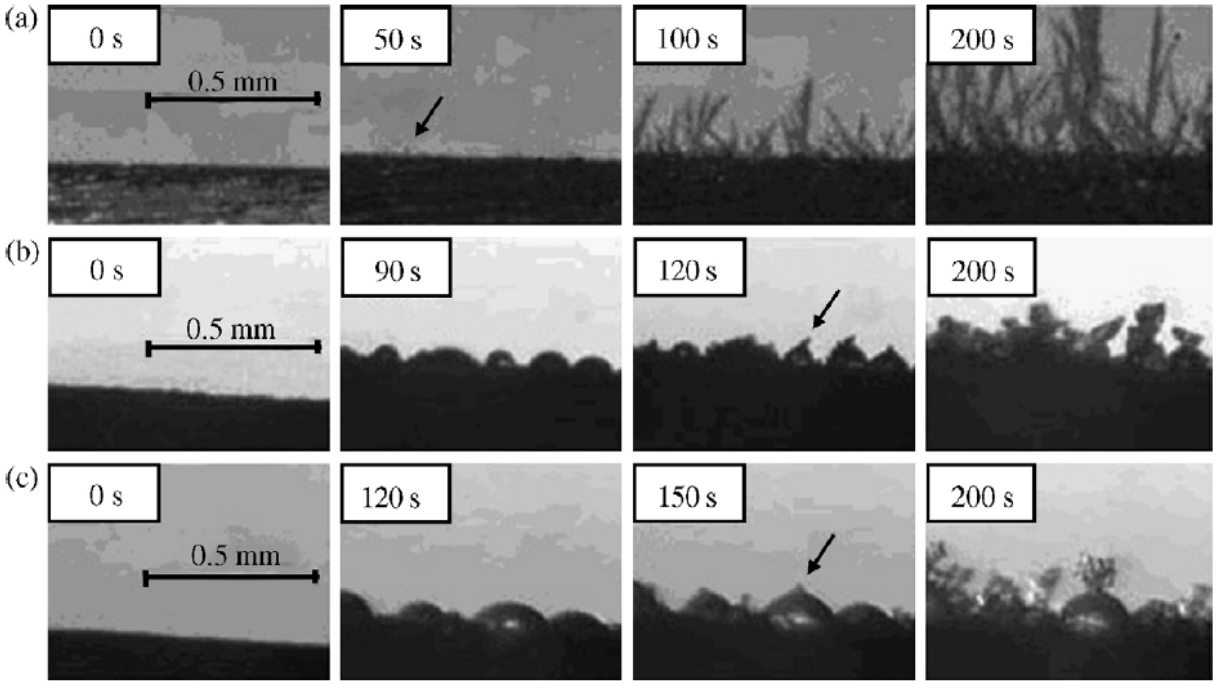

Figure 14: Formation of frosts on (a) bare copper surface (CA=64°), (b) hydrophobic surface with contact angle of 120°, and (c) superhydrophobic surfaces with contact angle of 150°. Conditions: temperature = -7.2°C, air relative humidity=55%. The arrow indicating the initial frost (Wang et al., 2007).

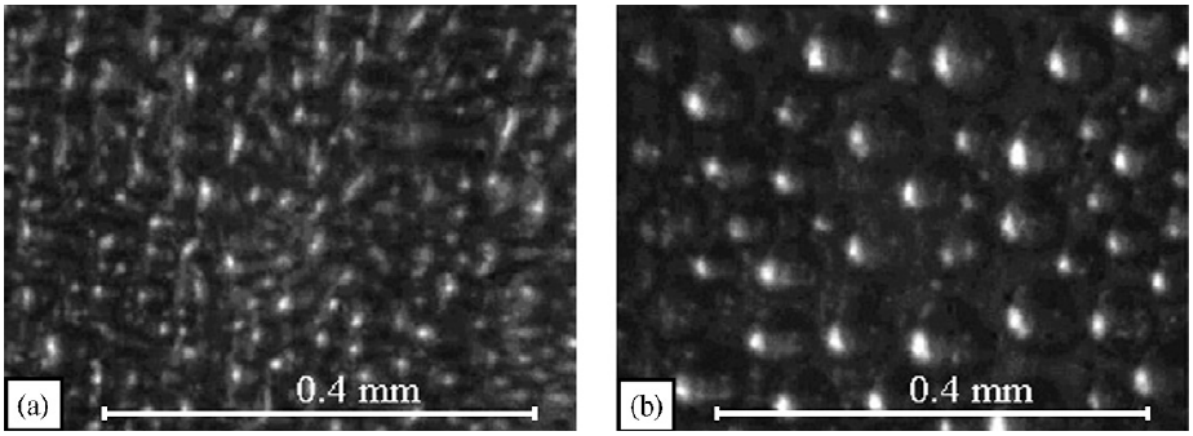

Figure 15: Initial formation of different size supercooled droplets prior to frost formation for (a) bare copper surface, and (b) hydrophobic surface with water contact angle of 120° (Wang et al., 2007).

In the present study, frost growth process was observed using a high resolution camera with a small probe tip that could take images or videos from the frost formation process as described in experimental setup chapter. It was found that it is very difficult to separate and demarcate the frost growth process into clearly distinct different stages. It was observed that on regular aluminium heat exchanger surface with contact angle of between 80 to 90°, first separate crystals appear on the surface which grows quickly into a white rough low thickness layer that covers the entire surface between 1 to 2 minutes (Moallem et al., 2012c). There were no supercooled droplets observed to form on the surface initially in all of the test cases except than on extremely hydrophobic coating with contact angle of 95 to 105°. Although a number of previous mentioned studies, that microscopically studied frost formation, stated that they have observed formation of supercooled droplets prior to formation of frost on the surface (Hoke et al., 2004; Na and Webb, 2003; Satio et al., 1984; Shinagawa et al., 1992; Tao et al., 1994; Wang et al., 2007; Wu et al., 2007a), there are other studies that did not observe any supercooled droplet forming on the surface (Hayashi et al., 1977b; Kamath, 1985). It is worth noting that for all the studies that observed supercooled droplets, their test surface was copper except for Hoke et al. (2004) that used glass and PTFE and Tao et al. (1994) and Na and Webb (2003) that observed supercooled droplets on the bare aluminium surface. The other fact is Tao et al. (1994) used air at temperature of 22°C on the cold surface in temperature of -6 to -20. There might be an argument that warm air might melt the initial ice embryos on the surface due to large magnitude of temperature difference and heat transfer. Moreover, as explained before, the classic theory of nucleation predicts that in such a large supersaturation levels, condensation is definitely preferred to ablimation (Fletcher, 1959b; Fletcher, 1962; Hobbs, 1974)[11]. Na and Webb (2003) used air at temperature of -5°C with surface temperature of -20°C. They stated that the contact angle of the surface for bare aluminium

[11] It is worth noting that actually a number of studies that observed condensation such as Satio et. al. (1984), Wu et al. (2007) and Tao et al. (1994) used high air temperatures around 20°C in their experiments which results in large levels of supersaturations. The air temperature in the works of Shinagawa et al. (1992) and Wang et al. (2007) was not reported. Hoke et al. (2004) used -1°C air temperature with substrate temperature of about -10°C.

was 31°. Aluminium has different alloys and probably their aluminium was different than one was used in the present study with contact angle of between 80 to 90°. Anyway, author of this dissertation does not intend to claim these differences explain completely all of the different observations of this study from theirs but just wants to point out the differences. From the observations of the present study, we could not verify formation of any supercooled droplet on the aluminium surface. One might argue that our observation technique was not fine enough to observe the tiny droplets on the surface. Considering the size of supercooled droplets according to previous studies which are between 0.1mm to 0.5mm in Wu et al. (2007a) study or smaller in Wang et al. (2007) work, and the fact that our camera had a magnifying power of 15 times, the final size of droplets in our images would be around 1.5 to 7.5mm. Thus it is hard to believe that those droplets are still not visible in our images. There were some tests that forming nuclei on the surface had a special different colour in the beginning of frost formation, but from images it is not possible to verify there are water droplets or ice embryos. Author has to conclude that the supercooled droplets did not form under most circumstances of this study (except where specifically mentioned) and the concept of special conditions of formation of these supercooled droplets are still open to further research. Our close observations revealed that after formation of the white mesh that could be heterogeneous nucleation of crystals on the aluminium surface, frost grows almost with a constant rate and frost thickness increases. Frost forms mostly a white rough and porous layer that grows and covers everywhere on the cold surface specially the leading edges of the fins. Then rate of thickness growth decreases when the air flow free areas are near blockage and thickness growth rates starts to flatten out. It was also found that frost growth on microchannel heat exchangers has its own complex nature and data from flat plates or simple geometries could hardly be applied to this geometry. As an example, some studies reported that frost grows on flat plates has only a slightly lower thickness in the trailing edge than the leading edge (Chen et al., 1999a; Mao et al., 1992; Tao et al., 1994) while in the current study, there was a considerable frost thickness on the leading edge of microchannel heat exchanger while there

was no visible frost at the trailing edge of the fins. The temperature of the air at the trailing edge of the coil is very close to the estimated surface temperature and the moisture content has reduced from 0.00348 kg/kg to approximately 0.00275, 0.00225 and 0.00175 for surface temperatures of -5, -8 and -11°C respectively. The air is still in supersaturated region at the trailing edges and still capable to deposit its moisture on the cold surface. However, the potential for mass deposition has reduced in comparison to initial condition[12]. Closer visual observation revealed that the trailing edge has a certain thickness of frost but there is a reason why it is not very apparent in visual observations. In the leading edge, the edges are covered with the frost and it makes a visible white cross section, however on trailing edges, there is no frost on the trailing edge itself because they are in the air wake regions. Inside the fins very near to leading edge, frost layer is visible. It can be possible that frost thickness in the depth of the fin is nearly uniform (or varying with a slight slope) from the leading edge to trailing edge. More discussion on this topic is trivial since there was no possible instrumentation and data from inside the depth of the coil to verify these hypotheses.

[12] As an example, for surface temperature of -5°C, air enters the leading edge region at 1.67°C/0.56°C (db/wb, AHRI condition). This air has a dew point temperature of -1.0°C, relative humidity of 82% and absolute humidity of 0.0035 kg/kg. As soon as air comes to contact with first leading edges and its local temperature drops to around -5°C, the relative humidity reaches 100% and even it moves into the supersaturated region where pressure of water vapor exceeds the saturated water vapor pressure that air can hold at the temperature of -5°C. So the dew point is still -5°C but supersaturation level is around 1.4. (The air temperature reaches -5°C but the moisture content is still temporarily at 0.0035 kg/kg so the air is somehow in the new unstable – metastable- relative humidity of 140% which is the ratio of pressure of existing water vapor to saturated water vapor at -5°C). This 1.4 is the potential for frost deposition and forces air to leave the extra moisture on the cold surface. However, when the air reaches the trailing edges, especially at the last minutes of the tests, according to our measurements, temperature of the bulk of fluid is around -5°C and the absolute humidity is 0.00275kg/kg. The supersaturation ratio for this air is around 1.1. Thus, the supersaturation level at leading edges adjacent to the cold surface is 1.4 and it drops to 1.1 at the trailing edges (This unstable air-moisture mixture with 110% relative humidity will dissociate to air with 100% relative humidity and tiny particles of water or fog). This suggests that air is not dry at the trailing edges and the moisture deposition has also not stopped at trailing edges but it has reduced to a lower rate. These ratio for the surface temperature of -8°C drops from around 1.8 to 1.2 (absolute humidity drops from 0.0035 to 0.00225 kg/kg). The ratio for surface temperature of -11°C drops from around 2.4 to 1.2 (absolute humidity drops from 0.0035 to 0.00175 kg/kg). The numbers mentioned in this footnote are general averages and approximates. They depend on geometry of microchannels and different samples have different values.

There was no obvious distinction between different images of different times of the tests to show something about "early or mature frost growth" as mentioned in some previous studies. All the frost growing period for all specimens seemed to be ablimation frosting and no frozen droplets were observed during the frost growth process (Figure 16). However in one extremely hydrophobic surface with contact angle between 95 to 105°, the structure of frost growth seemed to be condensation frosting dominant and there were visible frozen droplets that formed on the surface of heat exchanger although the surface temperature was constantly -6°C all during the test. These droplets seemed to be joining other droplets and make larger frozen droplets as Hoke et al. (2004) study had observed. The supercooled droplets seemed to be changing all the time and joining and coalescing with their neighbours. After a thick layer of ice and frost covered the surface, metal surface could not apply its surface energy effect. Then ablimation frosting continue to be dominant frost deposition mechanism and droplets remain unchanged while a porous layer of frost start to cover them as shown in Figure 16. The images of Figure 16 show the difference of frost growth between different surface coatings with different contact angles.

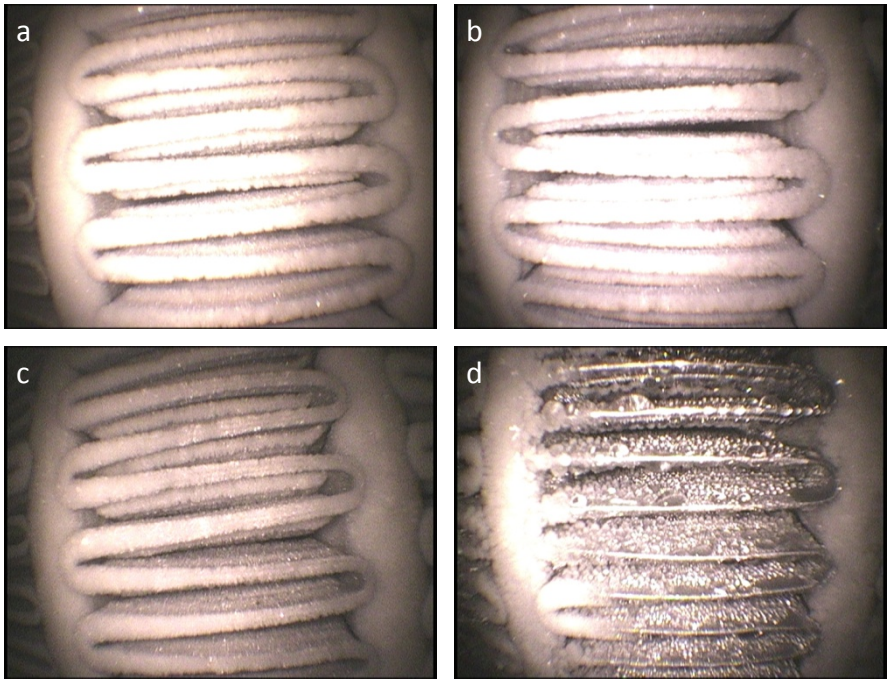

Figure 16: Frost growth on aluminum microchannel heat exchangers with different surface coatings: standard coil with no coating (a), hydrophilic coating with less than 5° contact angle (b), hydrophobic coating with contact angle between 90 to 95° (c) and hydrophobic coating with contact angle between 95 to 105° (d) for the same surface temperature of -6ºC. All the images show an example intermediate point in about the middle of the test Reproduced form (Moallem et al., 2012c).

CHAPTER IV

EXPERIMENTAL METHODOLOGY

4.1 INTRODUCTION

The literature review suggested that it is necessary to provide consistent transient frosting performance data sets for louvered folded fins adopted in microchannel heat exchangers. This dissertation describes a new experimental methodology to measure the frost mass, frost thickness and their growth rate during the actual operation of the louvered fins in cold ambient. Fin surface temperature, heat transfer, and air-side pressure drop across louvered folded fins were also measured during transient frosting cycles. The feasibility and repeatability of the measurements are demonstrated through a series of controlled laboratory experiments. These experiments highlighted the effects of fin surface temperature, geometry, air face velocity, and air humidity on the local frost growth on louvered folded fins.

4.2 Scope of Experimental Work and Test Matrix

The present study focuses on testing 12 different microchannel fin samples that were cut out from the commercial available microchannel coils and they have been selected so that they cover an acceptable range and variety of geometries for microchannel evaporators. 7 geometries and 5 different surface coatings on one geometry were selected to be the representatives of commonly accepted microchannel samples to be tested under frosting conditions. 7 different geometries were selected in a way to isolate effect of each design parameter such as fin density, fin width and fin depth in a parametric fashion. Table 2 shows the samples geometrical dimensions and gives an overview of the types of tests that were performed. Samples 1, 2 and 3 were tested under frosting condition to identify the effect of fin density or fin spacing on frost performance of microchannel while other geometrical parameters for these three samples were identical. For more details about dimensions of the samples and schematic demonstration of each parameter such as fin width, fin depth, etc. please see Figure 76 and Table 2.

Table 2: Overall dimensions of the samples and the purpose of their testing for 12 microchannel samples used in the present study.

		Fin Depth (Ch_d)	Fin Width (Ch_w)	Fin Spacing	Fin Density	Fin surface treatment	Fin Type	Surface temp.	Air face velocity (initial)		Air R. humidity	no. of tests	test objective
no.	Code	[mm]	[mm]	[mm]	[FPI]	-	-	[°C]	[m/s]	[fpm]	[%]	[ ]	effect of
1	Sample 1	27	8	2.44	10.4	None	Flat fin	-5, -8, -11	1.5	200	82	3	FPI
2	Sample 2	27	8	1.87	13.6	None	Louvered	-5, -8, -11	1.5	200	82	3	FPI
3	Sample 3	26	~8	1.25	20.3	None	Louvered	-5, -8, -11	1.5	300	82	3	FPI
4	Sample 4	25	10	1.31	19.4	None	Louvered	-5, -8, -11	1.5	300	82	3*	Width
								-8	1, 2	200, 400	82	2**	Velocity
								-8	1.5	300	72, 92	2***	Humidity
5	Sample 5	25	13	1.30	19.6	None	Louvered	-5, -8, -11	1.5	300	82	3	Width
6	Sample 6	30	8	1.37	18.5	None	Louvered	-5, -8, -11	1.5	300	82	3	Depth
7	Sample 7	19	8	1.45	17.5	None	Louvered	-5, -8, -11	1.5	300	82	3	Depth
8	Sample 8	19	8	1.45	17.5	Hydrophobic (AH 650) CA≈95~105°	Louvered	-5, -8, -11	1.5	300	82	3	Coating
9	Sample 9	19	8	1.45	17.5	Hydrophilic (AH 550) CA≈70~80°	Louvered	-5, -8, -11	1.5	300	82	3	Coating
10	Sample 10	19	8	1.45	17.5	Hydrophilic (FR 1000) CA≈10°	Louvered	-5, -8, -11	1.5	300	82	3	Coating
11	Sample 11	19	8	1.45	17.5	Hydrophobic (AH 653) CA≈95~105°	Louvered	-5, -8, -11	1.5	300	82	3	Coating
12	Sample 12	19	8	1.45	17.5	Medium (Alcoat® 5000) CA≈80~90°	Louvered	-5, -8, -11	1.5	300	82	3	Coating

: The specified parameter to investigate its effect

* 3 tests:(-5 -8 -11°C, 1.5m/s, 82%)- **2 tests: (-8°C, 1.0 2.0m/s, 82%)- ***2 tests:(-8°C, 1.5m/s, 72 92%)

All the coatings are Inorganic coatings

Sample 4 and sample 5 were tested to evaluate the effect of fin width or (Ch_w) and they are compared to sample 3 which has different fin width but identical fin density and fin depth. In this way, for each investigated parameter, there are 3 samples that could be contributing to provide data on the isolated effect of that particular geometrical dimension of the fins. The same is true for investigating the effect of fin depth in which sample 6, 7 and 3 are compared against each other to evaluate the effect of fin depth on frosting performance.

Each sample was tested at three different surface temperatures of about -5, -8 and -11°. The air temperature was held constant at dry bulb/wet bulb=1.7/0.6°C for all the frost tests according to standards of performance rating for the air source heat pumps (AHRI, Standard 210/240, 2008).

The effects of air velocity and air humidity were also evaluated on one of the samples with average medium dimensions as shown for sample 4 in Table 2.

Each test was repeated more than one time to ensure repeatability of the results and although the number of tests reported in Table 2 is 40, the total number of tests performed on the fin samples were more than 150 for data reduction and data analysis.

The fin temperature or surface temperature is defined throughout this dissertation as the tube wall surface temperature or fin root temperature. This value was directly measured by using a series of fine gauge thermocouples.

4.3 Construction and Geometry of the Fin Samples

4.3.1 Sample Preparation and Construction

In the present work, the fin samples were made of one column of louvered fins cut from commercially available microchannel coils. The tube of this one column of louvered fins was machined until a thin wall of metal attached to each side of the folded fins remained Since conduction heat transfer was employed in cooling the sample to the desired surface temperature, presence of tubes was not necessary in the present study. The removal of microchannel tube was also to eliminate the effect of different internal tube designs or microchannel ports. In addition the hollow ports in a tube were additional conduction thermal resistances that prevent uniform one-dimensional conduction heat transfer to the fin samples. The vertical height of each fin sample was about 15.24 cm (6 inches), while the fin density, fin depth, and fin height determined by the original design of the microchannel coils from which the samples were cut. The process of making the fin samples required a detail and careful machining due to the fragility of the microchannel fins. In this section, detail description on preparing the fin sample is provided.

The first step to prepare the fin sample is to examine the manufacture coils that are going to be used as the sample. From the coils, all the fin columns are examined to determine which fin column is good to be used as the test sample. After finding which column will be used, both fin columns adjacent to it need to be cut as shown in Figure 17. Aside from cutting the fin columns, the fin samples need to be cut to have vertical size of 15.24 cm (6 inches). This cutting process can be easily done using band-saw. While cutting the columns of fin, ensure that the band-saw

blade is as close to the microchannel tube as possible as seen in Figure 17. This method will cut the unused fins at the same time clean the fin residue from the tube.

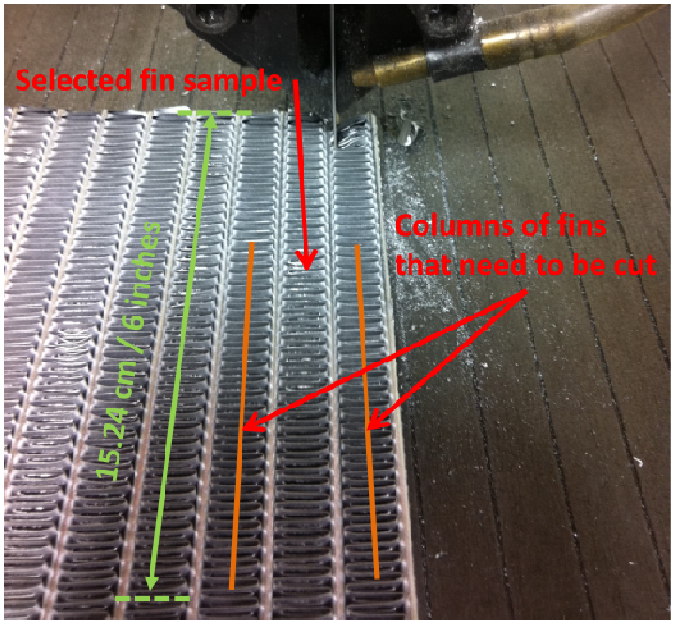

Figure 17: Preparation of the fin sample, Step 1, cutting procedure

The second step was to machine down both of the tubes in between the fins until a thin wall or metal attached to each side of the folded fins. This machining process could be done by using milling machine. Before milling the sample tubes, tools needed to be prepared in advance such as thin needles and sharp end mills bit with square end configuration. The needles were used to ensure that while machining the tubes, the sample stay flat on the vice of the milling machine. Also needles are necessary because without them due to high vertical pressure of the milling bit, the aluminum fins have to be clamped too tight and aluminum fins are deformed. These needles were placed in between the fins under the microchannel tube and put on the vice of the milling machine as shown in Figure 18. While clamping the sample, make sure that the clamping force is

good enough to keep the sample on the vice but at the same time not too much to damage the fin sample.

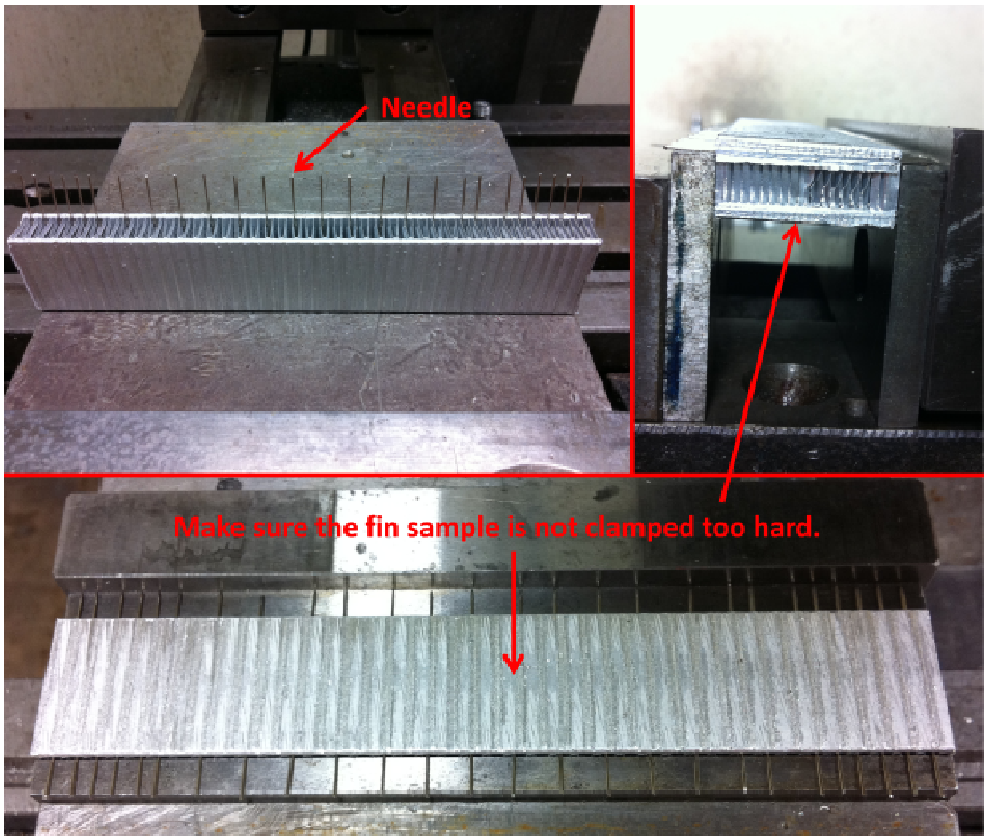

Figure 18: Preparation of the fin sample, step 2, usage of needles in milling process

The sharp end mill bit were important because it will prevent damaging the fin sample during the cutting process and produced flat & mirror finish. When doing the milling on the fin sample, couple of the first cuts on the sample can be done with 0.254 mm (0.01 inches) depth but afterwards the depth of cutting should be reduce to 0.127 mm (0.005 inches) to prevent cutting too deep into the tubes. Towards the end of the process when the microchannel tubes getting very thin, the depth of the cut should be reduced to (0.0254–0.0508 mm) 0.001-0.002 inches until all the surface of the sample become flat and clean. An example of a finished fin sample is shown in

Figure 19. This milling process needs to be done frequently and patiently to result in a good sample for the experiments.

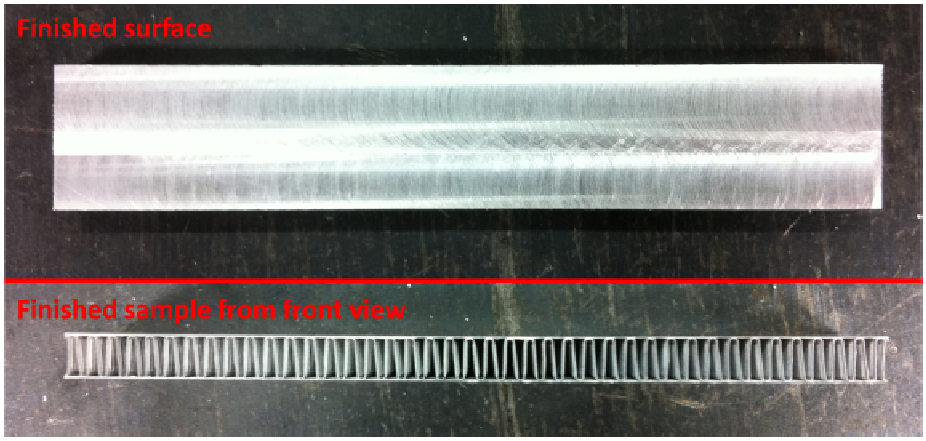

Figure 19: Finished fin sample

The plates attached to fin sample is designed to allow the measurement of fin temperature. As seen in Figure 20, the fin sample cut from the microchannel coil was placed in between two aluminum plates with 0.25 inch (6.4mm) thickness. These aluminum plates provided proper housing for the thermocouples and the plates were attached to the fin sample by using thermal epoxy (Duralco 132-IP-1). The plates were cut to have the exact same sizes as the fin sample and four small grooves were cut out in the aluminum plates for placing the thermocouple wires as. Four thermocouples are placed in between the aluminum plate and fin sample wall as shown in Figure 20. The readings of these thermocouples in the roots of the fins are referred to as the fin surface temperature in the present study. The fin efficiency of course will be applied as explained in the following chapters. It is obvious that the actual fin surface temperature along the edge of the fins varies depending upon the location in the fin and is a result of the local heat and mass transfer processes at the interface between frost and aluminum fins. Except than sample 5 that had a very wide width (13mm) and a fin efficiency of 0.91, the fin efficiency varied between 0.94 for

sample 4 to 0.97 for sample 1. This showed that due to short width of the fin in microchannel coils, the surface temperature of the middle of the fin is close to the temperature of the fin root.

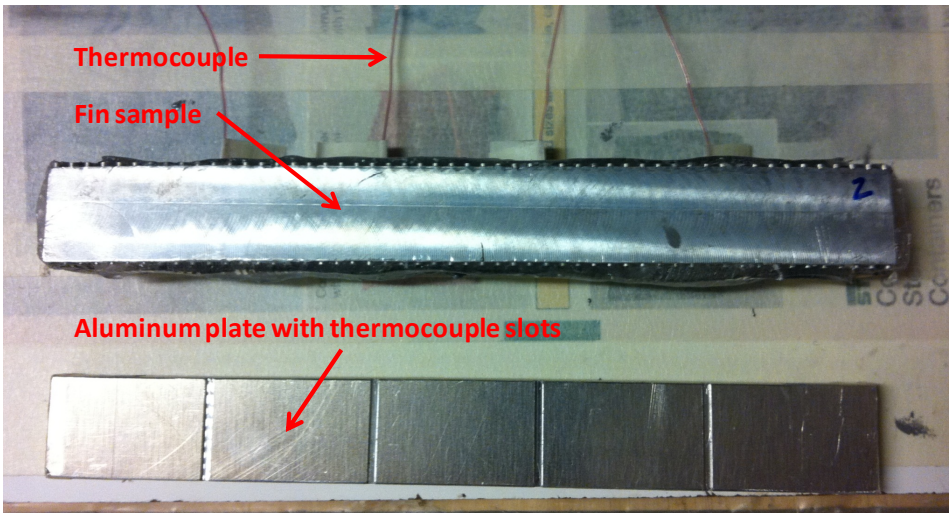

Figure 20: Aluminum Fin sample (top) with Aluminum plate (bottom) with 4 thermocouples grooves at one side of the Aluminum plate. Two identical Aluminum plate were mounted at each side of the sample.

4.3.2 Geometry of the Samples

The detail geometry of the samples is shown in Table 3. For schematic demonstration of each parameter such as fin width, fin depth, etc. please see Figure 76. The microchannel samples were chosen in a way that only one parameter (such as fin density, fin depth etc.) is varied at a time while all other dimensions remain constant. This allowed investigating the impact of frosting performance due to the variation of that particular parameter.

Table 3: Geometry of the microchannel fin samples used in the present study

Sample No.	Fin Depth (Ch_d) (mm)	Fin Width (Ch_w) (mm)	Channel Height (Ch_h) (mm)	Fin Density (FPI)	Tube thickness (mm)	Fin Thickness (mm)	Tube Type	Fin type	No of louvers	Louver pitch (mm)	Louver angle (Deg)	Louver Height (mm)	Louver Length (mm)
1	27.0	8.0	2.34	10.4	1.8	~0.1	MC 26 ports	Flat fin corrougated	-	-	-	-	-
2	27.0	8.0	1.77	13.6	1.8	~0.1	MC 26 ports	Louvered	16	1.50	~30	0.22	6.5
3	26.0	7.6	1.15	20.3	1.4	~0.1	Flat Tube	Louvered	24	0.94	~30	0.09	6.0
4	25.0	10.0	1.21	19.4	1.7	~0.1	MC 13 ports	Louvered	18	1.22	~30	0.24	7.5
5	25.0	13.0	1.20	19.6	2.0	~0.1	MC 18 ports	Louvered	20	1.23	~30	~0.21	9.5
6	30.0	8.1	1.27	18.5	1.4	~0.1	MC 18 ports	Louvered	28	0.86	~30	~0.2	7.0
7	19.0	8.0	1.36	17.4	3.0	~0.1	Flat Tube +Internal Fins	Louvered	16	0.94	~30	~0.2	6.5
8	19.0	8.0	1.34	17.6	3.0	~0.1	Flat Tube +Internal Fins	Louvered	16	0.94	~30	~0.2	6.5
9	19.0	8.0	1.34	17.6	3.0	~0.1	Flat Tube +Internal Fins	Louvered	16	0.94	~30	~0.2	6.5
10	19.0	8.0	1.34	17.6	3.0	~0.1	Flat Tube +Internal Fins	Louvered	16	0.94	~30	~0.2	6.5
11	19.0	8.0	1.34	17.6	3.0	~0.1	Flat Tube +Internal Fins	Louvered	16	0.94	~30	~0.2	6.5
12	19.0	8.0	1.36	17.4	3.0	~0.1	Flat Tube +Internal Fins	Louvered	16	0.94	~30	~0.2	6.5

The detail of surface treatments and coatings that was applied to some of the samples are shown in the Table 4.

Table 4: Surface treatments or coatings used for the microchannel samples of the present study

Sample No.	Coating
1	Uncoated
2	Uncoated
3	Uncoated
4	Uncoated
5	Uncoated
6	Uncoated
7	Uncoated (CA≈80~90°)
8	Hydrophobic (AH 650) CA≈95~105°
9	Hydrophilic (AH 550) CA≈70~80°
10	Hydrophilic (FR 1000) CA≈10°
11	Hydrophobic (AH 653) CA≈95~105°
12	Medium (Alcoat® 5000) CA≈80~90°

4.4 Experimental Apparatus

4.4.1 Sample Bounded in Small Air Tunnel

When frost started to accumulate on the fins, the air flow blockage caused an increased pressure drop. To eliminate a systematic error during the measurements of the air-side pressure drop across the fin sample in frosting conditions, the air steam should not be allowed to by-pass the fin sample through micro cracks and small fissure around the perimeter of the sample. To eliminate the risk of air by-pass the fin sample, a Plexi glass was installed at the inlet and outlet of the fin sample as shown in Figure 21. Other attempts of using accurately sized pieces which were moving parts of the vice to fit in place and prevent the air stream from bypassing the frosted sample were not successful. The prevention of air by-passing the fin sample when frost accumulates on the heat transfer surface was the key factor to achieve good repeatability of the measurements.

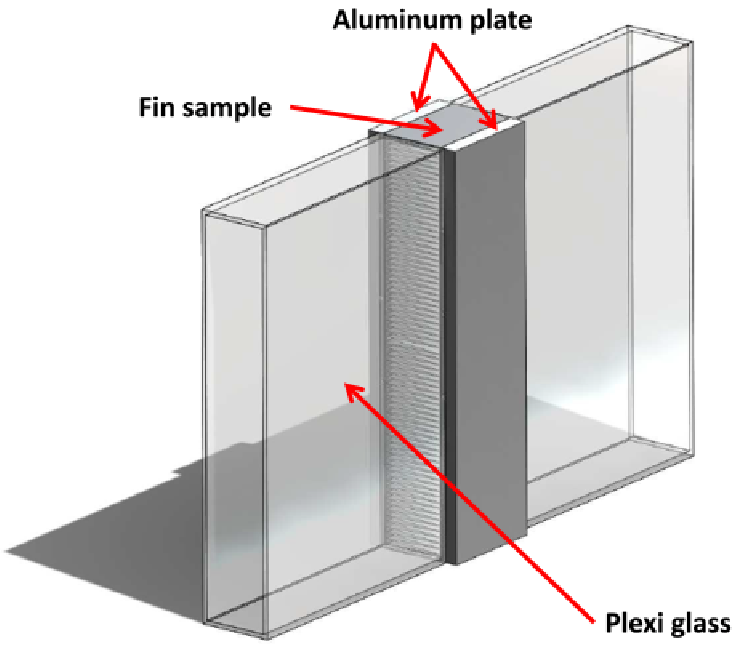

Figure 21: Fin sample with small Plexi glass tunnel around it to prevent air leakage

4.4.2 Thermo-electric Cooler Modules

In order to remove the heat from the sample fin shown in Figure 21, and cool it to the desired temperature, a method originally proposed by Thomas et al. (1999) was used. Four ThermoElectric Cooling (TEC)[13] modules were installed, two in each side of the fin sample to remove heat from the fin sample based on conduction heat transfer mechanism and to control the fin temperature during frosting period, as shown in Figure 22. The amount of heat transfer removed from the fin sample to the liquid heat sink was accurately controlled by variable power transformers connected to each TEC.

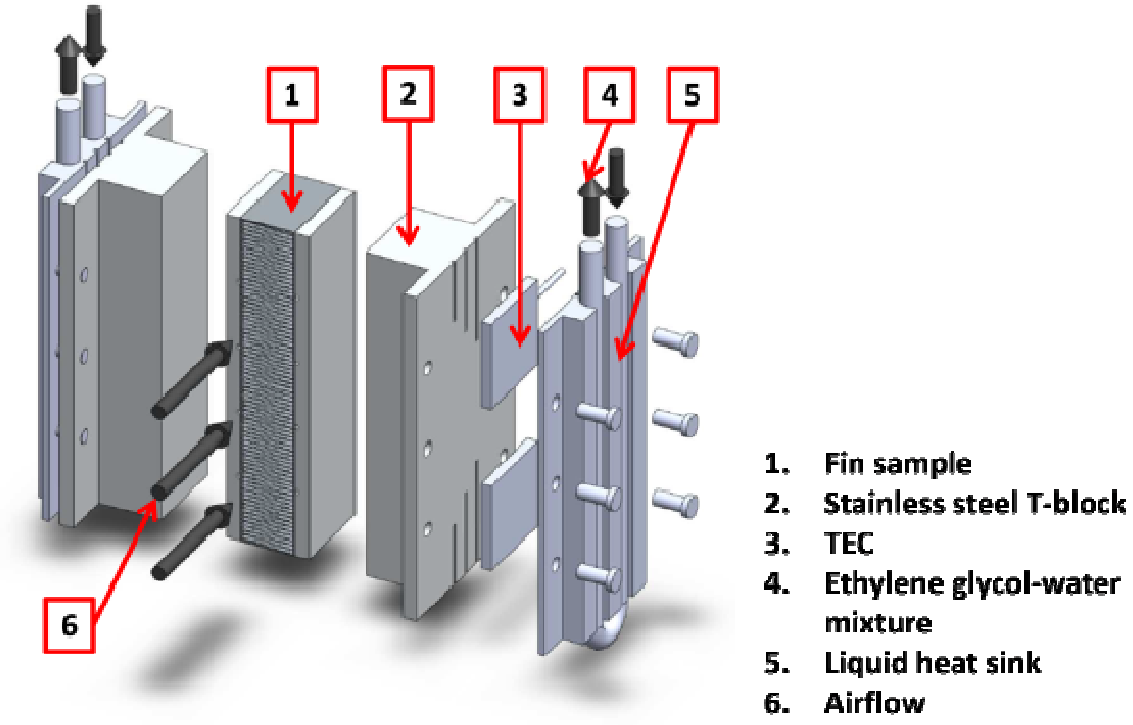

Figure 22: Part of the experimental apparatus that holds the sample and TEC's

[13] 44 watts (150.1 Btu/hr)-capacity TECs, manufactured by Custom Thermoelectric, Inc.

Ethylene Glycol water solution (50% volume concentration) was circulated inside the copper tubes of the liquid heat sink shown as component 4 in Figure 22 to remove heat from the hot side of the TECs. To be able to provide additional capacity for TEC's and to respond quickly to the control strategies, temperature of hot side of TEC were kept as low as around -4°C to -10°C with using cold Ethylene Glycol solution. The cold side of the TEC had different values at different tests ranging from -8°C to -14°C. This cold side of the TEC was removing heat from the sample via conduction heat transfer so that the thermocouples at the root of the samples show a constant temperature of -5, -8 and -11°C during the tests. Two custom made stainless steel T-shape blocks were inserted between the fin sample assembly and the cold side of the TECs. The T-blocks were machined to nearly the same depth as the fin sample assembly to provide uniform one dimensional heat flux perpendicular to the fin assembly walls. Each TEC was instrumented with six thermocouples, three on the hot side and three on the cold side, to monitor the temperature of each side of the device. The temperature difference between cold side of TEC and thermocouples at the root of the fin samples then was used to calculate the value of conduction heat transfer from the sample. The air flows into the fin sample along the x-direction as shown in Figure 23 (mention the other figure). Heat is removed from the air stream by the louvered fins and it is laterally transported along the y-direction by the T-blocks. The entire device was assembled in a compact test assembly, as shown in step (3) of Figure 23. Then the test assembly was mounted inside the low temperature air tunnel as shown in step (4), and exposed to frosting ambient conditions during the tests.

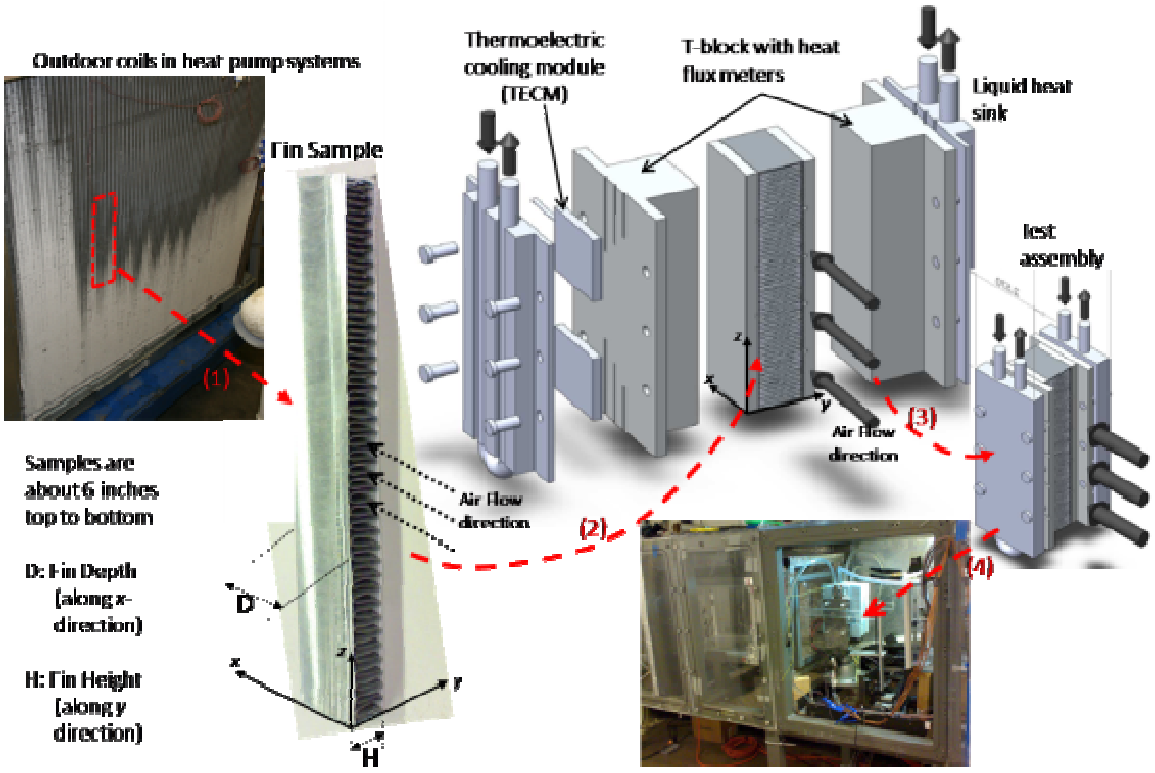

Figure 23: Procedure for the preparation of the test assembly set up inside the air tunnel

4.4.3 Sample and Components Mounted on Vice

Even though the temperature gradient was small, foam insulation boards were installed around the T-blocks to minimize the heat gain to the fin sample during the frosting experiments. The un-insulated and insulated test apparatus are shown in Figure 24 (a) and (b), respectively. The apparatus was mounted on an adjustable mechanical vice that was modified ad-hoc for these experiments with adjustable springs as shown in Figure 24(a). The springs redistribute the contact pressure along both surfaces of the fin sample assembly and the vice provides sufficient pressure on the fin sample to allow heat conduction across the surfaces in mechanical contact during the

frosting periods. The vice was opened to detach the fin sample at the end of the frosting period in order to quickly measure the weight of the frost accumulated on the fins.

Figure 24: Illustration of the test assembly mounted on the modified vice with springs (a) un-insulated test apparatus; (b) insulated test apparatus; and (c) zoom of the fin sample attached to transparent plastic channels at the inlet and at the outlet of the fin sample with respect to the air flow direction

4.4.4 Small Air Tunnel and Nozzle

When air leaves the sample, it is guided by the Plexi glass channel shown in Figure 21. This Plexi glass channel is attached at its end side to a small scale air tunnel to guide the air flow to a measuring section for air volumetric flow measurements as shown in Figure 25. A nozzle in compliance with ASHRAE air flow measurement requirements (ASHRAE Standard 41.2) was employed to measure the air flow rate and all the dimensions of the small tunnel in Figure 25 was designed and built according to ASHRAE standard 41.2. The calculation procedure and instrumentation will be described later.

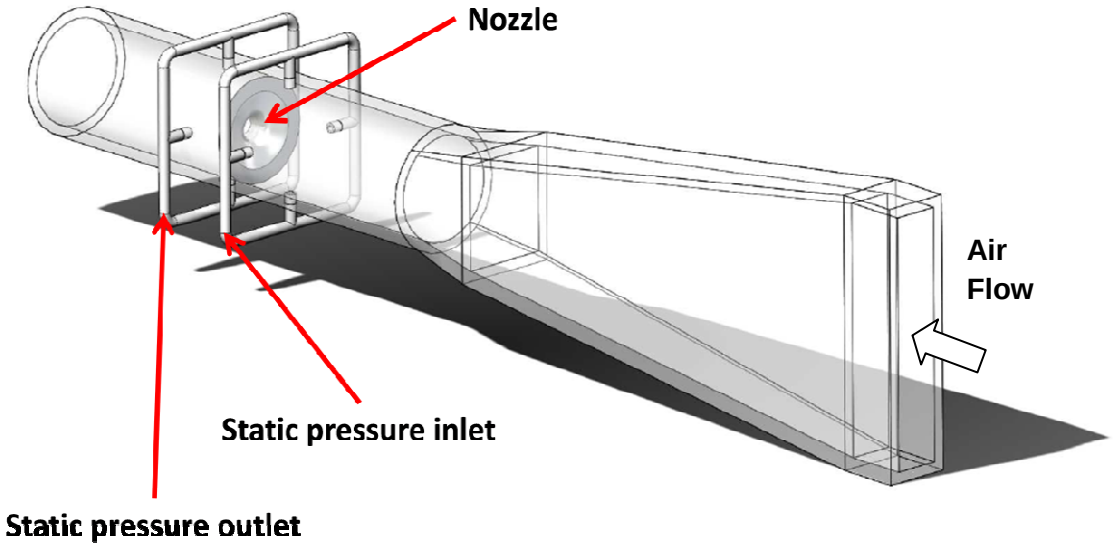

Figure 25: Structure of small tunnel to measure the air flow after the fin sample with nozzle and instrument locations.

4.5 General Test Setup Description

4.5.1 Air Tunnel

A large air flow test set up was designed and built in laboratory to investigate the thermal performance and frost deposition for microchannel heat exchanger. The basic layout of the test facility and the components are described in this section. The facility was designed to control the test condition specified in standard (AHRI, Standard 210/240, 2008).

The fin-TEC was mounted on a vice, which held the sample together and the entire assembly was placed inside the large air tunnel shown in Figure 23 (step 4) and component

2 in airflow loop in Figure 26. The airflow was a closed loop air tunnel that had a square cross sectional area of 0.6m×0.6m (2 ft × 2 ft) and span about 2.8m (109 in.) long. The air tunnel was a closed loop duct system that was equipped with instruments and censors to control and monitor the air condition inside the tunnel to simulate ambient air for heat pump winter operating condition. Main components of the air tunnel such as refrigeration coil, variable speed fan, electrical heater and ultrasonic humidifiers are used to cool and condition the air to the desired condition as shown in Figure 26.

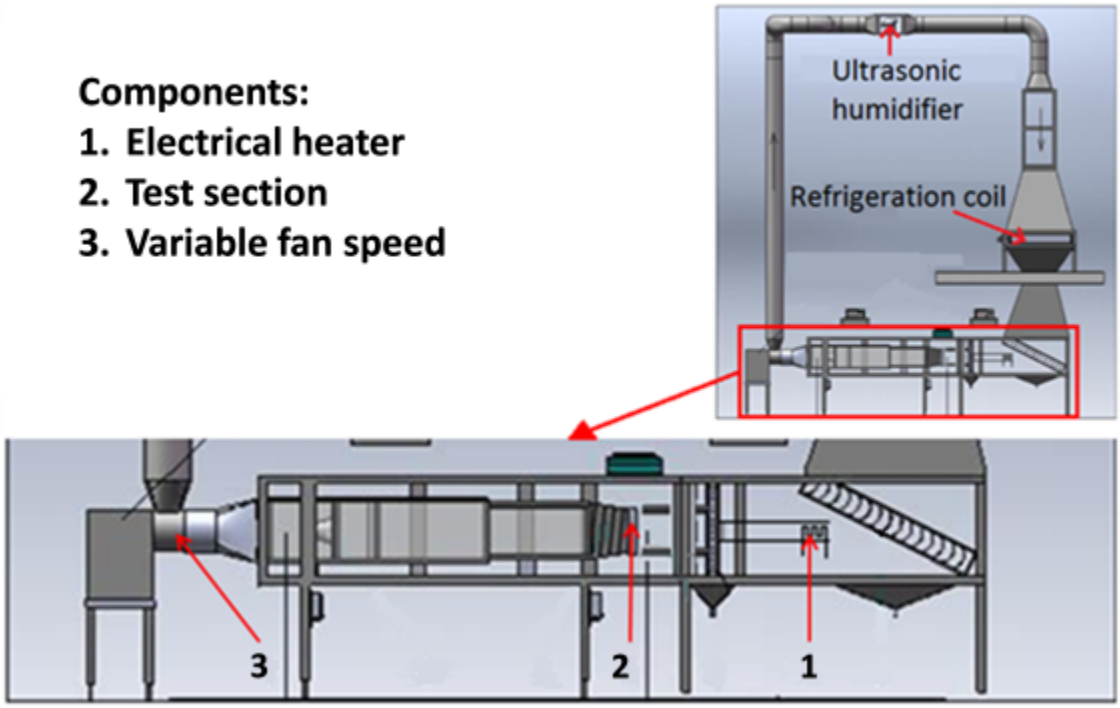

Figure 26: Schematic of air tunnel or airflow loop

The inlet air is controlled at 1.67/0.56°C (35/33°F) dry bulb/wet bulb temperature, unless otherwise specified. This air condition yields the air relative humidity of 82% during the experiment. The air face velocity at the inlet is controlled with a variable speed fan with a range of 0.8 to 1.5 m/s (157 to 295 fpm).

The control schematic that was adapted to control the air inside the air tunnel is shown in Figure 27. The set point condition of the air at the inlet of the fin sample is represented by point 4. The air was cooled when it passed through the fin sample, thus the temperature decreased and the humidity content in the air was reduced shown as point . The location of point 5 in Figure 27 can be varied depend on the capacity of the tested fin sample. The cold air that leaves the fin sample is being recirculated again inside the air tunnel. This air is being heated up from point 5 to point 1 due to the heat gain caused by temperature difference between the air inside the tunnel and the air around the tunnel at approximate 23.9°C (75°F). Additionally, the pressure difference between inside the tunnel and surrounding caused infiltration. Point 1 is the estimated air condition before the humidifiers. From point 1 to point 2, there is humidification process to increase the humidity content of the air before the refrigeration coil. The rate of humidification process can be adjusted by controlling the number of humidifiers that operates in the DAQ system at any given time during the experiment. Between point 2 and point 3, the heat in the air was removed by the refrigeration coil. This coil is directly connected to a low temperature chiller. The amount of the cooling can be adjusted by changing the high precision valve that regulates the amount of refrigerant flowing to the cooling coil. The air is then heated by a variable output electrical heater to control the air to the set point of 1.67/0.56°C (35/33°F) dry bulb/wet bulb temperature.

During the experiment, the control schematic must be adjusted to compensate for sudden change in the air condition. The adjustment can be done by modifying any of these three methods:

1. Adjusting the number of operating humidifiers (0 to 4) through the DAQ system. This adjustment is used to regulate the moisture in the air.
2. Adjusting the amount of refrigerant flowing to the refrigeration coil. This adjustment is used to regulate the amount of heat removal from the air, which translates to alteration in both air dry bulb temperature and the moisture content in the air.

3. Adjusting the power to the electrical heater. This adjustment is used to regulate the amount of heat addition into the air to modify both dry bulb temperature and moisture content in the air.

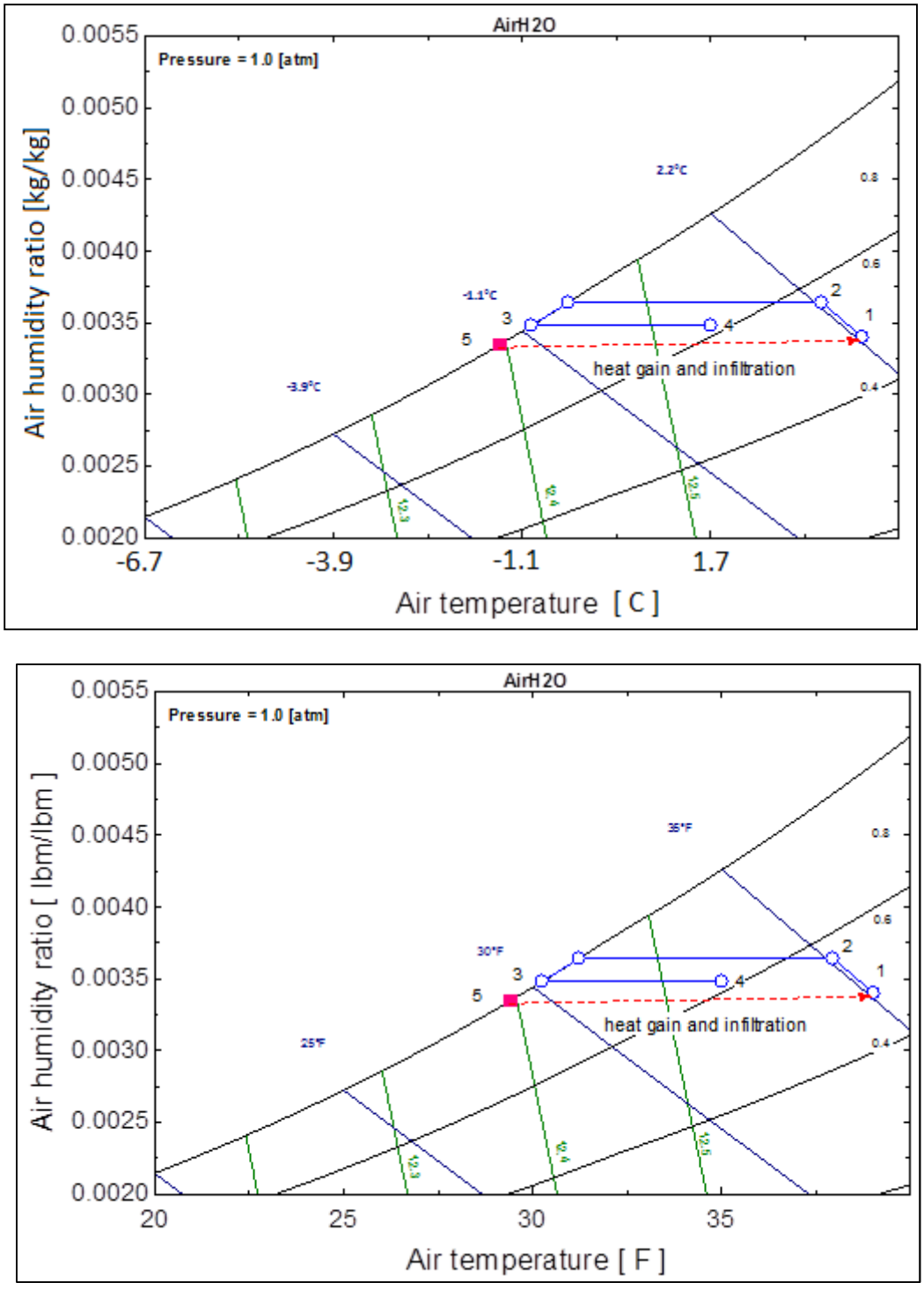

Figure 27: Schematic of controlling ambient air in the airflow loop (Reproduced from Cai (2009))

4.5.2 Ethylene Glycol (Heat Sink) Loop

The heat sink loop is designed to provide cooling to the TEC hot side on the apaaratus as described before. The heat sink loop consists of one plate frame heat exchanger, a gear pump, and a cold reservoir as seen in Figure 28 with red dash line. The Ethylene Glycol solution in the heat sink loop is cooled by the chiller loop described next utilizing the plate frame heat exhanger. The main refrigerant in this loop is Ethylene Glycol 50/50 volume concentration mixture.

The parameters that can be controlled in this loop is the fluid temperature and flow rate to the heat sink in the cooling loop. There are multiple methods that can be used to control the fluid temperature; adjusting the set point temperature in the chiller, adjusting the ammount of refrigerant flow from the chiller loop to the plate frame heat exchanger, and utilizing PID controller that made in the DAQ system to control the screw plug heater in the cold tank reservoir. The flow rate of the refrigerant inside the loop can be controlled by utilizing PID controller in the DAQ system. The PID controller is used to adjust the input frequency to the Variable Frequency Drive (VFD) that regulate the RPM on the pump and alter the flow rate.

4.5.3 Chiller and Secondary Coolant Loop

The chiller loop is utilized to provide cooling to the airflow loop. The overall schematic of chiller loop can be seen in Figure 28 with blue solid line. As seen in the figure, the chiller loop is directly connected to the low temperature chiller. The model number of this chiller is CPCW-12LT/TC2-1-9X2 manufactured by Cooling Technology Inc. This low temperature chiller supplies up to 2.0 tons capacity with leaving temperature of -31.67°C (-25°F). The secondary coolant used by this chiller is Dynalene HC 40, while R404A refrigerant is used in the refrigerant side of the chiller.

The chiller is equipped with recirculating pump that supply up to 6 to 8 gpm with pressure rise between 25 to 30 psi (172 to 207 kPa). This chiller is equipped with integrated temperature controller which can be used to set and control the leaving fluid temperature.

This chiller is directly connected to refrigeration coil used to provide cooling to the air in the airflow loop. Additionally, one plate frame heat exchanger is installed in the chiller loop. This plate frame heat exchanger is used to exchange heat between the refrigerant in the chiller loop and the heat sink loop.

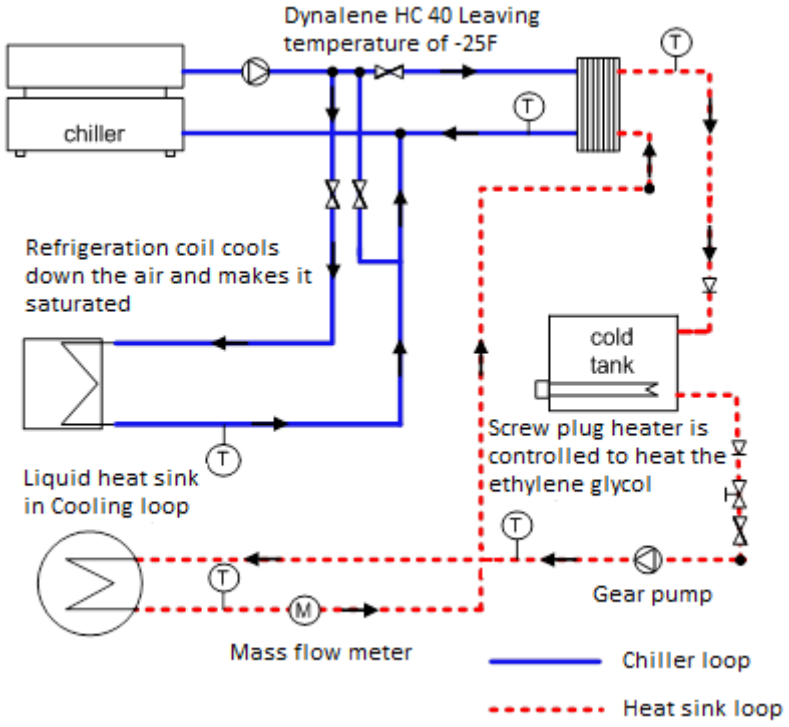

Figure 28: Chiller loop and heat sink loop (Reproduced from Cai (2009))

4.6 Instrumentation and Data Acquisition System

This section contains a brief description of the instumentation, the data acquisition system, and the various measurement and control devices installed throughout the entire experiemtnal setup.

4.6.1 Temperature Measurements

Thermocouple is used in the experiment to measure the dry bulb temperature of air at the inlet and outlet of the fin sample, surface temperature of the fin sample, and surface temperature of TEC (cold side). T-type thermocouples from Omega Inc. are used for all of the temperature measurement. Considering the possibility of a non-uniform measurement, the measurement of each parameters was done by using multiple thermocouples/thermocouple grids. The number of thermocouples used, nomial range, and acuracy of each measurement are shown in Table 5.

Table 5: Number, range and accuracy of temperature measurements using thermocouples

Measured parameter	Number of thermocouples	Nominal range	Accuracy
Fin temperature	8	-4 to -12°C (24.8 to 10.4°F)	± 0.43°C (0.77°F)
Inlet dry bulb temperature	3	2.22 to 1.11°C (36 to 34°F)	± 0.67°C (1.21°F)
Outlet dry bulb temperature	8	3 to -11°C (37.4 to 12.2°F)	± 0.28°C (0.50°F)
TEC surface temperature (Cold side)	12	-8 to -14°C (17.6 to 6.8°F)	± 0.63°C (1.13°F)

Each of the thermocouples was calibrated within their operating range using NesLab Instruments Inc. constant temperature bath chiller model RTE-140. One of the termocouples calibrations for fin temperature measurement can be seen in Figure 29.

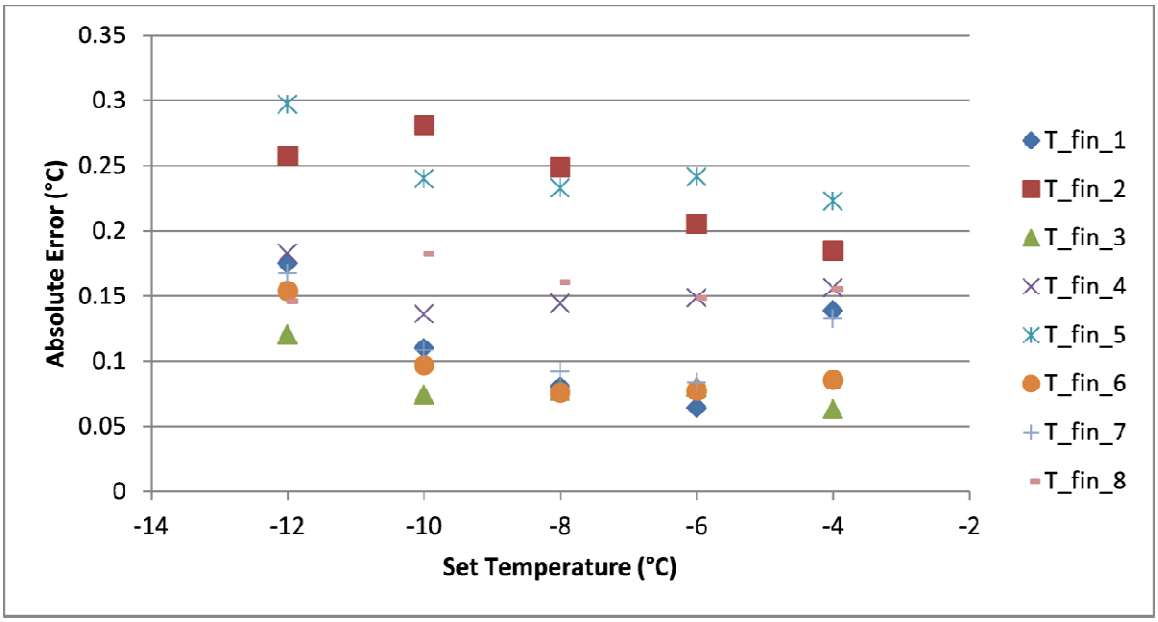

Figure 29: A sample data of absolute error in thermocouple calibration procedure for measuring surface temperature

4.6.2 Air Humidity Measurements - Dew point meters

The dew point temperatures of the air at the inlet and outlet of the sample were measured by using chilled mirror dew point meters. The dew point meters were selected from TTI Instruments, Inc. with model number of GE OP-D-1-0-A-A-1-0-0 of General Eastern Optica Series. The operating range of this device is between 0 to 50°C (32 to 122°F) with accuracy of ±0.2°C (0.36°F). The output of the device is 4 to 20 mA and 0 to 5 VDC signal to the DAQ system. The chilled mirror dew point meter requires additional sampling of the air to measure the dew point temperature. The sampling of the air is done by using Sample System Module (SSM) with model number of P40230968. This SSM consists of a vacuum pump, flow meter, and flow control valve which is enclosed in moisture resistance housing. The sampling airflow rate is about 0.5 ft^3/hr.

4.6.3 Air Flow Measurements

The air face velocity in the experiment was estimated by measuring the air volumetric flow rate across the fin sample as shown in Equation (1).

– (1)

Where is air face velocity (m/s or ft/min), is Air volumetric flow rate (m^3/s or ft^3/min) and A is entire fin sample frontal face area (m^2 or ft^2).

More details about calculation of air volumetric flow rate are offered in the next chapter and this section jut describes the instrumentation. Air volumetric flow rate was estimated from the static pressure difference across the nozzle that installed in a custom build tunnel as shown previously in Figure 25. The pressure difference between before and after the nozzle was measured by differential pressure transducer Setra model 264 as seen in Figure 30. The operating range of the pressure transducer is between 0 to 450 Pascal (0 to 1.81 inch H_2O) with accuracy of ±40 Pa (0.16 inch H_2O).

Figure 30: Differential pressure transducer

In-house checking of the pressure transducer was conducted by comparing the pressure readings with the ones of a high precision manometer that had accuracy of ±4.98 Pa (0.02 inch H_2O). The

results are shown in Figure 31 and the pressure transducer seemed to be shifted by a constant value of 40 Pa (0.16 inch H_2O) with respect to the manometer. This was a source of systematic error that was present in the air flow measurements. At the beginning of the test this systematic error had negligible impact on the absolute value of the air flow measurement. The error became significant toward the end of the frosting tests for which the measured pressure difference across the nozzle was about 30 Pa (0.12 inch H_2O). It should be noticed that since the error was constant throughout the entire flow rate range, the relative drop of pressure differential which corresponded to the drop in the air flow rate across nozzle, did not have such error. Thus, the relative comparison of initial and final velocity did not have this source of systematic error in it.

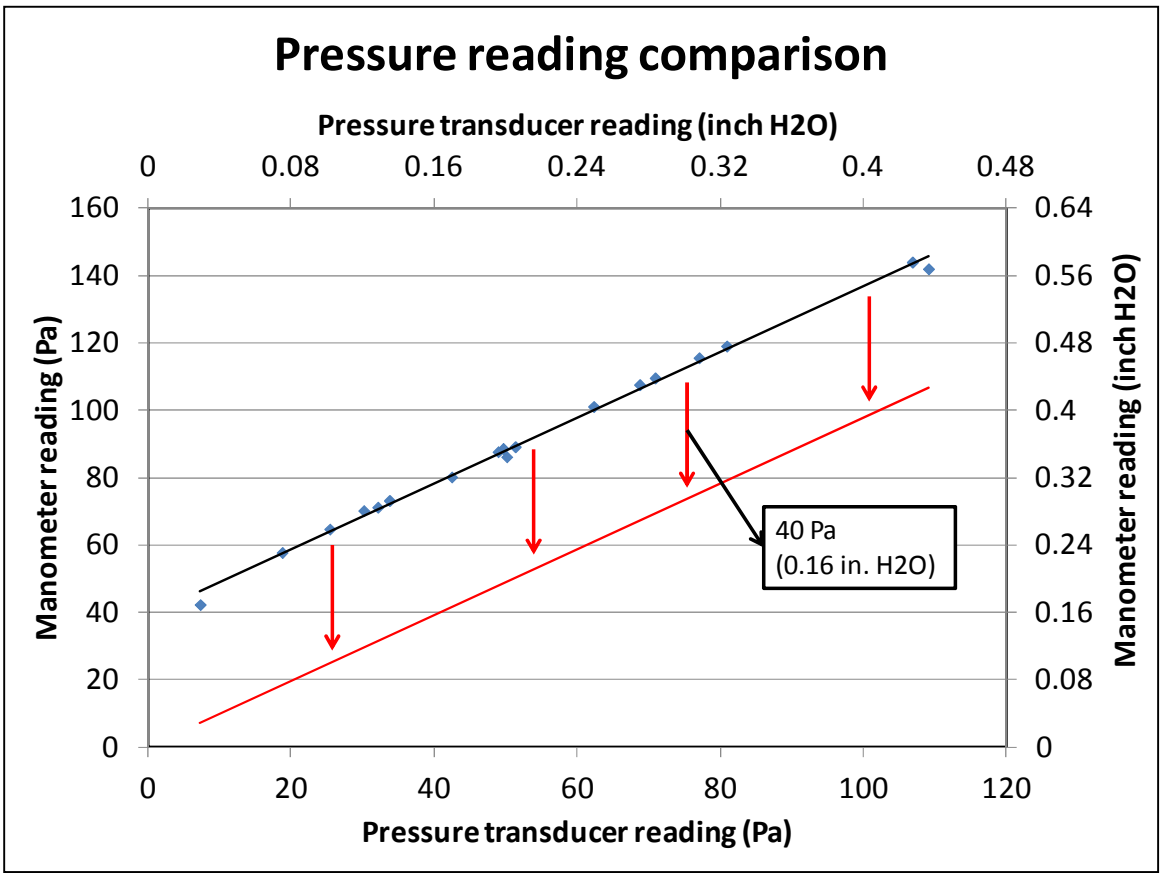

Figure 31: Pressure reading comparison between pressure transducer and manometer used for calibration procedure

4.6.4 Air Pressure Drop Measurements

A differential pressure transducer from Setra was used to measure the static pressure drop across the fin sample during the frosting experiment. The static pressure was measured at both inlet and outlet of the sample using static pressure tap as shown in Figure 32. The model of the differential pressure transducer is 264 as seen in Figure 30 The operating range of the pressure transducer is between 0 to 623 Pascal (0 to 2.50 inch H_2O) with accuracy of ±6.23 Pa (0.03 inch H_2O).

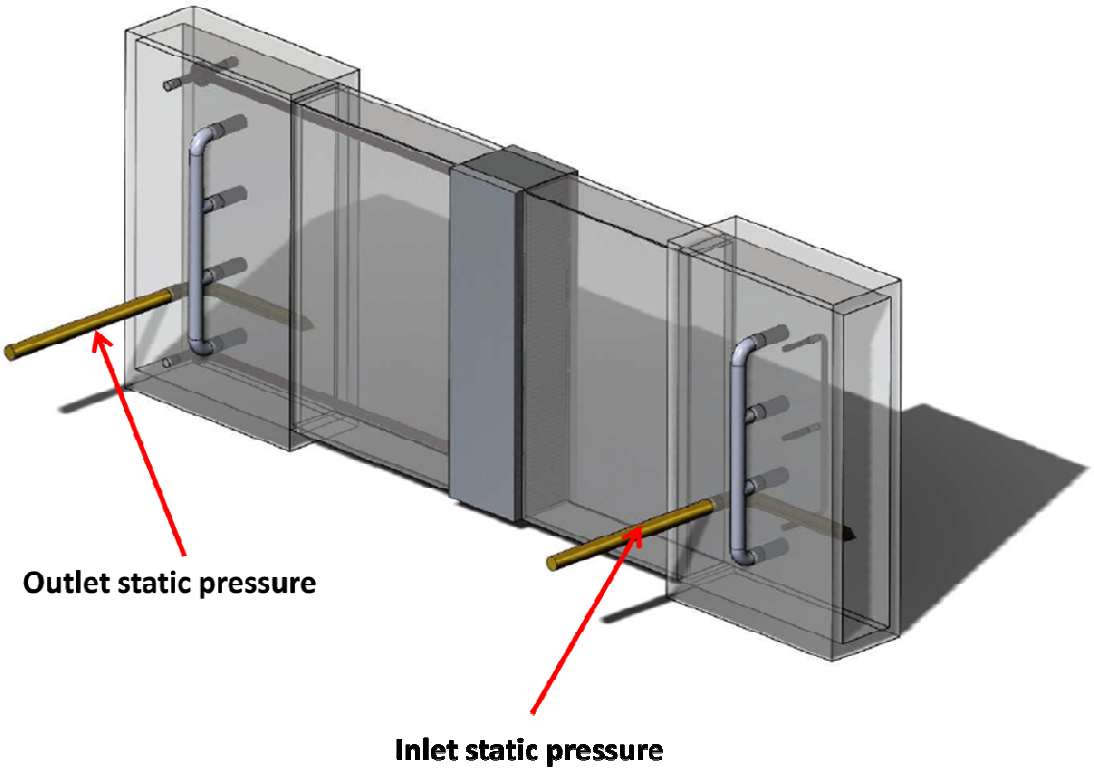

Figure 32: Air pressure drop measurement instrumentation across the fin sample. The other four branch connections shown are tubes for sampling air for dew point meters.

4.6.5 Frost Mass Measurements

The frost on the fin sample was weighed at the end of the test to measure the weight of frost accumulated during the experiment. At the end of the test, the fin sample was quickly removed from the vice and the weight was measured using a high precision digital scale (iBalance 401). For each sample, the weight with frost was compared to the initial weight of the sample (in dry conditions) so that the weight due to frost accumulated on the fins could be determined. During the weighing process, no water droplets were observed on the sample which indicated that frost did not melt. The accumulated frost on the fin sample can be used to identify the amount of water that is retained on the fin sample. The accuracy of frost weight measurement was ±0.2 grams.

4.6.6 Frost Thickness Measurements

The frost thickness provides information about the frost grew pattern and the type of frost that grew on the fin sample. It also identifies the location at which the airflow blockage occurred. Frost thickness was measured with a magnifying high resolution short focus CCD (Charge-Coupled Device) camera that has a borescope probe extending about 1 meter (3 feet) inside the air tunnel. The probe tip of the borescope was installed at the front of the fin sample. The value of frost thickness was obtained by scaling high resolution images using special imaging computer software (iView PC). The distance between two adjacent tubes was used as reference dimension and the fin edge in initial (dry) conditions was selected as starting point, that is, as reference for the frost thickness, as shown in the example of Figure 33 for the “start test” image. Figure 33 shows the images from the CCD camera at various instances during the frosting period, but it should be emphasized that this figure is only for illustrative purpose. The actual measurements were made on a much larger scale by using magnified high resolution photos of the frost on the

fin sample. Figure 33 depicts well the concept of the methodology adopted for the frost thickness measurements. The accuracy of frost thickness measurements was about ±0.03mm.

The cold base plates attached on the sides of the fins were maintained at constant fin temperature throughout the test period, and heat was continuously extracted from the fins along the transverse direction by the two TECs mounted on each side of the fin sample assembly. The power supplied to the TECs was controlled in order to keep T_{fin} constant during the entire frosting period. The second photo in Figure 33 shows the onset of frosting at about 2 minutes. After 5 minutes the frost profile became more defined, and then it continued to advance until 21 minutes, approximately the end of the test since the fin sample was completely covered with frost. Frost grew mainly perpendicular to the fin surfaces and the CCD camera captured digital photos every 1 minute. From these observations, it was emphasized that the growth of frost was in two directions: the main direction was perpendicular to the fin surfaces and the second direction was perpendicular to the fin leading edge toward the CCD camera. The frost growth in the direction perpendicular to the fin surface was prevalent during the initial frosting period. Some frost grew from the side tube wall along the horizontal direction, but it was mainly the frost growth in the main direction that was responsible for the air flow blockage of the coil. The main advantages of this technique were that it was not invasive and it did not interfere with the frost growth process. The data reduction of frost thickness from the digital photos requires considerable time and experience of the operator. Further details on the measurements of the frost thickness using this imaging technique are provided in the papers by Moallem et al. (2010a; 2010b).

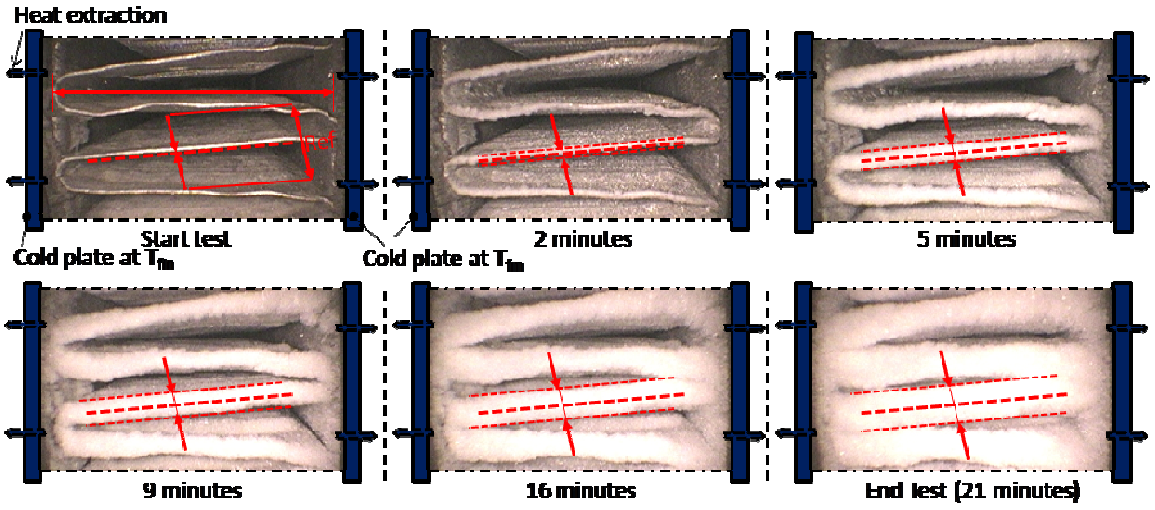

Figure 33: Frost thickness measurement

4.6.7 Data acquisition system

All of the measurements were taken using a Fluke® 2680 data logging acquisition system. The data looging acquisition system can hold from 1 to 6 analog modules. These modules are used to measure DC volts, AC volts, ohms, temperature, frequency, and DC current. In the experiment, the module is mainly used to measure DC volts and temperatures.

Couple of instrumentations such as differential pressure transducer requires power excitation. To provide low power voltage control signals, control boards PCI-DAC 6703 and PCI-DAS 6025 from Measurement Computing® were used.

LabView® ver.8.5 is the software used to communicate with the DAQ hardware. It is graphical programming software used to read, store, and visualize the measurement. LabView was selected for the data acquisition system because of its stability, high sampling rate, ease to use, and graphical interface.

A program was written in the LabView to record quantities, calculate the derived quantities, control the test facility, and plot the data. The recorded quantities in the experiments are the dry bulb temperatures (inlet and outlet of the fin sample), fin temperature, and TEC surface temperature (cold side). The derived quantities are humidity ratio of the air (inlet and outlet of the fin sample), pressure drop across the nozzle, and pressure drop across the fin sample. The air humidity ratio was calculated by applying equations obtained from ASHRAE fundamental with dew point temperature and dry bulb temperature as input variables. The pressure drop/pressure difference was calculated by applying the equation obtained from calibration process. The control on the test facility is only utilized to control the flow rate and temperature of ethyln glycol in the heat sink loop.

The main benefit of using LabView program for the frost experiment is its ability to plot the data simultaneously. The graphical representation of the data during the experiment assisted the people who conduct the frost experiment making necessary adjustment to control the quantities within the specified condition (i.e. inlet air condition, and fin sample).

4.7 Test Procedure

All experimental tests were conducted with the fin sample initially in dry condition. The fin sample assembly was left at room temperature overnight to achieve dry surface condition. Then, the assembly was installed into test apparatus and the air stream in the air tunnel was set to 1.7/0.6°C (35/33°F) dry bulb/wet bulb temperature in about 4 to 5 hours with the air velocity at 1.5 m/s (295 ft/min). Once the air tunnel reached steady state conditions, the experiment was started. The first step for the test procedure was to cool down the fin sample to the desire fin

temperature by using TECs. At the same time, the fan was turned off to ensure that frost did not accumulate on the surface while surface temperature was reaching the set point. This period was defined as "pull down" period and it occurred during the initial 3 to 5 minutes of each test which is shown in Figure 34. After the pull down period, the fin temperature (T_{fin}) was at the set point temperature of each test and at the same time, the timer for the frosting cycle was initiated and the fan was turned on. During this pull down period, no visible amount of frost was measured on the fins, and when fan turned on, it was kept at constant RPM throughout the entire test. This method of testing was preferred over a constant air velocity method since it was closer to the actual operation of the outdoor evaporator coils in air-source heat pump systems. The constant fan frequency method will result in decrease of the air inlet velocity resulting from the flow blockage on the fins once frost started to accumulate on the fin sample. According to the ASHRAE standard 41.2, the lower limit of the air velocity that could be measured with our flow nozzle was 0.7 m/s (138 ft/min). However, in order to extend the frosting period and detect a clear difference between the various frosting times, the frosting period was extended beyond the low air flow limit and down to the point at which the air flow across the fin sample was equal to or below 0.4 m/s (79 ft/min). This was approximately 26% of the initial face velocity.

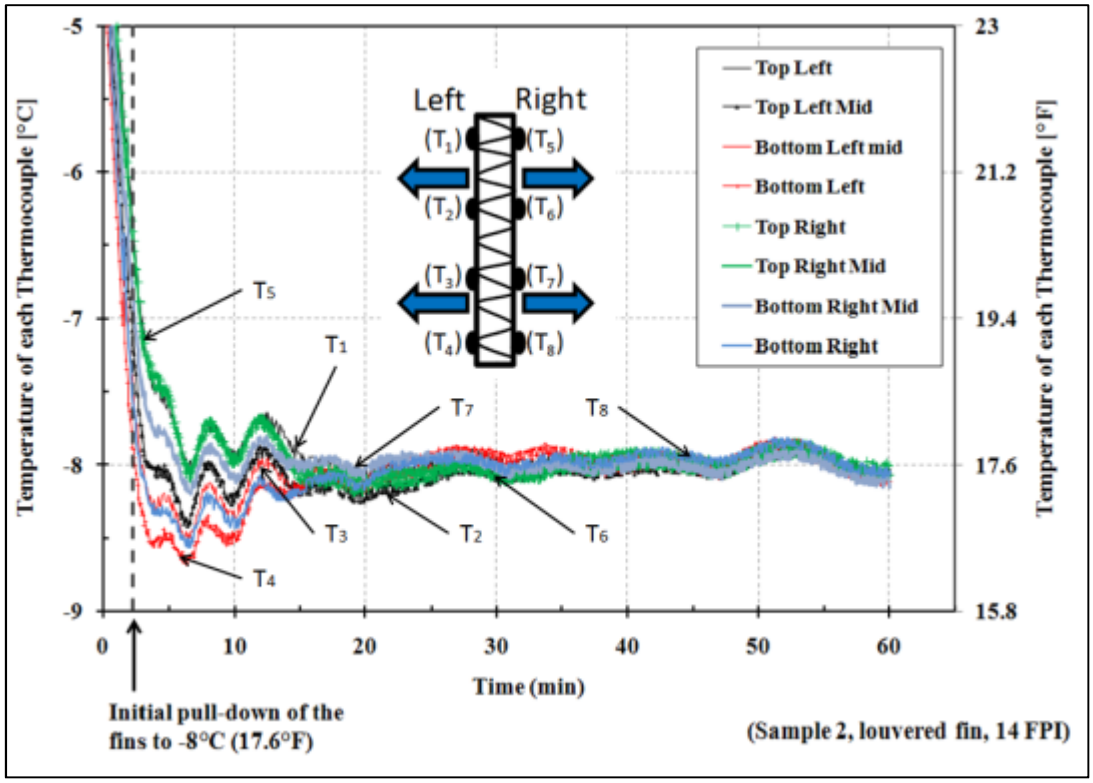

Figure 34: A sample of data on controlling the fin temperature (T_{fin}) during frosting operation and pull down period of the fin sample to the set point temperature of -8°C (17.6°F) for the frosting experiment

CHAPTER V

DATA REDUCTION AND UNCERTAINTY ANALYSIS

5.1 INTRODUCTION

In this section, the data reduction and uncertainty analysis at the heat transfer performance are discussed in more details. The heat transfer performance was evaluated over various fin geometries, and parameters such as fin temperature, air condition, and air face velocity. The heat transfer rate of the microchannel fin sample was computed using two different methods. The first method is calculated from the air side or enthalpy method, and the second method is calculated from the conduction side or conduction method. These two methods of estimating the heat transfer rate will be discussed in more detail later in this section.

5.2 DATA REDUCTION

As mentioned earlier, the data reduction in the experiment is mainly to investigate the heat transfer performance of the microchannel fin sample. The fin sample heat transfer rate was estimated using two different methods; air enthalpy method and conduction method. The intention of utilizing two redundant methods was to validate the experimental setup and to ensure the measured heat transfer rate wass accurate. Several parameters were measured such as mass flow rate, humidity ratio, total thermal resistance, and heat gain in the conduction side.

5.2.1 Heat Transfer Rate Calculation Using Enthalpy Method

The heat transfer rate for the fin sample was calculated through enthalpy method which utilized the air side. The heat transfer rate from the air side is separated into two parts. The first part is calculating the sensible heat transfer rate, and the second part is the latent heat transfer rate. Sensible heat transfer rate is the heat transfer rate due to the change in dry bulb temperature which can be calculated by using Equation (2).

$$Q_{air,sensible} = \dot{m}_{air} \cdot C_p \cdot \Delta T_{air} = \dot{m}_{air} \cdot C_p \cdot (T_{in} - T_{out})_{air} \quad (2)$$

Where :

- $Q_{sensible}$ = Sensible heat transfer rate (Watt)
- $\dot{m}$ = Mass flow rate (kg/s)
- C_p = Specific heat of air (J/kg-K)
- T_{in} = Dry bulb temperature at inlet (°C)
- T_{out} = Dry bulb temperature at outlet (°C)

Latent heat transfer rate is the heat transfer rate due to the change in state (e.g. liquid to gas) which can be calculated by using Equation (3).

$$Q_{air,latent} = \dot{m}_{air} \cdot h_w \cdot \Delta W_{air} = \dot{m}_{air} \cdot h_w \cdot (W_{in} - W_{out})_{air} \quad (3)$$

Where :

- Q_{latent} = Latent heat transfer rate (Watt)
- $\dot{m}$ = Mass flow rate (kg/s)
- h_w = Enthalpy of the condensate (J/kg)
- W_{in} = Humidity ratio at inlet (kg-water/kg-air)
- W_{out} = Humidity ratio at outlet (kg-water/kg-air)

The submission of both sensible heat transfer rate and latent heat transfer rate yields the total heat transfer rate that the sample produced as shown in Equation (4).

$$Q_{air,total} = Q_{air,sensible} + Q_{air,latent} \quad (4)$$

Several parameters used in the heat transfer calculation are measured during the experiment. These parameters are the dry bulb temperature at the inlet (T_{in}) and outlet (T_{out}) of the sample. Three other parameters in the experiment are derived paramter. The humidity ratio at inlet (W_{in}) and outlet (W_{out}) are derived from the dew point temperature measurement. Another derived paramter is the air mass flow rate ($\dot{m}_{air}$), derived from the measured air volumetric flow rate. As for the air specific heat (C_p) and enthalpy of condensate (h_w), they are constant parameters dependent on the condition of the air.

5.2.2 Humidity Ratio Calculation

The air humidity ratio at inlet and outlet of the fin sample were directly calculated by the LabView program using equations from ASHRAE Fundamental. Humidity ratio (W in kg-

water/kg-air) can be calculated by using the saturation pressure (p_{ws} in Pascal) and total pressure (p in Pascal) as shown in Equation (5).

$$W = 0.621945 \cdot \frac{p_{ws}}{p - p_{ws}} \quad (5)$$

The saturation pressure (p_{ws} in Pascal) is calculated from the dew point temperature or saturation temperature (T in Kelvin) as shown in Equation (6).

$$ln(p_{ws}) = C_1/T + C_2 + C_3 \cdot T + C_4 \cdot T^2 + C_5 \cdot T^3 + C_6 \cdot T^4 + C_7 \cdot ln(T) \quad (6)$$

Where:

- C_1 = -5.6745359 E+03
- C_2 = 6.3925247 E+00
- C_3 = -9.6778430 E-03
- C_4 = 6.2215701 E-07
- C_5 = 2.0747825 E-09
- C_6 = -9.4840240 E-13
- C_7 = 4.1635019 E+00

5.2.3 Air Flow Rate Calculation

Air mass flow rate is calculated using the air volumetric flow rate. As mentioned in the previous section, the air volumetric flow rate is estimated by taking the measurement of static pressure difference across the nozzle installed in the tunnel. The air volumetric flow rate (Q) in the experiment was calculated by using Equation (7) as a function of measured static pressure drop across the nozzle (Δp_{nozzle}).

$$Q = 1.414 \cdot Y \cdot \sqrt{\Delta p_{nozzle}/\rho} \cdot C \cdot A \quad (7)$$

Where :

- Q = Air volumetric flow rate (m^3/s)
- Y = Expansion factor
- Δp_{nozzle} = Static pressure difference across the nozzle (Pascal)
- ρ = Air density (kg/m^3) = 1.273 kg/m^3 taken at T = 1.667°C
- C = Nozzle discharge coefficient = 0.955[14]
- A = Area of cross section of the nozzle [m^2] (ft^2) = 7.13E-05 m^2 (0.000767 ft^2)

The Expansion factor (Y) is a function of pressure drop across the nozzle as seen in Equation (8).

$$Y = 1 - (0.548 + 0.71 \cdot \beta^4)(1 - \alpha) \quad (8)$$

Where:

- β = Ratio of nozzle exit diameter to approach duct diameter

$$\beta = \frac{D_{nozzle}}{D_{chamber}} = \frac{9.525\ mm}{57.15\ mm} = 0.1667 \quad (9)$$

- α = Ratio of nozzle throat total pressure to nozzle entrance total pressure

$$\alpha = 1 - \left[\frac{\Delta p}{\rho_x \cdot R \cdot (t_x + 273.2)}\right] \quad (10)$$

Where:

- Δp = Static pressure difference between before and after the nozzle (Pa)
- ρ_x = Air density (kg/m^3) = 1.273 kg/m^3
- R = Gas constant (287.1 J/kg-K)
- t_x = Air dry bulb temperature (°C) = 1.667°C

The mass flow rate ($\dot{m}$) is calculated by using the volumetric flow rate (Q) and air density (ρ) as shown in Equation (11).

[14] Table 4 in ANSI/ASHRAE 41.2-1987 (RA92)

$$\dot{m} = V \cdot A \cdot \rho = Q \cdot \rho \quad (11)$$

5.2.4 Heat Transfer Rate Calculation Using Conduction Method

The heat transfer rate of the fin sample was calculated using conduction method. The heat transfer rate from the conduction side was separated into two parts. The first part was calculating the conduction heat transfer neglecting the heat gain, and the second part was the heat gain due to the temperature difference between the fin temperature and inlet air temperature. The heat transfer from conduction across the metal plates on the sides of the fin sample was calculated by assuming a quasi-steady state heat conduction process. The heat transfer is calculated by taking the temperature gradient between the fin temperature (T_{fin}) and cold side temperature (T_{cold}) as seen in equation (12). This temperature difference along with the total thermal resistance (ΣR) of materials between the two temperatures readings were used to calculate the heat transfer rate ($q_{conduction}$) as shown in Equation (12).

$$q_{conduction} = \frac{\Delta T}{\Sigma R} = \frac{T_{fin} - T_{cold}}{\Sigma R} \quad (12)$$

Where :

- $q_{conduction}$ = Heat transfer rate using conduction method (Watt)
- ΔT = Temperature difference (°C or K)
- T_{fin} = Temperature of the fin (°C)
- T_{cold} = Temperature of cold side of TEC (°C)

– R = Total thermal resistance between the two temperature readings (1.58 K/Watt)

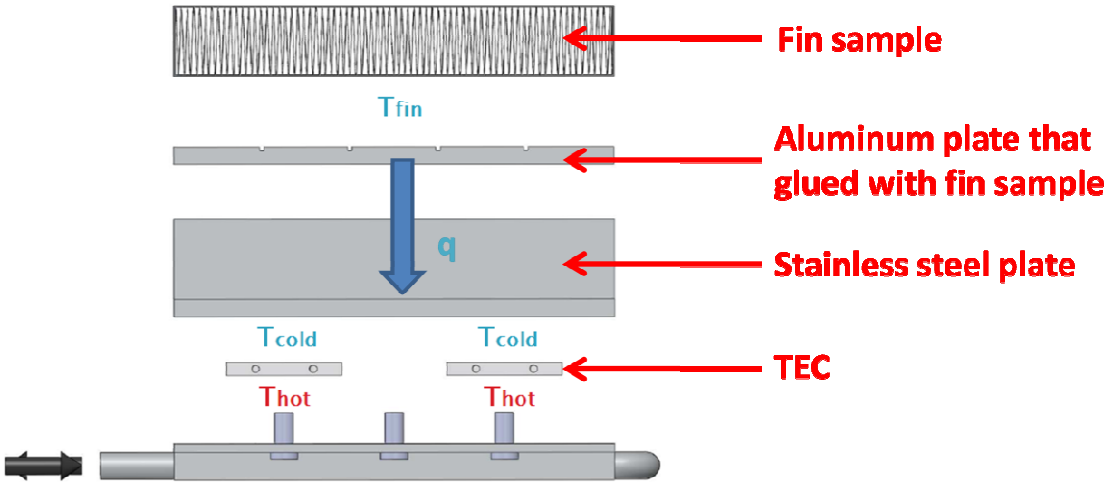

Figure 35: Schematic of conduction heat transfer

The $q_{conduction}$ above was used to calculate conduction heat transfer for each of TEC. The overall conduction heat transfer for the fin sample is the total of all four TECs' heat transfer rate.

The heat gain due to the temperature difference between the inlet air temperature and the fin temperature was investigated by conducting calorimeter test. The heat gain due to the temperature difference is summarized in Equation (13).

(13)

Where:

- $q_{conduction,gain}$ = Heat gain due to the temperature difference (Watt)
- $T_{air\ inlet}$ = Temperature at the inlet of the fin sample (°C)
- T_{fin} = Temperature of the fin (°C)

The total heat transfer using conduction method can be calculated using Equation (14).

(14)

Several parameters used in the heat transfer calculation are measured during the experiment. These parameters are the fin temperature (T_{fin}), TEC surface temperature (T_{cold}), and dry bulb temperature at the inlet of the sample (T_{in}). While total thermal resistance (ΣR) for conduction heat transfer and the heat gain due to temperature difference between fin temperature and ambient temperature are estimated through calorimeter test which will be explained in detail in the next chapter.

5.3 UNCERTAINTY ANALYSIS

5.3.1 Accuracy and Range of Measurements

Data logger from Fluke and LabView real time data acquisition system were used to record and store the experimental data. The experimental conditions were monitored at all times by LabView Real Time control module. The sampling rate of the DAQ system is for every 4 seconds and the average values of the operating parameters were calculated from the collected data. The amount of the measurement samples was statistically large enough to reduce the error from noise, random fluctuation of the sensor output signals, and sensors response time. The measured parameters and corresponding accuracies are summarized in Table 6.

Table 6: Accuracy of instrumentations for the frost experiments

Instrumentations	Nominal range	Accuracy
Inlet air dry bulb temperature	1.11 to 2.22ºC (34 to 36°F)	± 0.67°C (1.21°F)
Inlet air dew point temperature	-0.3 to -1.6 ºC (31.46 to 29.12°F)	± 0.2°C (0.36°F)
Outlet air dry bulb temperature	3 to -11°C (37.4 to 12.2°F)	± 0.28°C (0.50°F)
Outlet air dew point temperature	-0.3 to -4.9°C (31.46 to 23.18°F)	± 0.2°C (0.36°F)
Fin temperature	-4 to -12°C (24.8 to 10.4°F)	± 0.43°C (0.77°F)
TEC surface temperature (cold side)	-8 to -14°C (17.6 to 6.8 °F)	± 0.63°C (1.13°F)
Pressure difference (flow nozzle)	0 to 450 Pa (0 to 1.81 in.H_2O)	± 40 Pa (0.16 in.H_2O)
Pressure difference across fin sample	0 to 430 Pa (0 to 1.73 in.H_2O)	± 6.23 Pa (0.03 in.H_2O)

The accuracy of measured parameters are used to calculate the uncertainty of the derived parameters, i.e. humidity ratio and mass flow rate. The accuracy of measured parameters and uncertainty of derived parameters are used to estimate the overall uncertainty of the heat transfer rate.

5.3.2 Uncertainty of Humidity Ratio Measurements

The air humidity ratio at inlet and outlet of the fin sample is estimated from the dew point temperature measurement described in previous section. The source of uncertainty for humidity ratio is the accuracy of the dew point meter (±0.2°C or 0.36°F). The uncertainty was calculated using uncertainty propagation calculation in Enginnering Equation Solver (EES). The uncertainty was calculated within the operating range and the result is ±1.67% of the humidity ratio reading as seen in Table 7 below.

Table 7: Uncertainty of humidity ratio

T_{dew}				Humiditiy ratio (W)		% Uncertainty
°C		°F		kg water/kg air or lb water/lb air		
Value	Uncertainty	Value	Uncertainty	Value	Uncertainty	
-0.34	0.2	31.39	0.36	0.00367	0.000061	1.66
-0.48	0.2	31.13	0.36	0.00363	0.000060	1.66
-0.63	0.2	30.87	0.36	0.00358	0.000060	1.66
-0.77	0.2	30.61	0.36	0.00354	0.000059	1.67
-0.92	0.2	30.35	0.36	0.00350	0.000058	1.67
-1.07	0.2	30.08	0.36	0.00345	0.000058	1.67
-1.21	0.2	29.82	0.36	0.00341	0.000057	1.67
-1.36	0.2	29.56	0.36	0.00337	0.000056	1.67
-1.50	0.2	29.30	0.36	0.00333	0.000056	1.67
-1.65	0.2	29.04	0.36	0.00329	0.000055	1.68

5.3.3 Uncertainty of Air Face Velocity Measurements

The face velocity in the experiment is calculated from the volumetric flow rate and frontal area of the fin sample as seen in Equation (1). The air volumetric flow rate is estimated from static pressure difference as described in the previous section. The main parameter that affects the uncertainty is the accuracy of pressure transducer which is ±40 Pa (0.16 in.H_2O). The uncertainty analysis was done by using the experimental data from fin sample 2 with -5°C fin temperature. The uncertainty was calculated in EES program. The result of the uncertainty analysis can be seen in Table 8. At the beginning of the test, the uncertainty of air face velocity was estimated to be ±4.5% of the reading. As the face velocity decreased the uncertainty increased and reached ±63% at the end of the test. The uncertainty of the face velocity increased significantly towards the end of the frosting test because the pressure readings across the nozzle became considerably smaller than the full scale range of the pressure transducer. The uncertainty of the pressure transducer had a significant impact on the air face velocity measurements if the air flow velocity during the frosting period reduced to more than 50% of its initial value at the beginning of the test.

Table 8: Uncertainty of air face velocity

Δp				Face velocity (mdot)				% face velocity	% uncertainty
Pa		Inch H2O		m/s		ft/min			
Value	Uncertainty	Value	Uncertainty	Value	Uncertainty	Value	Uncertainty		
444.6	40.06	1.78	0.16	1.497	0.067	295	13	100.00	4.48
452.1	40.06	1.82	0.16	1.510	0.067	297	13	100.87	4.41
448.2	40.06	1.80	0.16	1.503	0.067	296	13	100.40	4.45
440	40.06	1.77	0.16	1.490	0.067	293	13	99.53	4.53
442.8	40.06	1.78	0.16	1.494	0.067	294	13	99.80	4.50
436.7	40.06	1.75	0.16	1.484	0.068	292	13	99.13	4.57
433.6	40.06	1.74	0.16	1.479	0.068	291	13	98.80	4.60
426.4	40.06	1.71	0.16	1.466	0.069	289	13	97.93	4.68
417.4	40.06	1.68	0.16	1.451	0.069	286	14	96.93	4.78
404.6	40.06	1.62	0.16	1.428	0.070	281	14	95.39	4.93
376.9	40.06	1.51	0.16	1.379	0.073	271	14	92.12	5.29
353.2	40.06	1.42	0.16	1.335	0.075	263	15	89.18	5.65
324.9	40.06	1.30	0.16	1.281	0.079	252	15	85.57	6.14
301.4	40.06	1.21	0.16	1.234	0.082	243	16	82.43	6.63
269.5	40.06	1.08	0.16	1.167	0.087	230	17	77.96	7.41
228.5	40.06	0.92	0.16	1.075	0.094	212	19	71.81	8.75
177.6	40.06	0.71	0.16	0.948	0.107	187	21	63.31	11.27
137.4	40.06	0.55	0.16	0.834	0.122	164	24	55.69	14.60
106.5	40.06	0.43	0.16	0.734	0.139	145	27	49.04	18.86
63.5	40.1	0.25	0.16	0.567	0.181	112	36	37.87	31.95
33.52	40.06	0.13	0.16	0.412	0.259	81	51	27.52	62.94

5.3.4 Uncertainty of Heat Transfer Rate Measurements for Air Enthalpy Method

Experimental data for fin sample 2 with -5°C (23°F) fin temperature was used to analyze the uncertainty of the heat transfer rate. The heat transfer rate calculated using enthalpy method is dependent on the accuracy of the air side measurement. In the ESS calculation, uncertainty of each parameters was included for the estimation of the overall uncertainty in the heat transfer rate using enthalpy method. The uncertainty is listed in Table 9 below.

Table 9: Uncertainty of different parameters for enthalpy method

Parameters	Uncertainty
ΔP for flow rate calculation	±40 Pa (0.16 in. H2O)
Dry bulb temperature at inlet	± 0.67°C (1.21°F)
Dry bulb temperature at outlet	± 0.28°C (0.5°F)
Humidity ratio at inlet	± 1.67%
Humidity ratio at outlet	±1.67%

The frosting test on sample 2 with -5°C (23°F) fin temperature lasts for 48 minutes. For simplification, in the EES calculation, only 20 data points out of the 48 minutes test with increment of approximately 2.4 minutes were used. The result of the uncertainty analysis done by EES code can be seen in below. From the Table 10 below, the uncertainty of the heat transfer is slightly higher at the beginning of the test due to the fact that the air side temperature difference across the fin sample was smaller. As the fan started and pulled the air flow into the fin sample, air accelerated to full speed and exchanged heat with the fins. Due to the thermal inertia of the test apparauts few minutes were needed before a quasi-steady state conditions was achieved. As soon as the air at the inlet reached a quasi-steady state, the uncertainty was about 12%. The uncertainty was also dependent on the control of the TECs that was used to set the conditions for the fin temperature. The uncertainty varied beween 10% to 13% during the majority of the frosting experiments. Towards the end of each test, the uncertainty of heat transfer rate became significantly larger due to the effect of the uncertainty in flow rate measurements. The average uncertainty throughout the entire test period was approximately 16.5%.

Table 10: Uncertainty of heat transfer rate (air enthalpy method)

Time (min)	% flow rate	q_{total}				% uncertainty
		Watt		Btu/hr		
		Value	Uncertainty	Value	Uncertainty	
0.0	100.00	12.31	1.843	42.00	6.29	14.97
2.5	100.88	18.74	1.943	63.94	6.63	10.37
4.8	100.44	18.39	1.931	62.75	6.59	10.50
7.2	99.52	17.74	1.908	60.53	6.51	10.76
9.6	99.82	16.8	1.894	57.32	6.46	11.27
12.1	99.12	15.75	1.87	53.74	6.38	11.87
14.4	98.77	14.93	1.854	50.94	6.33	12.42
16.9	97.94	14.29	1.834	48.76	6.26	12.83
19.3	96.94	13.88	1.815	47.36	6.19	13.08
21.7	95.45	13.49	1.792	46.03	6.11	13.28
24.0	92.12	13.84	1.769	47.22	6.04	12.78
26.4	89.19	14.17	1.752	48.35	5.98	12.36
28.8	85.56	13.99	1.723	47.74	5.88	12.32
31.2	82.41	13.69	1.7	46.71	5.80	12.42
33.6	77.94	13.37	1.683	45.62	5.74	12.59
36.0	71.77	12.88	1.685	43.95	5.75	13.08
38.5	63.33	12.07	1.752	41.18	5.98	14.52
40.9	55.71	11	1.877	37.53	6.40	17.06
43.3	49.06	9.623	2.007	32.84	6.85	20.86
45.7	37.87	7.7	2.5	26.26	8.68	33.07
47.9	27.53	6.078	3.855	20.74	13.15	63.43

5.3.5 Uncertainty of Heat Transfer Rate Measurements for Conduction Method

Experimental data for fin sample 2 with -5°C (23°F) fin temperature was used to analyze the uncertainty of the heat transfer rate. The heat transfer rate using conduction method is mainly dependent on the accuracy of the thermocople readings. In the ESS calculation, uncertainty on each parameter was included to estimate the overall uncertainty in the heat transfer rate. The uncertainty is listed in Table 11 below.

Table 11: Uncertainty of different parameters for conduction method

Parameters	Uncertainty
Dry bulb temperature at inlet	± 0.67°C (1.21°F)
Temperature at the cold side of TEC	± 0.63°C (1.13°F)
Temperature of the fin	± 0.43°C (0.77°F)

Identical to the enthalpy method, the uncertainty analysis for conduction method only took 20 data point with increment of 2.4 minutes. The result of the uncertainty analysis by EES code can be seen in Table 12 below. As seen in the table, the uncertainty of the heat transfer rate is a constant number throughout the test. This causes the % uncertainty to be low at the beginning of the test. On the other hand, once the frost starts accumulating on the fin sample the ammount of cooling load required to maintain the fin temperature become less, hence the % uncertainty increased accordingly. The average % uncertainty throughout the entire test is approximately 8%.

Table 12: Uncertainty of heat transfer rate (conduction method)

Time (min)	% flow rate	q_{total}				% uncertainty
		Watt		Btu/hr		
		Value	Uncertainty	Value	Uncertainty	
0.0	100.00	16.72	1.01	57.05	3.45	6.05
2.5	100.88	18.00	1.01	61.42	3.45	5.62
4.8	100.44	18.50	1.01	63.12	3.45	5.46
7.2	99.52	17.24	1.01	58.83	3.45	5.86
9.6	99.82	16.54	1.01	56.44	3.45	6.11
12.1	99.12	13.62	1.01	46.47	3.45	7.42
14.4	98.77	13.55	1.01	46.23	3.45	7.46
16.9	97.94	12.92	1.01	44.08	3.45	7.83
19.3	96.94	12.85	1.01	43.85	3.45	7.87
21.7	95.45	13.13	1.01	44.80	3.45	7.70
24.0	92.12	14.21	1.01	48.49	3.45	7.11
26.4	89.19	13.79	1.01	47.05	3.45	7.33
28.8	85.56	13.44	1.01	45.86	3.45	7.52
31.2	82.41	13.57	1.01	46.30	3.45	7.45
33.6	77.94	13.62	1.01	46.47	3.45	7.42
36.0	71.77	13.37	1.01	45.62	3.45	7.56
38.5	63.33	12.72	1.01	43.40	3.45	7.95
40.9	55.71	10.00	1.01	34.11	3.45	10.11
43.3	49.06	8.72	1.01	29.76	3.45	11.59
45.7	37.87	8.26	1.01	28.17	3.45	12.24

5.4 CONCLUSIONS

This chapter describes the test procedure, data reduction, and uncertainty analysis of the experiment. The test procedure explains in details the method used to conduct every frost experiment. The data reduction demonstrates method used to compute heat transfer rate of the microchannel fin sample. Lastly, the uncertainty analysis is done for the heat transfer performance. The result of the uncertainty is summarized in Table 13 below.

Table 13: Summary of Uncertainty Analysis

Parameters	**Uncertainty**
Fin Temperature	±0.4°C (0.7°F)
TEC surface temperature (cold side)	±0.6°C (1.1°F)
Inlet conditions	
Inlet dry bulb temperature	±0.4°C (0.7°F)
Inlet humidity ratio	±0.0002
Air flow rate	
ΔP nozzle	±40 Pa (0.16 in. H2O)
Uncertainty at the beginning	±4.5%
Uncertainty at the end	±25%
Outlet Air Condition	
Outlet Dry Bulb Temperature	±0.3°C (0.5°F)
Outlet humidity ratio	±0.0002
Pressure drop	±6.2Pa (0.02 in. H2O)
Frost thickness	±0.03mm (1.2×10^-3 in.)
Frost mass	±0.2gr (0.44×10^-3 in.)
Heat transfer rate	
Enthalpy method	
Uncertainty at the beginning	±12%
Uncertainty at the end	±63%
Average Uncertainty	±16%
Conduction method	
Uncertainty at the beginning	±6%
Uncertainty at the end	±12%
Average Uncertainty	±8%

CHAPTER VI

EXPERIMENTAL VALIDATION OF THE MEASUREMENTS

6.1 INTRODUCTION

The verifications on the instrumentation accuracy, signal processing, and data recording were demonstrated through two steps. The first step was performing calorimeter tests on the test apparatus. This calorimeter test were intended to verify that all the sensors were properly installed, and connected to DAQ system used in the lab. Also, these tests were used to estimate the total thermal resistance and the heat losses (heat gain) that occured in the measurement of the heat transfer rate (conduction method). The second step of experimental validation was the heat balance tests. The heat balance tests were performed on all of the fin samples. These tests were intended to verify that the heat transfer measured by the conduction method and the air-side enthalpy method was the same.

6.2 CALORIMETER TESTS

6.2.1 Terminology and Definitions

Calorimeter tests were performed on the experimental apparatus at the early phase of this project. The main objective for calorimeter tests was to ensure that the connectivity of the instruments to the data acquisition system used for the experiments were good. The calorimeter tests were performed in two different tests. The first test was done to measure the thermal resistance of the experimental setup, while the second one was performed to obtain calibration curve that correlates the heat gain due to temperature difference between apparatus and fin temperature and inlet air temperature. Both the thermal resistance and heat gain correlation were used in the measurements of the heat transfer rate (conduction method).

6.2.2 Measurement of Contact Resistance

The first step on the calorimeter test was done to obtain the total thermal resistance (ΣR). The total thermal resistance (ΣR) was compute for materials in between T_{fin} and T_{cold}. The test was conducted directly on the actual test apparatus with using fin sample number 3 without any airflow passing through the fin sample. An electrical heater with known capacity was installed on one side of the sample and conduction heat transfer rate was measured with the embedded thermocouples to calibrate the thermal resistance. The overall test setup is illustrated in Figure 36.

The test procedures used for the test were as follows:

1. Install the heater at one side of the fin sample.

2. Insulate the entire assembly to prevent heat loss to the ambient air.
3. Start the DAQ system to start monitoring and recording the fin temperature (T_{fin}) and TEC surface temperature (T_{cold}).
4. Power the electrical heater to 5 watts and wait for the temperature readings to reach steady state.
5. Record the temperatures and voltage applied to the heat resistor.
6. The data were analyzed to calculate for total thermal resistance (ΣR) by using Equation (15) with assumption that the power consumed by the electrical heater was fully converted to heat ($q_{electrical}$).

$$\Sigma R = \frac{T_{fin} - T_{cold}}{q_{electrical}} = \frac{T_{fin} - T_{cold}}{5\ Watts} \tag{15}$$

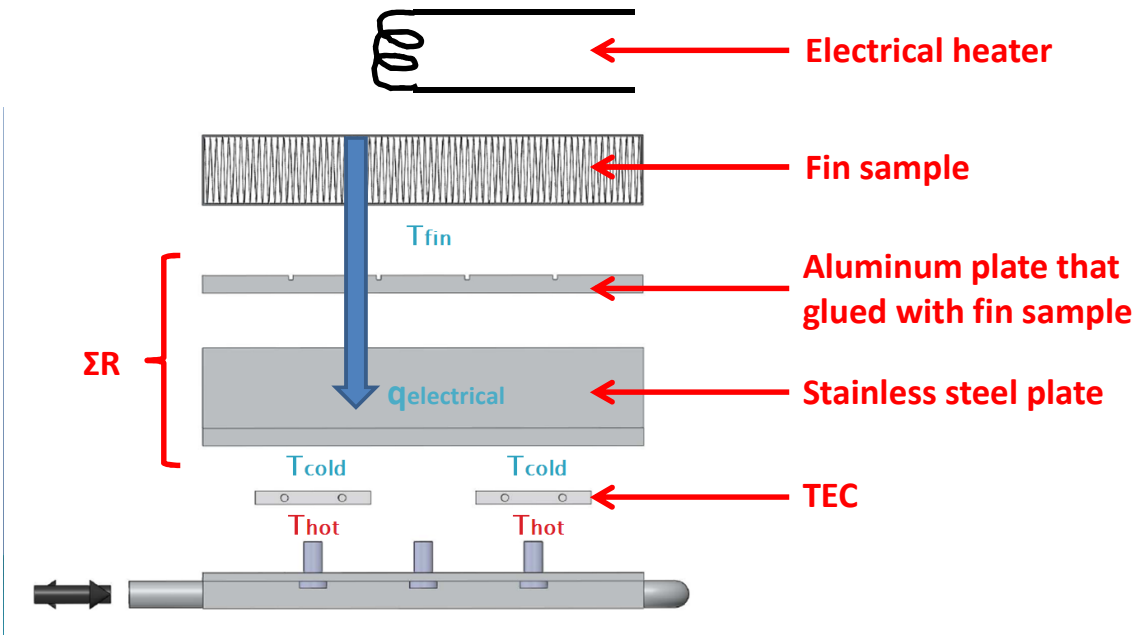

Figure 36: Calorimeter test to estimate the total thermal resistance

The test result showed that the DAQ system worked flawlessly in recording 12 hours of data continuously. The temperature difference between the T_{fin} and T_{cold} during the calorimeter test showed a constant 3.93°C (39.07°F). Using Equation (15), the total thermal resistance (ΣR) from the calorimeter tests was calculated to be 0.79 K/Watt (0.42 R-hr/Btu). As seen in Figure 36, the total thermal resistance obtained in this test is for both of the TECs. To modify the thermal resistance for calculating the heat transfer rate for one of TEC it is necessary to multiply the experimental ΣR value by 2 which results in 1.58 K/Watt (0.83 R-hr/Btu). This ΣR value was used to calculate the heat transfer rate (conduction method) for all the fin samples tested in the experiment.

6.2.3 Measurement of Heat Losses (Heat Gains)

The second step of calorimeter test was done to investigate the heat gain of the test apparatus for the conduction heat transfer. The heat gain is introduced into the test apparatus because of the fin temperature that is colder than the ambient temperature. The heat gain in the calorimeter test was estimated by the relation of temperature difference between the T_{cold} and T_{fin}. The test was conducted in the similar manner as the frosting test. The fan inside the tunnel was turned on to simulate the airflow passing through the fin sample. The difference between the frosting test and this test was the fin sample was heated using the electrical heater with the same configuration as the previous calorimeter test (Figure 36).

The test procedures used for this test are:

1. Install the heater at one side of the fin sample.
2. Insulate the entire assembly to limit the heat gain to the ambient air.
3. Start the DAQ system to start monitoring and recording temperatures and flow rate across the fin sample.

4. Turned the fan inside the tunnel and adjust the fan to provide air face velocity of 1.5 m/s (295 ft/min) on the fin sample which is the exact same condition on the actual frost test. The air condition inside the tunnel was kept at the ambient condition throughout this test.
5. Powered the electrical heater to 5 watts (17.1 Btu/hr) and wait for the temperature readings to reach steady state.
6. Kept the test to run for a period of time while all the temperature readings are recorded.
7. Analyzed the collected data using method introduced below.

The data processing is done by following these steps:

1. Get the inlet air temperature (T_{in}), fin temperature (T_{fin}) and TEC surface temperature (T_{cold}) from the data.
2. Calculate the heat transfer rate using Equation (12) with ΣR equal to 0.79 K/W (0.42 R-hr/Btu).
3. As mention in the test procedure, the electrical heater's input was set to 5 Watts. Using the calculated heat transfer in step 2 and 5 Watts of heat input, the heat gain can be calculated as shown in Equation (16) below.

   $$q_{conduction,gain} = q_{conduction} - 5\ Watts\ (17.1\ \text{Btu/hr}) \quad (16)$$

   The overall heat gain calculated above was calculated only for half of the test apparatus. Therefore, the heat gain was multiplied by 2 to consider the heat gain for the overall test apparatus.
4. The temperature difference between the fin temperature (T_{fin}) and inlet air temperature (T_{in}) was calculated.
5. The heat gain and the temperature difference calculated in step 3 and 4 were plotted as shown in Figure 37.
6. The relation between heat gain with temperature difference was estimated using the curve fit.

The function between heat gain and temperature difference can be seen in Figure 37.

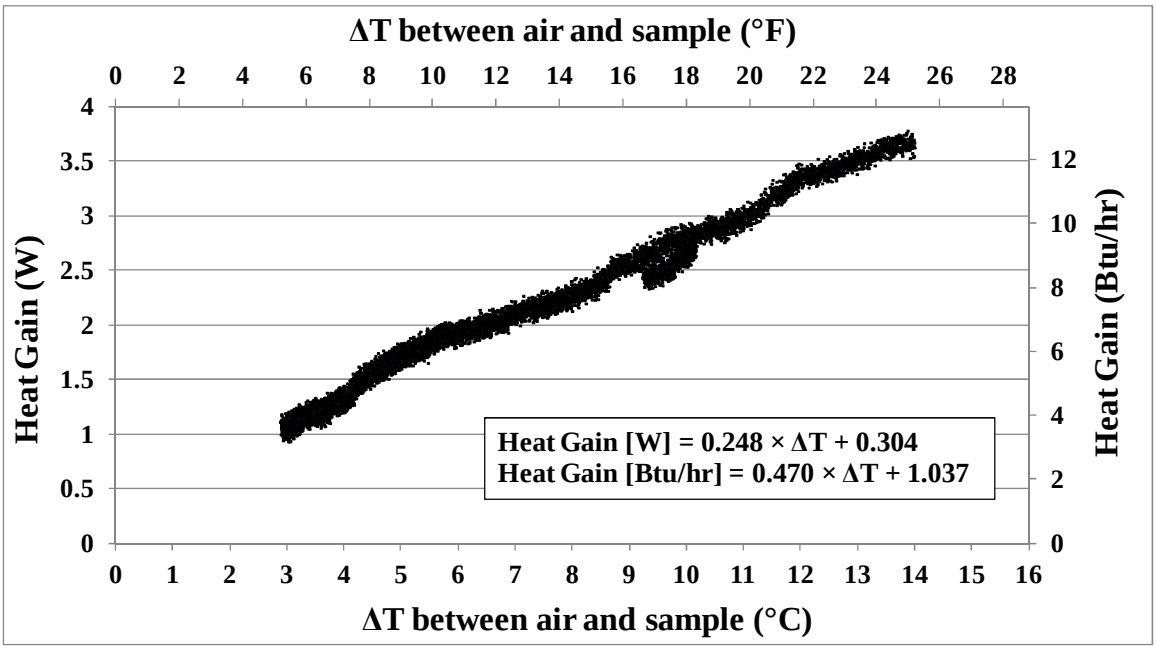

Figure 37: Heat gain of apparatus as a function of temperature difference

6.3 HEAT BALANCE TESTS

Heat balance test for the experimental measurement validation is reported on fin sample 3 as an example. The heat balance was calculated using Equation (17) shown below.

$$Heat\ balance\ (\%) = \frac{q_{conduction,total} - q_{air,total}}{q_{conduction,total}} \times 100\% \quad (17)$$

These tests were dry test and frost test. The dry test was performed by cooling the fin sample while keeping the fin sample dry (without frost deposition on the fin) throughout the test period. On the other hand, the frost test was performed by cooling the fin sample to the set fin temperature and allows the frost to grow on the fin sample as described in the previous chapter.

6.3.1 Heat Balance on Dry Tests

Heat balance balance for the dry test in the early stage of the project is imporant because it can used as one of the tool to evaluate the accuracy of heat transfer measurements. The dry test is done in the similar manner with the frosting test described in the testing procedure. The only difference is that in the dry test, the fin sample is kept dry throughout the experiment. The fin sample was cooled until the difference between fin temperature and inlet dry bulb temperature is approximately 10°C (50°F). The air temperature at the inlet of the fin sample was kept at the ambient temperature approximately at 22 to 24°C (71.6 to 75.2°F) by not conditioning the air inside the tunnel. Once the test had reached steady state condition, the test was continued for one hour while the data were recorded. The preliminary dry test was conducted on all the samples while exmaples for fin sample 3 are presented here. The test condition for dry test is shown in Table 14 below.

Table 14: Dry test condition

Test condition	Set point
Dry bulb temperature at inlet	22.5°C (72.5°F)
Humidity ratio at inlet	0.0058 kg-water/kg-air
Fin temperature	12.5°C (54.5°F)
Air face velocity	1.5 m/s (295 ft/min)

The calculation of heat transfer rate for both enthalpy and conduction methods are explained in detail in the previous chapter for data reduction. The heat transfer rate during the dry test is presented in Figure 38 below. The heat transfer rate calculated using both methods are close to each other.

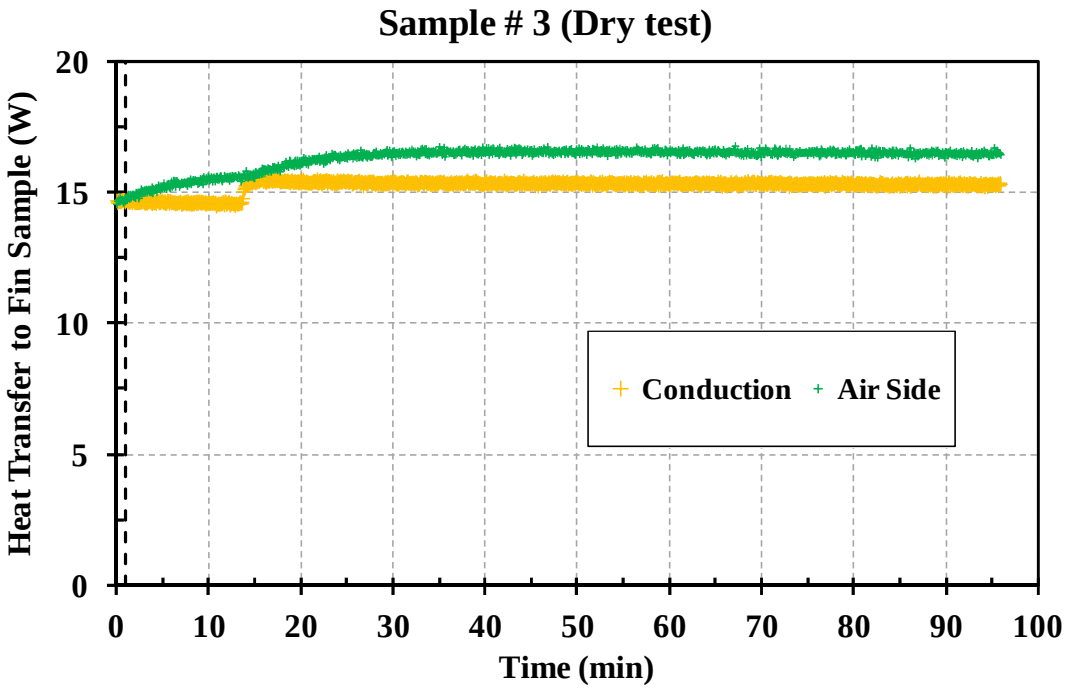

Figure 38: Heat transfer rate for dry test (sample 3)

The heat balance on the dry test is calculated using Equation (17) and the result is shown in Figure 39. The heat balance in the dry test is pretty constant after the test reach steady state condition and the average value of the heat balance throughout the test is about 8%. This value of heat balance is acceptable for our experiment because the heat transfer rate measured during the experiment is really small. Moreover, the theoretical uncertainty for each method is (8% for conduction method and 10% for entalpy method).

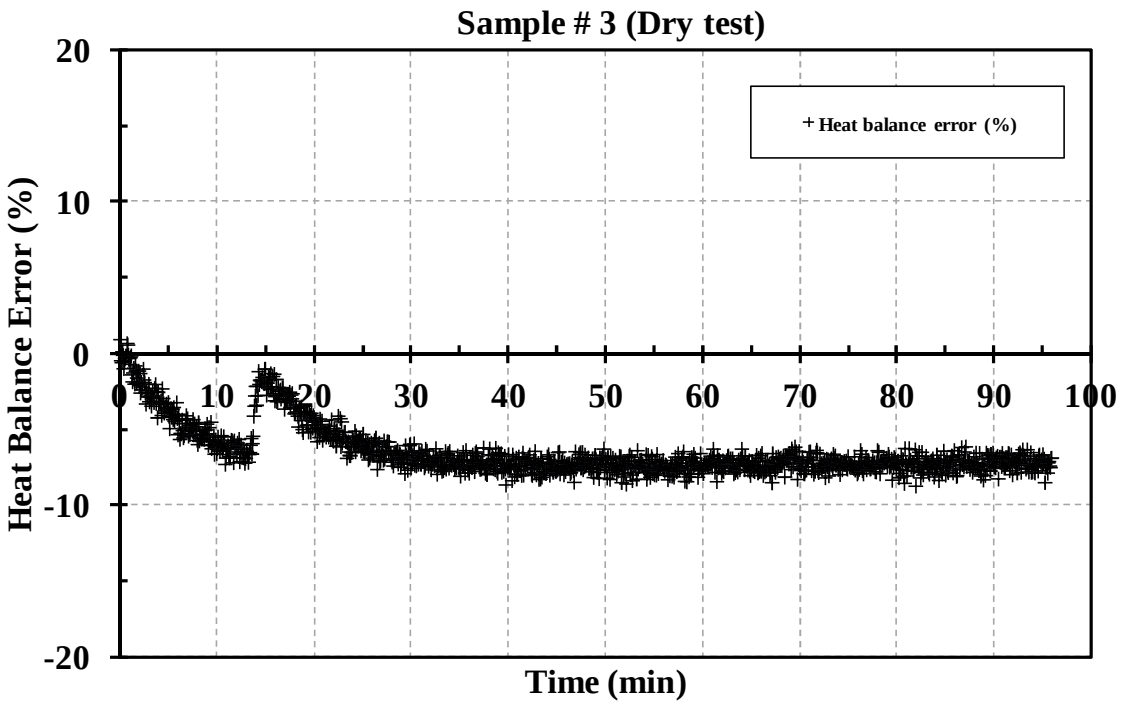

Figure 39: Heat balance for dry test for sample 3

6.3.2 Heat Balance on Frost Tests

Additional heat balance test were performed on frost test for all the samples and fin sample 3 data is presented here as an example. Frost test is the typical test that was conducted in this experiment as described in test procedure section. The test was carried out by maintaining the sample's fin temperature at the desired condition while keeping the ambient air at the set point. The selected condition for both fin temperature and ambient air would allow the frost growth on the fin sample. The test was performed until the frost on the microchannel blocked the airflow passage and reduced the airflow rate to 25% of the initial flow rate. In the experimental validation, additional heat balance for frost test is crucial because it would indicate the different performance of heat transfer measurement during the frost test comparing to the dry test. The test condition for frost test is shown in Table 15 below.

Table 15: Frost test condition

Test condition	Set point
Dry bulb temperature at inlet	1.67°C (35°F)
Humidity ratio at inlet	0.00348 kg-water/kg-air
Fin temperature	-5°C (23°F)
Air face velocity	1.5 m/s (295 ft/min)

The calculation of heat transfer rate for both enthalpy and conduction methods are explained in detail in the previous chapter for data reduction. The heat transfer rate during the frost test is presented in Figure 40 below. It is shown that the heat transfer rate calculated using both methods are similar. The heat transfer rate using conduction method is less stable due to the method of calculation assumming the steady state condition. Additionally, conduction heat transfer is also heavily dependent on the control of TEC. For example, the suddent drop in heat transfer at minutes 15 is the effect of reduction of the TECs capacity to maintain the constant fin temperature.

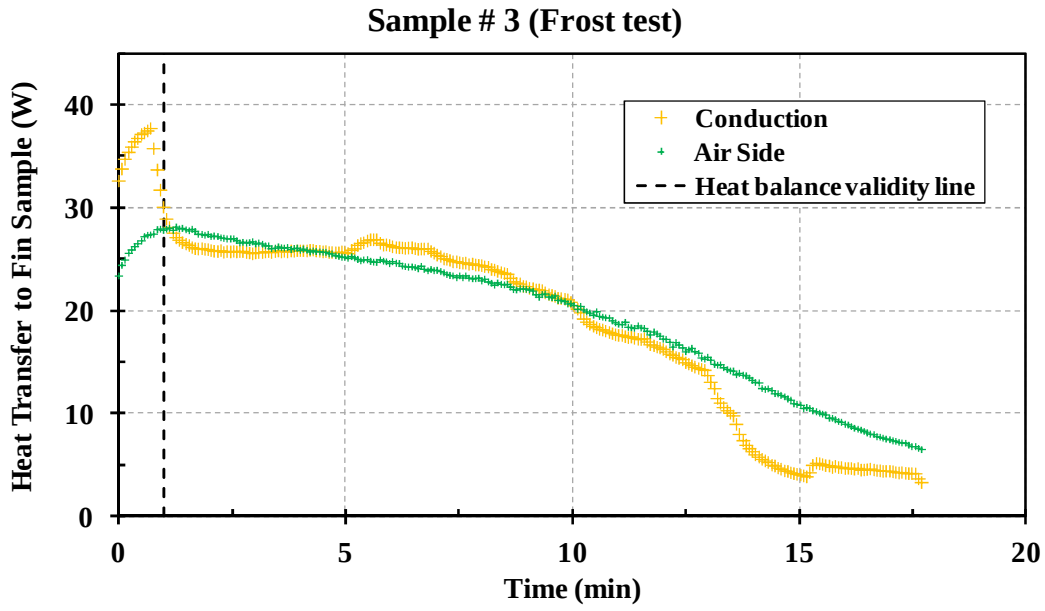

Figure 40: Heat transfer rate for frost test (sample 3)

The heat balance on the frost test is calculated using Equation (17) and the result is shown in Figure 41. There are more fluctuation observed in the heat balance for frosting test in comparison with the dry test. This phenomena is expected because the nature of frosting test is transient. Moreover the control on the TEC affect the heat balace significantly. Due to the test procedure that requires the fin temperature to be constant throughout the test, whenever the drastic adjustment was performed on the TEC (turning the TEC on or off temporarily), the conduction heat transfer will changed significantly as seen in Figure 40 at minutes 15. The conduction heat transfer at this point drop significantly because the power supply to the TEC was turned off momentarilly and hence the heat balance was increased from about 5% to more than -50%. Aside from the heat balance fluctuation due to TEC control, the overall heat balance during the entire frost test period was within ±10%.

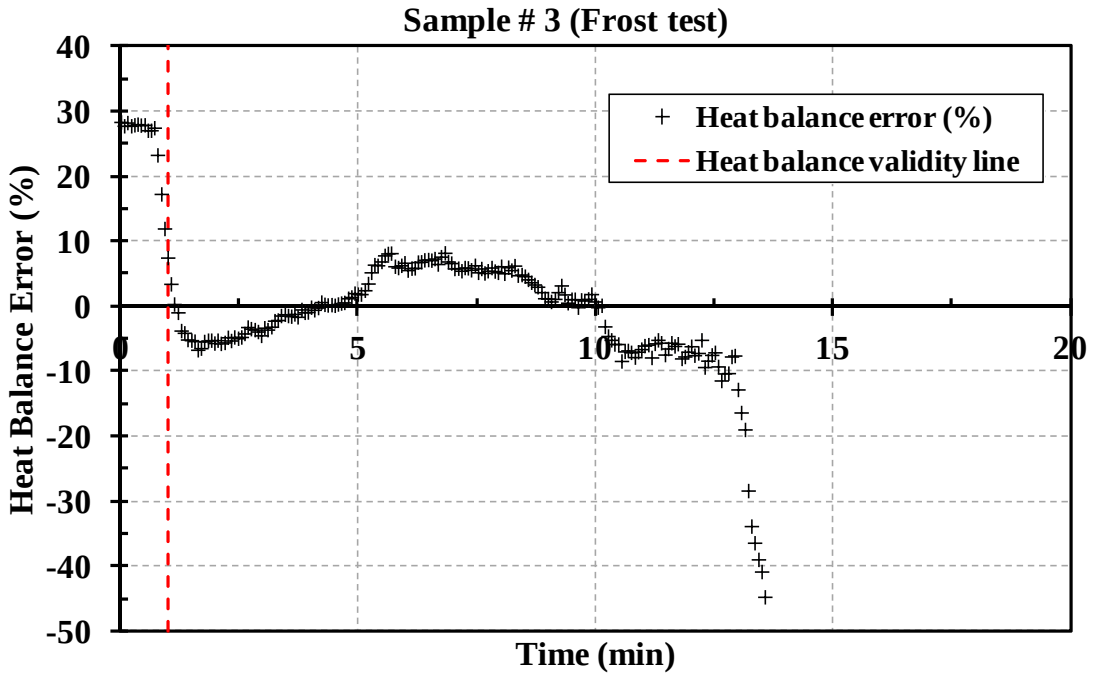

Figure 41: Heat balance for frost test (sample 3)

As mentioned in the earlier section, the heat transfer rate for the conduction method is calculated by assuming steady state condition while the actual state during the frosting experimenet was transient and dynamic. The steady state assumption was used in this experiment to reduce the complexity of the heat transfer calculation. Due to this assumption, the conduction heat transfer rate experiences a time delay compared to the air side heat transfer. To compensate for the time delay, the comparison between air side heat transfer and conduction heat transfer is done through integration of the capacity curve over time. As an example for sample 2 the integration of conduction heat transfer rate was 10.65 W·hr (36.34 Btu) and the air side heat transfer rate was 11.08 W·hr (37.81 Btu. The comparison between the two methods shows 4% difference, despite the luctuation in the instantanoues heat balance curve. This comparision demonstrates that heat transfer rate measured during the frosting experiments were accurate.

6.4 CONCLUSIONS

The experimental validation that perfomed through calorimeter tests and heat balance tests showed that the installed sensors and DAQ system performed well throughout all of the tests. The calorimeter tests provided crucial information for heat transfer rate calculation using conduction method. The tests provided the total thermal resistance of the experimental setup which were used in the measurement of the conduction heat transfer rate and the heat gain of the experimental setup as a function of temperature difference. Additionally, the heat balance tests were performed for dry test and frost test in all of the fin samples. The heat balance tests revealed the accuracy of heat transfer measurement in both steady state condition (dry test) and transient condition (frost test). The heat balance tests showed that the entalpy method to calculate heat transfer rate for the fin sample was more stable. The frost test in sample 3 showed that the conduction heat transfer experienced time delay due to the method of calculation, and it is also heavily dependent on the

the control of the TEC. Hence, the heat transfer rate curve had significant fluctuation in comparison to the one estimated by using the enthalpy method.

CHAPTER VII

RESULTS AND DISCUSSION

7.1 VISUAL OBSERVATIONS

Frost growth patterns on microchannel fin samples 1 through 7 with different geometry and 7 through 12 with different surface coatings are shown in Figure 42 through Figure 44. All pictures were taken during a frost test with the same fin surface temperature and same air entering conditions. Fin surface temperature was kept constant at -8°C and entering air was set at 1.7°C/0.6°C db/wb. The location of the camera was in the center of the 15cm (6 inch) long sample. Figure 42 shows the frost accumulation over time; the frost time was measured from the time the air flow was started on the cold sample to the end of the frosting period, that is, when the air face velocity reached 30% of its initial value. The duration of the frost cycles ranges from 18 min to 56 min for different geometries. For coated samples the frost cycle duration ranges from 14 to 18 min after 5 consequent frost/defrost cycles as shown in Figure 62. Frost grew on the fins with similar appearance for the geometries tested in the present work.

The end of the cycle occurred at a time when the air gaps between the fins were almost completely blocked by frost. There are some visible frozen water droplets on the samples 7 through 12 that are results of remaining residual water on the samples after previous defrost cycles. The water beads are frozen and remain unchanged all through the following frost test. The number of the remaining droplets seems to be more on hydrophobic samples rather than on hydrophilic samples. This might be due to the low contact angle of hydrophilic surfaces that prevents formation of individual droplets after each defrost cycle so that the film of water spreads on the fin surface and drains better. Even if the sample have good drainage characteristics and very few or no droplet remains on the fin after a defrost, as in the case of hydrophilic samples, there are still minor changes in frost time in comparison to the effect of fin geometry. The geometry effects especially in sample 1 with no louver fin design and very low fin density seems to extend the time of frost cycle much more than the effect of surface coating.

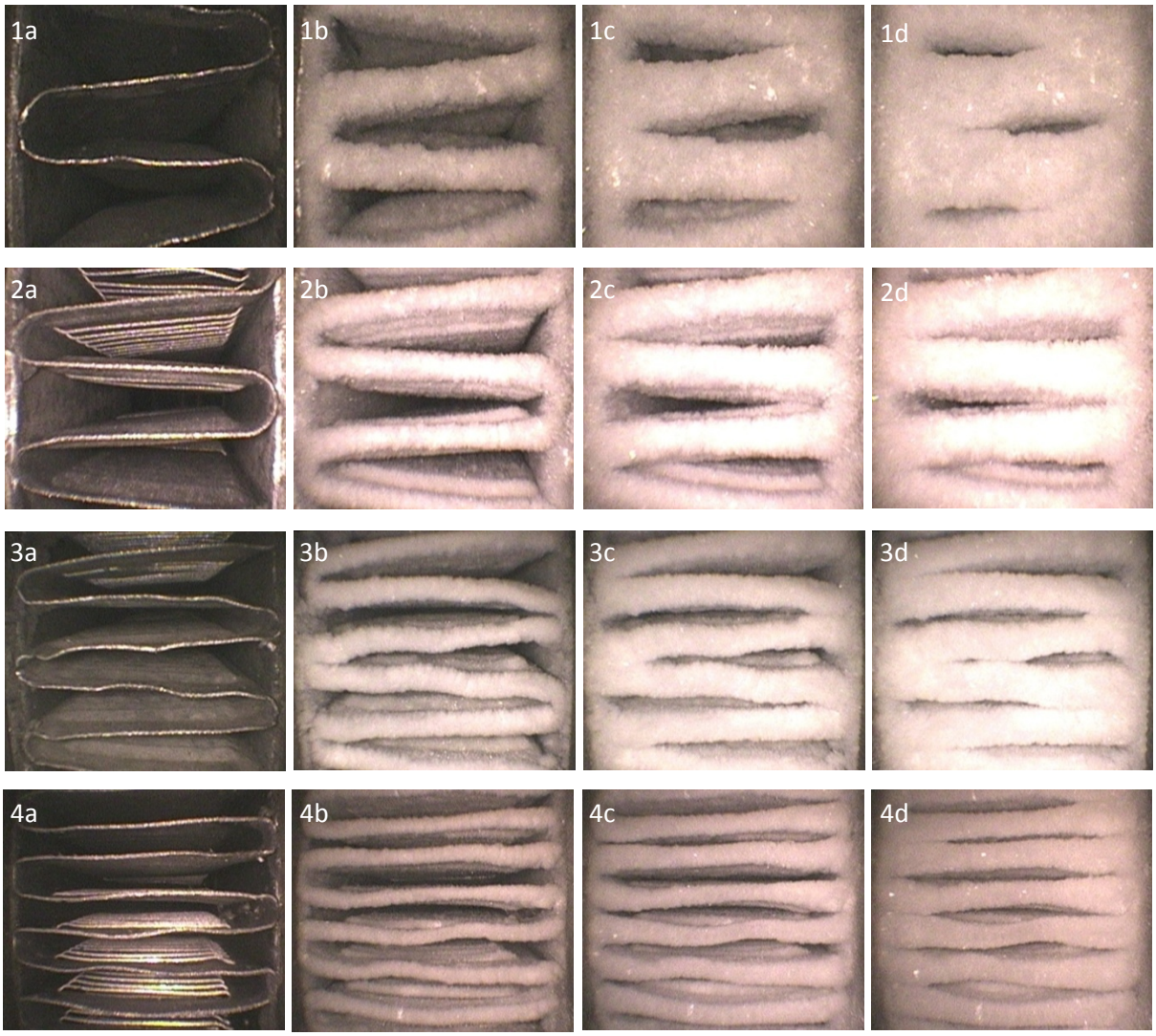

Figure 42: Microchannel uncoated samples 1~4 with different geometries under frosting conditions. For all cases (a) represents starting of the test at dry start condition and (d) represents the last minute of the test. For all the images Tsurf= -8°C and air temperature=1.7°C/0.6°C db/wb.
1- Sample # 1; time (min) a:0 b:19 c:38 d:56,
2- Sample # 2; time (min) a:0 b:8 c:16 d:24,
3- Sample # 3; time (min) a:0 b:6 c:12 d:18,
4- Sample # 4; time (min) a:0 b:9 c:17 d:25.

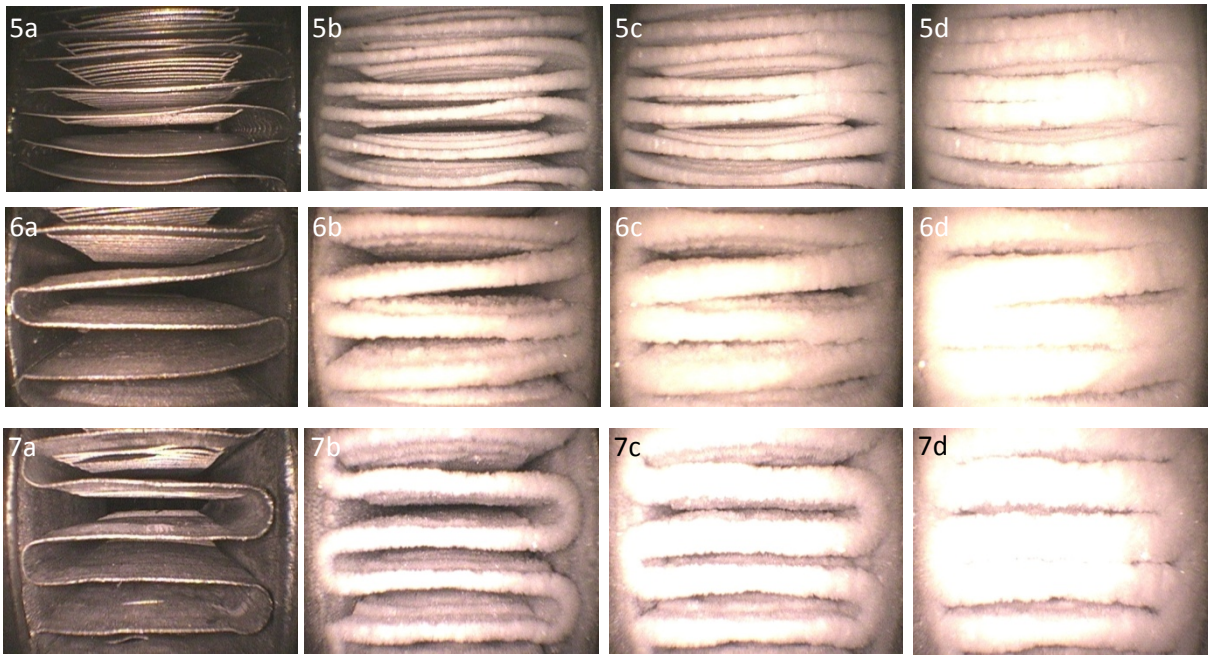

Figure 43: Microchannel uncoated samples 5~7 with different geometries under frosting conditions. For all cases (a) represents starting of the test at dry start condition and (d) represents the last minute of the test. For all the images Tsurf= -8°C and air temperature=1.7°C/0.6°C db/wb.
5- Sample # 5; time (min) a:0 b:19 c:38 d:25,
6- Sample # 6; time (min) a:0 b:6 c:12 d:18,
7- Sample # 7; time (min) a:0 b:6 c:13 d:19.

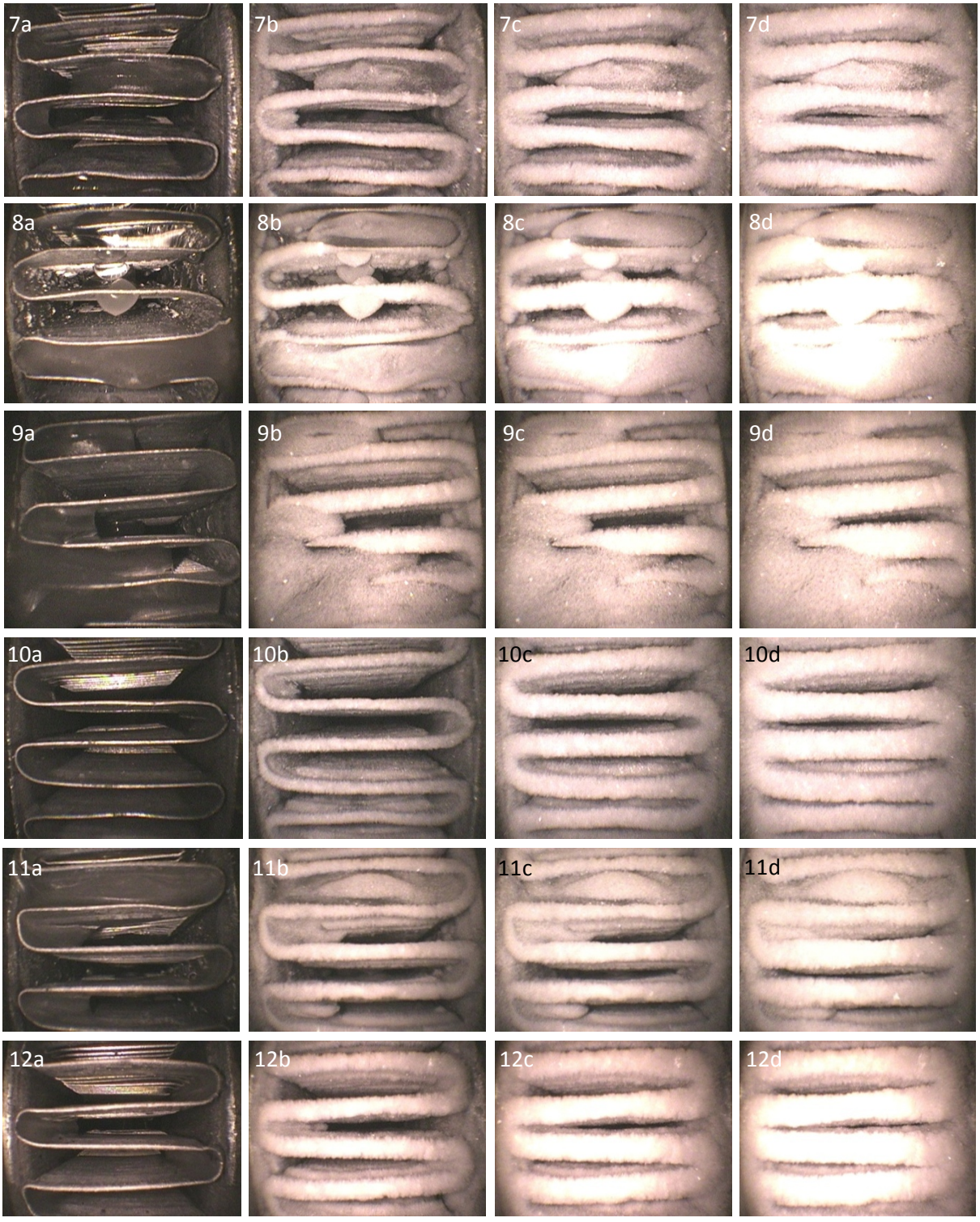

Figure 44: Frozen water droplets on microchannel samples 7~12 with different coatings for 5th frost cycle. For all cases (a) represents starting of the test at the beginning of the 5th frost cycle and (d) represents the last minute of the 5th frost cycle. For all the images Tsurf= -8°C and air temperature=1.7°C/0.6°C db/wb.
7: Sample 7; time (min) a:0 b:4 c:8 d:13; 8: Sample 8; time (min) a:0 b:6 c:10 d:15;
9: Sample 9; time (min) a:0 b:6 c:12 d:18; 10: Sample 10; time (min) a:0 b:6 c:12 d:18;
11: Sample 11; time (min) a:0 b:5 c:9 d:14; 12: Sample 12; time (min) a:0 b:6 c:10 d:15.

7.2 SURFACE TEMPERATURE EFFECTS

The effect of surface temperature on capacity degradation of the microchannel for fin sample 5 is shown in Figure 45. Similar results have been obtained for other fin geometries and a summary is given in Table 16. Normalized capacity on the y-axis is plotted versus time on the x-axis for three fin surface temperatures. Normalized capacity is defined as the fraction of the capacity at each minute of the test to the initial capacity at the beginning of the frost test for the surface temperature of -8°C. Results show that surface temperature has a significant effect on the rate of capacity degradation for the coil under frosting condition.

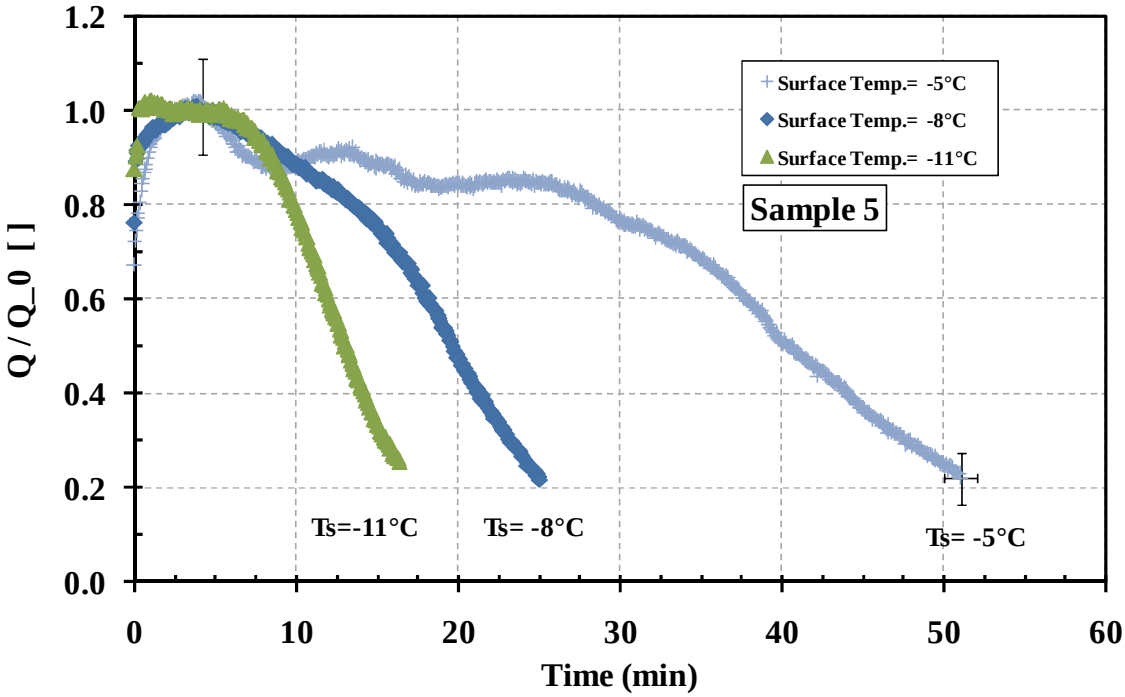

Figure 45: Experimental data of effect of surface temperature on capacity degradation of microchannel samples. The Q_0 for Temperature -5, -8 and -11°C is 23.5, 32.9 and 40.2W respectively. Data belongs to sample 6 but similar results were observed for other (see Table 16 and Appendix E).

For all surface temperatures, normalized capacity starts from 1 in the beginning of the test (The capacity fluctuations during the first two minutes of the test were the results of stabilization after the pull down period) and reduces to around 0.25 at the end of the test. Data shows that at lower surface temperatures the capacity reduces more quickly and for a 3 degree increase in surface temperature from -11°C to -8°C, a 50% increase in time of the frost cycle occurred. Also a 3 degree increase in surface temperature form -8°C to -5°C increases the time of the cycle more than 100%.

Table 16: Duration of the cycles and initial capacities for 7 microchannel geometries tested in the present study. Time represents the time required from the beginning of the test for the capacity to reduce to an average of 30% of its initial value. For more detail on capacity degradation see Appendix E.

Sam. No.	Time in [min] / Initial Cap. in [kW/m²] / frost mass in [kg/m²h]	Tsurf [℃]			Surf. temp. change -11°C to -5°C	
		-5	-8	-11	time / capacity / frost mass change fraction [ ]	Eval. Effect Des. : Desirable
1	time	135	57	42	+3.2	Des.
	Init. Cap.	9.7	14.8	18.6	-1.9	Un-des.
	frost mass	2.7	5.7	7.9	-2.9	Des.
2	time	48	23	14	+3.4	Des.
	Init. Cap.	15.0	22.2	28.4	-1.9	Un-des.
	frost mass	5.0	8.6	10.7	-2.1	Des.
3	time	46	18	12	+4.0	Des.
	Init. Cap.	15.8	24.2	27.4	-1.7	Un-des.
	frost mass	4.8	7.8	13.8	-2.9	Des.
4	time	50	25	15	+3.3	Des.
	Init. Cap.	11.8	17.1	21.7	-1.8	Un-des.
	frost mass	5.3	6.0	8.6	-1.6	Des.
5	time	50	24	17	+3.0	Des.
	Init. Cap.	12.1	16.9	20.7	-1.7	Un-des.
	frost mass	3.4	7.0	8.4	-2.4	Des.
6	time	38	18	12	+3.2	Des.
	Init. Cap.	16.3	25.5	32.5	-2.0	Un-des.
	frost mass	5.2	9.2	12.0	-2.3	Des.
7	time	48	20	15	+3.2	Des.
	Init. Cap.	14.1	18.0	23.0	-1.6	Un-des.
	frost mass	4.2	9.9	9.2	-2.2	Des.

When air comes into contact with a cold surface its temperature decreases until it gets to the dew point temperature (-1.0°C in the present study). When air is cooled below its dew point temperature, frost starts to accumulate on the surface. The difference between water vapor pressure of the entering air and the water vapor saturation pressure at the surface temperature is a main driving force for deposition of the frost. This quantity is referred to as supersaturation level of the air in the literature (Na and Webb, 2004a; Sanders, 1974). The water vapor pressure of the entering air was 560 Pa for all the frost tests conducted in the present study while the water vapor saturation pressure is 240, 310 and 400 Pa at the fin surface temperatures of -11, -8 and -5°C. Water vapor pressure difference showed that the frost deposition rate at high surface temperatures such, as -5°C was slower and yielded to longer frost time. Although a high surface temperature leads to a longer frost time, which is desirable to minimize the energy cost associated with the defrost cycle, the coil capacity is reduced at higher fin surface temperatures.

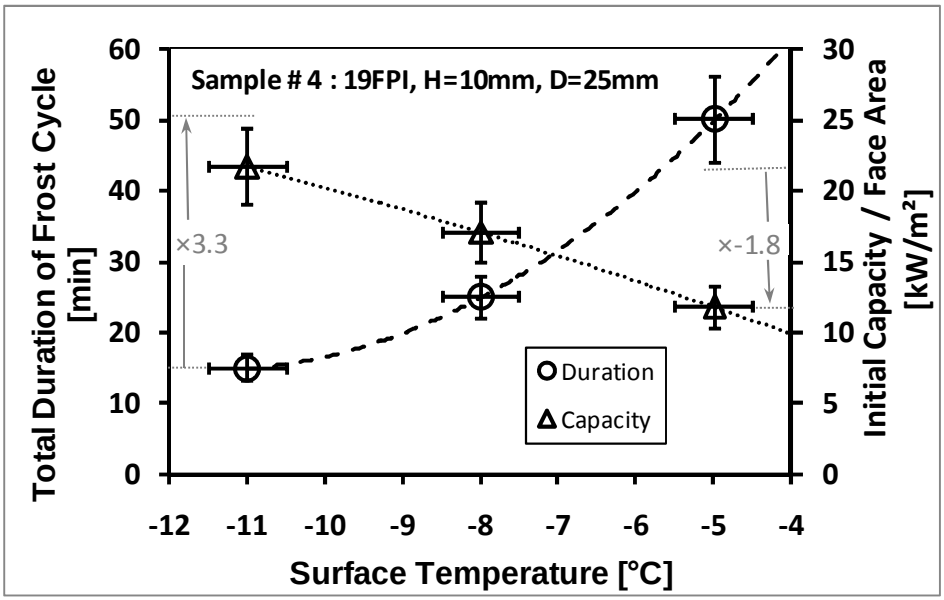

Figure 46: Effect of surface temperature on capacity degradation of microchannel samples (air temperature = 1.7°C/0.6°C db/wb). Data are for sample 4 and similar results were observed for other samples (see Table 16).

Thus increasing the surface temperature has the advantage of a longer frost cycle but the disadvantage of reduced coil capacity. Capacities for frost cycles at different surface temperatures are compared in Figure 46. This shows experimental data for sample 4 with the duration of the frost cycle for each test on the left-axis versus surface temperature, and initial capacity per face area of the sample on the secondary vertical-axis. Similar data was obtained for other samples and a summary is given in Table 16. The data showed that the gain in time of frost by changing the surface temperature form -11°C to -5°C is around 3.3 times, but the initial capacity of the sample was 1.8 times less. Normalization based on the face area was applied because different samples had different face areas based on their fin width[15].

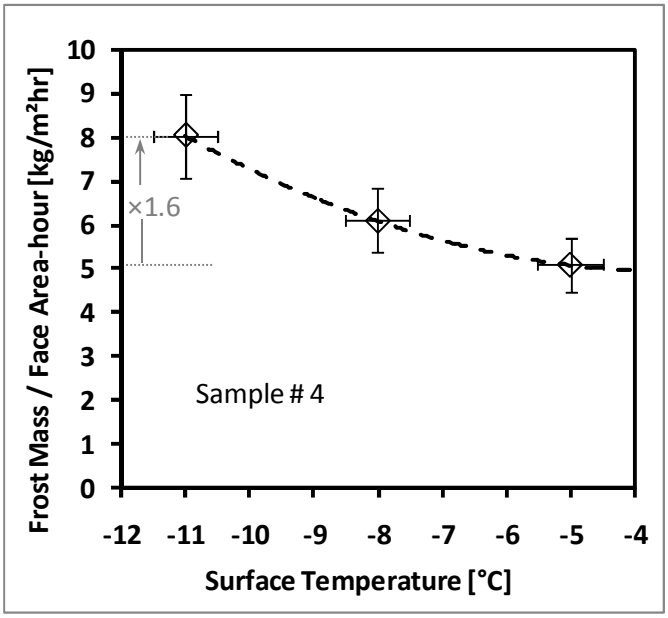

Figure 47: Effect of surface temperature on frost mass accumulated on microchannel samples. Data belongs to sample 4 but similar results were observed for other samples (see Table 16).

[15]Caution should be used with using the exact values of kW/m^2 to calculate the capacity of large scale microchannel coil since the tubes were eliminated in the present study.

The other parameter to be considered, in altering the surface temperature, is the amount of frost accumulated on the coil at each surface temperature. This quantity is important because it defines the amount of energy, or heat transfer, required during defrost mode to melt the frost accumulated on the coil. Since the duration of each frost test varied between different surface temperatures and samples had different heat transfer area, it was decided to normalize the frost mass based on the face area and time of the frost accumulation. This normalization accommodated a comparison between different working conditions and different geometries. In other words, the data in Figure 47 are meant to describe which surface temperature had minimum frost accumulation on a mass basis per square meter face area of the coil and per hour of operating time under frosting conditions. Data in Figure 47 shows that frost mass accumulated on sample 4 during one hour of operation at surface temperature of -11°C would be about 1.6 times higher than frost mass accumulated on the same coil under -5°C surface temperature working condition. Thus the higher surface temperature seems to have an advantage over the lower surface temperature in terms of frost mass deposition rate.

To determine the influence of surface temperature versus the effect of geometry on the frosting time of microchannels, the frost time of samples 1 through 7 with different geometries are shown versus surface temperature in Figure 48. Sample 1, which was a corrugated, low density (10 fpi) fin is the only non-louvered fin included in the comparison. Although the corrugated feature was undesirable for comparative analysis, non-corrugated, louvered, low density fins were not readily available for the study. Data shows that sample 1 has a very long frost time in comparison to the louvered fin geometries. Further investigation is necessary to isolate the effect of extreme low fin density and existence of louvers on the frosting performance. More discussion about the overall performance of sample 1 considering both time and capacity of the frost cycle and frost mass accumulated on it will be offered in the following sections of this dissertation.

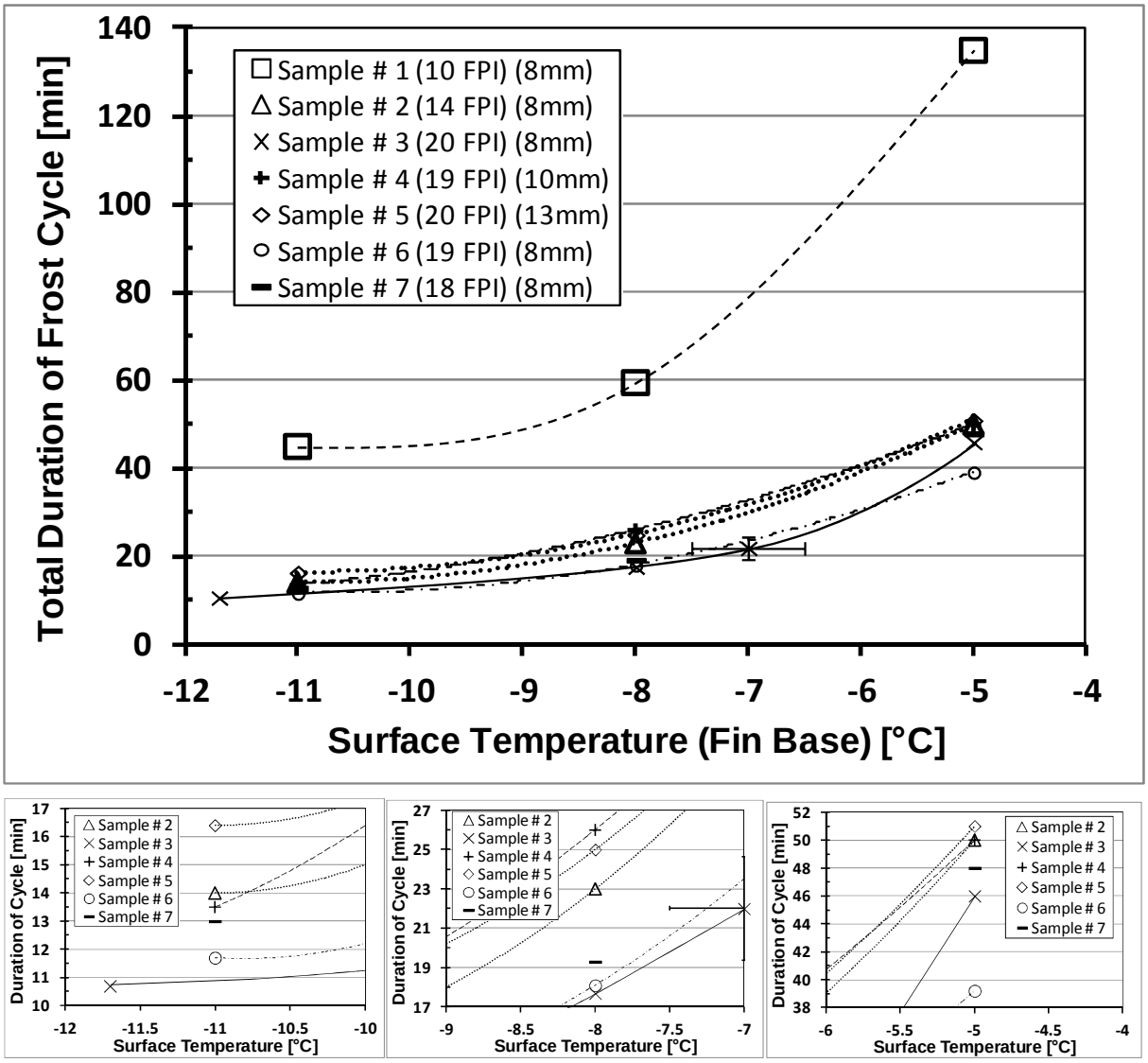

Figure 48: Effect of surface temperature on frost time for microchannel samples (air temperature = 1.7°C/0.6°C db/wb). The three small figures on the bottom show the zoomed in image of the top figure.

The other observation in Figure 48 is that if the non-louvered sample 1 is not considered, other geometries show very similar frost times, regardless of their particular geometry. It seems that the dominant factor that defines the frost time of a particular microchannel sample is first its working surface temperature and then the geometry. The behaviour of lower or higher depth or lower or higher width samples are not significantly different. The majority of the data shows that the

samples with larger width (sample 4 and 5) show a slightly higher frost time in comparison to other samples that have lower fin width. This could be attributed to higher average fin surface temperature over entire surface of the fin since only the fin bases were controlled at the constant temperature. Sample 2 also show relatively higher frost time in comparison to other samples because of its low fin density and the delay this effect makes on the blockage of the air flow by the frost.

7.3 GEOMETRY EFFECTS

7.3.1 Fin Density (Fin Spacing) Effect

Microchannel samples with three different fin densities of 10, 14, 20 were tested in the present study to evaluate the effect of fin density on frosting performance of microchannels. The experimental data obtained on frost time and capacity of samples with different fin density is shown in Figure 49. Data shows that low fin density samples have higher frost time in comparison to high fin density samples. Frost thickness data showed that this was due to air flow blockage caused by frost thickness growth which occurred faster when sample had a higher fin density. As shown in Figure 49, Sample 1 with density of 10.4, has a frost time of about 59 minutes while sample 3 with 20.3 fin per inch has a frost time of 18 minutes. Thus reducing the fin density from 20 to 10 will result in around 3.2 times increase in frosting time. However, lowering the fin density has an adverse effect on the capacity due to a reduction in heat transfer area. The data on the secondary axis of Figure 49 shows that the initial capacity of sample 1 is around 1.6 times lower than sample 3. In other words, Sample 1 starts with 1.6 times lower capacity but it can operate up to 3.2 times longer than sample 3 before its capacity drops significantly and the frost cycle terminates. The frost time is defined as the time required for the

air face velocity to drop to 30% of the initial face velocity for all the samples. During the frost time, the capacity dropped to around 30% of initial capacity. Normalization of the secondary vertical axis of Figure 49 onface area will allow capacity comparisons on a per square meter basis. The samples were normalized on face area instead of surface area since face area defines the actual size of the coil in heat pump systems and leads to a more meaningful comparison. Also sample 3 had a slightly different fin width (7.6mm) in comparison to sample 1 and 2 (8.0mm) and this caused slightly different surface area. Face area normalization also serves to isolate the effect of fin density for slightly different surface face areas.

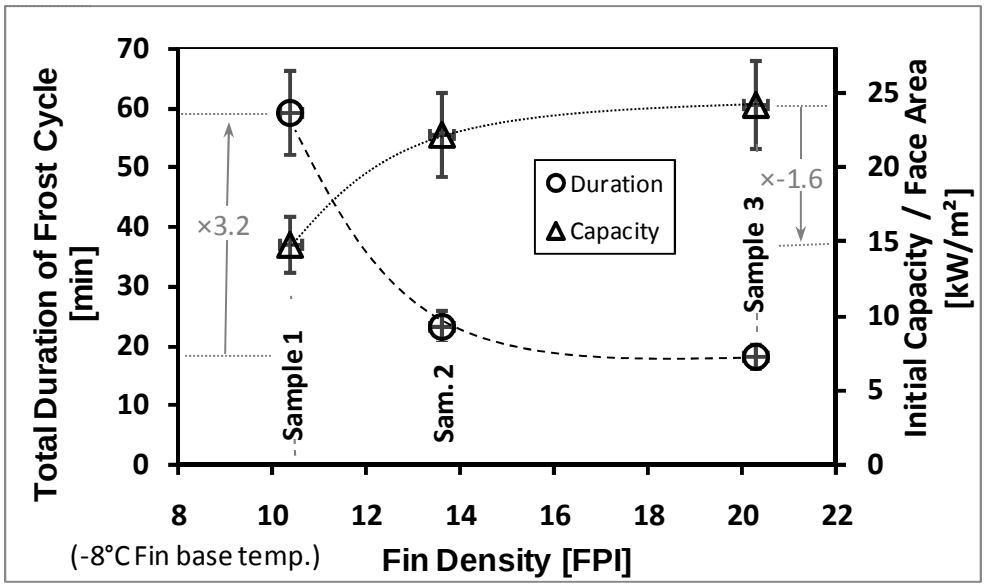

Figure 49: Effect of Fin Density on frost time and capacity of microchannel samples (Tsurf= -8°C, air temperature=1.7°C/0.6°C db/wb). Similar results observed for surface temperatures of -5° and -11°C (see Table 16).

As previously discussed, sample 1 (with the lowest fin density) was a wavy, corrugated, non-louvered fin. Therefore, longer frost time for sample 1 is due to the combined effect of channel (non-louvered) flow and significantly lower fin density. Based on our observations, we expect

that fin density to be the dominant effect, but additional tests with prototypical low density louvered fin are required to confirm this hypothesis.

Another result to be considered in assessing the effect of fin density on frosting performance of microchannels is the accumulated frost mass on each particular geometry. This information determines the amount of energy required for defrost of the sample. Figure 50 shows the effect of fin density on the accumulated frost mass for each geometry. The data has been normalized on face area and frost time. The time normalization is required to allow comparison of frost mass accumulated for tests of different duration. Data shows that sample 1, with the lowest fin density, has a very low frost mass accumulated on its surface per hour of operation. Samples 2 and 3 have higher frost mass accumulation rates than sample 1 while they are close to each other considering the uncertainty bars in the measurements.

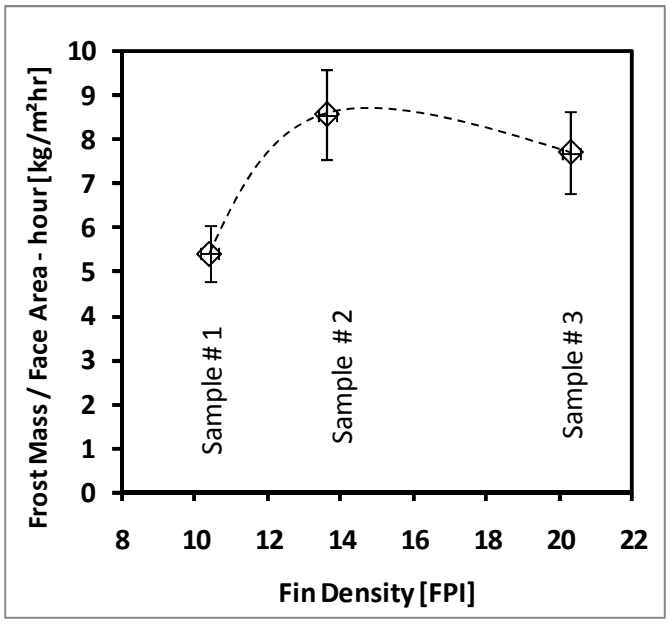

Figure 50: : Effect of Fin Density on frost mass accumulated on microchannel samples (Tsurf= -8°C, air temperature=1.7°C/0.6°C db/wb). Similar results observed for surface temperatures of -5° and -11° (see Table 16).

7.3.2 Fin Width (Tube Spacing[16], Ch_w) Effect

The effect of fin width (that is the distance between two parallel tube edges, Ch_w) on the frosting behavior of microchannel coils has been investigated by testing samples with widths of 8, 10 and 13mm as shown in Figure 51. The total duration of their frost time is shown on the primary y-axis, and the initial capacity is shown on the secondary y-axis. Data show that the sample with the smallest fin width had the shortest frost time of about 18 minutes; samples with fin widths of 10 and 13mm had a longer frost time of about 25 minutes. This increase in the frost time (about 139%) was considered to be due to the increase of the fin width and larger free flow areas which delayed the blockage of air flow. On the other hand, the smallest fin width (sample 3) showed the highest initial capacity per face area, that is, around 1.42 times higher than sample 5 with 13mm fin width.

Although we only measured fin base temperature, analytical and numerical analysis can be used to

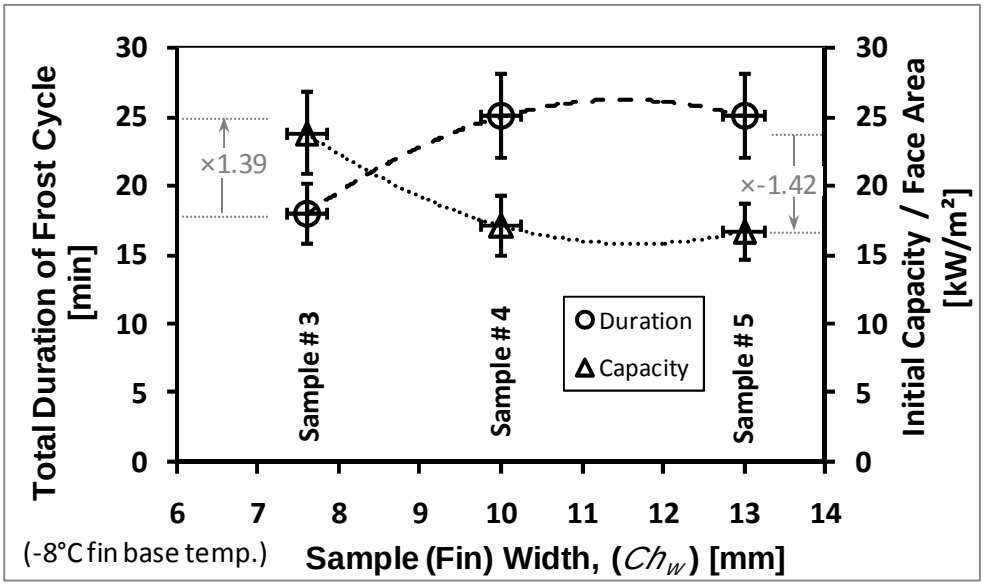

Figure 51: Effect of Fin Width on frost time and capacity of microchannel samples (Tsurf= -8°C, air temperature=1.7°C/0.6°C db/wb). Similar results observed for surface temperatures of -5° and -11°C (see Table 16).

[16] Actually Ch_w is tube spacing minus a tube thickness

demonstrate that the fin center temperature increases as the width increases for the air side condition. This explains the reduction in initial capacity of larger width samples.The improvement in time of the cycle by increasing fin width was almost the same order as the penalty in capacity reduction.

The amount of frost accumulated on coils with different fin widths are shown in Figure 52. Samples 4 with medium fin width and sample 5 with large fin width appear to have a lower frost mass accumulation per face area in each hour of operation compared to sample 3, the lowest fin width sample. In general sample 4 with medium width (10mm) does show a high frost time in between the other samples tested in the present study and it also has a capacity per face area that was considered acceptable. The amount of frost mass per face area accumulated on the surface of this sample seems to be slightly lower than other samples.

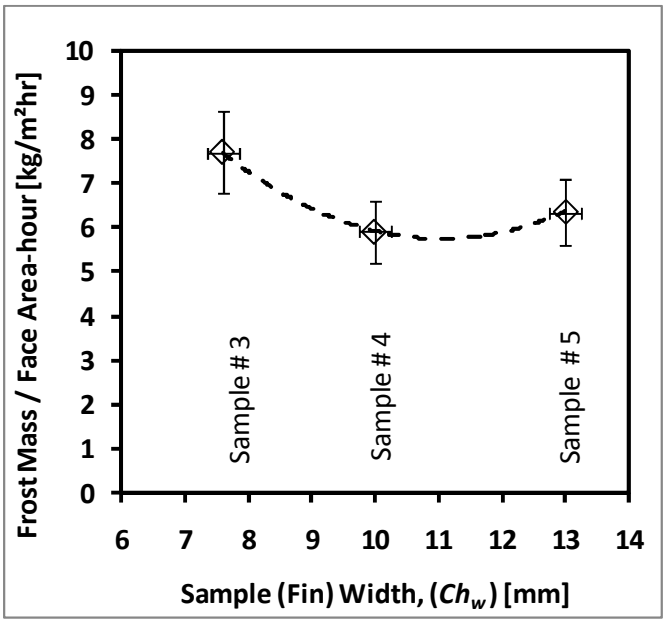

Figure 52: Effect of Fin Width on frost mass accumulated on microchannel samples (Tsurf= -8°C, air temperature=1.7°C/0.6°C db/wb). Similar results observed for surface temperatures of -5° and -11°C (see Table 16).

7.3.3 Fin Depth (Coil Depth, Ch_d) Effect

The effect of fin depth on frosting performance of microchannels for three fin depths of 19, 26 and 30mm is shown in Figure 53. Data show that sample depth has a small effect on frosting time when the uncertainty in measurements is considered. The capacity of the microchannel samples increase as the depth increases due to the increase of the coil heat transfer area. The capacity was about 1.4 times higher for a fin sample with the depth of 30mm instead of 19mm, without penalizing the time of frost significantly.

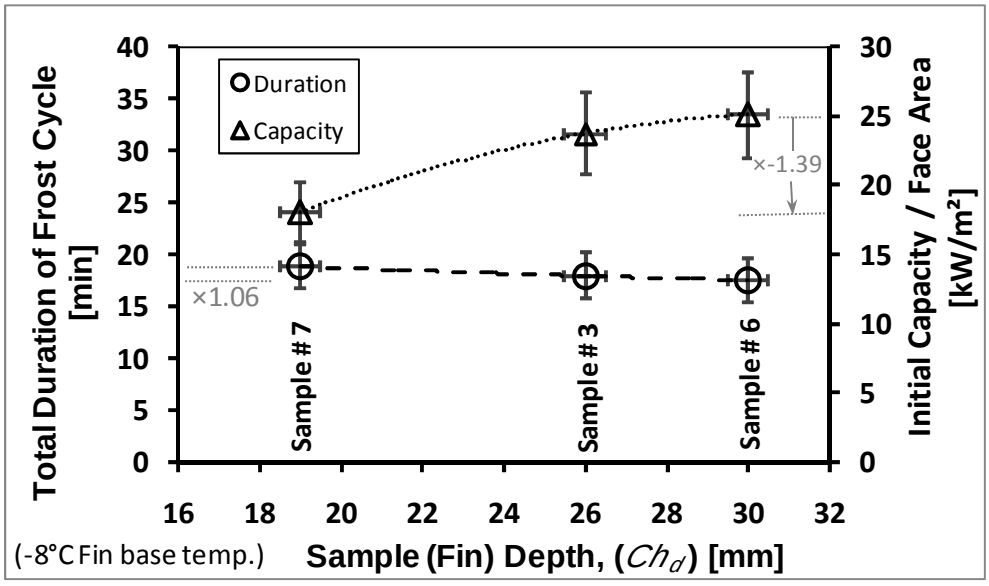

Figure 53: Effect of Fin Depth on frost time and capacity of microchannel samples (Tsurf= -8°C, air temperature=1.7°C/0.6°C db/wb). Similar results observed for surface temperatures of -5° and -11°C (see Table 16).

The amount of accumulated frost on each sample based on their fin depth are shown in Figure 54. Sample 3 with medium depth shows the minimum frost mass accumulation during each hour of operation. The difference between the frost mass accumulated on sample 3 and sample 6 is 15%. The capacity per face area of sample 3 is 24.2 kW/m^2 while sample 6 has a capacity of 25.5

kW/m^2 as shown in Figure 53. This was around 5% difference in capacity. We can summarize that sample 3 has 18% lower frost mass accumulation, 2% longer frost time, 5% less capacity per face area in comparison to sample 6. Considering the uncertainty in measurement of the data, sample 3 and sample 6 had practically the same frosting time and similar capacities per face area of the coil.

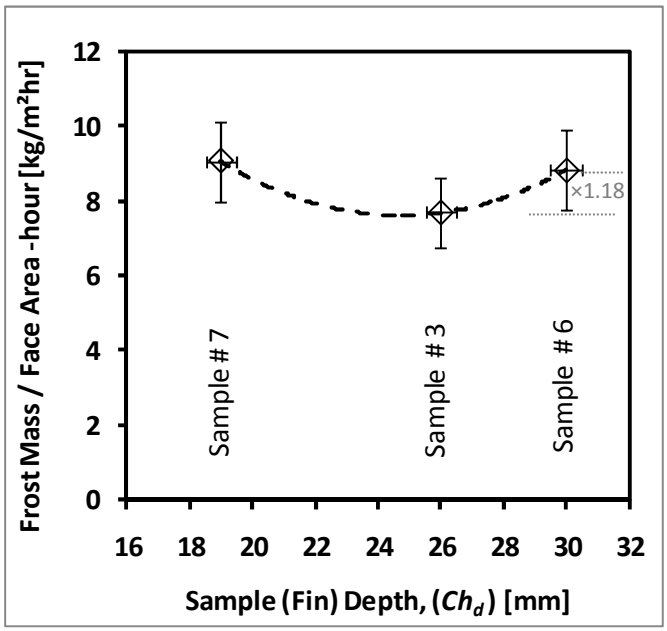

Figure 54: Effect of Fin Depth on frost mass accumulated on microchannel samples (Tsurf= -8°C, air temperature=1.7°C/0.6°C db/wb). Similar results observed for surface temperatures of -5° and -11°C (see Table 16)**.**

7.4 AIR HUMIDITY AND AIR VELOCITY EFFECTS

The effect of environmental parameters such as air humidity on the frosting performance of microchannels was also studied. Three different humidity levels of 0.003, 0.0035 and 0.0039 kg-water/kg-air (72%, 82% and 92% relative humidity) were tested. 82%relative humidity is the AHRI standard H2 frosting condition. The experimental data on sample 4 with medium width (10mm) and medium depth (25mm) are shown in Figure 55. As expected, higher air relative humidity caused faster frost growth rate, shorter frost time and slightly higher measured capacity. For an increase in relative humidity from 82 to 92%, the frosting time decreased from 26 minutes to 21 minutes. Decreasing humidity levels from 82% to 72% increased the frost time drastically to more than 120 minutes. After two hours of testing, the air flow remained constant and the process of frost deposition had slowed down considerably. We observed that the 72% humidity test could go on for even more than 2 hours. The reason for this drastic increase is that the dew point temperature for air at relative humidities of 72%, 82% and 92% and a dry bulb temperature of 1.7°C are -2.8°C, -1.0°C and +0.5°C respectively.

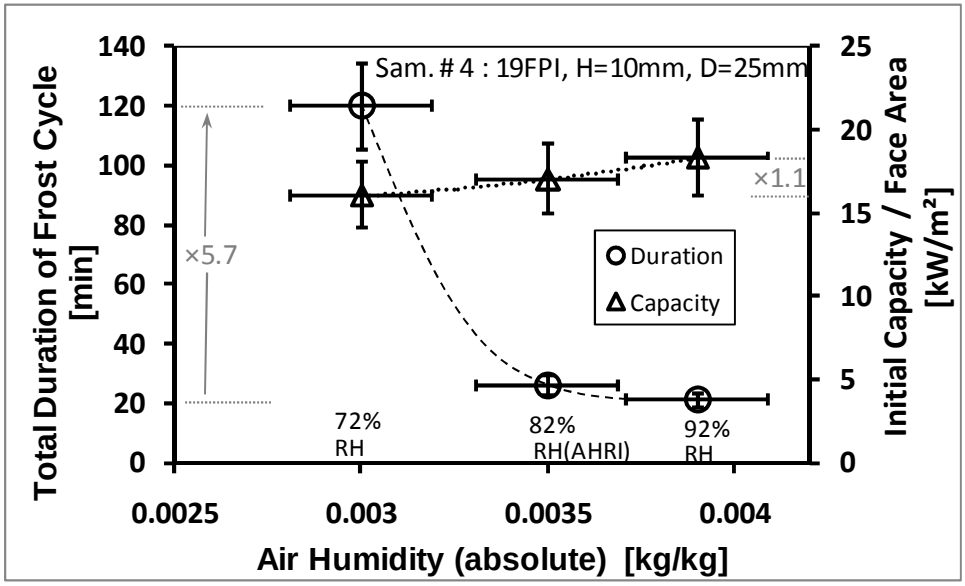

Figure 55: Effect of Air Humidity on frost time and capacity of microchannel samples (Tsurf= -8°C, Air temperature dry bulb = 1.7°C).

This different dew point temperature make the frost deposition rate very slow in the 72% case since only the surface temperature at the fin base is being kept at a constant temperature of -8°C. Once frost deposition starts, the frost surface temperature is certainly above -8°C and increases with the augmentation of the frost thickness. Therefore in the case of 72% air relative humidity with -2.8ºC dew point temperature, after two hours of frost deposition and a thick layer of frost on the fins, the frost surface temperature could get closer to -2.8ºC. This explains why the frost deposition rate slows down or almost stops at 72% relative humidity case. In other words, the difference between real frost surface temperature and dew point of the air is smallest in the case of 72% relative humidity and this reduced the driving force for continuous frost growth.

The total capacity however does not seem to be influenced significantly by a change in air humidity level. This was due to the fact that the magnitude of the latent component of heat transfer was about one third the sensible component of heat transfer.

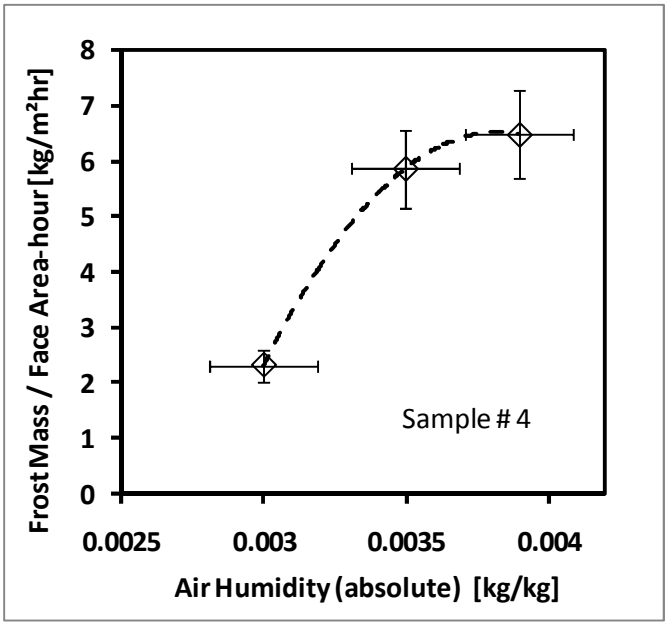

Figure 56: Effect of Air Humidity on frost mass accumulated on microchannel samples (Tsurf= -8°C, Air temperature dry bulb = 1.7°C).

Since changes in air humidity only affect the latent heat transfer, this did not influence the total heat transfer significantly.

The effect of air humidity on frost mass accumulation is shown in Figure 56. The lower humidity level deposits considerably lower mass of frost on the coil. This was due to lower moisture content of the air and the close proximity of the air dew point temperature to the frost surface temperature. Needless to mention, air humidity is an environmental parameter and it is set by standard requirements for testing performance rating of heat pump systems.

The effect of air velocity on frosting behaviour of microchannel fins was investigated using sample 4 with medium width (10mm) and medium depth (25mm). The data are shown in Figure 57. Three initial velocity of 0.8, 1.2 and 1.6m/s (157, 236, and 315 fpm) were investigated. As frost continued to deposit on the fin surface, air velocity reduced gradually until it reached 30% of initial air flow rate, which was the termination point of the frost cycle.

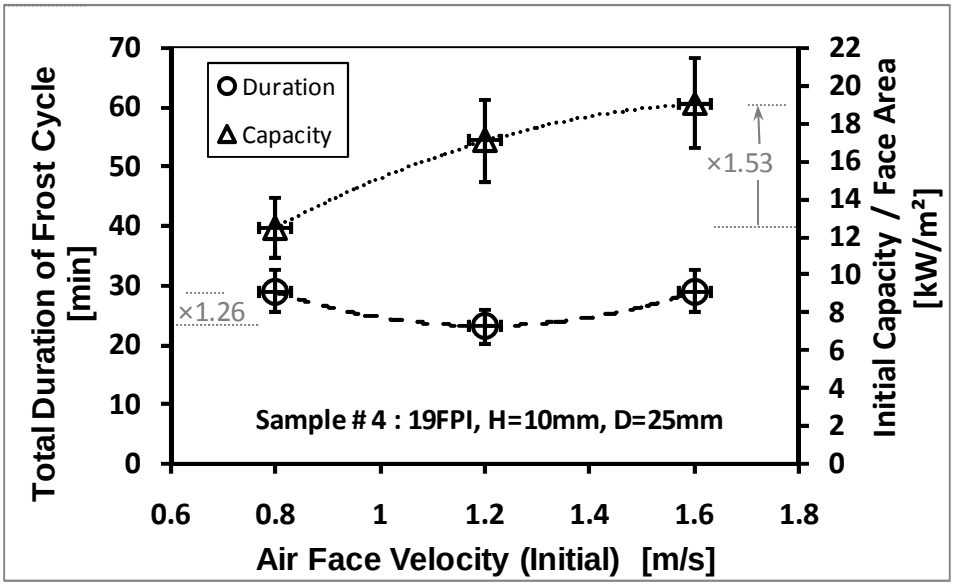

Figure 57: Effect of Air Velocity on frost time and capacity of microchannel samples (Tsurf= -8°C, air temperature=1.7°C/0.6°C db/wb).

Changing the velocity had a smaller effect on the time of the frost cycle than indicated since part of the 26% difference in the total duration of the frost cycle shown in the Figure 57 could be due to the uncertainty in measurements. However velocity seems to have a distinct effect on the capacity of the samples. The air velocity of 1.6 m/s shows 53% more initial capacity in comparison to 0.8 m/s while maintains the same frosting time.

The effect of air face velocity on frost mass deposition rate is shown in Figure 58. The higher air velocity results in 58% higher frost mass deposition per hour. Increasing the air face velocity increases capacity while increased the frost accumulation rate on the microchannel coil. Comparing the1.6 m/s air face velocity data to the 1.2 m/s data in Figure 57 and Figure 58 show that the 1.6 m/s test has 12% more capacity and 9% more frost mass deposition compared to the 1.2m/s test. Thus an increase in air face velocity increases both the capacity and the frost mass deposition rate of the coil.

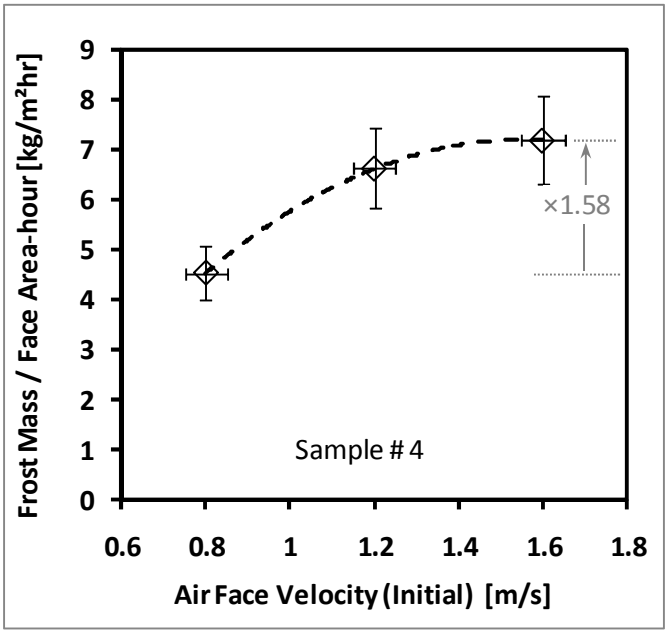

Figure 58: Effect of Air Velocity on frost mass accumulated on microchannel samples (Tsurf= -8°C, air temperature=1.7°C/0.6°C db/wb).

7.5 SURFACE COATING EFFECTS

To investigate the water retention characteristics of microchannel sample and understand the influence of remaining water droplets from previous defrost cycles on the coils, an uncoated sample and 5 different surface coatings with different contact angles were tested in the present study. 5 consecutive frost and defrost cycles were performed sample 7 (uncoated) to sample 12. Coatings include hydrophobic no 1 with Contact Angle (CA) from 95 to 105° for sample 8, medium hydrophilic no 2 CA from 70 to 80° for sample 9, Hydrophilic coating no 3 CA from 8 to 12° for sample 10, a type of hydrophobic coating no 4 with CA from 95 to 105° for sample 11 and a final medium hydrophobic with CA from 80 to 90° for sample 12. Sample 7 was untreated (uncoated) sample and the surface was a bare Aluminum with contact angle of about 80 to 90°.

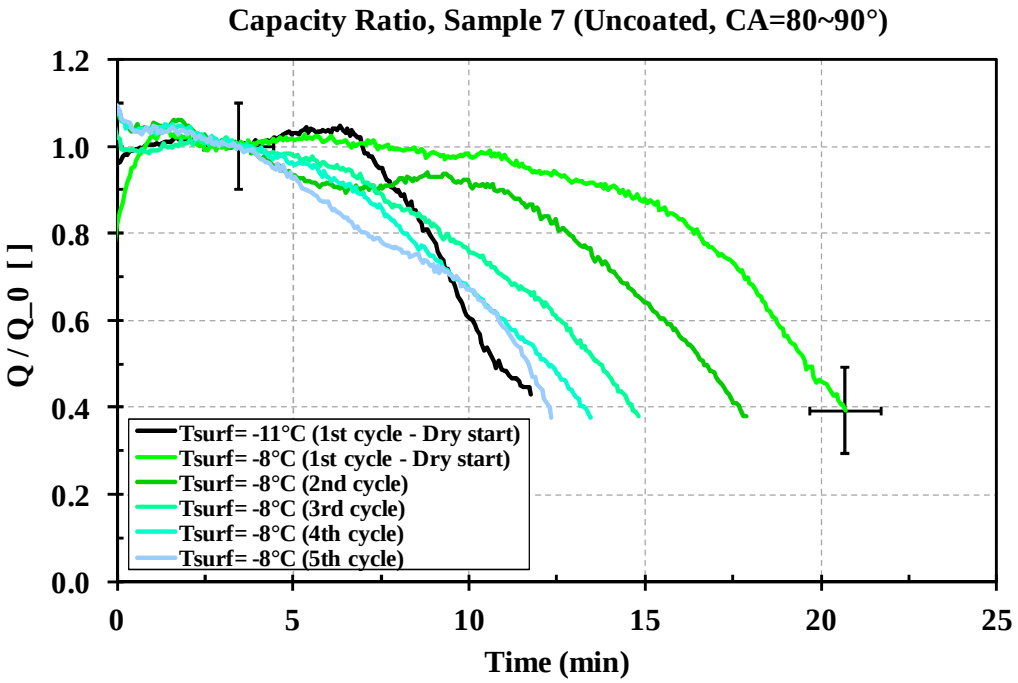

Figure 59: Experimental data of Capacity degradation for uncoated microchannel sample 7 during five consequent frost/defrost tests. The Q_0 for the surface temperature of -8 and -11°C is 22.5 and 27.6W respectively (capacity per face area: 18.8 and 23.0 kW/m^2). Air temperature = 1.7°C/0.6°C db/wb

The results of extreme hydrophilic coating sample 10 and extreme hydrophobic sample 11 are shown, discussed and compared in this section. The rest of the data showed a similar behavior and fell in between these two extreme cases presented in Appendix E. Figure 59 shows the capacity reduction in 5 consequent frost and defrost cycle performed on sample 7. Surface temperature and number of the cycle are given in the Figure 59.

For each cycle, normalized capacity starts at about 1 at the beginning of the cycle and deteriorates as frost accumulates on the surface of the coil. Data shows that the first dry-start cycle takes about 21 minutes (20':42sec) and the 5th frost cycle takes around 12 minutes (12':21sec). There is also a curve of a dry-start test at -11°C surface temperature that has been included in the figure to provide an order of magnitude of the effect of water retention in comparison with the effect of surface temperature.

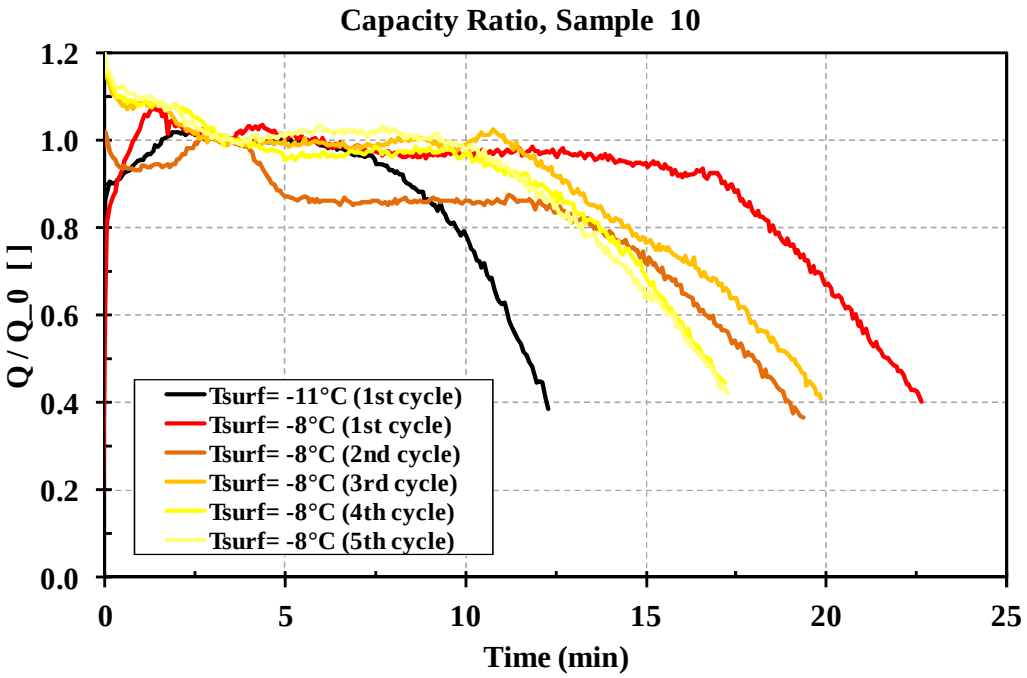

Figure 60: Effect of Hydrophilic Surface Coating (CA=8 to 12°) on capacity degradation of 5 consequent frost cycles for microchannel sample (Air temperature=1.7°C/0.6°C db/wb). Q_0 is 20.5 W (17.1 kW/m^2) for Tsurf= -8 °C and 28.4 W (23.7 kW/m^2) for Tsurf= -11°C.

As it is shown in the figure, the presence and remaining of frozen water droplets on the coil from the previous frost cycle cause the 5th cycle time to be similar to the time of a frost cycle which has 3 degrees Celsius lower surface temperature in dry start condition. The effect of hydrophilic coating (CA=8 to 12°) on the frosting behavior of microchannel is shown in Figure 60. The first frost cycle took 22':36sec and the 5th frost cycle took 17':16sec.

The effect of hydrophilic coating (CA=8 to 12°) on the frosting behavior of microchannel is shown in Figure 60. The first frost cycle takes 22':36sec and the 5th frost cycle takes 17':16sec.

Data shows that the reduction in time of the cycle for this hydrophilic sample is not as severe as the uncoated sample and this coating can maintain high capacity at the 5th cycle longer than sample 7. Image analysis that was presented in Figure 44 showed that this coating does not have many water droplets remaining on the coil from the previous frost cycles.

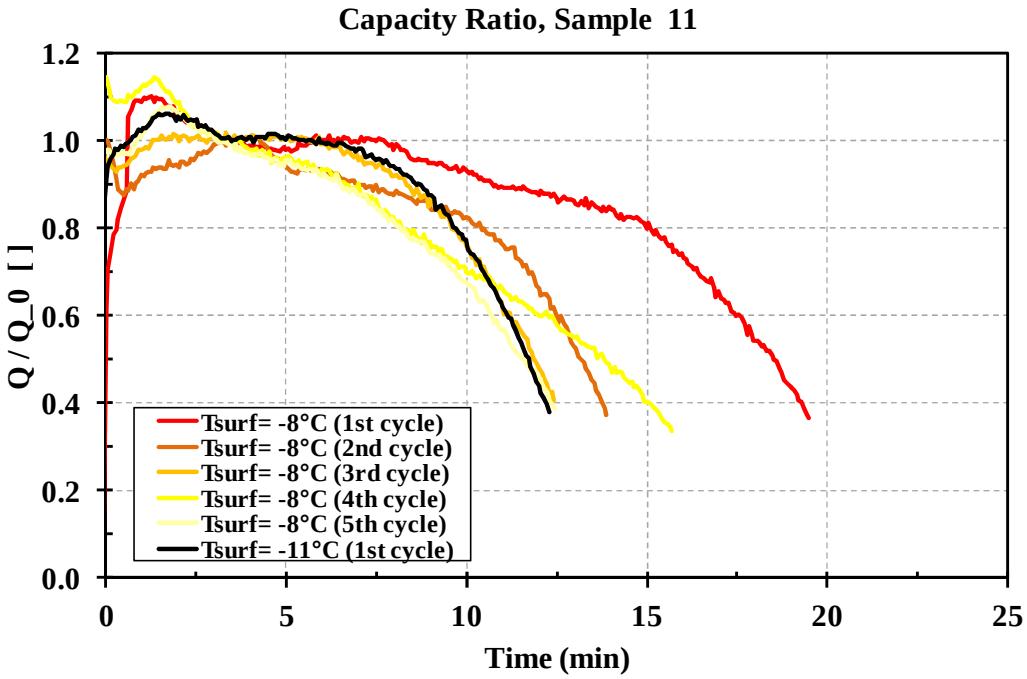

Figure 61: Effect of Hydrophobic Surface Coating (CA=95 to 105°) on capacity degradation of 5 consequent frost cycles for microchannel sample (Air temperature=1.7°C/0.6°C db/wb). Q_0 is 22.2 W (18.5 kW/m^2) for Tsurf= -8 °C and 28.8 W (24.0 kW/m^2) for Tsurf= -11°C.

This was attributed to good drainage characteristics of this coating and high tendency of water droplets to spread on the surface and drain. Therefore low contact angle has the advantage of draining the water droplets and this delayed the air flow blockage on the sample. Data also shows that after 5 frost/defrost cycle the time of the cycle is still quite longer than the dry-start test at -11°C surface temperature by using this same.

The effect of hydrophobic coating on frost / defrost performance of the microchannel sample is shown on Figure 61. The first frost cycle took 19':30sec and the last cycle took 12':27sec. There is a large reduction in time of the cycle especially after the first cycle. This was due to the fact that water droplets remained on the coil and did not drain well after first defrost cycle according to pictures taken from this coil.

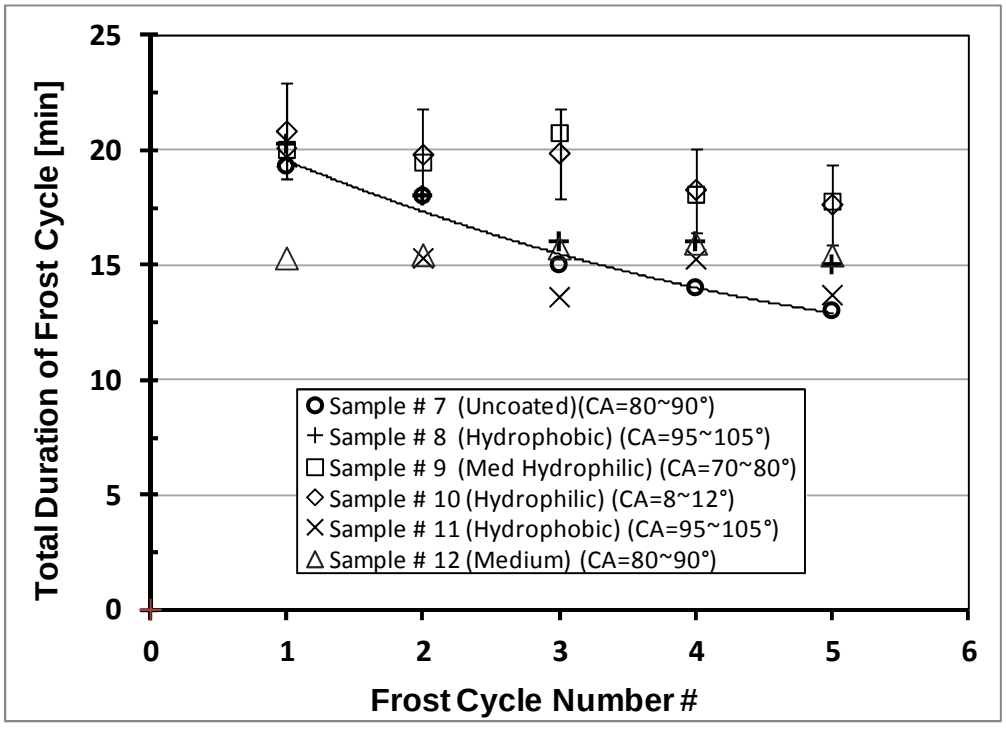

Figure 62: Effect of Surface Coating on duration of frost cycle for microchannel samples 7 through 12 (Tsurf= -8°C, air temperature=1.7°C/0.6°C db/wb).

The uncoated coil timing looks more similar to hydrophobic behavior than hydrophilic. In general, data shows that hydrophilic coil has a better drainage characteristics and longer frost cycles before the capacity drops to a certain minimum value and might be preferred in frosting behavior of microchannels. More comparison of time and capacity of the 5 different coatings is presented in Figure 62.

Sample 7, uncoated sample has been shown with circles and a solid curve fit line that shows baseline data. Data shows that there is no significant difference in time of the frost cycle for the first frost cycle. However as the frost and defrost continues, the hydrophilic samples (10 and 9) appears higher than the other samples. Even when considering uncertainty in measuring the time of the frost cycles, data shows that hydrophilic samples maintains higher frost times in comparison to hydrophobic and uncoated samples. This is attributed to good drainage characteristics of hydrophilic coated samples that prevent formation of individual large water droplets after each defrost cycle.

Each frost test on each sample was repeated several times and all the times of frost cycles presented in Figure 62 are averages. So the data in this figure might be slightly different with individual trends of Figure 61 and Figure 60.

Sample 12 showed a strange behavior that had a very short time in the first cycle and maintains this short time after 5 frost cycles. Although the coating of this sample was close to hydrophobic, the fact that water drains well in this sample was surprising. The type of coatings used for different samples were studied more in detail and it was revealed that had a different process of treatment and cure during manufacturing and no sealer was used during manufacturing to form a layer on the surface of this particular sample.

The duration of the frost cycle was investigated in detail for hydrophilic and hydrophobic samples. The capacity comparison is necessary to be able to judge about the frosting performance

of each surface coating characteristics. The detail effect of coating on capacity of microchannels for 5 frost and defrost cycles is shown in Figure 63. Sample number and cycle number are shown on the horizontal axis while the initial capacity is plotted on vertical axes. Sample 7 in the first frost cycle starts with 22.5W (18.8 kW/m2) capacity and it lasts 19 minutes as shown in Figure 62. The second cycle of sample 7 started with around 21W (17.5kW/m2) capacity and took about 18 minutes. The uncertainty for the capacity measurement is shown on the Figure 63 and this suggests that the fluctuations of the capacity measurements from one cycle to another should not be interpreted as improvements or deteriorations. However the general trends could be discussed, which suggest that the capacity decrease for wet starts in the most of the cases. The data in Figure 63 shows the averaged capacity of each test that has been repeated at least two times in different days to ensure repeatability of the experimental data. The fluctuations of the capacity from one cycle to another are due to uncertainty of the measurements.

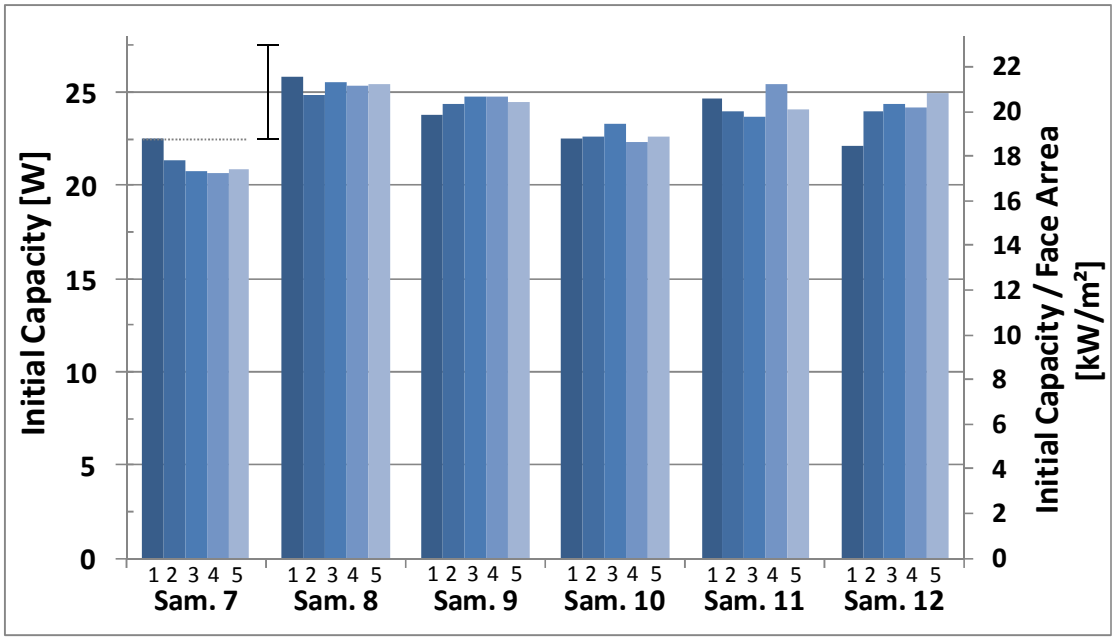

Figure 63: Effect of Surface Coating on initial capacity of each frost cycle for microchannel samples (Tsurf= -8°C, air temperature=1.7°C/0.6°C db/wb). 5 frost cycles are shown for different samples with cycle number on x axis above each sample number. The uncertainty bar applies to all columns.

There are two other minor reasons, apart from uncertainty, that prevents a monotonic decreasing of the capacity in next consequent frost cycles as one might expect. One is the fluctuation of initial capacity at the first minutes of the beginning of each frost test.

Because during the defrost cycle air flow was turned off on the heat exchanger (similar to real heat pump application), air around the device and air in the tunnel was at slightly higher temperatures. When frost cycle starts again, it took 2 to 3 minutes until another quasi steady state is reached again and sample and air temperature come back to stable conditions again. Although we applied improved procedure such as pre cooling of the sample prior to start of air flow stream and other averaging techniques to obtain a better estimation of the initial capacity at the beginning of the cycle, the transient effects of heat transfer were very difficult to eliminate completely. After 2 to 3 minutes from the start of the test when a quasi steady state has been achieved, a thin layer of frost had already covered the surface, and the capacity at that moment was less than initial capacity due to coverage of the aluminum surface.

The other reason that prevents the capacity to be monotonically decreasing is the presence of frozen droplets at the beginning of each frost cycle. As the frost and defrost cycle continues, the number of frozen droplets in between the fins of the heat exchanger statistically increase. Then, when air flow starts in the next frost cycles, the local air velocities in the remaining free flow gaps in between the fins increase in comparison to dry start condition due to some flow blockage. This increase in local air velocity increases the heat transfer coefficient and augments the heat transfer locally for a certain period of time. Considering uncertainties and transient effects, data shows that initial capacity of the cycle does not change significantly from a cycle to the next cycle, but what does change is the time of the frost cycle which is affected by presence of frozen droplets. Reduction of the air flow results in quicker deterioration of the capacity.

While the difference between frosting behavior of different coated microchannel coils cannot be explained by their initial capacity difference, there is a distinct difference in the duration of the frost cycles. Figure 62 showed that the hydrophilic coils have a longer frost time than hydrophobic coils. Data on Figure 60 and Figure 61 showed that the capacity of hydrophobic coil drops sooner than hydrophilic coils. Air side pressure drop of hydrophilic and hydrophobic coils are presented in Figure 64 and Figure 65. As time increases and frost occupies the free gaps between fins, air pressure drop across the heat exchanger increases. This pressure drop seems to rise faster for hydrophobic sample rather than hydrophilic sample as data shows in Figure 64 and Figure 65. The hydrophilic sample was less affected by next frost and defrost cycles from pressure drop point and the last cycle pressure drop was more similar to dry start pressure drop in comparison to hydrophobic sample. In hydrophobic sample air pressure drop curves showed significant changes when next frost cycles occurred.

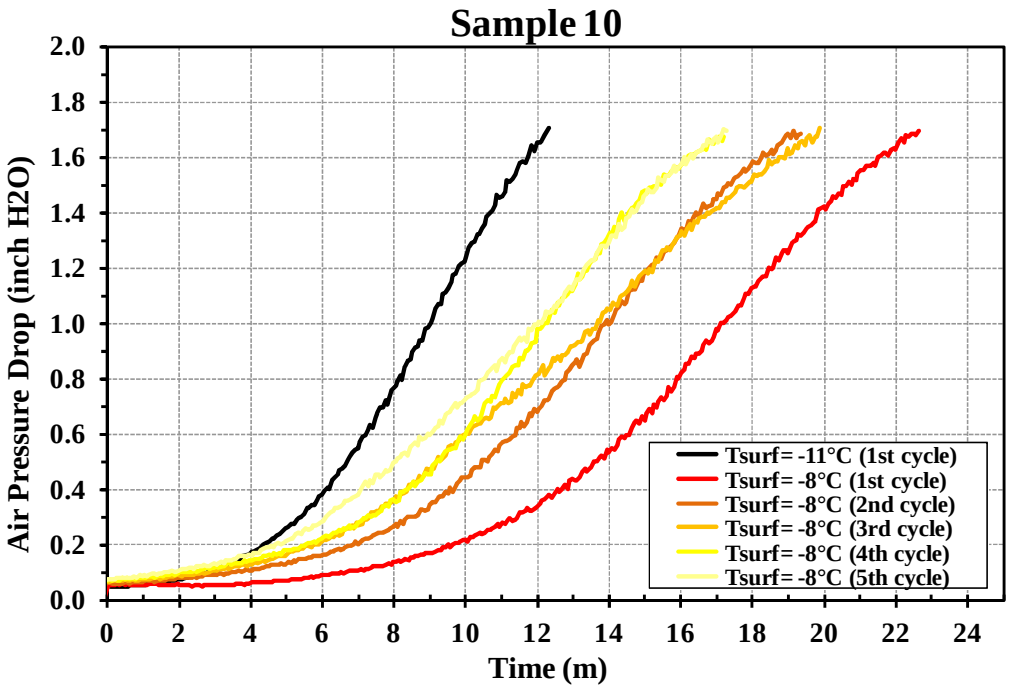

Figure 64: Effect of Hydrophilic Surface Coating on air side pressure drop of 5 consequent frost cycles for microchannel sample (Tsurf= -8°C, air temperature=1.7°C/0.6°C db/wb).

The images taken during the test showed that the number of frozen droplets in the fins of the hydrophobic coil is more than hydrophilic coil as shown in Figure 66 and this supports the hypothesis that the remaining frozen droplets in coil might be the main reason of increasing pressure drop quicker in hydrophobic coated coils.

The frozen droplets that have occupied some fin spacing of the hydrophobic coil, lead to higher pressure drop from the first moment of the test as it can be seen in the first 2 minutes of the hydrophobic coil in Figure 65. The initial pressure drop of cycle 4 and 5 in this figure is higher than the pressure drop of dry start condition while data in Figure 64, hydrophilic coil shows no difference between initial pressure drop of first and 5th cycle. In other words, frozen droplets help the increase in air pressure drop to occur sooner by blocking some parts of the fin from the beginning. The sudden change of slope in the pressure drop curves for cycle 4 and 5 are responses due to fluctuation of air humidity control.

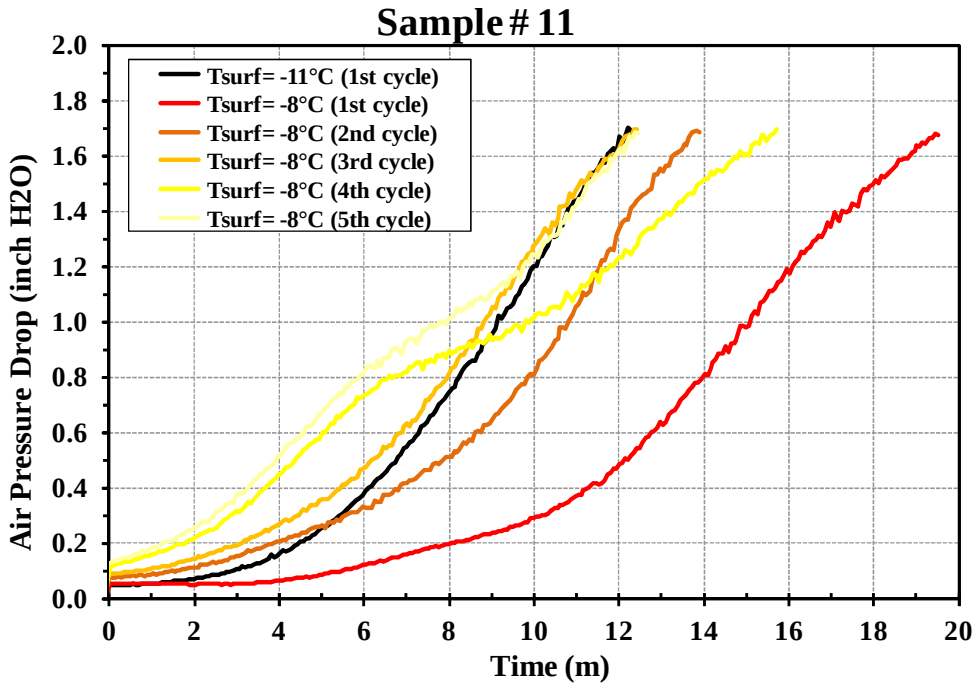

Figure 65: Effect of Hydrophobic Surface Coating on air side pressure drop of 5 consequent frost cycles for microchannel sample (Tsurf= -8°C, air temperature=1.7°C/0.6°C db/wb).

Although a good control strategy was used to keep the air humidity in the AHRI acceptable range, some occasional conditions in 4th and 5th frost cycle sometimes made the humidity falls slightly below the limit. This small decrease in the values of humidity level during the 4th and 5th cycle yielded to a delay in pressure drop increase in Figure 65.

In fact if the humidity was not reduced below the set points the curves for cycle 4 and 5 were expected to rise even faster than what appear in Figure 65. This was a limitation of the present facility to frost/defrost/ and refrost tests.

Figure 66 compares the hydrophilic sample 10 vs hydrophobic sample 11 at the end of the 4^{th} defrost cycle and in the beginning of the 5^{th} frost cycle. As images show, after the 4^{th} defrost cycle, there were no water droplets remained in the hydrophilic coated coil, while there are two small droplets and one large droplet that remained on hydrophobic coil. These droplets turned into ice beads as soon as frost cycle started. One of the water droplets was so large that it has completely blocked one row of the fins. This observation is consistent with air pressure drop data in Figure 64 and Figure 65.

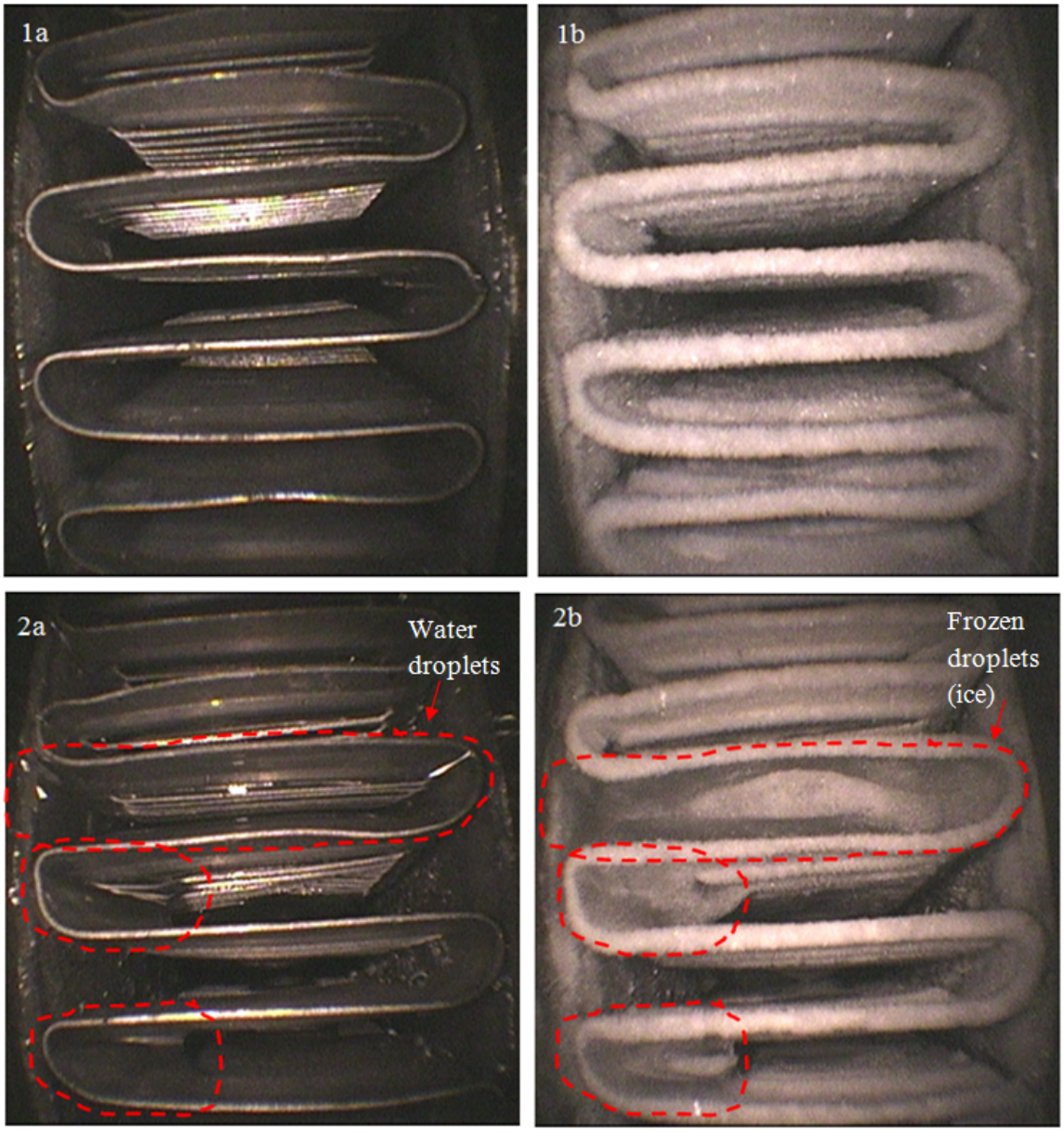

Figure 66: No visible water droplets are present at the end of 4th defrost cycle on hydrophilic sample 10 (figure 1a and 1b). However, visible water droplets stay still on the coil at the end of 4th defrost cycle on hydrophobic sample 11 and turns into ice beads after beginning of 5th frost cycle (figure 2a and 2b). (Tsurf= -8°C, air temperature=1.7°C/0.6°C db/wb).

The air side pressure drop increase is the main reason for dropping of the air face velocity during the frost cycle which resulted in reducing the air mass flow rate. This reduction is the main cause of the capacity degradation. The air face velocity data during the frost and defrost test of hydrophilic sample 10 are shown in Figure 67. Air face velocity starts at 1.5m/s at the beginning of the test and decreases as frost test progresses. Comparison of Figure 67 with pressure drop of Figure 64 shows that after minute 6 air pressure drop starts to rise quickly, and the air face velocity starts to decrease sharply as well. The increase in pressure drop causes the air flow to decrease and this reduces the capacity of the sample. The velocity data for hydrophobic sample 11 are shown in Figure 68. A comparison between pressure drop of Figure 65 and air face velocity of Figure 68 shows that as soon as pressure drop for cycles 4 and 5 of the hydrophobic sample rises after minute 2, the air face velocity starts to decrease considerably after this time in spite of hydrophilic sample at minute 2. Thus the air face velocity reduction was a result of increase in the air pressure drop. The pressure drop itself is a function of geometry change which depends on frost growth and the presence of ice beads. The hydrophilic coating in the present study showed was able to eliminate the existence of individual water droplets and provide a better drainage for the microchannel sample coil. This increased time of the cycle to some degree and prevented early blockage of the air flow.

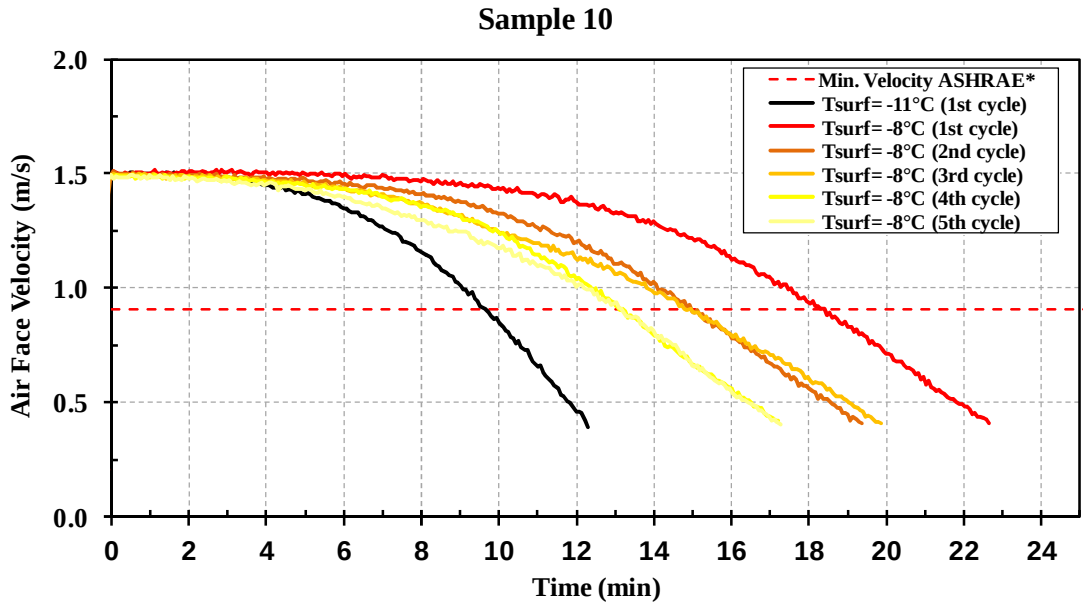

Figure 67: Effect of Hydrophilic Surface Coating on air side face velocity degradation of 5 consequent frost cycles for microchannel sample (Tsurf= -8°C,air temperature=1.7°C/0.6°C db/wb). * or dashed lined represents the minimum velocity for standard flow measurements with nozzle according to ASHRAE standard 41.2.

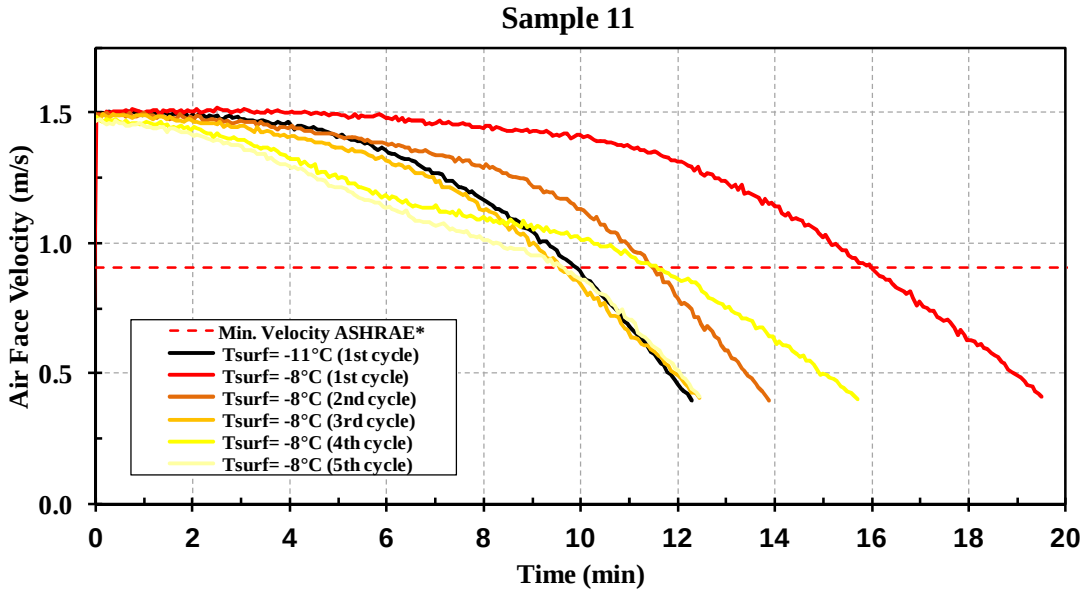

Figure 68: Effect of Hydrophobic Surface Coating on air side face velocity degradation of 5 consequent frost cycles for microchannel sample (Tsurf= -8°C, air temperature=1.7°C/0.6°C db/wb). * or dashed lined represents the minimum velocity for standard flow measurements with nozzle according to ASHRAE standard 41.2.

7.6 FROST MASS ANALYSIS

The frost mass accumulated on the microchannel coil is important since it defines the total energy required for a defrost cycle and maybe a useful parameter to estimate the optimum duration of a defrost cycle. The mass of frost accumulated on the surface depends on the duration of the frost cycle, surface temperature, geometry of the sample and the air humidity and velocity. Since different frost times result in different frost mass accumulation, frost mass should be normalized with time (i.e. kg per hour) to facilitate comparing different working surface temperatures and geometries. Also the effect of frost mass accumulation on the microchannels cannot be evaluated without considering the coil capacity. A very low capacity sample obviously has a relatively lower frost mass accumulation during its operation. That is the main reason the frost mass accumulated on microchannels were presented in previous sections along with the analysis of the time and capacity of the samples working under different surface temperature or geometry. Similar discussion is valid for frost/defrost/ and refrost tests. However, the mass of frost accumulated in multiple cycles was not measured. For results of direct measurement of frost mass on each sample please see Appendix A.

7.7 FROST THICKNESS, AIR PRESSURE DROP AND AIR FLOW CHARACTERIZATION ANALYSIS

When frost starts to deposit on the heat exchanger surface, it appears as a porous white layer that increases in thickness as shown in Figure 42 and Figure 43. The presence of the frost layer changes the geometry of the heat exchanger and the air flow pattern at each instant of the test. Ultimately frost fills the free area between adjacent fins and blocks the air flow. During the frosting process, the air pressure drop continuously increases. As shown in Figure 42 and Figure 43, the frost thickness at the leading edge of microchannel fins is relatively uniform and can be used to estimate the average thickness of the fins at discrete intervals during the frost tests.

To investigate this effect in detail, the thickness of the frost layer on fin leading edge of the heat exchanger has been measured using the images for all the instants during the frost tests. The procedure of frost thickness measurement was described in detail in Figure 33. Figure 69 shows frost thickness measurements on sample 6 for the different surface temperatures plotted in dimensionless form.

The dimensionless frost thickness, δ_f, is defined as follows:

$$\delta = \frac{t}{(Ch_h/2)} \tag{18}$$

where t is the frost thickness at the fin leading edge and Ch_h is the nominal space between two adjacent fins (fin spacing minus the fin thickness) as shown in Figure 76. δ is unity when the free flow area between two adjacent fins is completely blocked by frost. As Figure 69 shows, the frost thickness starts from 0 at the beginning of the test and nearly reaches 1 at the end of the test when the air flow passage is nearly blocked by frost.

The lower the surface temperature, the quicker frost blocks the free area between two adjacent fins. This time is about 12 minutes when the surface temperature is -11°C while it is around 38 minutes

for surface temperature of -5°C. At the end of the test, frost has nearly blocked the area between the fins and the air pressure drop across the sample has risen considerably as shown in Figure 70. Air pressure drop starts from 0.12 inch of water when no frost was on the coil and rose to 1.85 inch of water at the end of the test, an increase of fifteen times. Visual observations of the coil in Figure 43 also confirms this frost blockage effect and supports such an increase in air pressure drop through the heat exchanger toward the end of the test period.

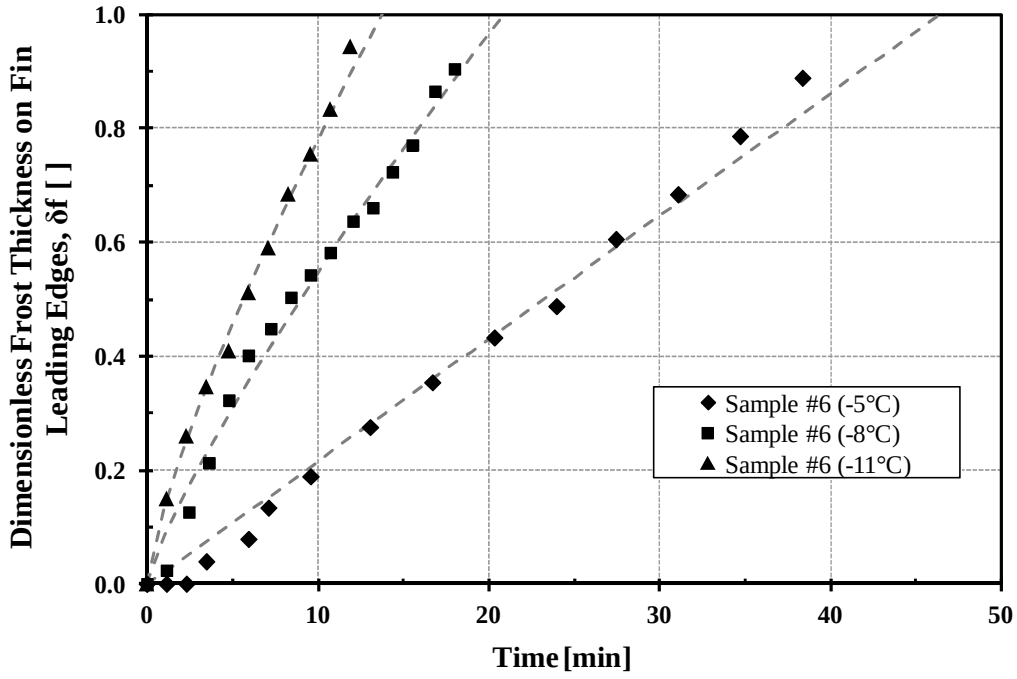

Figure 69: Frost thickness growth on microchannel sample 6 for different temperatures. Similar results were observed for other samples that are shown in Appendix B and C.

The rate at which the pressure drop becomes larger, as shown in Figure 70, depends heavily on the surface temperature, which determines the rate of frost growth (see Figure 69). The increase in pressure drop during the frost test affects the air face velocity and the air mass flow rate as shown in Figure 71. As the pressure drop across the sample gradually becomes larger, the air face

velocity on the coil starts to decrease. The air pressure drop across the sample increases slowly at the beginning of the test. However it accelerates toward the end of the test when the frost thickness becomes large enough to nearly block the entire area. Consequently, the air velocity decreases slowly at the beginning of the test and accelerates toward the end of the test.

The red dashed line in the Figure 71 shows the minimum velocity that can be measured with our test setup according to guidelines in ASHRAE Standard 41.2.

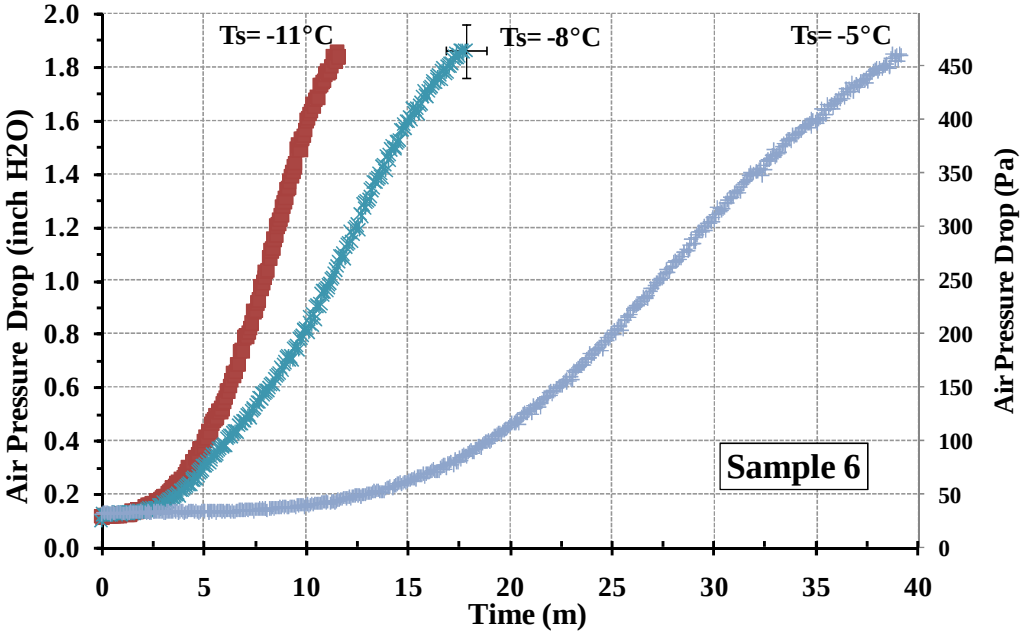

Figure 70: Pressure drop increase during a frost test for various surface temperatures for microchannel sample 6. Similar results were observed for other samples that are shown in Appendix D.

The nozzle used in the present study was one of the smallest available, but when the air flow drops to below 2 CFM (0.00094 m^3/s), and the measurement did not meet the guidelines of the ASHRAE standard. Extrapolation is possible given that the trends are smooth, but caution should be used

when considering the velocity measurements below the dashed horizontal line referred to as "Min. Velocity ASHRAE" in Figure 71.

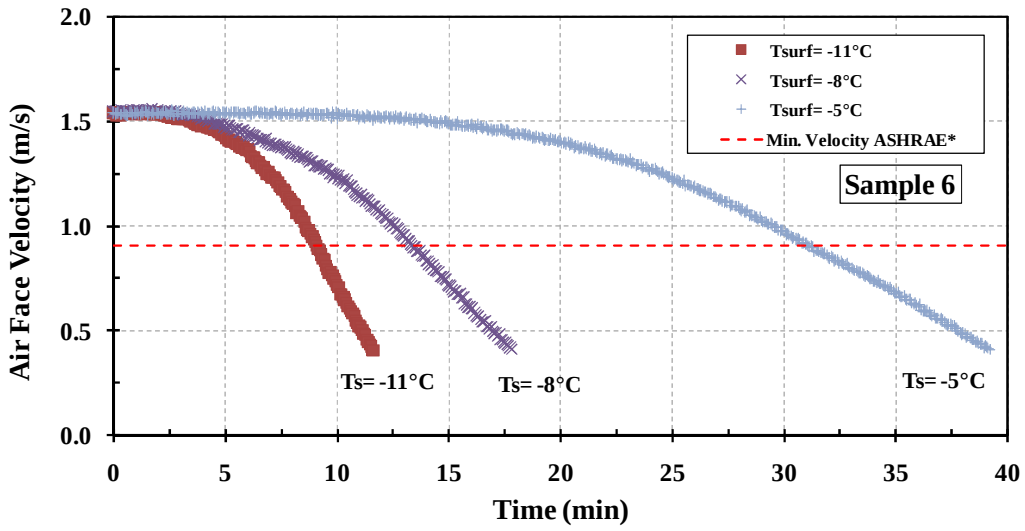

Figure 71: Air face velocity drop during the frost tests for microchannel Sample 6 with different surface temperatures. Similar results were observed for other samples. * or dashed lined represents the minimum velocity for standard flow measurements with nozzle according to ASHRAE standard 41.2.

7.8 CAPACITY DEGRADATION ANALYSIS

The increase in pressure drop due to frosting affects the air flow rate and reduces air face velocity continuously. The capacity drops with the air flow rate as shown in Figure 72. The change in air flow rate impacts the capacity of the heat exchanger according to the following expression: $\mathrm{Q} = \dot{\mathrm{m}}_{\mathrm{air}} \mathrm{c}_{\mathrm{p,air}} \left(\mathrm{T}_{\mathrm{air,ent.}} - \mathrm{T}_{\mathrm{air,exit}} \right) + \dot{\mathrm{m}}_{\mathrm{air}} h_{abl.} (\omega_{ent.} - \omega_{exit})$. In above equation, ent. represents entering and $h_{abl.}$ is the enthalpy of ablimation of water vapor into solid state on the surface. The data on Figure 72 shows the capacity degradation on the microchannel sample, which has similarity to the air face velocity curves (the same as air mass flow rate with a constant coefficient difference) in Figure 71. Data is presented using normalized capacity. This quantity is 1 at the beginning of the test and starts to drop as the frost test continues. It typically reduces to 30% of the initial capacity by the end of the test. The values of initial capacity may vary based on the surface temperature and geometry of the coil. In the microchannel sample presented in Figure 72 the initial capacities for surface temperatures of -5, -8 and -11°C were 19.5W, 30.6W and 39.0W. Comparison of the data in Figure 71 and Figure 72 shows that when the air flow rate drops to around 30% of its initial air face velocity, the capacity reduces to 30% of its initial value. This trend was observed also in the data of other microchannel samples. For other samples such as sample 1 with low fin density, the capacity was maintained for a much longer time before it dropped to very low values. This might suggests that air flow reduction has a direct influence on capacity degradation and any future attempt to delay the air flow reduction, might result in a delay for capacity degradation.

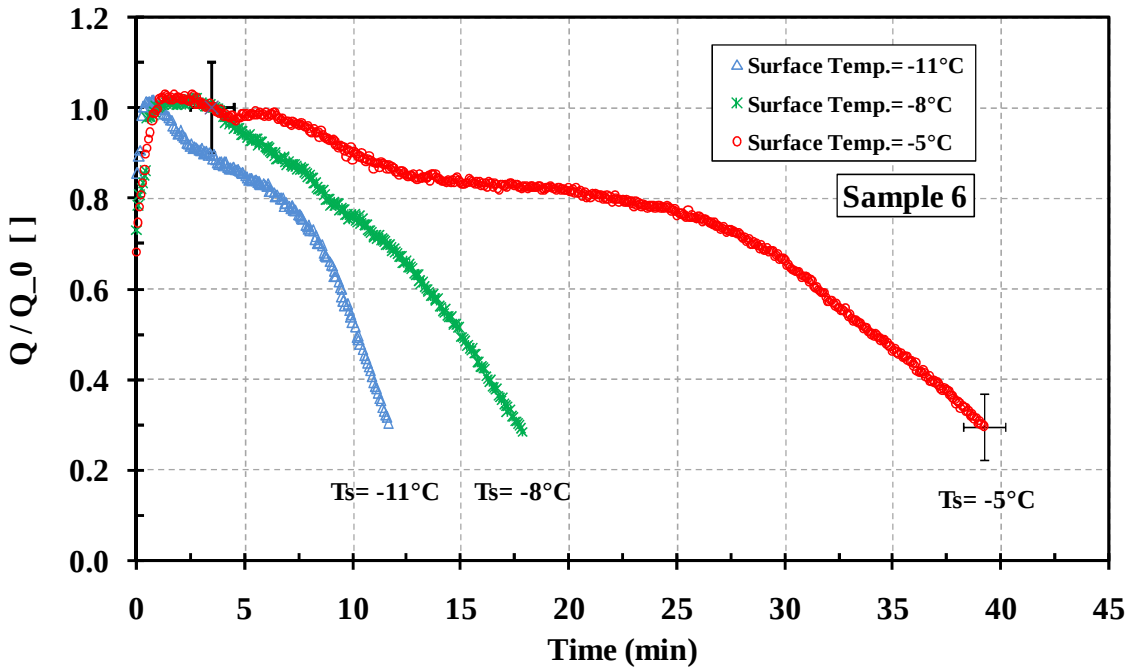

Figure 72: Capacity degradation during the frost tests for microchannel Sample 6 with different surface temperatures. The Q_0 for Temperature -5, -8 and -11°C is 19.5, 30.6 and 39.0W respectively (capacity per face area: 16.3, 25.5 and 32.5 kW/m^2). Similar results were observed for other samples that are shown in Appendix E.

7.9 HEAT TRANSFER COEFFICIENT CALCULATION

Based on air side heat transfer data, the heat transfer coefficients for the sample was calculated and plotted for the entire period of frosting test. The data is also presented in Colburn J-factor format for all the samples and are shown in Appendix F. The data of dry condition steady state heat transfer coefficient and Colburn J-factor was obtained extensively in the literature for different geometries of microchannels. As mentioned before in "Literature Review" chapter there are only a few studies that measured and presented the j-factor during the frost tests on microchannel geometry for a limited number of geometries. Also their j-factor was presented as a function of frost thickness or other unknown variables that required a model to be predicted. Moreover j-factors were obtained for one single surface temperature condition. As the air temperature or surface temperature changes, the frost deposition rate on each microchannel changes. This different frost deposition rates result in air flow blockage and fin free flow area geometry variation. Thus the heat transfer coefficient or j-factor deteriorates with different rates at different surface temperatures and different frost deposition rates. In the present study, heat transfer coefficients of 7 different geometries during their frost test each with three different surface temperatures were carefully measured and their j-factors are presented. In this section only one of the samples is going to be discussed in detail. The same discussion applies to the other samples that have similar trends which are shown in Appendix F. Needless to say the heat transfer coefficient only gives the value of sensible heat transfer on the microchannel sample. To obtain the total capacity of a microchannel sample under frosting condition, one has to know both the sensible and latent component of heat transfer and add them up together which is the same approach in the present study. If the latent component of heat transfer cannot be obtained via direct measurements, it then should be calculated via mass transfer coefficient. The mass transfer coefficient measurements and calculation have not been considered in the scope of the present work. Future studies are necessary to find the mass transfer coefficients on microchannel

samples. Experimental data of the present study showed that the ratio of latent magnitude of heat transfer to sensible magnitude of heat transfer varied between 20% to 25% for -5°C surface temperature test and varied between 25% to 30% for -8 and -11°C surface temperatures.

Overall data of air side heat transfer coefficient for sample 6 under frosting condition are shown on Figure 73. The dry steady state heat transfer coefficient has also been measured and shown in the data. The dry heat transfer coefficient was obtained though a long steady state test with no frost, mass or condensation deposition on the heat exchanger surface. Air was at 24°C and sample was kept constantly at 14°C. A difference of 10 degrees centigrade was chosen between air and the surface similar to the case in the frost tests. The dew point of the entering air was very below the surface temperature (around 11°C) to ensure no condensate deposition on the sample. After a long test to reach the steady state for about 2 hours, the value of dry heat transfer coefficient was recorder and plotted. Since the fin (root) surface temperature was known, the equation used for calculating the heat transfer coefficient did not contain any refrigerant side.

$$Q_{air,sensible} = \eta A h_{air} \Delta T_{LM} \tag{19}$$

In which η is the fin efficiency, A is the heat transfer area of the sample fin, h_{air} is the air side heat transfer coefficient and ΔT_{LM} is the logarithmic temperature difference between the surface and the air which is defined as the follows.

$$\Delta T_{LM} = \frac{(T_{air,ent} - T_{surf}) - (T_{air,exit} - T_{surf})}{Ln\left(\frac{(T_{air,ent} - T_{surf})}{(T_{air,exit} - T_{surf})}\right)} \tag{20}$$

The fin efficiency was calculated using the following expression and was considered to be a function of geometry and to be constant during the frost test (consistent with some of previous frost microchannel fin efficiency studies (Davenport, 1983)).

$$\eta = \frac{tanh(mL_p)}{mL_p} \tag{21}$$

Where L_p is fin louver pitch and m is defined as follows.

$$m = \frac{2h_{air}}{k_{fin}t_{fin}} \tag{22}$$

Where h_{air} is air side heat transfer coefficient, k_{fin} is the thermal conductivity of fin material and t_{fin} is the fin thickness. The value obtained for η of each sample 1 to 7 are shown in Table 17. Although η depends on air side heat transfer coefficient, the final value of η changes slightly with the change in h_{air}. Thus the value of η can be calculated by a reasonable approximation of h_{air} and can be corrected once we have the exact value of h_{air}. The differences were very small in all the cases investigated in the present study.

Table 17: fin efficiency and measured dry heat transfer coefficients for samples with different geometries. Samples 7 through 12 had similar geometries.

Sample	η	h_dry [W/m2K]
1	0.97	42
2	0.96	122
3	0.95	103
4	0.94	87
5	0.91	96
6	0.95	115
7	0.95	72

The $Q_{air,sensible}$ in the equation (2) is calculated using the air side heat transfer.

$$Q_{air,sensible} = \dot{m}_{air} c_{p,air} \left(T_{air,ent} - T_{air,exit}\right) \quad (23)$$

Where $\dot{m}_{air}$ is the air mass flow rate and $T_{air,ent}$ and $T_{air,exit}$ are entering and exiting air temperatures respectively and they are measured directly during the test. In this way, all the quantities are known in a frost test and air side heat transfer coefficient h_{air} can be calculate using equation (19).

The procedure of calculation of heat transfer coefficient for the frost tests was the same as the procedure for dry steady state test and the effect of transient change of geometry and frost were all grouped into the air side heat transfer coefficient. Experimental data on Figure 73 shows that the dry heat transfer coefficient for this geometry was around 109 W/m^{2}K. While in the frosting tests, the heat transfer coefficient seems to start from a point below the dry steady state value and decreases afterwards. For the surface temperature of -8°C as an example, the heat transfer coefficient starts from 70 to 75 W/m^{2}K at the beginning of the test. There are some fluctuations in the heat transfer coefficient during the entire test period. The increase in the first few minutes of the test is probably due to transient effect of starting of the air flow after a short period of rest before air gets to a quasi steady state condition at the inlet and outlet of the heat exchanger. Also velocity has not changed significantly from its initial value according to data presented in Figure 71. After the first few minutes, data shows that the heat transfer coefficient decreases gradually which is due to coverage of surface with a thin frost layer.

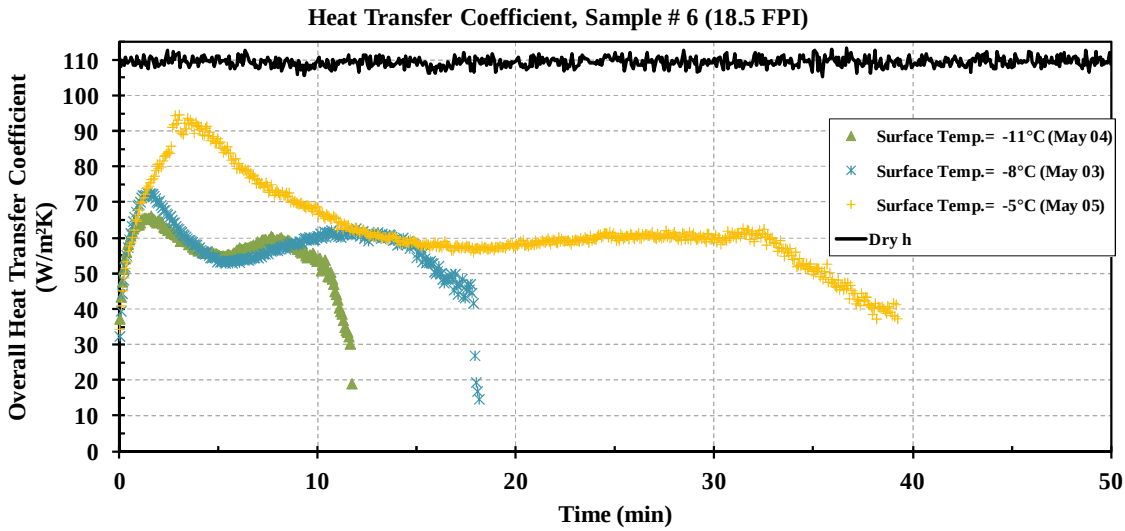

Figure 73: Overall air side heat transfer coefficient in the frost tests for microchannel Sample 6 with different surface temperatures. Similar results were observed for other samples.

At this stage, which takes around 5 minutes for the -8°C and -11°C tests and takes around 15 minutes for the -5°C surface temperature test, the thickness of frost is still a small value according to data presented in Figure 69. Therefore the thin layer of frost prevents the air from direct contact to the aluminium surface and heat transfer coefficient deteriorates as expected. After the thickness continues to grow nearly linear during the test free flow area reduction becomes more significant and this change increases the local velocity in between the fins. The fact that thickness increases almost linearly but velocity has a long delay before it drops, makes a temporarily increase in local air velocities and make a temporary slight increase in heat transfer coefficient. This local increase in heat transfer coefficient is observed between minutes of 5 to 13 for -8°C surface temperature. This temporary improvement of heat transfer cannot continue since the air flow dropped quicker. As a result of the air flow reduction, the amount of heat transfer on the microchannel fins becomes very small and the heat transfer coefficient reduces too.

The trend of changes in heat transfer coefficient as explained depends on various factors. One is the thickness and effective conductivity of the frost layer that forms on the surface. This factor

works to reduce the heat transfer coefficient and its effect can be observed in the beginning of the tests. The second factor is the geometry of the sample itself and free flow area between the fins that shows different reaction to frost growth based on fin density and other geometrical considerations. This reduction in area mostly tends to increase the local heat transfer coefficient because it causes increase in local air velocities between the fins. The other factor is the drop in the air face velocity which is a function of air pressure drop of the coil and it is directly affected by reduction in free air flow area between the fins. This factor is also affected by geometrical parameters such as fin density, tube spacing and other geometrical factors. There are other minor factors as well such as increased surface roughness when frost starts to grow on the flat aluminium surface, blockage of the louvers after first half of the test resulting in a channel flow instead of louver flow. Each of these factors make their own influence on the final heat transfer coefficient and the final value of the heat transfer coefficient follows a complex profile which is the superposition of all these affecting parameters. It is clear that geometry has a very important influence on all of these factors and thus it should not be expected that every geometry has the exact same trend of heat transfer coefficient profile discussed in Figure 73. In fact data shows that samples with different fin density, fin depth and fin width show different trend of fluctuation of heat transfer coefficient at various times of the frost test. The complete set of heat transfer coefficient profiles for all the geometries are shown in Appendix F.

By knowing the heat transfer coefficient, Colburn j-factor can be calculated using following expressions:

$$Nu = \frac{h_{air} L_p}{k_{air,avg}} \tag{24}$$

Where L_p is fin louver pitch k_{air} is the average conductivity of air. Reader should have in mind that in microchannel heat transfer discussion most of the calculation flow dynamics and heat

transfer such Re number and Nu number are defined based on Louver pitch according to findings of the previous studies.

$$Re_{Lp} = \frac{\rho_{air,avg} V_{air,face} L_p}{\mu_{air,avg}} \quad (25)$$

$$St = \frac{Nu}{Re_{Lp} Pr_{air}} \quad (26)$$

In which Pr_{air} is air Prandtl number at average air temperature.

$$j = St\ Pr_{air}^{2/3} \quad (27)$$

In calculating j-factor some points should be clarified. All of the studies in the literature have used the above approach to calculate j-factor for microchannel heat exchangers, but all of the studies focused on the dry steady state heat exchangers. During frost tests, the gaps between adjacent louvers are quickly filled with frost and the geometry changes continuously, which affects the flow characteristics. Using the louver pitch, which remains constant during the entire test for calculating Reynolds number, can hardly be accepted to be representative of flow dynamics which is occurring on microchannels covered with frost. Using the face velocity in calculating Re number was appropriate in previous studies in dry microchannel heat exchanger since the geometry was fixed during the heat transfer process. In frost test however, the face velocity may or may not drop based on the fan working strategy or operating conditions. Thus a constant air face velocity might not be the best choice in calculating j-factor in frosting condition. To be consistent with the previous studies and in order to make comparison possible between the j-factor in the present study and dry j-factors obtained in previous studies on microchannel, our research group decided to take the same common and well-known accepted calculation procedure

for j-factor calculation i.e. with a constant louver pitch and a constant initial air face velocity for the entire frost test. In this way, j-factor would have the same trend as the heat transfer coefficient (h_{air}) for the entire frost test. This would be the easiest way to connect j-factors to the corresponding heat transfer coefficients.

Figure 74 shows the j-factor obtained for microchannel sample 6 under frosting condition. As explained above, the similar trend to heat transfer coefficient is expected for j-factor. The j-factor starts from a higher value at the beginning of the test and starts decreasing toward the end of the test after some fluctuations during the test period. The same discussion about reasons of fluctuations and variations of heat transfer coefficient (h_{air}) applies for the j-facyor.

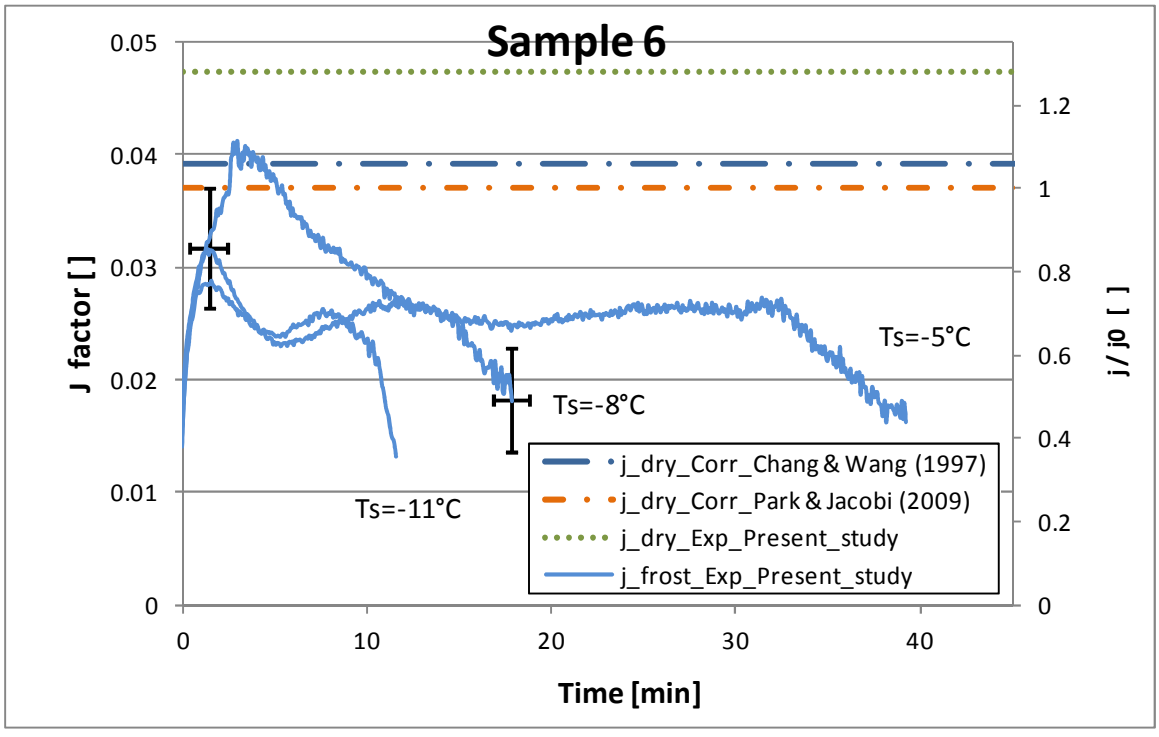

Figure 74: j factor obtained from experimental data during frost test for microchannel Sample 6 with different surface temperatures. Similar results were observed for other samples that are shown in Appendix F.

There are previous studies that obtained the j-factors on microchannel under dry steady state condition with a large bank of microchannel geometries such as Chang and Wang (1997) and Park and Jacobi (2009). These studies developed a j-factor correlation to predict the dry j-factor of microchannel for any desired geometry based on experimental results obtained from their own experiments and other studies. Since a general correlation was aimed to be developed to predict all the data on existing microchannel data bank, the correlation had good predictions for some geometries and relatively weaker predictions for others. Chang and Wang (1997) correlation could predict j-factor of 89% of a bank of experimental data consisting of 91 different samples within an average of ±15%. Park and Jacobi (2009) correlation could predict 83% of a data bank of 126 samples within an average of ±15%[17]. Thus it is clear that their correlation might not agree precisely with experimental data especially if the geometry or air velocity conditions fall into the region of their higher region of uncertainty. As an example, the general correlation of Park and Jacobi (2009) could predict up to 95% of the data within ±25% of error and in occasional cases deviation from correlation up to 45% was observed. Similar situation was true about Chang and Wang (1997) correlation. Bearing this statistical data in mind, it is still useful to compare their predicted dry j-factor correlation with experimental dry j-factor obtained from the present study.

As data on Figure 74 shows, the dry j-factor obtained from the our experimental data has a higher value (0.047) in comparison to Chang and Wang (1997) correlation for dry j-factor (0.039) and Park and Jacobi (2009) correlation for dry j-factor (0.037).

[17] This error shows the actual deviation of experimental j-factor form correlation predicted j-factor. It does not represent rms error or rms residuals. For more detail discussion please see Park and Jacobi (2009).

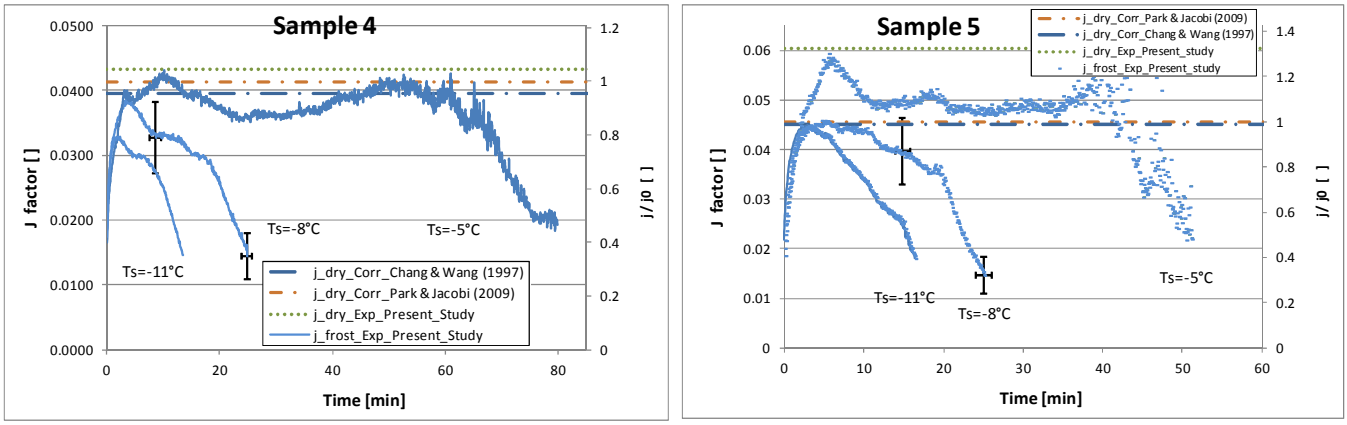

Figure 75: j factor obtained from experimental data during frost test for microchannel Sample 4 and 5 with different surface temperatures. Similar results were observed for other samples that are shown in Appendix F.

The difference between findings of the present experimental dry j-factor and previous dry j-factors correlation was not always very significant as the case for sample 6 in Figure 74. Other samples have different results as shown in Figure 75. The results of entire samples are shown in Appendix F. Another observation in the data presented in Figure 74 and Figure 75 is the dry heat transfer coefficient and j-factor obtained in the present study was most of the times (except sample 1 and 7, see Appendix F) higher than the dry j-factor offered by previous correlations. Other than discussed uncertainty issues associated with the previous correlations and uncertainty of measuring the heat transfer coefficient and j factor in the present study (around 20%). It is worth noting that the heat transfer coefficient at the beginning of the test ($h_{0,air}$) does not seem to be the same for all the surface temperatures and in fact it has a monotonous trend to change from higher values in higher surface temperature and vice versa. In other words, if the rate of frost deposition is slow as the condition in -5°C tests, the $h_{0,air}$ is nearer to the experimental dry $h_{0,air}$. Then in other tests with lower surface temperatures such as -8°C tests or -11°C tests, the $h_{0,air}$ has a lower value in all of the samples. This might be due to the fact that the rate of frost deposition affects the final sensible magnitude of heat transfer so that it makes different $h_{0,air}$ at the beginning of the tests.

CHAPTER VIII

FROST EMPIRICAL CORRELATIONS

8.1 INTRODUCTION

In the present chapter, a new set of frost correlations based on experimental data were obtained in the present study and are going to be introduced and verified against measured data. This correlation is also verified against another set of experimental data on a larger real scale microchannel coils with different microchannel dimensions and surface temperatures. The correlation is also finally verified against the data presented in other previous studies in the literature using a different and independent experimental setup and the results are presented, which were in satisfactory agreement with each other.

8.2 AIR SUPERSATURATION LEVEL, THE DRIVING FORCE FOR FROST DEPOSITION

The frost properties and growth rate depends on parameters such as cold surface temperature, air temperature, air moisture content and other parameters. To develop correlation for frost for frost growth rate, one method is to employ all of these parameters and assign a coefficient and power

to them and then adjust the coefficients or increase the order of polynomial and number of terms until it matches the experimental data. This has been followed by some previous works. The problem with this approach is that these polynomials do not represent the real phenomenon for frost deposition on the cold surface. Although researchers are trying to make non-dimensional temperatures and humidity to make them meaningful quantities, still the usage scope of these curve fits are still limited to the ranges that they are developed and also they do not reflect the physical meaning and theoretical governing forces driving the frost formation mechanism. There have been fundamental frost formation theories in the previous works that their findings and results associated the frost formation rate with vapor pressure of the air and temperature at which frost forms which is basically the surface temperature. In crystallization theory, for the phase transition of the water vapor into ice crystals, air should be in a supersaturation level. Air supersaturation is the driving force for migration of water vapor particles and their deposition on the cold surface which is defined as the following (Na and Webb, 2004a; Sanders, 1974):

$$Fs = S = \frac{P_{air} - P_{surf}}{P_{surf}} \tag{28}$$

Where P_{air} and P_{surf} are water vapor pressure of air at free stream temperature and water vapor pressure of saturated air at local surface temperature respectively. In this study, we call this quantity, which is the driving force for the frost deposition, frost number (Fs) and it can have any positive value greater than 0. When frost number is negative or equal to 0, no frost forms on the surface while on the other hand, the greater than zero this number, the greater the potential force of frost deposition. Then the properties of frost such as thickness will be a function of a few number of non-dimensional parameters that reflect the potential force driving the frost mechanism as well. In this way we will have:

$$\delta = f\left(t_t, T_{surf}, T_{air}, \omega_{air}, Geometry\right) \quad \Rightarrow \quad \delta = f(Fo, Fs, Geometry) \tag{29}$$

In which δ is the frost thickness, t_t is time, T_{surf} and T_{air} are surface and air temperature respectively, ω_{air} is the absolute humidity of air, Fo is Fourier number or non-dimensional time and Fs is frost number. One might argue that in crystallization theory, rate and shape of deposition of ice crystals depend on both supersaturation of water vapor and temperature of formation and these parameters should be separated and enter independently into the correlation. Previous studies revealed that the basic shapes (habit) of formed ice crystals are mainly determined by temperature of formation (Hallett and Mason, 1958; Hanajima, 1949; Kobayashi, 1958; Nakaya, 1954; Shaw and Mason, 1955) while frost rate of growth is controlled by supersaturation of water vapor (Nakaya, 1954). Because in developing correlation to predict thickness, the visual shape of ice crystals are not the main importance while the growth rate and height of the frost layer is the main focus, for the purpose of predicting the thickness of frost, supersaturation level as an independent parameter seems to be sufficient. This showed to be in agreement with the regression of experimental data later and Fs number was enough to predict the growth rate and thickness of the frost versus time for every sample tested in the present study. Thus, for developing correlation for frost thickness air pressure drop and heat transfer coefficients instead of entering all parameters into correlation, the dimensionless groups such as Fs, Re, Fo and geometry will be used.

For geometry parameters, it could be possible to enter all of the geometrical dimensions of the coil into the correlation such as fin pitch, fin length, fin depth, tube pitch, tube thickness, tube depth, louver length, louver height, louver pitch, louver angle and so on. However, instead of making the correlation long and elaborated, it might be a better idea to pick up the minimum number of parameters that could have captured the experimental data points with sufficient accuracy and discard the rest. After a number of tries, we found that the except than a few

discrepancies, three parameters of fin pitch, fin length and fin depth could predict the experimental data within sufficient accuracy. As in case of frost thickness this accuracy was about 0.03mm which was the tolerances of frost thickness measurements. These three parameters are referred to as channel height (Ch_h), channel width (Ch_w) and channel depth (Ch_d) in the present study as shown in Figure 76[18]. Note that (Ch_h) is the average free distance between two fins.

$$\delta = f(Fo, Fs, Geometry) \quad \Rightarrow \quad \delta = f(Fo, Fs, Ch_w, Ch_h, Ch_d) \tag{30}$$

Further attempts to reduce the number of geometrical parameters from three to two parameters such as using hydraulic diameter of the channel instead of height and width of the channel in developing the correlation were not successful.

The sample dimensions were chosen so that at each sample one geometric parameter was changed while the others were kept constant so that it was possible to isolate the effect of that particular parameter on the frost formation behavior. So eventually samples with three different channel height, three different channel width and three different channel depth were tested and the effect of each changing parameter were investigated in developing the new correlation. The other reason than we did not include the louver dimension into this correlation was, we did not have enough variety of samples with different louver dimensions while all the rest of parameters remain unchanged. Finally it was not possible to parametrically isolate the effect of louvers in each set of tests. Although adding more variables such as louver pitch, louver angle, etc. could make the

[18] The term microchannel is assigned to these type compact Aluminum heat exchangers because of the small scale ports that exist inside their tubes. In the present study however, the refrigerant side has not been considered and term "channel" refers to the air passage between two adjacent fins. This convention is made just for convenience to refer to different geometrical aspect of fin geometry and does not have a physical interpretation necessarily. Authors are well aware of the fact that air regime in louver dominated flow is absolutely different from air in the general simple channel flow. The fact that frost blocks only the free flow area between two adjacent fins encouraged the authors to prefer to use channel height (fin spacing minus a fin thickness) instead of fin spacing in non-dimensionalization process that will be introduced later.

regression process easier due to offering more coefficients for tuning, it was somehow statistically inappropriate to enter them into the correlation as one additional single independent variable. Moreover, similarity or predictability of the louver overall geometries relative to width and depth of the fins, plus the fact that the frost thickness was measured at the leading edge and was somehow independent of effect of louvers, encouraged us to keep the louver dimensions out of correlations. Isolate the effect of louvers might be a subject for future studies with more variety of coil samples.

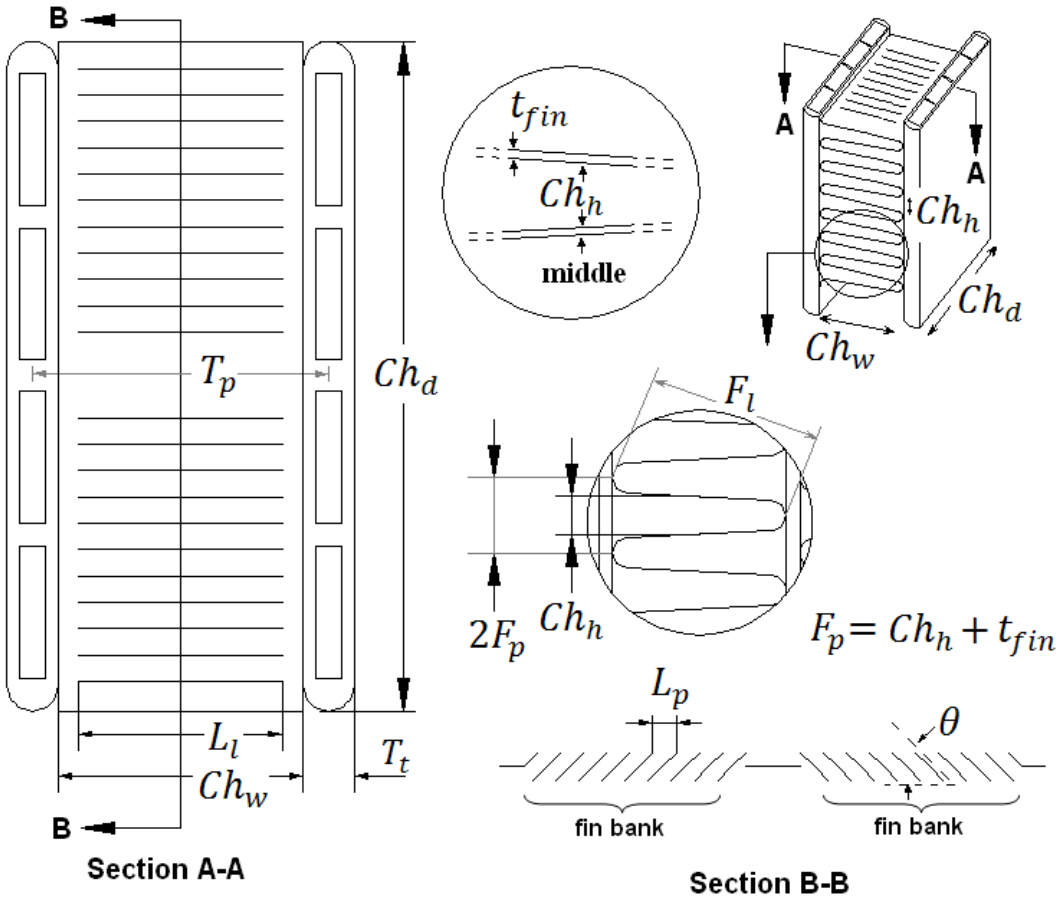

Figure 76: Schematic drawing of a microchannel sample with geometrical parameters shown in the figure. Here, the open space or air passage between two adjacent fins is referred to as channel. (These drawings were made at Oklahoma State University and they were not given by the manufacturers)

8.3 FROST THICKNESS CORRELATION

8.3.1 Developing the Non-Dimensional Frost Thickness Correlation

In order to predict the frosting behaviour of microchannel heat exchanger, it is first necessary to notice the geometrical changes the heat exchanger goes through when frost starts to deposit on the surface. This change of geometry affects the flow characteristics, free flow area, Reynolds number, Nu number and heat transfer coefficients and eventually capacity of the heat exchanger. To address the change the heat exchanger go through and predict the capacity degradation correctly, the frost thickness should be known to allow calculation of the correct Reynolds number and other related flow dynamic parameters. Also offering transient heat transfer correlations without being able to offer a correct Re number at each minute of the frosting time will be an inaccurate method and a trivial attempt. The frost starts to deposit on the surface from the beginning of the frost test and forms a layer that grows in thickness with time. This starts to change the free flow area between two adjacent fins and obviously affects the local velocity and Reynolds number. A precise estimation of the frost thickness then will be necessary to estimate other quantities. It is worth noting that although the frost thickness was measured only at the leading edge of the samples in the present study, this would be sufficient to calculate the correct Reynolds number and critical velocities since in the heat exchanger heat transfer handbooks, the Re number for the heat exchanger is always calculated at the maximum velocity or minimum cross section area wherever it happens along the depth of heat exchanger, which is the leading edge in the case of microchannel frost formation. In the present study, 7 samples that have different geometry in fin pitch (channel height), fin height (channel width) and fin depth and they are tested each in 3 different surface temperature conditions.

Other form of frost thickness correlations from the previous studies were studied such as thickness correlation on flat plates offered by Mao et al. (1993) that had the following form:

$$\delta = 0.176\left(\frac{x}{D}\right)^{0.238} W^{2.106}\left(\frac{T_{tp}-T_{surf}}{T_{air}-T_{surf}}\right)^{1.712} \quad (31)$$

In which δ is the dimensional frost thickness, x is the distance from leading edge into depth of the plate along the penetration direction of air stream, D is the hydraulic diameter of the channel flow, W is the air inlet absolute humidity, T_{tp} is the triple point of water (0°C), T_{surf} is surface temperature of the plate and T_{air} is the dry bulb air temperature.

Other frost thickness correlations on fin and tube geometry were studied such as Chepurnoi et al. (1985) that had the following form:

$$\delta = \left(0.00084(\rho_{air}V_{air})^{0.15}\varphi^{5}\left(\frac{T_{surf}}{T_{air}}\right)^{-3.8}\tau^{0.5}\right)\left(1-0.0057\varphi^{-2.33}\left(\frac{l}{l_0}\right)^{1.75}\right) \quad (32)$$

In which δ is the dimensional frost thickness, ρ_{air} and $V_{air}$are density and velocity of entering air, φ is the relative humidity of air between 0 and 1, T_{surf} and T_{air} are absolute temperatures of surface and the air respectively, τ is time in hour, l is total length of equipment and l_0 is length of the initial section. The author failed to make the previous frost thickness correlations work with the microchannel thickness data measured in the present study.

There was another study on a geometry very similar to microchannels by Xia et al. (2006) and Xia and Jacobi (2010) on flat tube heat exchangers. Their frost thickness prediction approach was a model-base set of expressions which the main equation had the following form:

$$\delta = \int_0^{\tau} (1-\sigma)\left(\frac{\dot{m}_f}{A_h \rho_{fs}}\right) dt \tag{33}$$

In which δ is the dimensional frost thickness, τ and t is time, σ is a constant absorption factor which describes the fraction of freezing water vapor contributing to the densification of frost layer, $\dot{m}_f$ is the frost mass deposition rate, A_h is the heat transfer area and ρ_{fs} is the frost surface density. All the quantities in the equation (33) are known or can be found from previous frost studies except $\dot{m}_f$, frost mass deposition rate, which is the key to estimate the frost thickness during the time of frost formation period. To estimate the $\dot{m}_f$ authors set more than 20 other analytical and empirical equations that need to be solved iteratively in a form for model to converge to the right value of frost mass deposition rate. This way the frost thickness could be calculated in any time step of the frosting test using equation (33). This approach however requires setting up this model with the necessary equations and cannot be accounted as a frost thickness correlation. Moreover, the heat transfer coefficient needs to be known in the mentions set of equations and this is not possible most of the times. In most cases we need to know the frost thickness to be able to calculate or estimate the velocity, Reynolds number and heat transfer coefficient. Eventually, the author could not find the appropriate frost thickness correlation in the literature to match with the experimental frost thickness measurements on the microchannels of the present study and therefore decided to develop a form of correlation of our own.

Many dimensional and non-dimensional form of frost thickness correlation were tried and parameters and independent geometrical variables were tested in dimensional and non-dimensional form. The approaches of trying to predict frost thickness in the dimensional form was not successful thus the approach of correlating the frost thickness in non-dimensional form was taken. Although it was tried to keep everything non-dimensional, this full non-dimensional form of correlation could not predict the frost thickness data within an acceptable tolerance for all the geometries used in the present study. Therefore, the author had to keep some of the geometrical parameters in dimensional form. Many forms of correlations with different constant coefficient were tried and minimizing mean root square errors approach was taken to find the optimum coefficients using solvers of Excel and EES[19]. The final form of frost thickness correlation is as follows:

$$\delta = \alpha \, {Fo_m}^{\beta} \tag{34}$$

$$Fo_m = \frac{D_{ab} t_t}{Ch_h^2} \tag{35}$$

$$\alpha = \left(\frac{1}{\beta^{5.5}}\right)\left[\left(c_1 {Ch_w}^2 + c_2 Ch_w + c_3\right)\left(c_4 {Ch_h}^2 + c_5 Ch_h + c_6\right)\left(c_7 {Ch_d}^2 + c_8 Ch_d + c_9\right)(Fs - c_{10}) + \right.$$

$$c11Chw2 + c12Chw + c13c14Chh2 + c15Chh + c16c17Chd2 + c18Chd + c19 \tag{36}$$

$$\beta = 0.75 + \left(c_{20} {Ch_w}^2 + c_{21} Ch_w + c_{22}\right)\left(c_{23} {Ch_h}^2 + c_{24} Ch_h + c_{25}\right)\left(c_{26} {Ch_d}^2 + c_{27} Ch_d + \right.$$

$$c28Fs - c10 \tag{37}$$

[19] Engineering Equation Solver, Academic Professional Version 8.874

In above equations δ is the frost dimensionless thickness, Fo_m is Fourier number, α and β are functions of geometry and Frost number which are going to be described in details below. δ is the dimensionless frost thickness at the fin leading edges defined in equation (18). It is basically the ratio of frost thickness on one side of the fin (top or bottom) to the half of the free space between two adjacent fins or half of Ch_h. Fo_m is mass transfer Fourier number which is the dimensionless time and fundamentally refers to ratio of water vapor diffusion rate to the rate of water vapor storage as frost. In Fourier number, D_{ab} is the binary diffusion coefficient of water to air which has a constant value of 2.28E-5 [m^2/s] estimated at the average frost surface temperature in the present study. t_t is time in seconds and Ch_h is the average free space between two adjacent fins in meter (fin spacing minus a fin thickness) shown in Figure 76. A similar definition of mass transfer Fourier number was also used and found to be useful in non-dimensionalizing the time in previous studies such as Storey and Jacoby (1999).

α and β are functions of geometry of sample which are c and Frost number defined in equation (28). α is the coefficient of the Fourier number and ranges from 1.2E-5 to 1.9E-3 and β varied from 0.55 to 0.99 for the range of geometries investigated in the present study. Ch_h, Ch_w and Ch_d used in the equations (36) and (37) are supposed to be inserted in mm for just convenience of use due to their small numerical values. One might consider entering them in meter and this just changes some of the coefficients (c's) in Table 18 accordingly. The power of Fo or power of time is at most of the times less than one and this shows that according to data, frost thickness is not growing exactly linear. The averaged power of time (β) in the frost thickness growth between all samples tested in the present study was around 0.75 and this indicates that the frost thickness growth rate has a faster rate at the beginning of the test and slows down as frost test reaches the end. This is consistent with visual observations and theoretical analysis about deposition of frost. When a thick layer of frost has covered the surface, the frost surface temperature is expected to be higher than the surface temperature itself, which is kept constant during the frost tests and this

should reduces the deposition rates at the final stages of the frost test. The previous studies in the literature on frost thickness growth also showed that the power of time is less or equal to 1.

The coefficient c_1 to c_{28} are constants that modify and finalize the value of α and β to capture the trend of frost thickness growth on each geometry; their values are shown in Table 18.

Table 18: Coefficients of geometry in general frost thickness correlation

c1	-2.24444E-06	c6	-2.16158E+00	c11	-3.82446E-07	c16	-1.62560E+00	c21	-5.555E-01	c26	-1.099E-02
c2	4.34942E-05	c7	2.47364E-03	c12	-6.77335E-06	c17	-2.86864E-03	c22	4.275E+00	c27	5.164E-01
c3	-7.89706E-05	c8	-1.03390E-01	c13	2.58664E-04	c18	1.33878E-01	c23	1.619E+00	c28	-5.848E+00
c4	-1.22951E+00	c9	1.96625E+00	c14	-9.36590E-01	c19	-5.38708E-01	c24	-5.678E+00		
c5	4.16146E+00	c10	1.36432E+00	c15	3.35870E+00	c20	1.28500E-02	c25	6.102E+00		

Non-dimensional form of correlation was not successful in giving out reasonable values of α and β since geometric parameters such as non-dimensional channel width, etc. end up similar or close to each other at least between a pair of samples. Some of the previous studies in the literature used some of the fin geometrical dimensions such as louver pitch to non-dimensionalize the fin width and fin depth etc. (Chang and Wang, 1997). Other researchers used a mixed set of parameters such as louver pitch, fin width, or fin or tube distance for non-dimensionalization (Park and Jacobi, 2009). Others used a mixture of both dimensional form for some and non-dimensional form for some other geometrical parameters in a single correlation (Davenport, 1983). There were also other studies which used the dimensional form of geometrical parameters in their correlations (Chepurnoi et al., 1985; Hosoda and Uzuhashi, 1967).

Author attempted offering a correlation in which all of the used parameters are non-dimensional but one of the main reasons for failure of this approach was the following reason. Author tried all the fin geometrical parameters for non-dimensionalization one by one at each time, dividing the geometrical parameters by one of the others made a non-dimensional group that had a similar numerical values at least for two samples of the present study. Then correlation used to predict

the same frost behavior for both of these samples while they had in fact different geometry and different frost growth rate. In every non-dimensionalization approach taken in the present study at least a part of the geometrical distinction between two different samples was lost and correlation used to predict incorrect result about that particular geometry. Therefore, in spite of my initial expectations, the correlation had to keep the dimensional form in geometrical part to avoid sacrificing the accuracy to a great extent. Author is optimistic that the present form of correlation that has been developed will be able to predict the results of frost growth on other geometries other than used in the present study with a very good accuracy. In support of this theory, other verification cases with other geometries obtained in independent studies are going to be presented later in the next section.

8.3.2 Experimental Validation and Error Analysis of the Non-Dimensional Thickness Correlation

The present form of thickness correlation in equation (34) was able to capture the experimental data of frost thickness on 21 different frost tests including 7 different geometries each tested in 3 different surface temperatures. The prediction of correlation versus experimental frost thickness data for sample 6 and sample 2 at three working temperatures is shown in Figure 77 and Figure 78. Similar results were observed with other geometries which are shown in Appendix B.

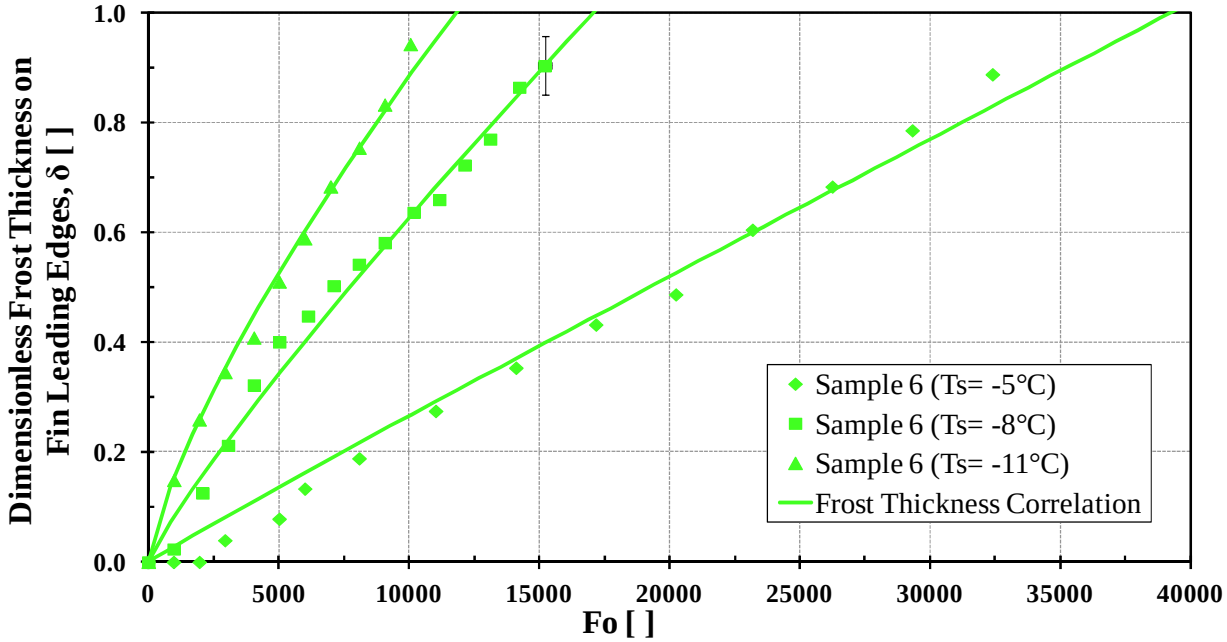

Figure 77: Frost Thickness Correlation versus experimental measured frost thickness data for Sample 6. Similar results were observed for other samples that are shown in Appendix B.

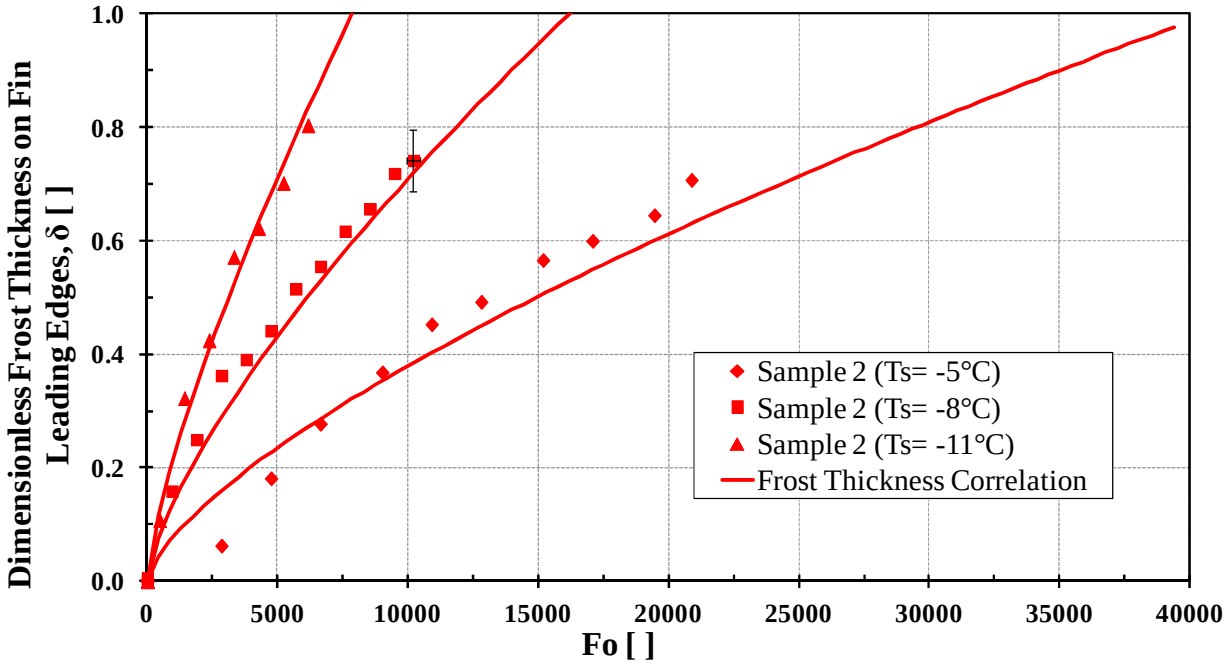

Figure 78: Frost Thickness Correlation vs experimental measured frost thickness data for Sample 2. Similar results were observed for other samples that are shown in Appendix B.

In addition to these 21 different geometry and test conditions, which the correlation was designed and developed to predict these data, other experimental data of frost thickness obtained on other microchannel geometries with different surface temperatures in other independent test data with larger 0.3m by 0.3m (1ft by 1ft) microchannel coils (Moallem et al., 2012b) were also used to verify the present correlation and the result was very satisfactory as shown in Figure 79. Also the present form of correlation was able to predict other frost thicknesses obtained in previous studies such as data of Xia et al. (2006) who used a completely different experimental setup (psychrometric chamber versus air tunnel) with different surface temperature and air condition than the present study. The correlation results showed a satisfactory agreement with their experimental data, which is shown in Figure 80. It should be emphasized once more that the constant of the present correlation was not tuned to capture the experimental results of Moallem et al. (2010a) and Xia et al. (2006) as shown in Figure 79 and Figure 80.

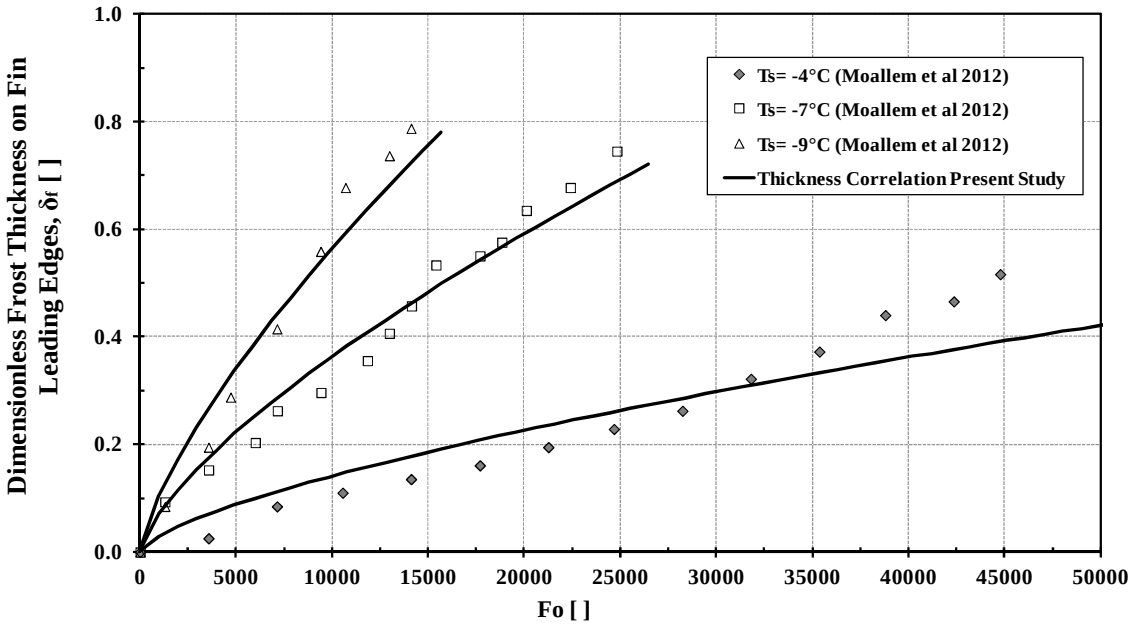

Figure 79: Frost Thickness Correlation versus experimental measured previous published frost thickness data of (Moallem et al., 2012b).

The correlation was just developed with considering the data of 7 samples tested in the present study and final form of correlation was established. Then the final form was plotted against experimental data of the previous studies and Figure 79 and Figure 80 show the validation of the developed correlation with data from other sources in the literature.

The current assessment of the present frost thickness correlation is that it can be used and is valid in the following range of microchannel geometries:

$$7.6mm < Ch_w < 13mm$$

$$1.15mm < Ch_h < 2.34mm$$

$$19mm < Ch_d < 30mm$$

For microchannel geometries outside this range, caution should be used to apply the present thickness correlation to predict the experimental frost thickness data.

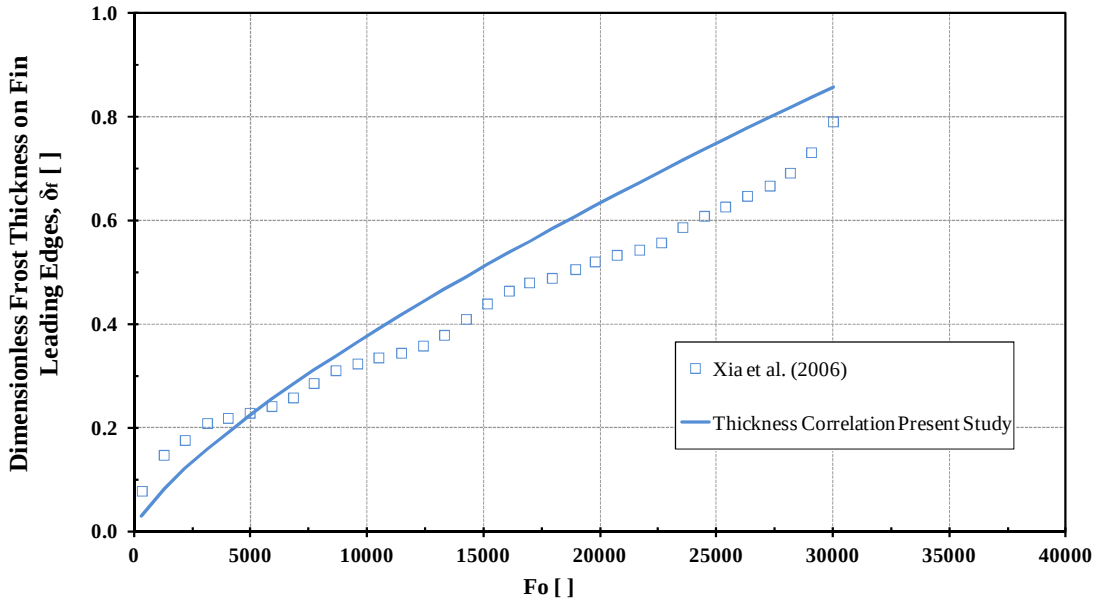

Figure 80: Frost Thickness Correlation versus experimental measured previous published frost thickness data of (Xia et al., 2006).

The overall performance of frost correlation is shown in Figure 81 in which frost thickness ratios $\delta_{correlation}/\delta_{experimental}$ is shown on vertical axis versus the actual frost thickness measurement data.

The correlation seems to be able to predict the experimental frost thickness reasonably well for the whole bank of data and there are some data points that have deviation from correlation prediction when the frost thickness is less than 0.2. This is due to the fact that experimental data of frost thickness as shown in Figure 69 (especially for temperatures of -5ºC and -8ºC) and other figures of Appendix B have some delay in deposition in the beginning of the frost test. Data shows that for some tests in the first five minutes, the frost thickness was near zero due to formation of condensation frosting and occasional formation of supercooled droplets and this fact delays the process of frost thickness growth for a short period of time.

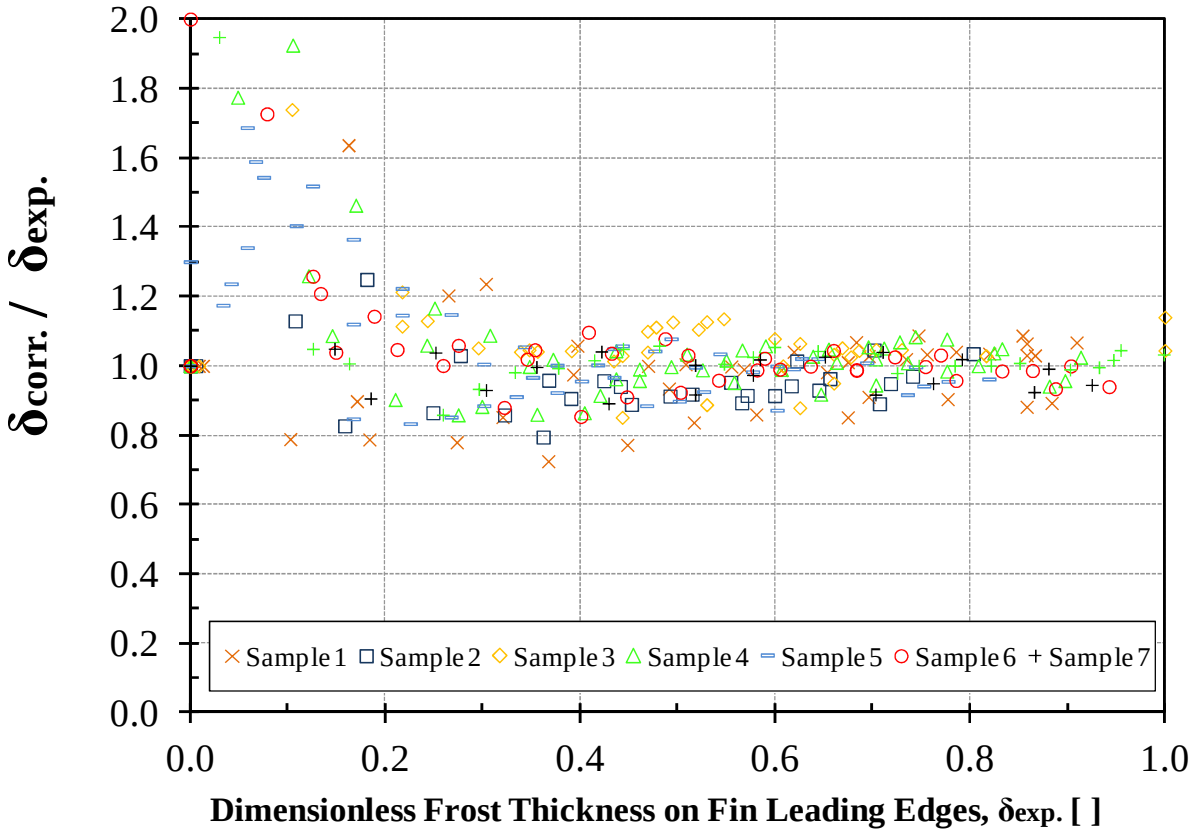

Figure 81: Frost Thickness Correlation versus experimental measured dimensionless frost thickness data for Samples 1 ~ 7.

After few minutes however frost starts to grow normally with almost a constant rate on the surface. The subject of formation of supercooled droplets and condensation frosting in early stages of frost growth have been discussed in detail in other frost studies (Hoke et al., 2004; Na and Webb, 2003) and also another work by the author (Moallem et al., 2012c). This is out of scope of the present study, but the this delay in the frost formation and proximity of experimental frost thickness to zero causes a sort of singularity point and division by zero for the ratio of $\delta_{correlation}/\delta_{experimental}$ and makes large percentages of error as shown in Figure 81. This might not be accounted as weakness of the correlation but rather as the unpredictability of this frost nucleation period in the very early stages of frost formation. As figures of frost thickness show, this delay is not present in every case of frost formation and correlation captures the majority of the data. If we eliminate this unusual singularity point, a good prediction of frost thickness could be made by using the present correlation as shown in Table 19 for 95% of the data points.

The error analysis has been performed on the present frost thickness correlation and relative errors and RMS (Root Mean Square) errors have been reported in Table 19.

Table 19: Correlation overall performance in prediction of dimensionless frost thickness for 7 different geometries of microchannel samples.

ERROR	Sam. #1	Sam. #2	Sam. #3	Sam. #4	Sam. #5	Sam. #6	Sam. #7	70% of Entire Data Base	80% of Entire Data Base	90% of Entire Data Base	**95% of Entire Data Base**	**Entire Data Base**
δ predicted within average of ± [%]	17.4	11.5	26.4	29.0	16.4	16.2	6.5	4.3	5.2	7.2	**9.8**	**17.6**
RMS Error [%]	50.4	21.5	34.7	38.8	28.4	28.2	13.4	-	-	-	-	30.8

The relative error indicates that the frost thickness correlation can predict the experimental data within a certain average percentage of accuracy calculated according to the following.

$$Relative\ Error = \frac{1}{n}\sum \frac{ABS(\delta_{corr.} - \delta_{exp.})}{\delta_{exp.}} \times 100 \quad (38)$$

In which n is the total number of data points, which is 320 point in the present study. A few minor normalizations have also been applied to make the tests with less number of measured data points participate in error propagation the same as the test with a large number of data points.

RMS error was calculated using the following approach.

$$RMS\ Error = \sqrt{\frac{1}{n}\sum \left(\frac{\delta_{corr.} - \delta_{exp.}}{\delta_{exp.}}\right)^2} \times 100 \quad (39)$$

As data in Table 19 shows, the present frost thickness correlation predicts the whole bank of experimental data with average ±17.6% accuracy. As discussed before with eliminating the points of singularity which frost has a near zero values at those points, the correlation can predict 95% of the thickness experimental data within ±9.8 accuracy, respectively, which is reasonably good enough.

8.3.3 Developing a Compact Dimensional Frost Thickness Correlation

The previous non-dimensional form of frost correlation had many terms to predict the frost thickness in each particular geometry and temperature. Some of these terms are playing as a modifier and influence the thickness curve slightly to match the slope of experimental data more precisely. In cases where an approximate estimation with slightly less accuracy satisfies the purpose of the user, a more compact form of correlation can be offered and used which contains only significant geometrical and surface temperature effect main parameters. This new form eliminated

the minor geometrical effect while still offered a good estimation of frost thickness with slightly less accuracy. The error analysis will be presented later. First, the new compact form of correlation is introduced and the reasons for physical significance of main affecting parameters are explained and discussed.

After analyzing the data, it was clear that surface temperature has a major effect on the rate of frost thickness growth as Figure 77, Figure 78 and other figures of Appendix C show. Therefore, Fs number which is representative of the surface temperature needs still to be employed. Between geometrical parameters of channel height, width and depth (Ch_h, Ch_w and Ch_d), Ch_w was found to be the most influential geometrical parameter. Ch_d effect was minor since the blockage of the air flow mostly happens in the front leading edge of the microchannel sample. Using a deeper or shallower sample with the other parameters fixed, had small effect on the rate of frost thickness growth since frost thickness was measured on the leading edges. Also it was found during analyzing the data that the channel height or fin spacing (Ch_h) has minor effect on the rate of frost thickness growth if dimensional form of frost thickness is used. It is true that when the fin spacing is larger, it takes more time for the frost to cover the distance between two adjacent fins. However, the thickness grows on one fin almost independent of another fin and this growth rate will not be affected much by presence of other fin. The flow field might be slightly affected by the distance of the adjacent fin but the effect is minor since the boundary layers of air on the fins are much smaller (~0.1 mm) that fin spacing order of magnitude (1.3 ~ 2.5 mm).

Channel width (Ch_w) had a more sensible effect on the rate of frost thickness growth since it affected directly the fin efficiency. Increasing the fin width increases the distance between two bases of a single fin. Since only bases are in touch with the tubes and refrigerant, the temperature of the center of the fin would be higher than the bases. The numerical and analytical calculation shows the temperature of the center of the fin will be higher with increasing the distance from fin bases. Therefore, with increasing the fin width (Ch_w), the center of the fin experiences slightly higher

temperature. Although, this minor changes in surface temperature have minor effects on thickness as they are hardly noticeable in Figure 42 and Figure 43, they affect the average value of the thickness at each moment. In the figures Figure 42 and Figure 43, sample 4 and 5 that have larger fin width have thicker frost thickness near the fin bases while they have slightly thinner frost thickness near the center of the fin. Although this change is not so large to require two model of frost thickness for the center and the bases of the microchannel fins, it affects the average thickness of frost for each geometry. Thus, the sample with large fin width has smaller average frost thickness than smaller fin width sample at the same surface temperature and air condition. Statistical analysis shows that if we consider the dimensional thickness, the trend of the data of all samples more or less could be captured by Fs number and channel width (Ch_w) with reasonable accuracy. It is clear that this accuracy is less than the previous non-dimensional thickness correlation. However, considering the compactness of the correlation and incorporating only the significant parameters with highest physical degree of influence, the new form can still have some values to be presented.

The compact dimensional form of the thickness correlation has the following form:

$$t = \alpha \, {t_t}^{0.75} \tag{40}$$

$$\alpha = c_1 Fs + c_2 {Ch_w}^2 + c_3 Ch_w + c_4 \tag{41}$$

in which t is the frost dimensional thickness in mm and t_t is time in minutes. The power of time, which is 0.75, has been calculated using an optimization and averaging process of the powers of data curves for all the geometries tested in the present study at different surface temperatures. The fact that the averaged power of time was around 0.75 indicates that the frost thickness growth rate has a faster rate at the beginning of the test and slows down as frost test reaches the end. This is

consistent with visual observations and theoretical analysis about deposition of frost. When a thick layer of frost has covered the surface, the frost surface temperature is expected to be higher than the surface temperature itself, which is kept constant during the frost tests and this should reduces the deposition rates at the final stages of the frost test. The previous studies in the literature (Brian et al., 1970; Mao et al., 1992; Yamakawa et al., 1972; Yang et al., 2006b; Yonko and Sepsy, 1967) on frost thickness growth also showed that the power of time is less than 1. α is a slope coefficient and is a function of channel width (Ch_w) and Frost number. Ch_w is again the average free space between two adjacent tubes in mm (tube spacing minus a tube thickness) shown in Figure 76. The values of coefficients (c's) are shown in Table 20 accordingly.

Table 20: Coefficients of the dimensional frost thickness correlation

c1	c2	c3	c4
0.0629	0.001144	-0.0282	0.16222

The experimental frost thickness data was predicted using the present dimensional form of correlation with reasonable accuracy as shown in Figure 82 and Figure 83 for sample 6 and sample 2 as examples. Although the non-dimensional form of correlation introduced earlier showed a better match especially for sample 6 as shown in Figure 77 and Figure 78, the dimensional form still has reasonable accuracy for these samples as shown in Figure 82 and Figure 83.

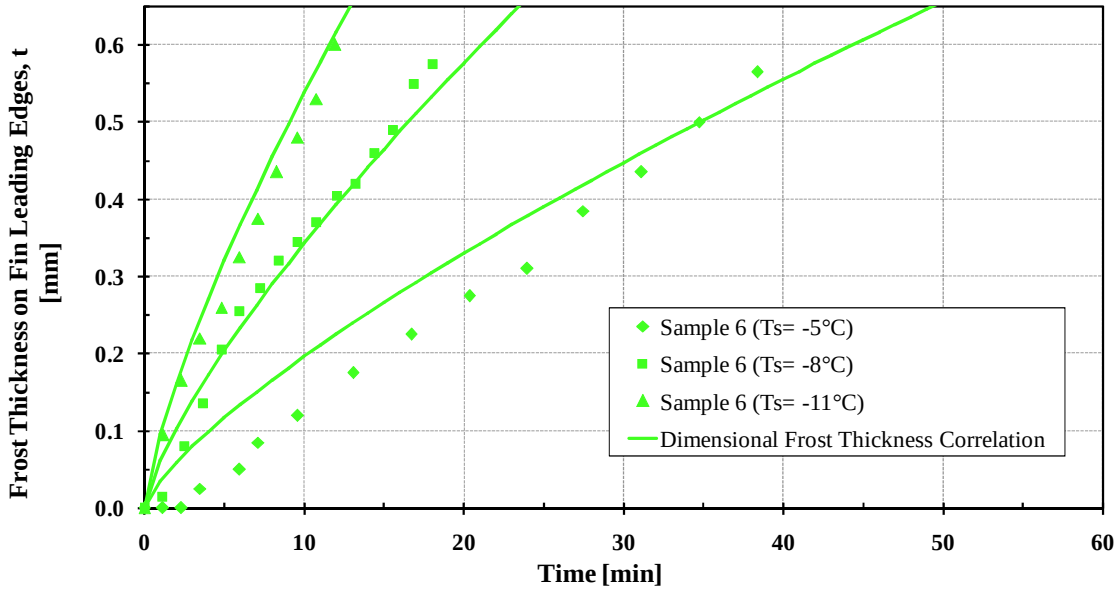

Figure 82: Dimensional frost thickness correlation versus experimental measured frost thickness data for sample 6. Similar results were observed for other samples that are shown in Appendix C.

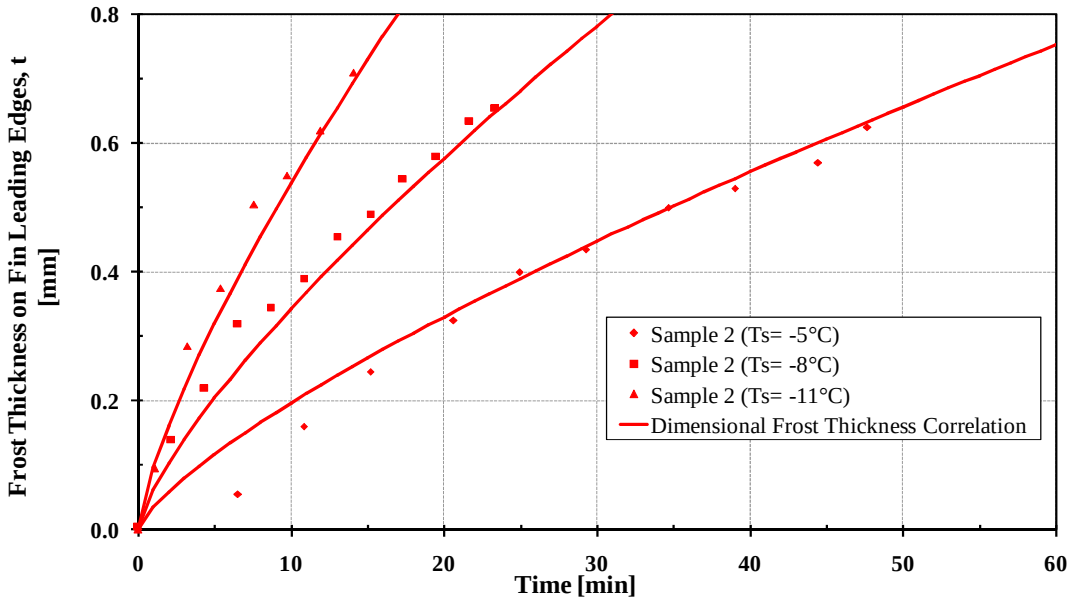

Figure 83: Dimensional frost thickness correlation versus experimental measured frost thickness data for sample 2. Similar results were observed for other samples that are shown in Appendix C.

The present dimensional form of the correlation was also tested against frost thickness experimental data of other samples in the present study and was verified in total against 7 geometries each at 3 surface temperatures. The correlation showed reasonable accuracy to predict the 21 different test conditions and the results are shown an Appendix C.

The dimensional form of correlation was verified against the experimental data of other studies (Moallem et al., 2012a) with 0.3m by 0.3m (1ft by 1ft) microchannel coil and the results are shown in Figure 84.

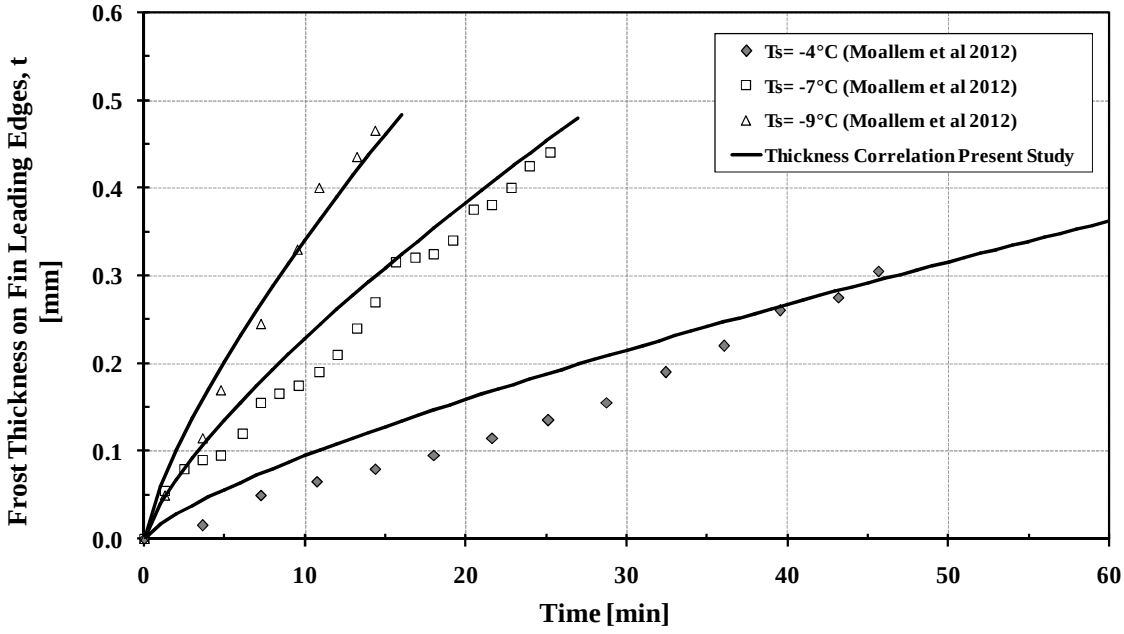

Figure 84: Dimensional frost thickness correlation versus previously published measured experimental frost thickness data of Moallem et al. (2012b).

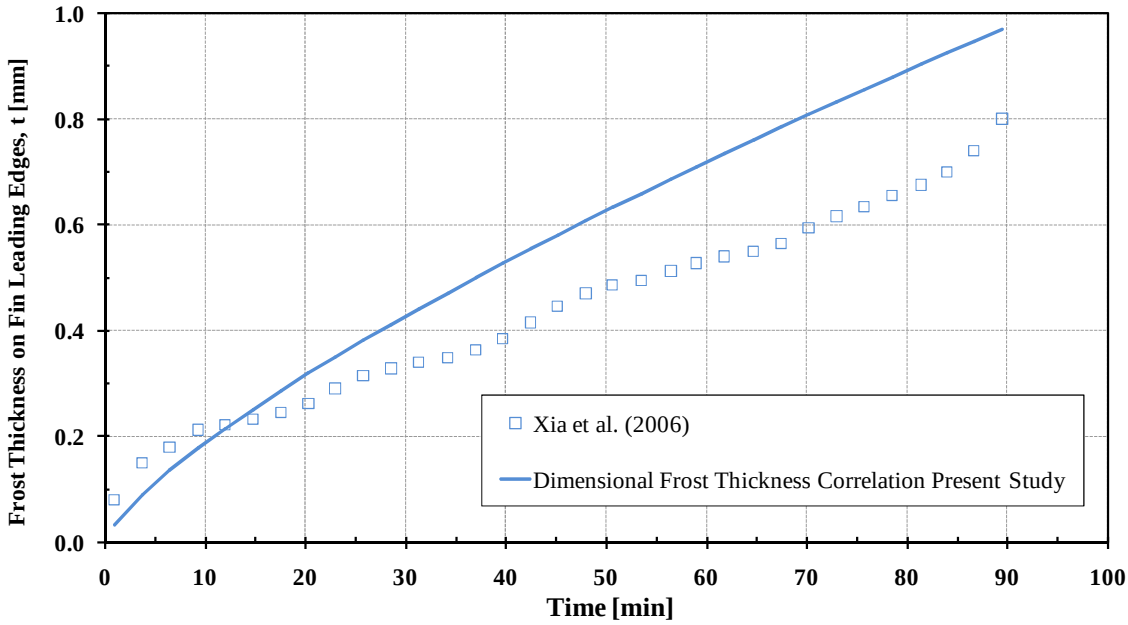

Figure 85: Dimensional frost thickness correlation versus previously published measured experimental frost thickness data of Xia et al. (2006).

The dimensional correlation was verified against data of other independent researches such as Xia et al. (2006) and the results are shown in Figure 85. Although the dimensional form of correlation cannot capture the experimental data as well as non-dimensional form of correlation (Figure 80), it is within a reasonable accuracy.

The error analysis of the dimensional form of the correlation is shown in Figure 86. In comparison of Figure 86 with Figure 81, it is clear that the non-dimensional form of correlation was able to match the experimental data better than the dimensional form. However, the dimensional form has large deviation from 1 only in the case of sample 1 which was non-louvered microchannel fin and a single set of data for one particular temperature for sample 3 and sample 5.

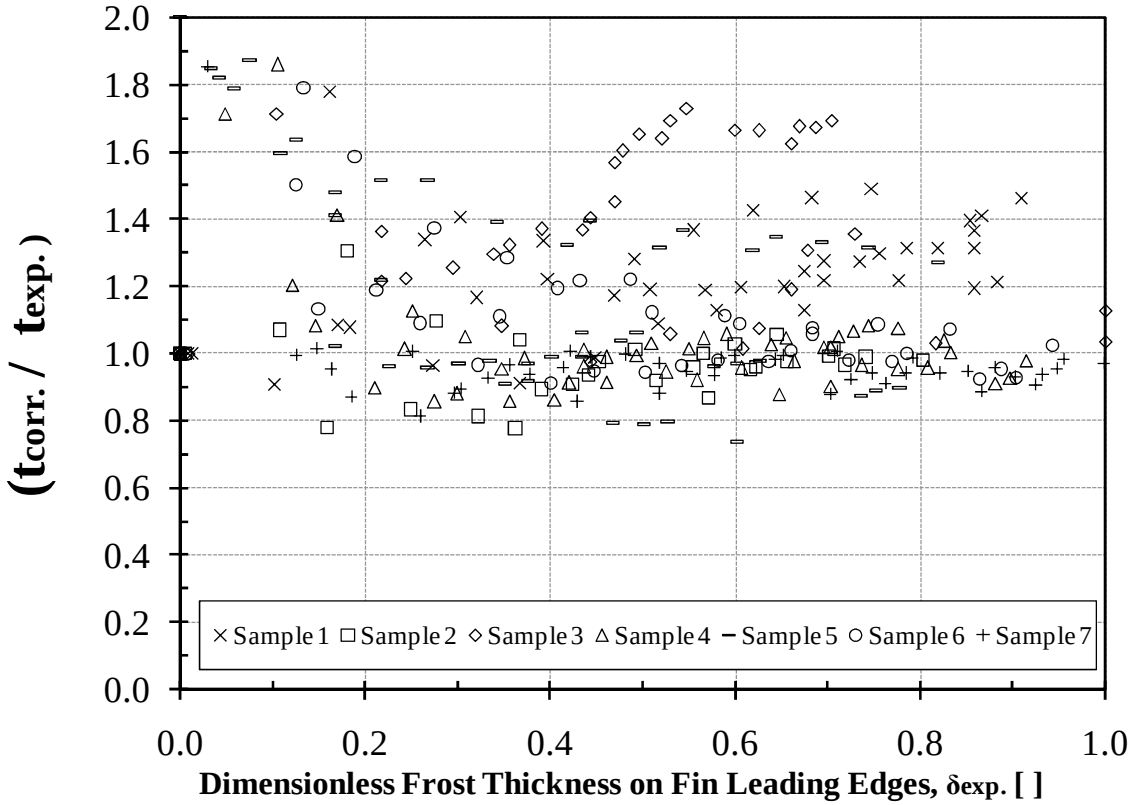

Figure 86: Dimensional frost thickness correlation versus experimental measured dimensionless frost thickness data for Samples 1 ~ 7.

Therefore, dimensional form of correlation is still acceptable to predict a large range of experimental data with reasonable accuracy. For quantifying the error and evaluating the performance of dimensional form of the correlation, Table **21** is given.

Table 21: Correlation overall performance in prediction of dimensionless frost thickness for 7 different geometries of microchannel samples.

ERROR	Sam. #1	Sam. #2	Sam. #3	Sam. #4	Sam. #5	Sam. #6	Sam. #7	70% of Entire Data Base	80% of Entire Data Base	90% of Entire Data Base	**95% of Entire Data Base**	**Entire Data Base**
t predicted within average of ± [%]	30.8	11.7	31.6	19.3	37.3	27.2	7.9	10.6	12.1	14.6	**18.7**	**23.7**
RMS Error [%]	64.3	23.2	43.7	37.6	46.0	48.8	13.4	-	-	-	-	39.6

In cases where a quick estimation of frost thickness is sufficient, the dimensional form might be very useful while in models where a higher accuracy might be necessary, the non-dimensional form of correlation might be preferred.

8.4 AIR FACE VELOCITY DEGRADATION CORRELATION

8.4.1 Developing the Air Face Velocity Degradation Correlation

In the previous section, a frost thickness correlation was introduced which was shown to be able to capture the experimental measured data of frost thickness on 7 different microchannel geometry tested in the present study. The next step to predict the frosting performance of a microchannel heat exchanger would be calculation of the velocity changes during the frost test due to the growth of frost thickness. In order to calculate the air face velocity through the fins simply knowing the air face velocity coil free flow area would be sufficient. In the frosting test, when the frost forms a layer on the fins, the free flow area reduces and it can be calculated via the frost correlation offered on the previous section. Frost grows extensively on front leading edge of the fins and the maximum thickness on the leading edge, making this point having the critical velocity for Reynold number calculation. Thus the free flow area calculation at the fin leading edge is required for further evaluation of the problem. Although it might be trivial, here some hints and techniques are being offered for calculation of free flow area using the thickness correlation introduced earlier. Assuming the value of thickness can be found from thickness correlation, the free flow area of the frontal side of the microchannel can be obtained with geometrical calculation using Ch_w and Ch_h. As shown in

Figure 42 and Figure 87 below, free flow are of each opening gap of the microchannel can be estimated by $Ch_w \times Ch_h$, so the only necessary step is to apply the frost average thickness at each desirable time instant to this calculation to find the free flow area of that particular moment.

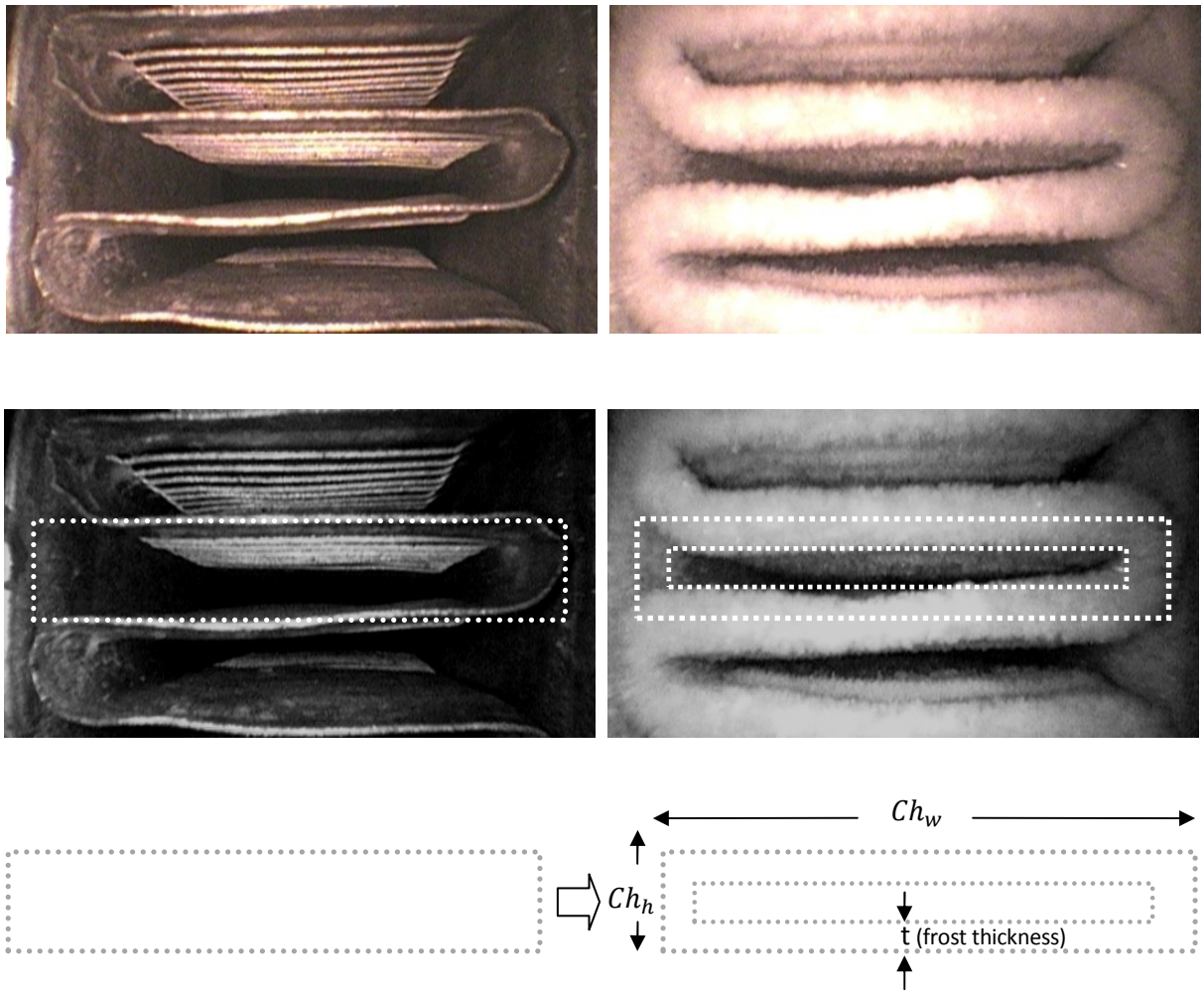

Figure 87: Schematic of free air flow area calculation during a frost test on microchannel sample. Images on the bottom are the identical to the images on top with reference lines on them. Left side images show the microchannel in dry start and right side images show the same coil in the middle of a frost test.

Using the following geometrical calculations, the free flow area could be simply obtained from dimensionless frost thickness:

$$A_{total\ freeflow,0} = No.of\ coil\ flow\ openings \times (Ch_h \times Ch_w) \quad (42)$$

$$A_{freeflow,0} = Ch_h \times Ch_w \quad (43)$$

$$A_{freeflow,frost} = (Ch_h - 2t) \times (Ch_w - 2t) \quad (44)$$

$$\frac{A_{freeflow,frost}}{A_{freeflow,0}} = \frac{Ch_h Ch_w - 2tCh_h - 2tCh_w + 4t^2}{Ch_h Ch_w} = 1 - \frac{2t}{Ch_w} - \frac{2t}{Ch_h} + \frac{4t^2}{Ch_h Ch_w}$$

$$= 1 - \frac{t}{\left(\frac{Ch_h}{2}\right)}\left[\frac{Ch_h}{Ch_w} + 1 - \frac{2t}{Ch_w}\right] = 1 - \frac{t}{\left(\frac{Ch_h}{2}\right)}\left[1 + \frac{Ch_h}{Ch_w}\left(1 - \left\{\frac{t}{\left(\frac{Ch_h}{2}\right)}\right\}\right)\right] \quad (45)$$

Using equation (18) we can rewrite equation (45) as the following:

$$\frac{A_{freeflow,frost}}{A_{freeflow,0}} = 1 - \delta\left(1 + \frac{Ch_h}{Ch_w}[1 - \delta]\right) \quad (46)$$

$A_{freeflow,0}$ is the initial free flow area of the microchannel coil and is constant area (unchanged through the frosting test) which is calculated from face area and geometrical dimensions of the microchnanel coil such as tube thickness, fin thickness, etc.

Equation (46) can be used at any time instant of the frost test to calculate the free flow area of the small openings of the coil while dimensionless frost thickness is known at every moment from correlation presented in equation (34).

With knowing the initial air face velocity, the air face velocity of free flow area or at the minimum cross section area at the fin leading edges can be obtained using the following equation:

$$V_{air,free\ flow,t_t} = V_{free,flow,frost} = \frac{A_{face}}{A_{freeflow,frost}} \times V_{air,face} \quad (47)$$

Note that A_{face} is the face area of the microchannel coil which is constant during the entire frosting period and $A_{freeflow,frost}$ can be calculated from equation (46) at each moment of the frost test. Thus $V_{air,free\ flow,t}$, which varies with time, can be obtained at every moment of the frost test using equation (47) and can be used in calculating Reynolds number. Before we get into calculation of Re number, there is an important discussion that needs to be addressed.

In dry and wet microchannel coils that were subject of study for decades, the geometry was assumed to be in steady state condition and every parameter were measured on the heat exchanger in a steady state mode. In frosting however, there is no steady state condition, the geometry is changing every moment, the velocity adjusts itself with these effects, the surface temperatures get affected by formation of a layer of frost and so forth. So while, in previous studies, the performance of coil was rated in a certain air face velocity or a constant Re number, there is no such concept in frost formation. The Re number are changing due to change in hydraulic diameter of the opening gaps and changes in velocities. With equation (47), (46) and using equation (34) to obtain frost thickness it should be possible to calculate the variable Re number at each stage of the frost formation. Some of the previous studies used the following definition for defining Re number based on louver pitch for louvered flow in the microchannels in dry and wet condition since the geometry was unchanging and a steady state geometry was present through all stages of the heat transfer or hydraulic performance evaluation:

$$Re_{Lp} = \left(\frac{\rho V_{free,flow} L_p}{\mu}\right) \quad (48)$$

In which L_p is the fin louver pitch and $V_{free,flow}$ is the air velocity at minimum free flow area wherever happens in the depth of heat exchanger. This form of calculation of Re number was majorly introduced by Davenport (1983) and used ever since. Other studies, following this approach, considered replacing the Re number calculated with hydraulic diameter (Re_{Dh}) with Re number based on louver pitch and entirely eliminated Re_{Dh} from the investigation of different aspects of flow in dry microchannel heat exchangers (Chang and Wang, 1997; Park and Jacobi, 2009). In the original Davenport (1983) study in 1983, both Re_{Dh} and Re_{Lp} was used to evaluated the characteristics of flow in microchannels. Re_{Lp} was used in Colburn j-factor correlation but Re_{Dh} was used to define the regime of flow and clarify which range or coefficients for the correlation should be used. Many other studies after Davenport (1983) also found using of Re_{Dh} very useful in defining the regime of flow, behavior of flow in passing though fins and predicting the thermal and hydraulic performance of louvered fin microchannel heat exchangers (Achaichia and Cowell, 1988; Webb and Jung, 1992).

In addition to previous findings on this topic, it is clear that Re number calculated in equation (48) will have a constant value since all the other variables remain unchanged in dry or wet test. So it might be acceptable to use this definition of Re number for dry and wet tests. In frost tests however, the geometry is continuously changing and local velocities in minimum cross section area of heat exchanger tend to increase due to increase in frost thickness on the surface of the fins. Thus to have a Re number to be able to reflect these change of geometry and change in local velocities, definitions other than equation (48) should also be considered. This is the reason that analyzing the Re_{Dh} gets important in the frost formation context. Re_{Dh} defined by previous studies has the following definition:

$$Re_{D_h} = \left(\frac{\rho V_{freeflow} D_h}{\mu}\right)_{Dry} \tag{49}$$

Which D_h is hydraulic diameter of small air openings

$$D_h = 4\frac{A_c}{P} \tag{50}$$

In which A_c is the cross section of the minimum flow area and P is the wetted perimeter of the same cross section.

It is obvious that D_h and $V_{freeflow}$ remain constant in dry and wet test however they are changing through the frost formation process. Since the Re number will have the following form:

$$Re_{D_h frost} = \left(\frac{\rho V_{free,flow} D_h}{\mu}\right)_{frost} = \left(\frac{\rho V_{free,flow,frost} D_{h,frost}}{\mu}\right) \tag{51}$$

In which $V_{free,flow}$ and D_h have both the same definition of equation (47) and (50) respectively, while they have to be calculated in every moment of frost progression since their value is changing continuously. D_h in fact should be calculated considering the frost thickness on the fin surface as the following:

$$D_{h,frost} = 4\frac{A_c}{P} = 4\frac{(Ch_h - 2t)\times(Ch_w - 2t)}{2\times[(Ch_h - 2t)+(Ch_w - 2t)]} \tag{52}$$

In which t is the frost thickness. With knowing the frost thickness at each moment of the frost formation using equation (34) and employing equations (46), (47) and (52), Reynolds number ($Re_{D_h frost}$) can be calculated using equation (51). Thus with such Re number which varies with time and also reflects the true physical characteristic aspects of the flow such as geometry and air local velocity, it would be possible to get one step closer to calculate a heat transfer coefficient which also varies in time according to variable air flow conditions.

In all this discussion, one might assume that the face velocity is considered to be constant all through a frost test. In reality the face velocity of a coil under frosting condition does not remain constant and reduces gradually through time. This reduction is not insignificant and in fact as data in Figure 88 shows the air normalized air face velocity is 1 at the beginning of the frost test and reduces as frost test continues. Normalized air velocity is defined as the ratio of air face velocity ($V_{air,face}$) to the air face velocity at the beginning of the frost test ($V_{air,face_0}$) which starts at 1 and approaches zero as frost accumulates on the coil.

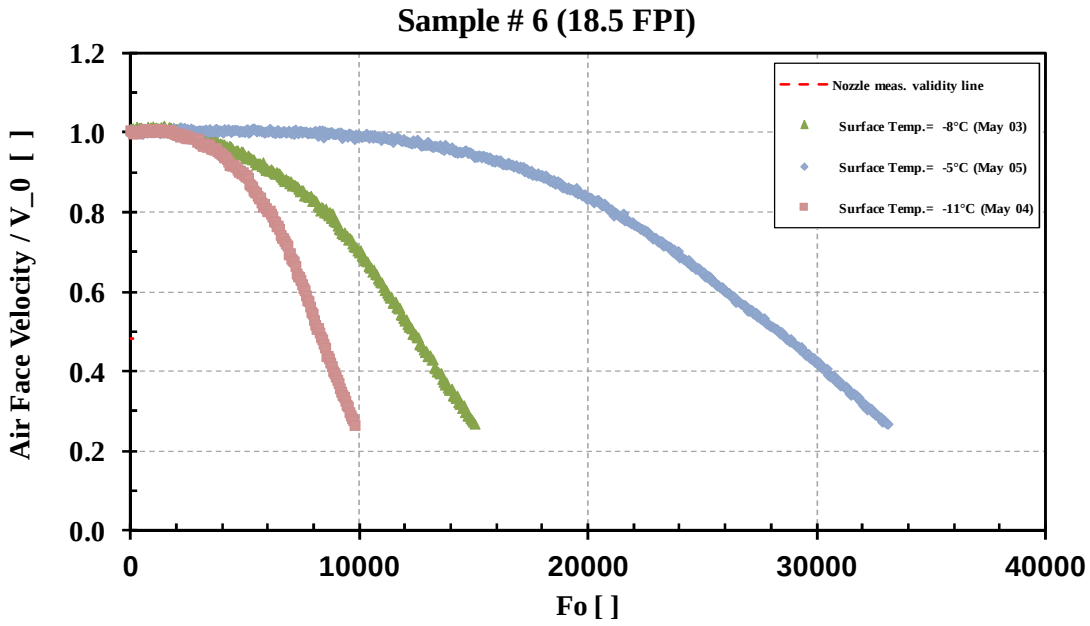

Figure 88: Experimental data of air face velocity reduction for Sample 6. Similar results were observed for other samples.

$$Normalized\ Air\ Face\ Velocity = \frac{V_{air,face}}{V_{air,face_0}} \quad (53)$$

Since frost is a porous media, this air flow or air face velocity might not get to exact zero and in the present study the frost test continued until a very small air flow value was present.

Continuing the frost test further was not possible due to the measuring equipment accuracy limitation and minimum flow requirement according to standards. Data shows that lower surface temperature have a faster rate of air face velocity reduction and eventually air face velocity reduces to as low as less 25% of its initial value.

This air face velocity reduction adds another complexity to the frost prediction problem since the $V_{air,face}$ in equation (47), which was assumed to be a known constant quantity, starts to be a function of time which varies through the test. Thus with the continuous reduction of air flow rate or air face velocity, other quantities such as $V_{free,flow,frost}$ in equation (47) and eventually Re number in equation (51) could not be calculated properly unless precise profile or historical information about air face velocity reduction in each moment of the test could be achieved. Since it was mentioned earlier, the air face velocity was allowed to drop during the frost test in the present study. It is also possible to force the air face velocity to remain constant all through a frost test on a heat exchanger by increasing the air flow fan rotational speed. In addition to the fact that it is not similar to what really happens in air heat pumps real working conditions, it requires large amount of additional fan power especially with progression of frost deposition. In addition, our calculation showed it causes the local air velocity in between the frosted fins to increase by more than 10 times with respect to initial dry conditions due to presence of thick layers of frost on the surface and small free flow area. For more detailed discussion about this topic see Moallem et al. (2012b; 2012c).

What happens on the air flow side of a heat exchanger under frosting condition is as the frost starts to deposit on the surface and makes a frost layer with a considerable thickness on the fin surface as shown in Figure 69, the air pressure drop in passing through the microchannel increases considerably as shown in Figure 70. With increasing the pressure drop, the total air flow rate will be affected and air face velocity on the microchannel sample starts to decrease accordingly. The rate of this decrease in air face velocity does not depend only on air pressure drop passing through the microchannel but also depends on the fan curve and the resistance of the rest of air flow components. Thus, with every new value of air flow pressure drop through microchannel in the test, one should add this value to the values of other air flow pressure drops of the rest of the components in the air flow system (circuit) and cross it with the fan curve to find the new air flow rate and new air face velocity. This requires a detailed model to calculate and converge in every frost step on the air flow and also it needs to employ the full characteristics of the fan curve and the system curves. Knowing that this theoretical case resolution is not always possible, there might be other alternative ways to estimate the flow reduction based on a number of factors and simplifying assumptions. In the present study, a special fan was carefully chosen to be representative of a mid class well sized fan with a near linear curve in the range of operating condition. The operating point was selected to be far enough from the two end side of the fan curve when steep changes occurs in the flow. When the pressure drop increases, the rate of flow drop would change in a manner very close to an appropriately selected fan in its mid range of operation. The other fact to be noted is, in the present study a small part of air flow was only used on the small microchannel samples and the rest of flow was unaffected. The amount of flow that was diverted to microchannel samples was around 5cfm versus the total flow which was around 100cfm. Thus even with increasing the pressure drop of a small part of flow and reducing this 5 cfm to zero, the rest of flow was unaffected and the fan working condition was not influenced much. Therefore it is reasonable to assume that data obtained in the present study on air face velocity reduction was almost independent of the fan curve and was due to intrinsic behavior of the geometry and air pressure drop characteristics of microchannel

samples. It was mentioned that a detail profile of air face velocity drop such as one shown in Figure 88 is necessary to calculate the correct Re number at each moment of the test. Thus the only way possible to solve this was to develop an independent correlation for air face velocity, too. This correlation should be able to give the value of air face velocity at each moment of frost test.

It is worth noting that obtaining Fanning f-factor does not help in predicting the face velocity drop on the microchannel sample. In other words, face velocity correlation is not needed due to the absence of information about Fanning f-factor or friction factor. The f-factor can be employed to obtain the air side pressure drop of each geometry if the entering velocity or face velocity is known. The fundamental problem here is the face velocity reduction profile cannot be calculated by knowing only the air side pressure drop of microchannel itself but indeed it can only be calculated if the fan curve and resistance of the circuit are also known in detail. To achieve this goal, the same fundamental steps taken for developing frost thickness correlation were taken and geometrical parameters as well as environmental parameters were investigated. Because the procedure is very similar to what used in developing frost thickness correlation and to avoid repetition, only results will be presented in this section. Needless to say, different form of correlation was used and parameters were optimized with various approaches until the final form of correlation was chosen between a set of candidates.

The final form of velocity correlation would be as the following:

$$\frac{V_{air,face}}{V_{air,face_0}} = aFo_m{}^2 + bFo_m + 1 \tag{54}$$

$$a = (c_1 Ch_w^2 + c_2 Ch_{w+} c_3)\left(c_4 Ch_h^2 + c_5 Ch_h + c_6\right)\left(c_7 Ch_d^2 + c_8 Ch_{d+} c_9\right)(Fs)^{p_1} \tag{55}$$

$$p_1 = (c_{10} Ch_w^2 + c_{11} Ch_{w+} c_{12})(c_{13} Ch_h + c_{14})\left(c_{15} Ch_d^2 + c_{16} Ch_{d+} c_{17}\right) \tag{56}$$

$$b = (c_{18}Ch_w^2 + c_{19}Ch_{w+} c_{20})\left(c_{21}Ch_h^2 + c_{22}Ch_h + c_{23}\right)\left(c_{24}Ch_d^2 + c_{25}Ch_{d+} c_{26}\right)(Fs)^{c_{27}} + c_{28} \qquad (57)$$

In the above equations, Fo_m has the same definition as in equation (35) and a and b are functions of geometry and Frost number Fs as explained before in thickness correlation. There are a set of constant associated with the present velocity correlation that are shown in Table 22. Ch_h, Ch_w and Ch_d used in the equations (55) to (57) are supposed to be inserted in mm for just convenience of use due to their small numerical values. They can be entered in meter and this just changes some of the coefficients (c's) in Table 22 accordingly.

Table 22: Coefficients of geometry in general frost air face velocity correlation

c1	2.36032E-02	c6	5.90549E-08	c11	9.29921E-01	c16	1.12464E-01	c21	4.46048E-03	c26	-7.70151E+01
c2	-5.50886E-01	c7	9.37121E-04	c12	-3.22532E+00	c17	-1.92793E-01	c22	-6.67660E+00	c27	2.50000E+00
c3	3.74068E+00	c8	-3.02470E-02	c13	-3.31519E-01	c18	-2.08972E-06	c23	9.30292E+00	c28	6.00000E-05
c4	2.22105E-08	c9	1.24149E+00	c14	2.40261E+00	c19	4.74618E-05	c24	-1.22558E-01		
c5	-7.95832E-08	c10	-4.68794E-02	c15	-2.63953E-03	c20	-2.55006E-04	c25	6.16741E+00		

8.4.2 Experimental Validation and Error Analysis of the Velocity Correlation

The present form of velocity correlation offered in equation (54) was able to predict the velocity reduction on the 7 different geometries tested in the present study. Each sample were tested under three different surface temperature and new correlation was able to predict 21 frosting conditions for the different microchannel geometries. The result of correlation prediction on microchannel sample 6 is shown in Figure 89. Data shows that the velocity correlation can predict the experimental data of air face velocity reduction for each surface temperature reasonably well. Similar results were obtained for other samples.

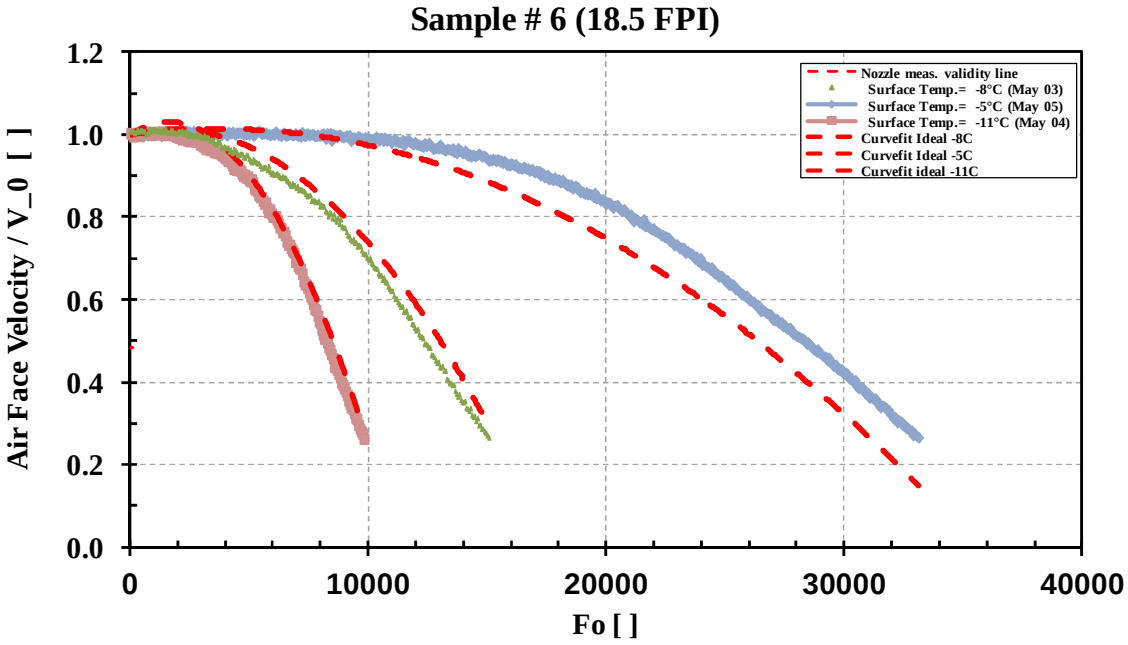

Figure 89: Air face velocity drop correlation vs experimental measured air face velocity data Sample 6. Similar results were observed for other samples.

Similar to what was done on thickness correlation, error in the present correlation needs to be evaluated. The overall performance of velocity correlation is shown in Figure 90 in which the ratio of correlation predicted amount of normalized velocity introduced in equation (54) to the experimental value of this variable is shown on vertical axis versus the actual experimental measurement data. There is a concentration of data points on the right side of the horizontal axis where the normalized experimental air face velocity is near 1. This point indicates the starting of the frost test when the frost test starts and the ratio of actual velocity to initial velocity is 1. As frost test progresses, the normalized velocity decreases from 1 and the data points move to the left side of the plot. Figure 90 also shows that near the end of the test where the air velocities are low the error percentage in prediction of correlation increases. These points are the same points similar to what can be observed in thickness data in Figure 89 at the end of each test when the velocities are very low. As shown in Figure 89, correlation does not fail to predict the

experimental data at the end of each frost test. However because the magnitude of velocity is small, a large percentage of error occurs even with relatively limited deviation.

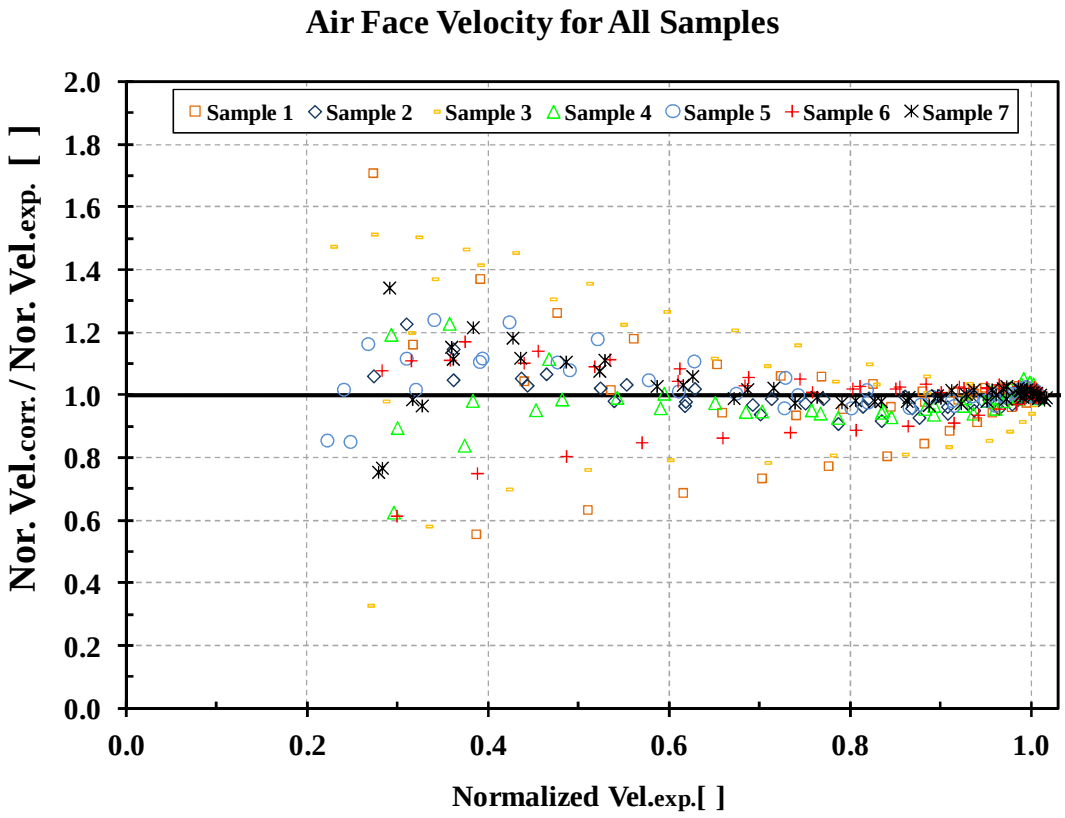

Figure 90: Frost air face velocity correlation versus normalized experimental measured air face velocity data for Samples 1 ~ 7.

Figure 90 can be deceiving to present how much percentage of the data are within a certain percentage of error since the concentration of data point is not uniform all through the horizontal axis. The data points have been collected in equal time intervals in the frost test however since for considerable time of the test the air velocity is near initial velocity as shown in Figure 89, the concentration of data point are more around 1 in the horizontal axis of Figure 90. A small percentage of the whole data points are located outside 10% accuracy of the present correlation according to the following analysis. To evaluate statistically how much error the correlation has

for predicting the experimental velocity data, Table 23 is given. Error analyzing data in Table 23 are calculated for 375 data points in 21 frost tests on 7 geometries of the present study each in three different working conditions. The error was calculated the in the same method described in thickness correlation section in equation (38) and (39). Data shows that velocity correlation can predict the entire data points with an average error of 7.7% which is a reasonable accuracy.

Table 23: Velocity correlation overall performance in prediction of normalized air face velocity for 7 different geometries of microchannel samples.

ERROR	Sam. #1	Sam. #2	Sam. #3	Sam. #4	Sam. #5	Sam. #6	Sam. #7	70% of Entire Data Base	80% of Entire Data Base	90% of Entire Data Base	**95% of Entire Data Base**	**Entire Data Base**
Nor. Air Vel. predicted within average of ± [%]	9.2	3.1	21.6	4.6	4.8	6.2	4.7	3.2	3.9	5.4	**6.2**	**7.7**
RMS Error [%]	15.0	4.8	34.7	7.5	7.2	8.7	8.5	-	-	-	-	12.3

It is worth noting that all of the equations mentioned in this section, equation (34) to (57), are explicit equations that can be setup using an excel sheet and give the exact value of frost thickness, air velocity, hydraulic diameter of flow opening, etc. at each desirable moment frost test. When using the air face velocity correlation offered in equation (54), the exact value of air face velocity at each moment of frost test can be known. Then equations (46), (47), (51) and (52) can be used to calculate the correct Re number ($Re_{D_h frost}$) at each desirable time of the frost period. This Re number will be used to predict the heat transfer coefficient in the next section.

8.5 HEAT TRANSFER CORRELATION

8.5.1 Developing the Heat Transfer Correlation

A detailed discussion about importance of heat transfer coefficients and the approach to calculate it was presented in previous section "Heat Transfer Coefficient Calculation". In the present section, a correlation is offered to predict the experimental data of measured heat transfer coefficients in the form of dimensionless form of Colburn j-factor. In the previous sections, correlations for frost thickness and air face velocity were presented and this foundation is needed for describing the heat transfer behaviour. Since there have been a number of studies in the past that obtained the heat transfer coefficient for dry and wet microchannel coils on a large bank of geometries (Chang and Wang, 1997; Kim and Bullard, 2002; Park and Jacobi, 2009), it was found more appropriate to try to modify their general correlation to include additional terms for frosting behaviour. In this approach, not only the new correlation remains valid for about more than 100 previously investigated geometries in dry condition, but it can also predict the frosting behaviour of at least 7 new geometries from the present work. Since the present form of frost correlation contains the previous dry correlation as basic terms, the structure of the previous correlations should be explained a little bit in details. One of the most famous microchannel coil j-factor correlations is Chang and Wang (1997) correlation that investigated the 91 different microchannnel samples under dry condition. Some of these samples were experimentally investigated by the authors and some others experimental data were gathered from a large data base of previous studies (Achaichia and Cowell, 1988; Davenport, 1983; Webb and Jung, 1992). Chang and Wang (1997) investigated all of the experimental data and developed a j-factor that

could predict 89% of the data within ±15% average accuracy. The final form of their correlation was as the following:

$$j = Re_{Lp}^{-0.49}\left(\frac{\theta}{90}\right)^{0.27}\left(\frac{F_p}{L_p}\right)^{-0.14}\left(\frac{F_l}{L_p}\right)^{-0.29}\left(\frac{Ch_d}{L_p}\right)^{-0.23}\left(\frac{L_l}{L_p}\right)^{0.68}\left(\frac{T_p}{L_p}\right)^{-0.28}\left(\frac{t_{fin}}{L_p}\right)^{-0.05} \quad (58)$$

In which Re_{Lp} is the Reynolds number based on louver pitch defined in equation (48), θ is the louver angle in degrees while all other geometrical parameters are in mm. L_p is louver pitch, F_p is fin pitch[20] (fin distance), F_l is fin length[21], Ch_d is coil depth or fin depth[22], L_l is louver length, T_p is tube pitch and t_{fin} is the fin thickness as shown in Figure 76.

Chang and Wang (1997) correlation offers one value for each particular geometry since it was developed for dry conditions and there is no time dependency in the correlation.

Park and Jacobi (2009) took this correlation and progressed it one step further to capture j-factor of 126 samples from nine independent experimental setups in dry conditions. Authors showed that their correlation have advantage over the Chang and Wang (1997) correlation since their new form of correlation could predict 92.6% of the data of 126 samples within ±20% or 83.2% of the data with ±15%. This was true while Chang and Wang (1997) correlation could predict the 84.3% of the data of 126 samples within ±20% or 74.0% of the data of 126 samples within ±15%. A minor disadvantage however was the correlation was more elaborated and needed a few separate terms to be evaluated to obtain the final results. The final form of Park and Jacobi (2009) correlation was as the following:

$$j = C_1 j_{Re} j_{low} j_{louver} \theta^{C_2} N_{LB}^{C_3}\left(\frac{F_l}{L_p}\right)^{C_4}\left(\frac{Ch_d}{F_p}\right)^{C_5}\left(\frac{L_l}{F_l}\right)^{C_6}\left(\frac{F_l}{T_p}\right)^{C_7}\left(1-\frac{t_{fin}}{L_p}\right)^{C_8}\left(\frac{L_p}{F_p}\right)^{C_9} \quad (59)$$

[20] It is equal to $Ch_h + t_{fin}$.

[21] It is equal to $\sqrt{F_p^2 + Ch_w^2}$.

[22] It is defined as tube depth in Chang and Wang (1997) study. It is considered the same as fin depth in the present study.

$$j_{Re} = Re_{Lp}^{\left[C_{10}+C_{11}\cosh\left(\frac{F_p}{L_p}-1\right)\right]} \tag{60}$$

$$j_{low} = 1 - sin\left(\frac{L_p}{F_p}\cdot\theta\right)\left[\cosh\left(C_{12}Re_{Lp} - C_{13}\frac{Ch_d}{N_{LB}F_p}\right)\right]^{-1} \tag{61}$$

$$j_{louver} = 1 - C_{14}tan(\theta)\left(\frac{Ch_d}{N_{LB}F_p}\right)cos\left[2\pi\left(\frac{F_p}{L_p tan(\theta)} - 1.8\right)\right] \tag{62}$$

In the above relations, C_1 to C_{14} are numerical constants that are shown in Table 24[23]. Other quantities such as j_{Re}, j_{low} and j_{louver} are functions Re_{Lp} or other geometrical parameters that are expressed in equations (60) to (62). θ is louver angle in radians, N_{LB} is number of louver banks[24], F_l is the fin length, L_p is louver pitch, Ch_d is fin depth or channel depth, L_l is louver length, T_p is tube pitch, t_{fin} is fin thickness and F_p is the fin pitch as shown in Figure 76.

Table 24: Constants used in (Park and Jacobi, 2009) j factor correlation.

c1	0.872	c4	0.149	c7	-0.902	c10	-0.458	c13	0.142
c2	0.219	c5	-0.259	c8	2.62	c11	-0.00874	c14	-0.0065
c3	-0.0881	c6	0.540	c9	0.301	c12	0.049		

The first attempt to develop a frost correlation might be trying to start from a validated dry microchannel j-factor correlation and add non-dimensional terms to it to be able to capture degradation of heat transfer coefficient or j-factor. The assumption however then would be the heat transfer coefficient at the beginning of the frost test would be equal to the dry steady state heat transfer coefficient. Although this might be the common believe since the surface is assumed to be dry at the beginning of frost test, this was not verified with the data collected in the present study as shown in data of , Figure 74 and Figure 75.

[23] The accuracy of the constants are different from one another however they were published in Park and Jacobi (2009) study in the same format. It is due to the uncertainty analysis and confidence intervals. For more details please see Park and Jacobi (2009).

[24] Most of the ordinary microchannels have 2 banks (groups) of louvers in each fin that are aligned in opposite direction as shown in Figure 76.

The reasons for this difference will be discussed next. Since it seems it is a common belief, the first attempt would be trying to relate the existing dry heat transfer coefficient with the heat transfer coefficient experimental data in the frost tests via a possible form of correlation. Assuming the heat transfer coefficient to be equal to the dry heat transfer coefficient in the beginning of the frost test, allows only particular form of terms to be added to equation (59) to account for effect of frost. These terms must be equal to 1 at the beginning of frost test if they are being used as a coefficient. On the other hand, the dependency of heat transfer coefficient on Reynolds number especially in the cases that geometry is changing is a well established fact in heat transfer and is well explained in heat transfer handbooks. In the previous section the Re number that accounts for the change of hydraulic diameter and free flow area velocity was introduced. To incorporate the effect of this Reynolds number into the dry correlation of equation (59) and find the appropriate power seems to be a reasonable approach. Adding any power of Reynolds number diverts the results of equation from the initial dry start value of j-factor. Therefore a ratio of Reynolds number was added to the correlation equation (59) and the power was adjusted. The result of preliminary form of equation is as the following:

$$j = C_1 j_{Re} j_{low} j_{louver} \alpha^{C_2} N_{LB}^{C_3} \left(\frac{F_l}{L_p}\right)^{C_4} \left(\frac{F_d}{F_p}\right)^{C_5} \left(\frac{L_l}{F_l}\right)^{C_6} \left(\frac{F_l}{T_p}\right)^{C_7} \left(1 - \frac{\delta_f}{L_p}\right)^{C_8} \left(\frac{L_p}{F_p}\right)^{C_9} \left\{\frac{Re_{D_h frost}}{Re_{D_h dry}}\right\}^{0.5} \qquad (63)$$

All the terms of equation (63) were defined in equations (60) to (62). The last term on the right hand side of equation (63) is the ratio of Reynolds number based on hydraulic diameter during the frost progression to the Reynolds number of dry condition. $Re_{D_h frost}$ and $Re_{D_h dry}$ can be calculated from equation (51) and equation (49) respectively.

This ratio of Reynolds number is 1 at the beginning of the frost test since both Reynolds numbers are equal. As the frost test progresses however, $Re_{D_h frost}$ responds based on the rate of change of its components $D_{h,frost}$ and $V_{free,flow,frost}$ while $Re_{D_h dry}$ remains constant all during a frost test. Since $D_{h,frost}$ is calculated based of the free flow area, it is continuously decreasing during

the frost test while the $V_{free,flow,frost}$ increase at first because of growing of frost thickness at the surface with a linear rate while face velocity drop has an initial delay to drop. The result of these influences cause the entire ratio of the Reynolds numbers to increase or decrease at different times of the test. The result of equation (63) in predicting microchannel samples j-factor under frosting condition are shown in the Figure 91 and in figures of the next section.

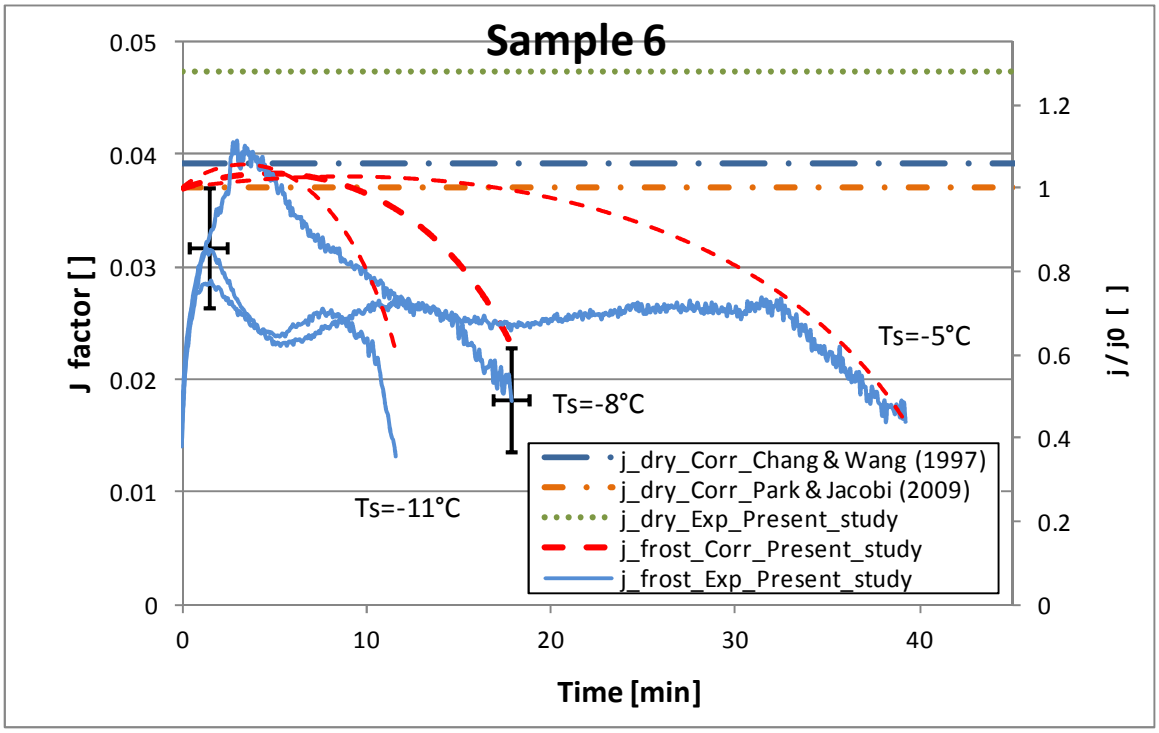

Figure 91: Comparison of preliminary j-factor correlation with experimental data during frost tests on microchannel Sample 6 with different surface temperatures. Preliminary correlations is developed based on the assumption that j-factor at the beginning of the test is equal to dry steady state j-factor. Similar results for tother samples are shown in Appendix F.

8.5.2 Experimental Validation and Error Analysis of the Preliminary Form of Heat Transfer Correlation

Figure 91 shows the result obtained using the developed correlation in equation (63) versus experimental data obtained for j-factors based on experiments. The red dashed line is the new preliminary version of correlation while the straight lines shows the values of previous dry j-factor correlations. Dry j factor obtained in the present study and experimental data for j factor during frosting tests for three working surface temperatures are also shown. Data shows that the correlation is able to recognize the time of the frost cycle and the moment in which the heat transfer starts to drop significantly is captured by this form of correlation due to presence of velocity effect in the Reynolds number employed. Figure 91 also shows that the new correlation over predicts the experimental data significantly and only at the end of the frost test the results of the correlation gets closer to experimental values of j-factor.

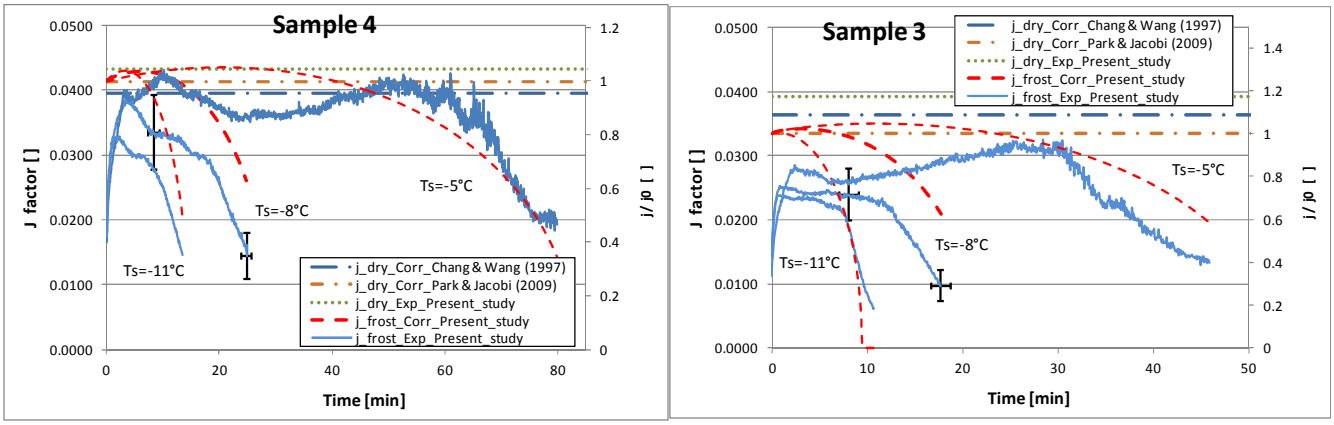

Figure 92: Comparison of preliminary j-factor correlation with experimental data during frost tests on microchannel Sample 3 and 4 with different surface temperatures. Preliminary correlations is developed based on the assumption that j-factor at the beginning of the test is equal to dry steady state j-factor.

The other fact is, regardless of fluctuations of experimental data, it seems that the average starting point of the correlation at time equal to zero is considerably higher than the average starting point of experimental data at the time t=0 especially for the tests with surface temperature of -8°C and -11°C. Investigating other samples showed the same kind of mismatch between the experimental data and correlation predictions as shown in Figure 92.

Data of sample 3 and sample 4 in Figure 92 shows that before considering any further modification on the form of correlation to capture the fluctuation of the data, the starting point at t=0 seems to be an extremely elevated point to estimate the starting j factor at the beginning of the frost test. It should be noted however that in the first 1 minute of the test the trend of experimental data should not be interpreted as j factor is rising from a value near 0 to the value of around 0.003. Time zero is the moment that air flow starts on the cold sample and it takes around one minute until a quasi steady state condition between surface temperatures and heat transfers components is achieved. Thus the value of j factor at the first minute could not be determined with certainty however it is also hard to accept that the j factor starts with the initial dry correlation value of 0.041 in sample 4 or 0.033 in sample 3 and suddenly in less than 1 minutes, before the pictures even could record a barely visible thin layer of frost on the surface, the j factor drops to around 0.035for sample 4 or 0.025 for sample 3. This very high value of starting point prevents the correlation to make a reasonable prediction of the experimental data no matter how many different form of correlation were attempted. Actually author tried various different forms of correlations however no form was found to be able to predict the experimental data well due to presence of this steep descent or high starting value. Investigating all of the experimental data on all other samples showed that the experimental data of average j-factor are considerably lower than j-factor offered by previous correlations for dry steady state condition. The results of error analysis showed that if the assumption of equality of heat transfer coefficient or j factor in dry steady state condition and in the beginning of the frost test is taken then the error in the

correlation prediction can not be reduced beyond around 29% even with the best form of correlation according to Table 25. Data on Table 25 shows the overall performance of the best correlation that could be found which is the same as equation (63) with the assumption of equality of heat transfer coefficients in dry test and initial frost test[25].

Table 25: j factor preliminary correlation overall performance with assumption of equality of j factors at initial stages of frost formation and dry steady state test.

ERROR	Sam. #1	Sam. #2	Sam. #3	Sam. #4	Sam. #5	Sam. #6	Sam. #7	70% of Entire Data Base	80% of Entire Data Base	90% of Entire Data Base	**95% of Entire Data Base**	**Entire Data Base**
j factor predicted within avergare of ± [%]	10.5	37.4	35.0	27.1	13.5	35.7	45.2	22.8	23.9	26.3	**27.7**	**29.2**
RMS Error [%]	12.4	41.2	40.5	28.4	16.3	38.5	48.6	24.5	25.7	28.5	30.4	32.3

Data on Figure 93 shows the ratio of predicted j factor to experimental j factor by assuming that j factors are equal at the beginning of the frost test and dry steady state condition. According to the data, that large deviation of data from one in most of the cases is obvious and this indicates that correlation over predicts significantly the experimental data of heat transfer coefficient or j factor.

The other fact is, if the assumption of equality of heat transfer coefficients at the beginning of the frost test and dry steady-state test is abandoned, the heat transfer coefficient could be lower than the dry steady state value. This is mainly because the temperature difference that is the temperature difference between air inlet and outlet which is the main component in calculating heat transfer coefficient is affected by presence of ablimation (sublimation). Although in

[25] If the dry test results obtained from the present study is decided to be employed, they show even a higher value than existing correlations for dry microchannels. So even with the assumption that the present experimental facility over predicts the heat transfer coefficients, the initial frost heat transfer coefficient is still lower than the existing dry heat transfer coefficient or j factor correlations. Authors purposely did not chose their own dry test experimental results for developing the correlation first to show that analogy of reduced heat transfer coefficient in the beginning of frost test is also valid by using other validated previous dry heat transfer coefficients. In addition to that, for dry steady state tests, larger coils might give a better and more accurate results since Logarithmic temperature difference could be employed with larger temperature difference in refrigerant side.

calculating the heat transfer coefficient only sensible magnitude of heat transfer is being considered, the presence of latent magnitude of heat transfer or its absence have effect on the value of the sensible magnitude of heat transfer. This process is well understood in reverse condition in cases such as evaporative cooling when presence of latent magnitude of heat transfer due to evaporation affect the outlet dry bulb temperature of outlet air and of course thermocouples can measure a different value of sensible heat transfer when evaporation is present. In the sublimation or ablimation where water vapour in the air deposits on the cold surface same mechanist of altering the sensible magnitude of heat transfer happens. One might argue the following. It is assumed that when magnitude of sensible heat transfer changes, the temperature difference between air inlet and outlet changes with the same magnitude so that heat transfer coefficient should remain the same whether or not ablimation exist.

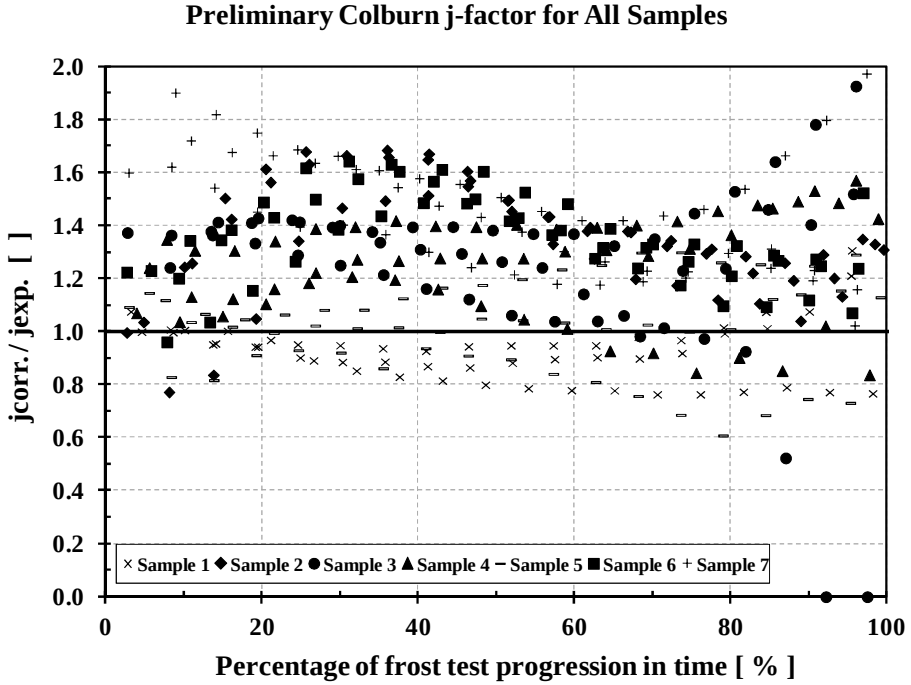

Figure 93: Overall performance of preliminary correlation results versus experimental data for Samples 1 ~ 7 with assuming the j factors are equal at the beginning of the frost test and in the dry steady state test.

This assumption might not be true. It is very true that when magnitude of sensible heat transfer increases 20%, the temperature difference between air inlet and outlet also increase 20% too due to linear relation they have according to equation (23). However it is not true to assume that same 20% exist in a logarithmic function of temperature difference used in calculation of heat transfer coefficient in equation (19) and (20). Logarithmic temperature difference changes with a different rate than does sensible magnitude of heat transfer. Thus, the fraction of these two quantities which is the heat transfer coefficient does not remain the same between two cases of dry steady state condition and initial frost test stages. Also the logarithmic temperature difference is affected by other components such as surface temperature as well which have different values in different tests. This even make it more improbable that sensible magnitude of heat transfer and logarithmic temperature difference vary with the same rate between two cases of dry steady state condition and initial frost formation stages even if similar temperature differences are used for both condition[26]. That might be the reason that in Figure 91 and Figure 92, for the lower the surface temperatures, the initial heat transfer coefficients at the beginning of the frost test is lower. The summary is the results of all of the experiments in the present study for all the geometries showed that the experimental dry steady state heat transfer coefficient or j factor was considerably higher than the heat transfer coefficient or j factor under frosting condition as Figure 91 and Figure 92 show examples of it. The lower the surface temperature the lower the initial heat transfer coefficient.

This fact leads to give up the limitation of forcing the initial heat transfer coefficient to be equal to it's dry steady state value. Therefore again the correlation and data was modified to find a

[26] As it was verified in the present study, although the same temperature difference between air entering temperature and surface temperature was employed in two cases of dry steady state test and frost test, still dry heat transfer coefficient was much higher than frosting heat transfer coefficient at initial stages of frost formation as shown in the figures of this section. This was attributed to effect of latent magnitude of heat transfer on the temperature difference while this effect does not appear with the same magnitude in the sensible heat transfer as explained above. As a result heat transfer coefficient in the frost test has a different value in comparison to dry test.

better match. Data analyzing showed that in average, the frost initial heat transfer coefficient or j factor was around 79% lower than the dry steady state heat transfer coefficient. This was incorporated into the correlation which led to final form of correlation as the following:

$$j = C_1 j_{Re} j_{low} j_{louver} \alpha^{C_2} N_{LB}^{C_3} \left(\frac{F_l}{L_p}\right)^{C_4} \left(\frac{F_d}{F_p}\right)^{C_5} \left(\frac{L_l}{F_l}\right)^{C_6} \left(\frac{F_l}{T_p}\right)^{C_7} \left(1 - \frac{\delta_f}{L_p}\right)^{C_8} \left(\frac{L_p}{F_p}\right)^{C_9} 0.79 \left\{\frac{Re_{D_h frost}}{Re_{D_h dry}}\right\}^{0.5} \quad (64)$$

$$j_{Re} = Re_{Lp}^{\left[C_{10} + C_{11}\cosh\left(\frac{F_p}{L_p} - 1\right)\right]} \quad (65)$$

$$j_{low} = 1 - sin\left(\frac{L_p}{F_p} \cdot \theta\right) \left[\cosh\left(C_{12} Re_{Lp} - C_{13} \frac{Ch_d}{N_{LB} F_p}\right)\right]^{-1} \quad (66)$$

$$j_{louver} = 1 - C_{14} tan(\theta) \left(\frac{Ch_d}{N_{LB} F_p}\right) cos\left[2\pi \left(\frac{F_p}{L_p tan(\theta)} - 1.8\right)\right] \quad (67)$$

In the above relations, C_1 to C_{14} are numerical constants that are shown in Table 24. Other quantities such as j_{Re}, j_{low} and j_{louver} are functions Re_{Lp} or other geometrical parameters that are expressed in equations (65) to (67). θ is louver angle in radians, N_{LB} is number of louver banks, F_l is the fin length, L_p is louver pitch, Ch_d is fin depth or channel depth, L_l is louver length, T_p is tube pitch, t_{fin} is fin thickness and F_p is the fin pitch as shown in Figure 76. Although the coefficient of 0.79 could be merged into coefficient C_1 it was preferred to keep it in the current form to remind the user that only when the microchannel is working under frosting condition this coefficient and Re ratio on the right hand side of this equation should be used and in other cases to obtain the dry steady state j factor, the original Park and Jacobi (2009) correlation in equation (59) should be used.

Figure 94 shows the results obtained from the final form of correlation for sample 6 under frosting condition. Although the correlation is not still able to capture the fluctuations of

experimental data there are two facts that prevent the author from employing more sophisticated form of correlation. First, the uncertainty on measurement of the heat transfer coefficient and j factor which was around 20% according to calculations. This suggests that major part of fluctuations of experimental data in Figure 94 is simply anomalies of measured data and does not reflect a significance physical behaviour pattern of frost formation phenomena. Second fact is this pattern was not consistent through all of the samples and the other microchannel samples have a different shape of increase and decrease as shown in Figure 95 and Figure 96.

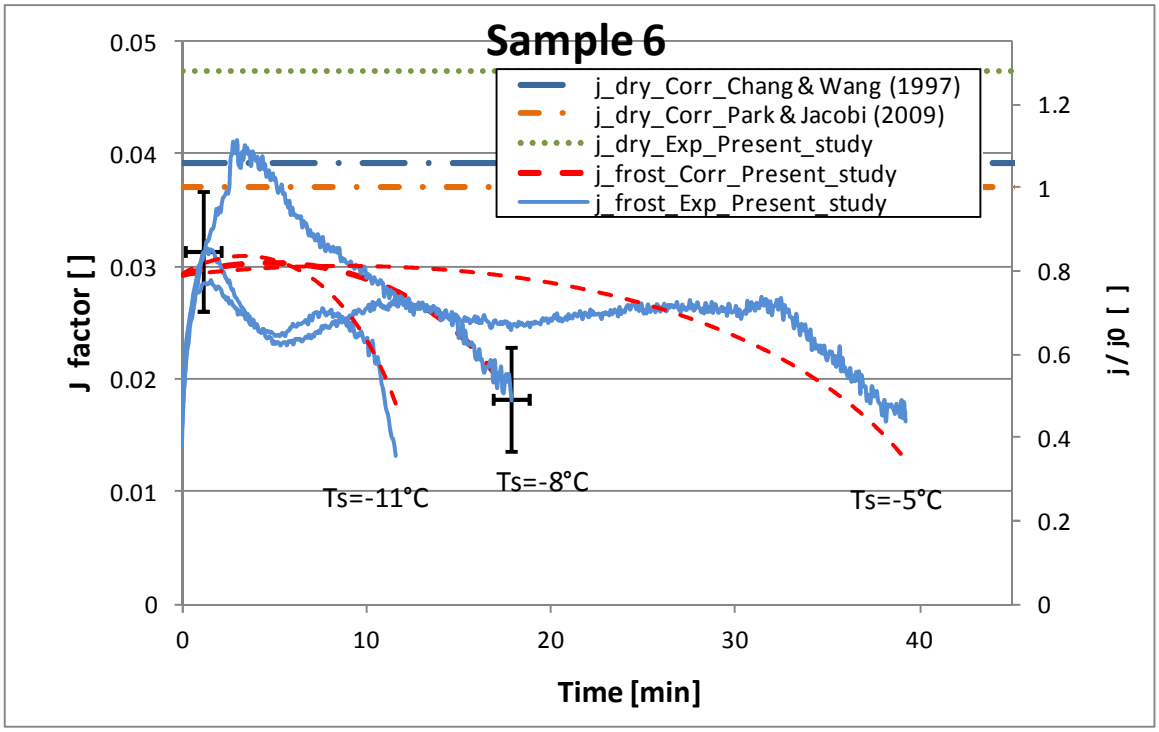

Figure 94: Comparison of final form of j-factor correlation with experimental data for frost tests on microchannel Sample 6 with different surface temperatures. Similar results for other samples are shown in Appendix F.

Results of correlation prediction on sample 4 and sample 3 are shown in Figure 95 and Figure 96. Similar results for other samples are shown in Appendix F.

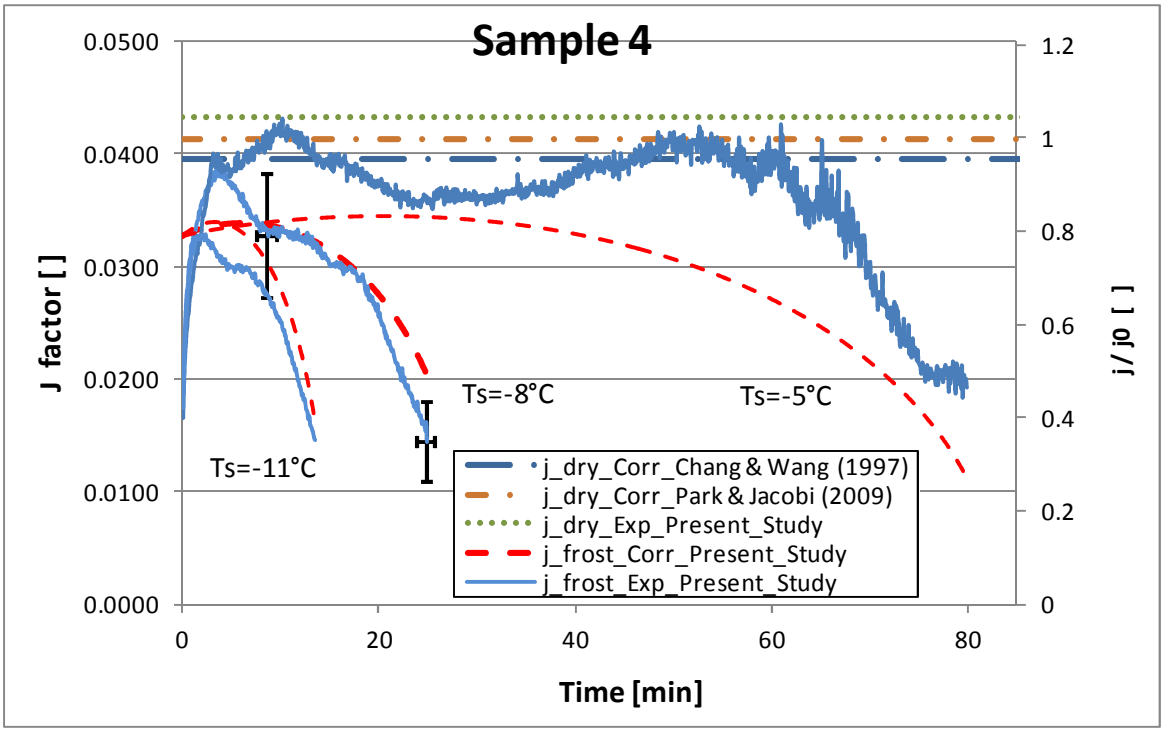

Figure 95: Comparison of final form of j-factor correlation with experimental data for frost tests on microchannel Sample 4 with different surface temperatures. Similar results for other samples are shown in Appendix F.

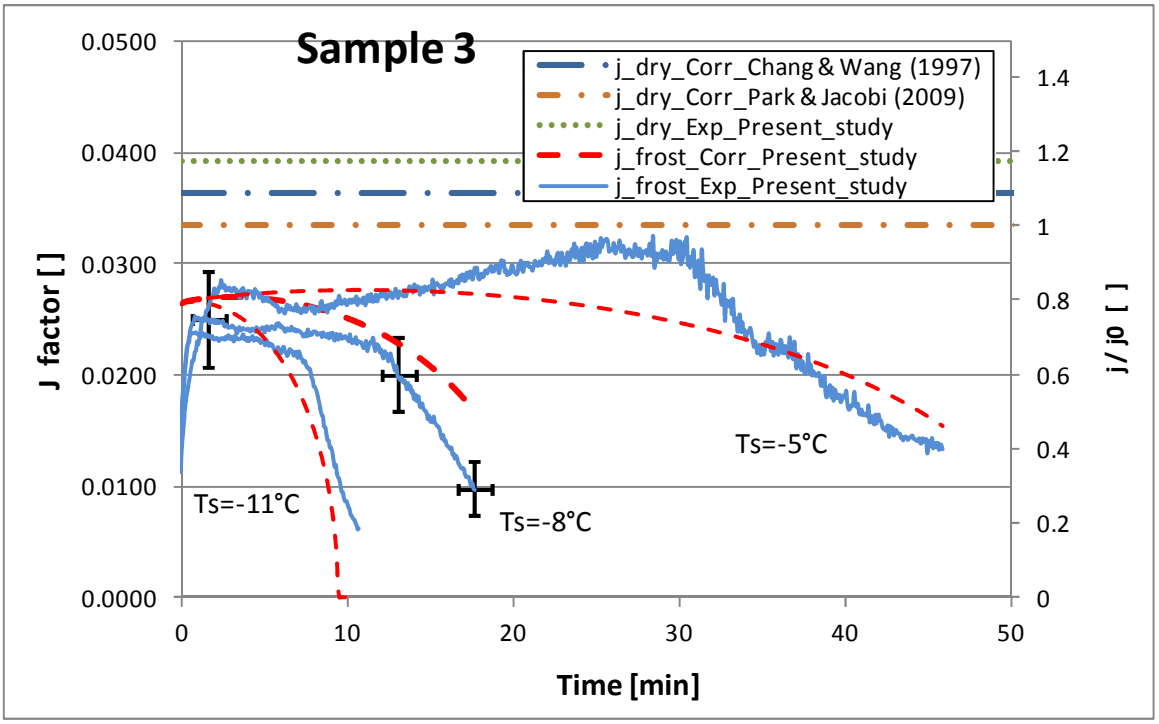

Figure 96: Comparison of final form of j-factor correlation with experimental data for frost tests on microchannel Sample 3 with different surface temperatures. Similar results for other samples are shown in Appendix F.

The correlated frost thickness and velocity has been used to calculate the ratio of hydraulic diameter Reynolds number to be used in j factors correlation since the end user might not possess the detailed experimental data of thickness and velocity during frost operation. If the real measured data are used to calculate the Reynolds number and j factor, some improvements were observed on predictions of j factor as shown in Figure 97.

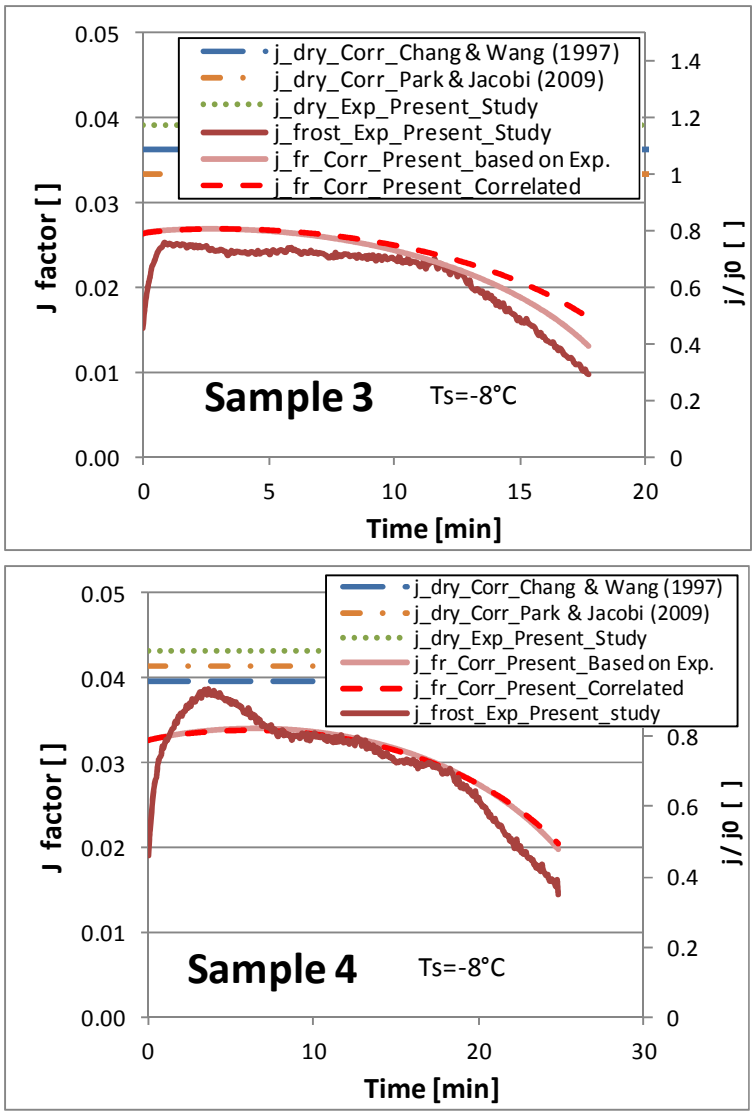

Figure 97: Comparison of j factor correlation calculated based on real experimental data versus using correlated data of frost thickness and air velocity for sample 3 and sample 4.

For two samples shown in Figure 97, data shows that using real measured data improves the correlation to predict experimental measured j factor; the improvement for sample 3 is more visible. In general, for the remaining samples, a significant improvement of the correlation was not observed when using the real measured data of frost thickness and face velocity. This was because the thickness and velocity correlations were good enough approximations of the experimental data at every instant during the period of the test.

8.5.3 Experimental Validation and Error Analysis of the Final Form of Heat Transfer Correlation

The overall performance of the final form of j-factor correlation for the frosting conditions is reported in Figure 98, which plots the ratio of correlated j factor to experimental j factor for all the samples used in the present study. The data of Figure 98 shows improvement in comparison to previous error ratio on Figure 93.

The correlation has been able to predict majority of the data points with acceptable accuracy. There is an interesting behaviour of the predicting correlation at the very end of the frost period. An example is discussed for sample 3 at the end of the frosting period, for which there appears to be a large deviation between the predicted j-factors in a completely blocked frosted coil and the experimental measurements. It should be noticed that there are two points for sample 3 on the x-axis of Figure 98, in which the ratios of j-factor from the correlations to the j-factor measured result in zero.

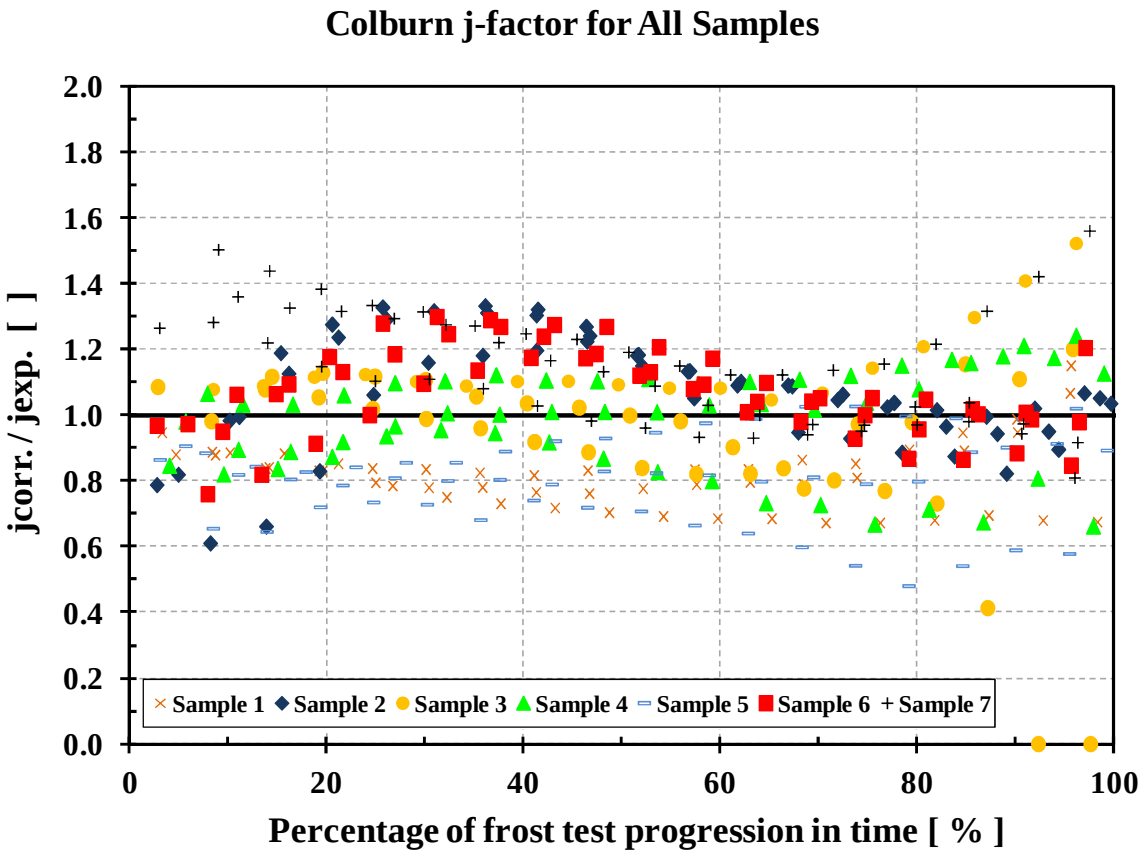

Figure 98: Overall performance of final form of j factor correlation versus experimental data for Samples 1 to 7.

For those two points, the surface temperature was -11°C and frost grew quickly blocking the entire apparent flow free area at the end of the test. Due to the high porosity of the frost at a fin surface temperature of -11°C a very small air flow rate was measured even during the last few minutes of the test. Thickness plots in Figure 108 of Appendix B for sample 3 confirm that the thickness of frost at -11°C was high enough to cover the entire vertical gap in between the fins at the front of the coil. Therefore the calculated Re number from Eq. (51) yielded to zero and the corresponding predicted j-factor from Eq. (64) resulted in a zero value. This is a singular situation in which the correlation predicts full blockage of the flow and thus zero heat transfer coefficient. The experimental j-factor had still small but measurable values. The ratio of the predicted to the

measured j-factor is of course zero as shown in the last two data points for sample 3 in Figure 98. This behaviour shows one of the limitations of the heat transfer correlation developed in this work, that is, the porosity of the frost is not taken into account when determining the actual free flow area in between the frosted fins. While this effect is most likely to be negligible for most part of the frost period, it seems to become significant for sample 3 at -11°C for which the porosity of the frost plays a dominant role during the last couples of minutes of the frosting period.

The error analysis showed that the current version of correlation could predict the experimental data of j factor under frosting condition for the entire bank of the microchannel samples used in the present study within an average of 16.7%, as shown in Table 26. The RMS error for the entire set of data is 19.8%.

Table 26: j factor correlation overall performance

ERROR	Sam. #1	Sam. #2	Sam. #3	Sam. #4	Sam. #5	Sam. #6	Sam. #7	70% of Entire Data Base	80% of Entire Data Base	90% of Entire Data Base	**95% of Entire Data Base**	**Entire Data Base**
j factor predicted within average of ± [%]	18.9	14.9	21.3	12.2	19.7	12.2	17.6	11.9	12.7	14.4	**15.6**	**16.7**
RMS Error [%]	19.9	18.3	29.0	14.2	21.0	14.8	21.0	13.3	14.3	16.6	18.3	19.8

One might point out that not all of the microchannel geometrical parameters such as louver dimensions, pitch, and angle, were used when developing the heat transfer coefficient and j-factor correlations during frosted conditions. This is a first approximation and the geometry of the louvers were considered in the first terms of Eq. (64) from Park and Jacobi (2009) correlation. This equation served to predict the j-factors in dry operating conditions for all the fin samples tested in the present work. The effect of the louver geometry, pitch, and angle was also accounted for in evaluating the initial value of j at the beginning of the frost test. After frost begins to

accumulate on the surface and create a resistance to the free flow area, the hydraulic diameter of the rectangular space in between the fins at the leading edge of the fin sample was considered to be the main parameter that restricts the air flow. This flow restriction was captured by the Reynolds number ($Re_{D_h frost}$) calculated using equation (51).

CHAPTER IX

SUMMARY AND CONCLUSIONS

The present work focused on various aspects of frost formation on louvered folded fins in outdoor microchannel heat exchangers used in air source heat pump systems. The approach taken was to perform laboratory experiments on small scale coils and sample fins that were cut out from commercially available heat exchangers and to replicate their operating conditions in laboratory. A special setup was built in a wind tunnel at Oklahoma State University to provide small and uniform conditioned air stream on microchannel fin samples that had various fin density, fin height, and fin width. In this project, more than 150 tests with various surface temperature, air velocity and air humidity were performed on 12 different microchannel fin samples; 7 fin samples had differences in the geometry and 5 fin sample had identical geometry but with various surface coatings. The effects of surface temperature, fin geometries, surface coatings and environmental parameters such as air humidity and velocity on the thermal and hydraulic performance of the microchannel heat exchangers under frosting conditions were studied. Hydrophilic and hydrophobic fin samples were tested to evaluate the effect of hydrophilicity on water drainage characteristics of microchannels under frost, defrost, and re-frost operating conditions.

Frost thickness and frost mass were measured and the small samples allowed for uniform frost

growth on the entire face area of the fins. In addition to air inlet and outlet dry bulb and humidity measurements, surface tube wall temperature during frost operating conditions was directly measured which was a major innovation of the developed methodology. Air pressure drop across the coil, heat transfer rate degradations and heat transfer coefficients in form of Colburn j-factor during the frosting periods were also measured and discussed in details.

The work presented in this study suggests that non-louvered low fin density sample had longer frost time but lower capacity in comparison to louvered samples. The gain in frost time was more than 3.2 times while the reduction in capacity was about 1.6 times. When considering louvered fins, variation of the fin width did not improve the frosting performance of the fins significantly, but increasing the fin depth seemed to increase the fin capacity (+39%) with some penalization of the frosting time (-6%). Increasing air velocity from 0.8 m/s (157 fpm) to 1.6m/s (315 fpm) could improve the capacity of the fins up to 53%. Decreasing air humidity from 0.004 to 0.003 kg-water per kg-air (92% R.H. to 72% R.H.), increased frosting time as expected by as much as 5.7 times higher while initial capacity decreased by 14%. Surface temperature had the highest impact on frosting time and capacity of all fin samples. 6 degrees Celsius higher surface temperature resulted in around 1.8 times decreased initial capacity but as much as 3.3 times longer frost time.

The data suggest that the hydrophilic coated sample resulted in slightly increased frost time in comparison to hydrophobic sample. This was attributed to better drainage characteristics of this sample. Five frost/defrost cycles were performed on each coated sample and time of the next consequent frosting cycles decreased as the cycling progressed. Although the time of frost cycle for the first frost cycle was almost equal for all coated samples, the time of the fifth frost cycle was considerably lower (30%) than the first cycle for the hydrophobic sample. This reduction in time was less noticeable (15%) in the hydrophilic sample. For uncoated sample the reduction in time was 27% that is in between the value of hydrophilic and hydrophobic sample. Based on the results obtained in the present study, the impact of surface coating on the frosting performance

was considered secondary with respect to the effect due to surface temperature and geometry. This might be due to the fact the sample used as baseline reference had already fairly good water drainage characteristics.

This study also broke new ground on developing a set of three empirical correlations for frost thickness, air face velocity drop, and heat transfer coefficient that properly account for frosting operating conditions of 7 fin geometries for microchannel heat exchangers. The developed correlations were verified for fin surface temperature ranging from -11°C (12°F) to -5°C (23°F) and were able to predict the frost thickness, air face velocity degradation and dimensionless heat transfer Colburn j-factor within ±17.6% and ±7.7% and ±16.7%.

Frosting heat transfer coefficients were developed based on the LMTD method and by considering existing correlations available in the public domain for louvered fins in dry steady state conditions. One heat transfer correlation was found to be particularly suitable to be modified in order to account for frosting operating conditions of the folded fins with louvers. Additional terms were included to account for the frosting behavior and the new heat transfer correlation was experimentally validated for seven fin geometries tested in the present study. Correlations that predict the frost thickness and the reduction of air face velocity during frosting operation were developed in order to calculate the instantaneous air-side Reynolds number during frosting operation of the fins. These parameters were keys for predicting the heat transfer rates of the microchannel coils in quasi-steady state frosting operating conditions. Future work might include more testing and modelling on full-scale coils in order to extend the developed frost heat transfer correlation for a larger set of fin geometry and operating conditions.

REFERENCES

Achaichia A., Cowell T.A. (1988) Heat transfer and pressure drop characteristics of flat tube and louvered plate fin surfaces. Experimental Thermal and Fluid Science 1:147-157.

AHRI. (Standard 210/240, 2008) Performance Rating of Unitary Air Conditioning and Air-Source Heat Pump Equipment. Air Conditioning, Heating and Refrigeration Institute.

Aihara T., Gakumasawa H., Maruyama S., Hongoh M. (1989) Frost formation and defrosting on tube-array evaporators in a fluidized bed and an impinging jet. Experimental Thermal and Fluid Science 2:65-71.

Ameen F.R. (1993) Study of frosting of heat-pump evaporators. ASHRAE Transactions 99:61-71.

Auracher H. (1987) Effective thermal conductivity of frost. Heat and Mass Transfer in Refrigeration and Cryogenics:285-301.

Barrow H. (1985) A note on frosting of heat pump evaporator surfaces. Journal of Heat Recovery Systems 5:195-201.

Bayardelle M. (1955) Influence des dimensions des noyaux de congelation sur la temperature de congelation de l'eau. C. r. hebd. Seance. Acad. Sci. Paris 241:232-33.

Bentley W.A., Humphreys W.J. (1931) Snow Crystals. McGraw-Hill Book Co., Inc., New York and London.

Biguria G. (1968) The Moving Boundary Problem with Frost Deposition to a Flat Plate at Subfreeaing Temperatures and Forced Convection Conditions. The Measurement and Corelation of Frost Properties. Ph.D. Dissertation, Chemical Engineering, Lehigh University, Bethlehem, PA, USA

Biguria G., Wenzel L.A. (1970) Measurement and Correlation of Water Frost Thermal Conductivity and Density. Industrial and Engineering Chemistry Fundamentals 9:129-138.

Birstein S.J. (1955) The role of adsorption in heterogeneous nucleation. J. Met. 12:324-331.

Boer J.H.D. (1950) Atomic forces and adsorption. Adv. Colloid Sci. 3:1-66.

Brazinsky I. (1967) Properties of water frost formed at cryogenic temperatures. Sc. D. Thesis (PhD Dissertation) Massachusetts Institute of Technology, Cambridge, MA, USA.

Brian P., Reid R., Brazinsky I. (1969) Cryogenic Frost Properties. Cryogenic Technology 5:205-212.

Brian P.L.T., Reid R.C., Shah Y.T. (1970) Frost deposition on cold surfaces. Industrial and Engineering Chemistry Fundamentals 9:375-380.
Bryant G.W., Hallett J., Mason B.J. (1959) Epitaxial growth of ice on single-crystalline substrates. J. Phys. Chem. Solids 12:189-195.
Burley G. (1964) Ice nucleation by photolyzed silver iodine. Phil. Mag. 10:527-534.
Burton W.K., Cabrera N., Frank F.C. (1951) The growth of crystals and the equilibrium structure of their surface. Phil. Trans. 243.
Cai S. (2009) Design of an Experimental Facility for Measurement of Frost Growth on Heat Exchangers. Master Thesis Mechanical and Aerospace Engineering Department, Oklahoma State University, OK, USA.
Chang Y.-J., Wang C.-C. (1997) A generalized heat transfer correlation for Iouver fin geometry. International Journal of Heat and Mass Transfer 40:533-544.
Chen H., Thomas L., Besant R.W. (1999a) Prediction of Frost Height on Heat Exchanger Fins. Proceedings of ASME Heat Transfer Division 364-2:199-206.
Chen H., Thomas L., Besant R.W. (1999b) Measurement of frost characteristics on heat exchanger fins, Part II: Data and analysis. ASHRAE Transactions 105:294-302.
Chen H., Thomas L., Besant R.W. (2000a) Modeling frost characteristics on heat exchanger fins, part II: model validation and limitations. ASHRAE Transactions 106:368–76.
Chen H., Thomas L., Besant R.W. (2000b) Modeling frost characteristics on heat exchanger fins, Part I: Numerical modeling. ASHRAE Transactions 106:358-67.
Chen H., Thomas L., Besant R.W. (2003) Fan supplied heat exchanger fin performance under frosting conditions. International Journal of Refrigeration 26:140-149.
Chen M.M., Rohsenow W. (1964) Heat, mass and momentum transfer inside frosted tubes - experiment and theory. Journal of Heat Transfer 99:334-340.
Cheng C.-H., Cheng Y.-C. (2001) Predictions of frost growth on a cold plate in atmospheric air. International Communications in Heat and Mass Transfer 28:953-962.
Cheng C.-H., Shiu C.-C. (2002) Frost formation and frost crystal growth on a cold plate in atmospheric air flow. International Journal of Heat and Mass Transfer 45:4289-4303.
Chepurnoi M.N., Lomakin V.N., Shnaider V.E., Chepurnoi V.M. (1985) Study of the Process of Frost Formation in Finned Air Coolers. Vinnitskii Polytechnical Institute, Translated from Inzhenern-Fizicheskii Zhurnal 48:44-48.
Cho E.S., Koa J.-M., Jiang L., Prasher R.S., Kim M.S., Santiago J.G., Kenny T.W., Goodson K.E. (2003) Experimental Study on Two-Phase Heat Transfer in Microchannel Heat Sinks with Hotspots. 19th IEEE SEMI-THERM Symposium 0-7803-7793-1/02:242.
Cleland D.J. (2005) Implications of Coil Frosting on System Designs for Low-Temperature Applications. ASHRAE Transactions 111:336-345.
Corrin M.L., Storm N.C. (1963) The surface chemistry of condensation nuclei I. The sintering of silver iodine. J. Phys. Chem. 67:1509-1511.
Corrin M.L., Edwards H.W., Nelson J.A. (1964) The surface chemistry of condensation nuclei II. The preparation of silver iodine free of hygroscopic impurities and its interaction with water vapor. J. Atmos. Sci. 21:565-567.

Cwilong B.M. (1947) Sublimation in Wilson chamber. Proc. R. Soc. A190:137-143.
Cwilong B.M. (1949) Sublimation in outdoor air and seeded sublimation. Nature Lond. 163:727-728.
D'Albe F.F. (1949) Some experiments on the condensation of water vapour at temperature below 0°C. Q. Jl. R. met. Soc. 75:1-14.
Davenport C.J. (1983) Correlations for heat transfer and flow friction characteristics of louvered fin AIChE Symposium series:19-27.
Dietenberger M.A. (1982) A Frost Formation Model and Its Validation Under Various Experimental Conditions. NASA Contmctor Rept 3595 Ma&all Space Flight Center under Contract NASS-33369.
Dietenberger M.A. (1983) Generalized correlation of the water frost thermal conductivity. International Journal of Heat and Mass Transfer 26:607-619.
Dorsch R.G., Hacker P.T. (1950) Photomicrographic investigation of spontaneous freezing temperatures of supercooled water drops. NACA Tech. Note, Washington D.C. USA 2142:57.
Dufour L., Defay R. (1963) Thermodynamics of Clouds. Academic Press, New York.:255.
Dyer J.M., Storey B.D., Hoke J.L., Jacobi A.M., Georgiadis J.G. (2000) An experimental investigation of the effect of hydrophobicity on the rate of frost growth in laminar channel flows. ASHRAE Transactions 106:143–151.
Edwards G.R., Evans L.F. (1960) Ice nucleation by silver iodine I. Freezing vs. sublimation. J. Met. 17:627-634.
Edwards G.R., Evans L.F. (1962) Effect of surface charge on ice nucleation by silver iodine. Trans. Faraday Soc. 58:1649-1695.
Edwards G.R., Zipper A.F. (1970) Two-dimensional phase changes in water adsorbed on ice-nucleating substrates Trans. Faraday Soc. 66:220-234.
Emery A.F., Siegel B.L. (1990) Experimental measurements of the effects of frost formation on heat exchanger performance. AIAA/ASME Thermophysics and Heat Transfer Conference, ASME HTD 139:1-7.
Fahrenheit D.G. (1724) Experimenta & observationes de congelatione aquae in cacue factae. Phil. Trans. 33:78-84.
Fletcher N.H. (1958) Size effect in heterogeneous nucleation. J. chem. Phys. 29:572-576.
Fletcher N.H. (1959a) Entropy effect in ice crystal nucleation. J. chem. Phys. 30:1476-82.
Fletcher N.H. (1959b) On ice crystal production by aerosol particles. J. Met. 16:173.
Fletcher N.H. (1960) Nucleation and growth of ice crystals upon crystalline substratets. Aust. J. Phys. 13:408-418.
Fletcher N.H. (1962) The Physics of Rainclouds. Cambridge University Press.:386.
Fletcher N.H. (1969) Active sites and ice crystal nucleation. J. Atmos. Sci. 26:1266-1271.
Fossa M., Tanda G. (2010) Frost formation in vertical channels under natural convection. International Journal of Multiphase Flow 36:210-220.
Fournier F.D.A. (1949) Some experiments on condensation of water vapor at temperature below 0°C. Q. Jl. R. met. Soc. 75:1-14.
Frank F.C. (1949) The influence of dislocations on crystal growth. Disc. Faraday Soc. 5:48.
Frenkel J. (1946) Kinetic Theory of Liquids. Oxford University Press.:P. 488.
Fukuta n. (1958) Experimental investigations on the ice-forming ability of various

chemical substances. J. Met. 15:17-26.
Fukuta N. (1963) Ice nucleation by metaldehyde. Nature Lond. 199:475-476.
Goodman J. (1972) Free convection frost formation on cool surfaces. Ph.D. Dissertation State University of New York at Buffalo, NY, USA.
Goodman J., Kennedy L.A. (1972) Free Convection Frost Formation on Cool Surfaces. Proceedings of the 1972 Heat Transfer and Fluid Mechanics Institute, Stanford University Press.:338-352.
Hallett J., Mason B.J. (1958) The influence of temperature and supersaturation on the habit of ice crystals grown from the vapor. Proc. Roy. Soc. A 247:440.
Hamilton W.C., Katsanis E.P., Zettlemoyer A.C. (1968) An IR investigation of water adsorbed at different relative hunidities on silicas of varying ice nucleation capabilities. In proc. 1st national conference on weather modification, Albany, New York, American Meteorological Society, Boston:336-342.
Hanajima M. (1944) On the conditions of growth of snow crystals. Low Temperature Science A1:53-65.
Hanajima M. (1949) On the growth conditions of man-made snow. Low Temperature Science A2:23-29.
Hayashi Y., Aoki K., Yuhara H. (1977a) Study of Frost Formation Based on a Theoretical Model of the Frost Layer. Heat transfer, Japanese research 6:79-94.
Hayashi Y., Aoki A., Adachi S., Hori K. (1977b) Study of Frost Properties Correlating with Frost Formation Types. Journal of heat transfer 99:239-245.
He Z., Peng X., Xing Z., Shu P. (2003) Operating characteristics of an air-source heat pump under frosting/defrosting conditions. Proc. Instn Mech. Engrs Vol. 217 Part A: J. Power and Energy:623.
Head R.B. (1961) Steroids as ice nucleators. Nature, Lond.:1058-1059.
Head R.B. (1962) Ice nucleation by some cyclic compounds. J. Phys. Chem. Solids 23:1371-1378.
Heverly J.R. (1949) Supercooling and crystallization. Trans. Am. geophys. Union 30:205-210.
Hobbs P.V. (1974) Ice Physics Oxford University Press, London, UK.
Hoke J.L. (2000) The Interaction between the Substrate and Frost Layer through Condensate Distribution. PhD Dissertation University of Illinois Urbana-Champaign. Department of Mechanical and Industrial Engineering.
Hoke J.L., Georgiadis J.G., Jacobi A.M. (2004) Effect of substrate wettability on frost properties. Journal of Thermophysics and Heat Transfer 18:228-235.
Hong T., Moallem E., Cremaschi L., Fisher D. (2012) Measurements of Frost Growth on Louvered Folded Fins of Microchannel Heat Exchangers, Part 1: Experimental Methodology. ASHRAE Transactions 118:(Preprint under preparation).
Hosler C.L. (1951) On the crystallization of supercooled clouds. J. Met. 8:326-331.
Hosoda T., Uzuhashi H. (1967) Effects of frost on the heat transfer coefficient. Hitachi Review 16:254-259.
Huang C.H. (2002) An Inverse Geometry Problem in Estimating Frost Growth on an Evaporating Tube. Heat and Mass Transfer 38:615-623.
Huang D., Yuan X., Zhang X. (2004) Effects of fan-starting methods on the reverse-cycle defrost performance of an air-to-water heat pump. International Journal of Refrigeration 27:869-875.

Huang D., He Z.L., Yuan X.L. (2007) Dynamic characteristics of an air-to-water heat pump under frosting/defrosting conditions. Applied Thermal Engineering 27:1996-2002.
Huang L., Liu Z., Liu Y., Gou Y., Wang J. (2009) Experimental study on frost release on fin-and-tube heat exchangers by use of a novel anti-frosting paint. Experimental Thermal and Fluid Science 33:1049-1054.
Iragorry J., Tao Y.-X. (2004) Frost density measurement for evaporator defrosting control. Proceeeding of IMECE04, ASME International Mechanical Engineering Congress and Exposition Novermber 13-20, 2004, Anaheim, CA, USA 441.
Iragorry J., Tao Y.-X. (2005) Frost temperature relations for defrosting sensing system. Transactions of ASME 127:344-351.
Ismail K.A.R., Salinas C.S. (1999) Modeling of frost formation over parallel cold platesModélisation de la formation de givre sur les plaques froides parallèles. International Journal of Refrigeration 22:425-441.
Jacobi A.M., Park Y., Zhong Y., Michna G., Xia Y. (2005) High Performance Heat Exchangers for Air-Conditioning and Refrigeration Applications (Non-Circular Tubes). Final Report ARTI 21CR Program Contract Number 605-20021.
Jaffray J., Montmory R. (1957a) Epitaxies de la glace sur l'iodure d'argent. C.r. hebd. Seanc. Acad. Sci., Paris 245:2221-2224.
Jaffray J., Montmory R. (1957b) Congelation orientee de l'eau sur fondue sur une surface cristalline. Cas de l'argent et de l'iodure d'argent. C.r. hebd. Seanc. Acad. Sci., Paris 244:859-861.
Jeffreys H. (1918) Some problems of evaporation. Phil. Mag. 35:270.
Jhee S., Lee K.-S., Kim W.-S. (2002) Effect of surface treatments on the frosting/defrosting behavior of a fin-tube heat exchanger. International Journal of Refrigeration 25:1047-1053.
Joardar A., Gu Z., Jacobi A.M. (2006) Off-cycle condensate drainage behavior of compact heat exchangers: assessment and enhancement. International Refrigeration and Air Conditioning Conference at Purdue, Purdue University, West Lafayette, IN.
Jones B.W., Parker J.D. (1975) Frost Formation with Varying Environmental Parameters. ASME Journal of Heat Transfer 1915:255-259.
Kamath J. (1985) Frost Formation between Closely Spaced Parallel Plates. PhD Dissertation University of Michigan, USA.
Karasz F.E., Champion W.M., Halsey G.D. (1956) The growth of ice layers on the surfaces of anatase and silver iodine. J. Phys. Chem. 60.
Kennedy L.A., Goodman J. (1974) Free convection heat and mass transfer under conditions of frost deposition. International Journal of Heat and Mass Transfer 17:477-484.
Kim J.-H., Groll E.A. (2003a) Microchannel Heat Exchanger Defrost Performance and Reliability. ASHRAE final report 1195-RP, Atlanta, GA, USA.
Kim J.-S., Yang D.-K., Lee K.-S. (2008) Dimensionless correlations of frost properties on a cold cylinder surface. International Journal of Heat and Mass Transfer 51:3946-3952.
Kim J.-S., Lee K.-S., Yook S.-J. (2009) Frost behavior on a fin considering the heat conduction of heat exchanger fins. International Journal of Heat and Mass

Transfer 52:2581-2588.
Kim J., Groll E.A. (2002) Performance comparisons of a unitary split system using microchannel and fin-tube outdoor coils, part II: heating test. Proceedings of the 2002 International Refrigeration and Air Conditioning Conference at Purdue, West Lefeyette, IN, USA 1:249-256.
Kim J., Groll E.A. (2003b) Performance comparisons of a unitary split system using microchannel and fintube out-door coils. ASHRAE Transactions 109:219-229.
Kim M.-H., Bullard C.W. (2002) Air-side performance of brazed aluminum heat exchangers under dehumidifying conditions. International Journal of Refrigeration 25:924-934.
Kleber W., Weis J. (1958) Keimbildung und epitaxie von eis. I. Z. Kristallogr 110:30-46.
Kobayashi T. (1957) Experimental researches on the snow crystal habit and growth by means of a diffusion cloud chamber. Meteorological Society of Japan 75th anniv. vol.:38.
Kobayashi T. (1958) On the habit of snow crystals artificially produced at low pressures. Journal of the Meteorological Society of Japan series 2 36:193.
Kondepudi S.N. (1988) The Effects of Frost Growth on Finned Tube Heat Exchangers under Laminar Flow. PhD Dissertation Mecahnical Engineering Department, Texas A&M University, TX, USA.
Kondepudi S.N., O'Neal D.L. (1989) Effect of frost growth on the performance of louvered finned tube heat exchangers. International Journal of Refrigeration 12:151-158.
Kondepudi S.N., O'Neal D.L. (1991) Frosting performance of tube fin heat exchangers with wavy and corrugated fins. Experimental Thermal and Fluid Science 4:613-618.
Kondepudi S.N., O'Neal D.L. (1993) Performance of finned-tube heat exchangers under frosting conditions: I. Simulation model. International Journal of Refrigeration 16:175-180.
Krastanow L. (1940) Uber die bildung der unterkuhlten Wasserstrophen und der Eikristalle in der freien Atmosphare. Met. Z. 57:357-371.
Krastanow L. (1943) Uber die bildung und das wachstum der eiskristalle in der atmosphare. Met. Z. 60:15.
Kulkarni T., Bullard C.W., Cho K. (2004) Header design tradeoffs in microchannel evaporators. Applied Thermal Engineering 24:759-776.
Lafargue C. (1950) On the freezing of droplets of water and of aqueous solutions. Centenary Proceedings of the Royal Meteorological Society:61-63.
Langer G., Rosinski J., Bernsen S. (1963) Organic crystals as icing nuclei. J. Atmos. Sci. 20:557-562.
Le Gall R., Grillot J.M., Jallut C. (1997) Modelling of frost growth and densification. International Journal of Heat and Mass Transfer 40:3177-3187.
Lee H., Shin J., Ha S., Choi B., Lee J. (2004) Frost formation on a plate with different surface hydrophilicity. International Journal of Heat and Mass Transfer 47:4881-4893.
Lee K.-S., Kim W.-S., Lee T.-H. (1997) A one-dimensional model for frost formation on a cold flat surface. International Journal of Heat and Mass Transfer 40:4359-4365.
Lee K.-S., Jhee S., Yang D.-K. (2003) Prediction of the frost formation on a cold flat

surface. International Journal of Heat and Mass Transfer 46:3789-3796.
Lee Y.B., Ro S.T. (2002) Frost formation on a vertical plate in simultaneously developing flow. Experimental Thermal and Fluid Science 26:939-945.
Lee Y.B., Ro S.T. (2005) Analysis of the frost growth on a flat plate by simple models of saturation and supersaturation. Experimental Thermal and Fluid Science 29:685-696.
Lenic K., Trp A., Frankovic B. (2009) Transient two-dimensional model of frost formation on a fin-and-tube heat exchanger. International Journal of Heat and Mass Transfer 52:22-32.
Liu L., Jacobi A.M. (2008) Issues affecting the reliability of dynamic dip testing as a method to assess the condensate drainage behavior from the air-side surface of dehumidifying heat exchangers. Experimental Thermal and Fluid Science 32:1512-1522.
Liu L., Jacobi A.M., Chvedov D. (2009) A surface embossing technique to create micro-grooves on an aluminum fin stock for drainage enhancement. Journal of Micromechanincs and Microengineering 19:1-9.
Lüer A., Beer H. (2000) Frost deposition in a parallel plate channel under laminar flow conditions. International Journal of Thermal Sciences vol. 39:85-95.
Mao Y., Besant R.W., Rezkallah K.S. (1992) Measurement and Correlations of Frost Properties with Airflow over a Flat Plate. ASHRAE Transactions 98:65-78.
Mao Y., Besant R.W., Falk J. (1993) Measurements and Correlations of Frost Properties with Laminar Airflow at Room Temperature over a Flat Plate. ASHRAE Transactions 99:739-745.
Mao Y., Besant R.W., Chen H. (1999) Frost Characteristics and Heat Transfer on a Flat Plate Under Freezer Operating Conditions: Part I, Experimentation and Correlations. ASHRAE Transactions 105:231-251.
Martinez-Frias J., Aceves S.M. (1999) Effects of Evaporator Frosting on the Performance of an Air-to-Air Heat Pump. ASME Journal of Energy Resources Technology 121:60-65.
Martinez-Frias J., Aceves S.M., Hernandez-Guerrero A. (1996) A transient analysis of frost formation on parallel plate evaporator. Proceedings of the ASME Advanced Energy Systems Division, ASME AES 36:101-106.
Mason B.J. (1953) The growth of ice crystals in a supercooled water cloud. Quart. J. R. Met. Soc. 79:104.
Mason B.J. (1957) The Physics of Clouds. Oxford University Press.
Mei V.C., Domitrovic R.E., Chen F.C., Kilpatrick J.K. (2002) A Frost-Less Heat Pump. ASHRAE Transactions 108:AC-02-5-2 (4543).
Moallem E., Cremaschi L., Fisher D.E. (2010a) Experimental Investigation of Frost Growth on Microchannel Heat Exchangers. International Refrigeration and Air Conditioning Conference at Purdue University West Lafayette, IN, USA, July 12-15, 2010.
Moallem E., Padhmanabhan S., Cremaschi L., Fisher D.E. (2010b) Experimental Study of Onset and Growth of Frost on Outdoor Coils of Air-Source Heat Pump Systems. Proceedings of ASME-ATI-UIT, Conference on Thermal and Environmental Issues in Energy Systems May 16-19, Sorrento, Italy.
Moallem E., Padhmanabhan S., Cremaschi L., Fisher D.E. (2011) Effect of surface

coating on frosting performance of microchannel heat exchangers for heat pump systems, Proceedings of International Conference on Air-Conditioning & Refrigeration, July 6-8, 2011, Yongpyong Resort, Gangwon-Do, KOREA.
Moallem E., Hong T., Cremaschi L., Fisher D.E. (2012a) Experimental Investigation of Adverse Effect of Frost Formation on Microchannel Evaporators, Part 1: Effect of Fin Geometry and Environmental Effects. International Journal of Refrigeration (Under Review).
Moallem E., Padhmanabhan S., Cremaschi L., Fisher D.E. (2012b) Experimental investigation of the surface temperature and water retention effects on the frosting performance of a compact microchannel heat exchanger for heat pump systems. International Journal of Refrigeration 35:171-186.
Moallem E., Cremaschi L., Fisher D.E., Padhmanabhan S. (2012c) Experimental measurements of the surface coating and water retention effects on frosting performance of microchannel heat exchangers for heat pump systems. Experimental Thermal and Fluid Science 39:176-188.
Moallem E., Hong T., Cremaschi L., Fisher D.E. (2012d) Experimental Investigation of Adverse Effect of Frost Formation on Microchannel Evaporators, Part 2: Effect of Surface Coating and Water Retention. HVAC & R Journal (Under Review).
Montmory R. (1956) La congelation de l'eau surfondue sur une surface crystalline. Bull. Obs. Puy de Dome Ser. 2:126-147.
Mossop S.C. (1955) The freezing of supercooled water. Proceedings of the Physical Society 68:193-208.
Mossop S.C. (1956a) The nucleation of supercooled water by various chemicals. Proc. phys. soc. 69:165-174.
Mossop S.C. (1956b) Sublimation Nuclei. Proc. Phys. Soc. B69:161-164.
Na B. (2003) Analysis of frost formation on the evaporator, Ph.D. Thesis, The Pennsylvania State University, PA, USA.
Na B., Webb R.L. (2003) A fundamental understanding of factors affecting frost nucleation. International Journal of Heat and Mass Transfer 46:3797–3808.
Na B., Webb R.L. (2004a) Mass transfer on and within a frost layer. International Journal of Heat and Mass Transfer 47:899-911.
Na B., Webb R.L. (2004b) New model for frost growth rate. International Journal of Heat and Mass Transfer 47:925-936.
Nakaya U. (1954) Snow Crystals, Natural and Artificial. Harvard University Press, Cambridge.
O'neal D.L. (1982) The effect of frost formation on the performance of a parallel plate heat exchanger, Purdue University, West Lafayette, IN, USA.
O'neal D.L., Tree D.R. (1982) Seasonal performance of air conditioners - the effect of frost formation on the performance of a parallel plate heat exchanger. Sponsored by Department of Energy Report no. 6.
Okoroafor E.U., Newborough M. (2000) Minimising frost growth on cold surfaces exposed to humid air by means of crosslinked hydrophilic polymeric coatings. Applied Thermal Engineering 20:737-758.
Ostin R., Johannesson G. (1991) A polymeric approach to couteract frosting in ait to air heat exchangers. Heat Recovery Systesms and CHP 11:415-421.
Östin R., Andersson S. (1991) Frost growth parameters in a forced air stream.

International Journal of Heat and Mass Transfer 34:1009-1017.
Padhmanabhan S., Fisher D.E., Cremaschi L., Knight J. (2008) Comparison of frost and defrost performance between microchannel coil and fin-and-tube coil for heat pump systems. 12th International Refrigeration and Air Conditioning Conference at Purdue West Lafayette, IN, USA, paper no. R2202.
Padhmanabhan S.K., Fisher D.E., Cremaschi L., Moallem E. (2011) Modeling non-uniform frost growth on a fin-and-tube heat exchanger. International Journal of Refrigeration 34:2018-2030.
Park C.Y., Hrnjak P. (2007) Effect of heat conduction through the fins of a microchannel serpentine gas cooler of transcritical CO2 system. International Journal of Refrigeration 30:389-397.
Park Y.-G., Jacobi A.M. (2009) Air-side heat transfer and friction correlations for flat-tube louver-fin heat exchangers. Journal of heat transfer 131:1-12.
Power B.A., Power R.F. (1962) Some amino acids as ice nucleators. Nature Lond. 194:1170-1171.
Pruppacher H.R., Sanger R. (1955a) Mechanismus der vereisung unterkuhlter wassertrophen durch disperse keimsubstanzen I. Experimentelle untersuchunger uber die eiskeimfahigkeit der stoffe. Z. angew. Math Phys. 6:406-416.
Pruppacher H.R., Sanger R. (1955b) Mechanismus der vereisung unterkuhlter wassertrophen durch disperse keimsubstanzen II. Zur deutung der eiskeimfahigkeit der stoffe. Z. angew. Math Phys. 6:485-493.
Rau W. (1951) Eiskeimbildung durch dielektrische polarisation. Z. Naturforsch 6a:649-657.
Reynolds S.E., Vonnegut B., Schaefer V.J. (1951) Effect of sunlight on the action of silver iodine particles as sublimation nuclei. Bull. Am. met. Soc. 32:47.
Rice C.K. (1991) The ORNL Modulating Heat Pump Design Tool - User's Guide. Oak Ridge National Laboratory Report ORNL-CON 343.
Robinson C.M., Jacobi A.M. (2001) A study of frost formation on a plain fin. Technical report, Air Conditioning and Refrigeration Center. TR-188:61.
Rosner D.E., Epstein M. (1968) Fog formation conditions near cool surfaces. Journal of Colloid and Interface Science 28:60-65.
Rumpf E., Geigl E. (1938) Uber Beobachtungen an kleinen Flussigkeit stropfchen. Z. Phys. 111:301-313.
Sahin A.Z. (1988) Nucleation of Frost on Cold Surfaces. Ph.D. Dissertation, University of Michigan, Mechanical Engineering Department.
Sahin A.Z. (1994) An experimental study on the initiation and growth of frost foramation on a horizontal plate. Experimental Heat Transfer: An International Journal 7:101-119.
Sahin A.Z. (2000) Effective thermal conductivity of frost during the crystal growth period. International Journal of Heat and Mass Transfer 43:539-553.
Sami S.M., Duong T. (1988) Numerical Prediction of Frost Formation on Cooled Heat Exchangers. International Communication of Heat and Mass Transfer 15:81-94.
Sami S.M., T. Duong. (1989) Mass and Heat Transfer during Frost Growth. ASHRAE Transactions 95:158-165.
Sanders C.T. (1974) The influence of frost formation and defrosting on the performance of air coolers, Ph.D. Thesis, Technische Hogeschool, Delft, Netherlands.

Satio H., Tokura I., Kishinami K., Uemura S. (1984) A Study of Frost Formation (Dimensinless parameters correlating Density and Thickness of Frost Layer. Heat Transfer, Japanese Research 13:76-88.
Schaefer V.J. (1952) Continuous cloud chamber for studying small particles in the atmosphere. Ind. Engng Chem. 44:1381-83.
Schaefer V.J. (1954) Silver and lead iodine as ice crystal nuclei. J. Met. 11:417-419.
Schneider H.W. (1978) Equation of the growth rate of frost forming on cooled surfaces. International Journal of Heat and Mass Transfer 21:1019-1024.
Schulte D.W., Howell R.H. (1982) EFFECT OF AIR TURBULENCE ON THE RATE OF FROST GROWTH ON A HORIZONTAL FLATE PLATE, Technical and Symposium Papers Presented at the 1982 Annual Meeting of the American Society of Heating, Refrigerating and Air-Conditioning Engineers, Inc., ASHRAE, Toronto, Ont, Can. pp. 201-217.
Seker D., Karatas H., Egrican N. (2004a) Frost formation on fin-and-tube heat exchangers. Part I--Modeling of frost formation on fin-and-tube heat exchangers. International Journal of Refrigeration 27:367-374.
Seker D., Karatas H., Egrican P.D.N. (2004b) Frost formation on fin- and- tube heat exchangers. Part II--Experimental investigation of frost formation on fin- and-tube heat exchangers. International Journal of Refrigeration 27:375-377.
Shah Y.T. (1969) Theory of frost formation. Ph.D. Thesis MassachuseIt Institute of Technolog.
Shao L.-L., Yang L., Zhang C.-L. (2010) Comparison of heat pump performance using fin-and-tube and microchannel heat exchangers under frost conditions. Applied Energy 87:1187-1197.
Shaw D., Mason B.J. (1955) The growth of ice crystals from the vapour. Phil. Mag. 46:249.
Sherif S.A., Raju S.P., Padki M.M., Chan A.B. (1993) A semi-empirical transient method for modelling frost formation on a flat plate. International Journal of Refrigeration 16:321-329.
Shimomura N., Kumada M., Cho R., Mizuno T. (2003) A Study of Thermal Performance with Frosting under Forced Convection on a Flat Plate: Prediction of Frost Growth Using Nonhomogeneous Property. Heat Transfer—Asian Research 32.
Shin J., Tikhonov A.V., Kim C. (2003) Experimental study on frost structure on surfaces with different hydrophilicity: density and thermal conductivity. ASME Journal of Heat Transfer 125:84-94.
Shinagawa H., Okuyama K., Kawamura Y. (1992) Observations of Heterogeneous Nucleation of Water vapor on a Cold Substrate. Journal of Chemical Engineering of Japan 25:448-450.
Shinagawa H., Hamada T., Amoto K.-I.M., Okuyama K. (1994) Heterogeneous Nucleation Characteristics of a Eutectic-Forming Vapor Mixture on a Cold Substrate. Separation Science and Technology 29:1823-1840.
Shinagawa H., Miyamoto K.-I., Okuyama K., Wyslouzil B.E. (1995) Simulation of A Transient Heterogeneous Phase Transition. Journal of Chemical Engineering of Japan 28:456-461.
Smith M.H., Griffiths R.F., Latham J. (1971) The freezing of raindrops falling through strong electric fields. Q. Jl. R. met. Soc. 97:495-505.

Sommers A.D., Jacobi A.M. (2006) Creating micro-scale surface topology to achieve anisotropic wettability on an aluminum surface. Journal of Micromechanincs and Microengineering 16:1571–1578.

Sommers A.D., Jacobi A.M. (2008) Modeling the retention of water droplets on topographically modified micro grooved Aluminum. Proceedings of the 2008 ASME Summer Heat Transfer Conference (HT 2008). Aug. 10-14. HT 2008 - 56440:317-326.

Song S., Bullard C.W., Hrnjak P.S. (2002) Frost deposition and refrigerant distribution in microchannel heat exchangers. ASHRAE Transactions 108:944–953.

Steele R.L., Krebs F.W. (1965) Characteristics of silver iodine ice nuclei originating from anhydrous ammonia-silver iodine complexes, p. 52. Colorado State University, Mechanical Engineering Technical Paper 66-1.

Stoecker W.F. (1957) How frost formation on coils affects refrigeration systems. Refrigerating Engineering 65:55.

Stoecker W.F. (1960) Frost formation on refrigeration coils. ASHRAE Transactions 66:91-103.

Storey B.D. (1997) Frost Growth in Laminar Channel Flows. Master Thesis, University of Illinois at Urbana-Champaign, IL, USA.

Storey B.D., Jacobi A.M. (1999) The effect of streamwise vortices on the frost growth rate in developing laminar channel flows. International Journal of Heat and Mass Transfer 42:3787-3802.

Sulakvelidze G.K., Bibilashuli N.S., Lapecheva V.F. (1965) The formation of precipitation and modification of hail processes. Geometeorologicheskoe Izdatel'stvo, p. 207. Leningrad, SSSR (English translation (1967) from U.S. Clearinghouse Frd. Soc. Tech. Inf., U.S. Dept. of Commerce, Washington , D.C.

Tao Y.X., Besant R.W. (1992) Prediction of Spatial and Temporal Distributions of Frost Growth on a Flat Plate under Forced Convection. Journal of Heat Transfer 115:278-281.

Tao Y.X., Besant R.W., Rezkallah K.S. (1993a) A mathematical model for predicting the densification and growth of frost on a flat plate. International Journal of Heat and Mass Transfer 36:353-363.

Tao Y.X., Besant R.W., Mao Y. (1993b) Characteristics of Frost Growth on a Flat Plate during the Eraly Growth Period. ASHRAE Transactions 99:746-753.

Tao Y.X., Mao Y., Besant R.W. (1994) Frost Growth Characteristics on Heat Exchanger Surfaces: Measurement and Simulation Studies. Fundamentals of Phase Change: Sublimation and Solidification, ASME HTD 286:29-38.

Thomas L., Chen H., Besant R.W. (1999) Measurement of frost characteristics on heat exchanger fins, part I: test facility and instrumentation. ASHRAE Transactions 105:283-293.

Tian C., Li X., Yang X. (2005) Numerical analysis of evaporator frosting in automotive air-conditioning system with a variable-displacement compressor. Applied Energy 82:1-22.

Tso C.P., Cheng Y.C., Lai A.C.K. (2006) An improved model for predicting performance of finned tube heat exchanger under frosting condition, with frost thickness variation along fin. Applied Thermal Engineering 26:111-120.

Turnbull D., Fisher J.C. (1949) Rate of nucleation in condensed systems. Journal of

Chemical Physics 17:71-73.
Turnbull D., Vonnegut B. (1952) Nucleation catalysis. Ind. Engng Chem. 44:1292-98.
Verma A.R. (1953) Crystal Growth and Dislocations. London: Butterworth.
Vonnegut B. (1947) The nucleation of ice formation by silver iodine. J. appl. Phys. 18:593-595.
Wang H., Tang L., Wu X., Dai W., Qiu Y. (2007) Fabrication and anti-frosting performance of super hydrophobic coating based on modified nano-sized calcium carbonate and ordinary polyacrylate. Applied Surface Science 253:8818-8824.
Wang S.W., Liu Z.Y. (2005) A new method for preventing HP from frosting. Renewable Energy 30:753-761.
Webb R.L., Jung S.H. (1992) Air-side performance of of enhanced brazed aluminum heat exchangers. Proceedings of ASHRAE Transactions, ASHRAE, Atlanta, GA 98:391-401.
Weickmann H. (1949) Des Eisphase i der Atmosphare. Ber. Deutsch. Wetterd. U.S. Zone 6:54 (Rep. and Trans. 716, Min. of Supply, London).
Weyl W.A. (1949) The surface of glasses as affected by heavy metal ions. Trans. Soc. Glass Tech. 32:247-259.
Woodside W. (1958) Calculation of the thermal conductivity of porous media. Canadian Journal of Physics 36:815-823.
Wu X., Dai W., Xu W., Tang L. (2007a) Mesoscale investigation of frost formation on a cold surface. Experimental Thermal and Fluid Science 31:1043-1048.
Wu X., Dai W., Shan X., Wang W., Tang L. (2007b) Visual and theoretical analyses of early stage of frost formation on cold surfaces. Journal of Enhanced Heat Transfer 14:257-268.
Wu X.M., Webb R.L. (2001) Investigation of the possibility of frost release from a cold surface. Experimental Thermal and Fluid Science 24:151-156.
Wulff G. (1901) Zur frage der geschwindigkeit des wachstums und der auflosung der kristallflachen. Z. Kristallogr 34:449.
Xia Y., Jacobi A.M. (2004) An exact solution to steady heat conduction in a two-dimensional slab on a one-dimensional fin: application to frosted heat exchangers. International Journal of Heat and Mass Transfer 47:3317-3326.
Xia Y., Jacobi A.M. (2005) Air-side data interpretation and performance analysis for heat exchangers with simultaneous heat and mass transfer: Wet and frosted surfaces. International Journal of Heat and Mass Transfer 48:5089-5102.
Xia Y., Jacobi A.M. (2010) A model for predicting the thermal-hydraulic performance of louvered-fin, flat-tube heat exchangers under frosting conditions. International Journal of Refrigeration 33:321-333.
Xia Y., Hrnjak P.S., Jacobi A.M. (2005) Air-Side Thermal-Hydraulic Performance of Louvered-Fin, Flat-Tube Heat Exchangers with Sequential Frost-Growth Cycles. ASHRAE Transactions, Winter Meeting, Orlando, FL, USA 111:487-495.
Xia Y., Zhong Y., Hrnjak P.S., Jacobi A.M. (2006) Frost, defrost, and refrost and its impact on the air-side thermal-hydraulic performance of louvered-fin, flat-tube heat exchangers. International Journal of Refrigeration 29:1066-1079.
Yamakawa N., Takahashi N., Ohtani S. (1971) Heat and mass transfer by forced convection under frosting condition. International Chemical Engineering (Japan) 11:566-573.

Yamakawa N., Takahashi N., Ohtani S. (1972) Forced convection heat and mass under frost condition. Heat transfer, Japanese research 1:1-10.
Yang D.-K., Lee K.-S., Song S. (2006a) Fin spacing optimization of a fin-tube heat exchanger under frosting conditions. International Journal of Heat and Mass Transfer 49:2619-2625.
Yang D.-K., Lee K.-S., Song S. (2006b) Modeling for predicting frosting behavior of a fin-tube heat exchanger. International Journal of Heat and Mass Transfer 49:1472-1479.
Yonko J.D., Sepsy C.F. (1967) An Investigation of the Thermal Conductivity of Frost While Forming on a Flat Horizontal Plate. ASHRAE Transactions 73, Part 2:1.1-1.11.
Yun R., Kim Y., Min M.-k. (2002) Modeling of frost growth and frost properties with airflow over a flat plate. International Journal of Refrigeration 25:362-371.
Zakrzewski B. (1984) Optimal defrost cycle for the air cooler. Butterworth Et Co (Publishers) Ltd and IIR 7:41-45.
Zettlemoyer A.C., Hosler C.L. (1963) Ice nucleation by hydrophobic substrates. J. appl. Math. Phys. 14:496-502.
Zettlemoyer A.C., Tcheurekdjian N., Chessick J.J. (1961) Surface properties of silver iodine. Nature Lond. 192:653.
Zhang P., Hrnjak P.S. (2009) Air-side performance evaluation of three types of heat exchangers in dry, wet and periodic frosting conditions. International Journal of Refrigeration 32:911-921.
Zhang P., Hrnjak P.S. (2010) Air-side performance of a parallel-flow parallel-fin (PF2) heat exchanger in sequential frosting. International Journal of Refrigeration 33:1118-1128.
Zhao Y., Ohadi M.M., Radermacher R. (2001) MICROCHANNEL HEAT EXCHANGERS WITH CARBON DIOXIDE. Final Report, Center for Environmental Energy Engineering, Department of Mechanical Engineering University of Maryland, College Park, College Park, MD, USA.
Zhong Y., JacobiI A.M., Georgiadis J.G. (2006) Condensation and wetting behavior on surfaces with micro-structures: super-hydrophobic and super-hydrophilic. International Refrigeration and Air Conditioning Conference at Purdue University July 17-20, 2006:1-8.
Zhong Y., Joardar A., Gu Z., Park Y.-G., Jacobi A.M. (2005) Dynamic dip testing as a method to assess the condensate drainage behavior from the air-side surface of compact heat exchangers. Experimental Thermal and Fluid Science 29:957-970.

APPENDICES

APPENDIX A: FROST MASS MEASUREMENTS DATA

In the present appendix, the detailed measurements of frost mass for each frost test on each microchannel sample starting form dry-start condition for the first frost cycle are presented.

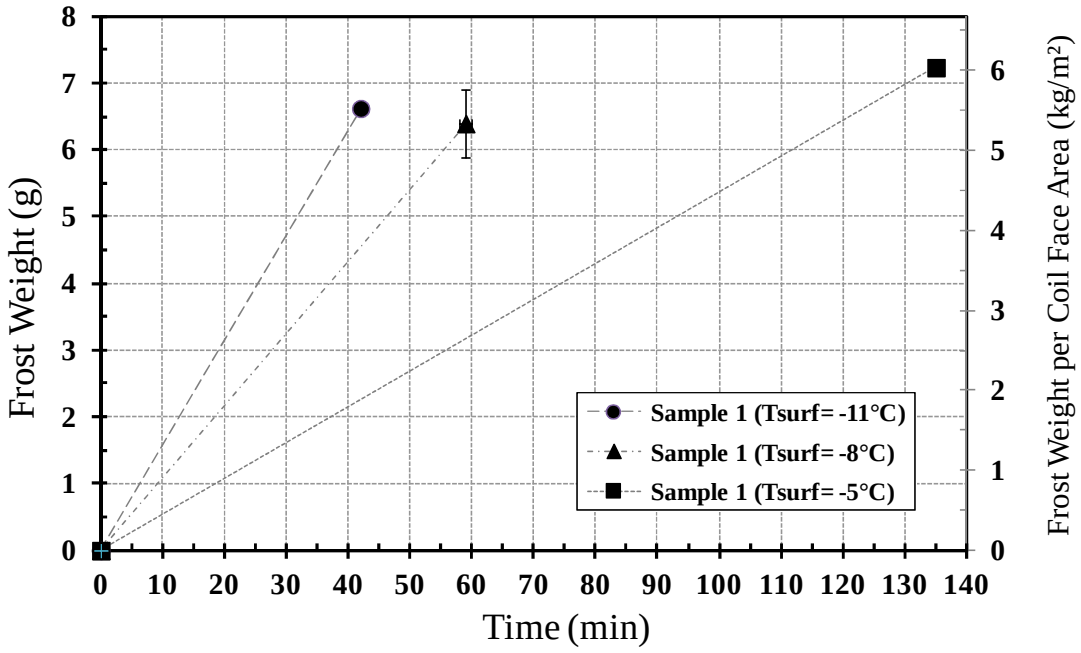

Figure 99: Frost weight measurements on microchannel sample 1 at different surface temperatures.

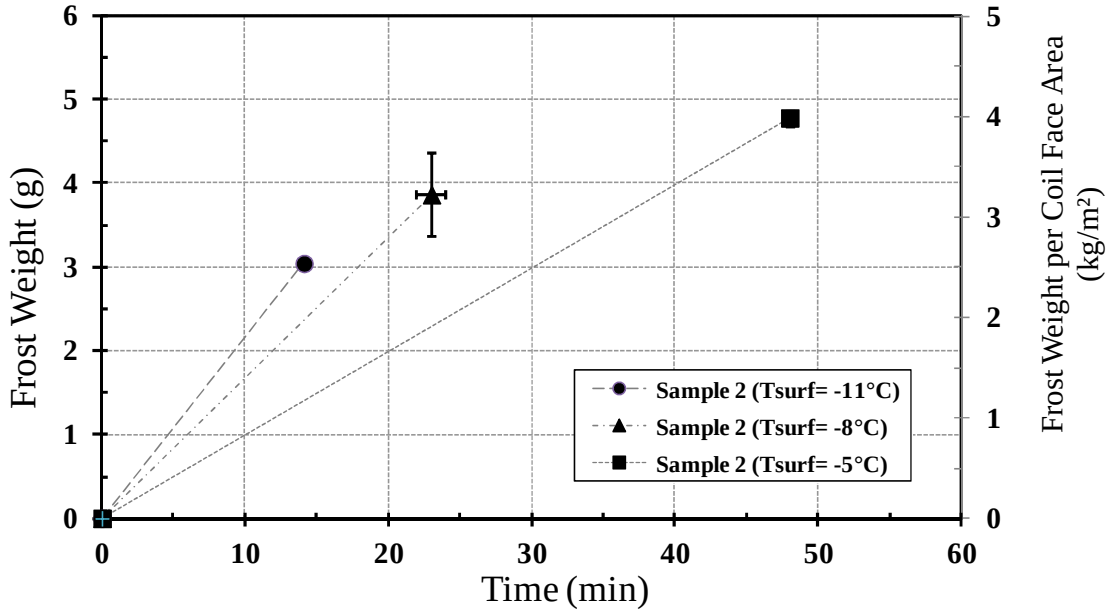

Figure 100: Frost weight measurements on microchannel sample 2 at different surface temperatures.

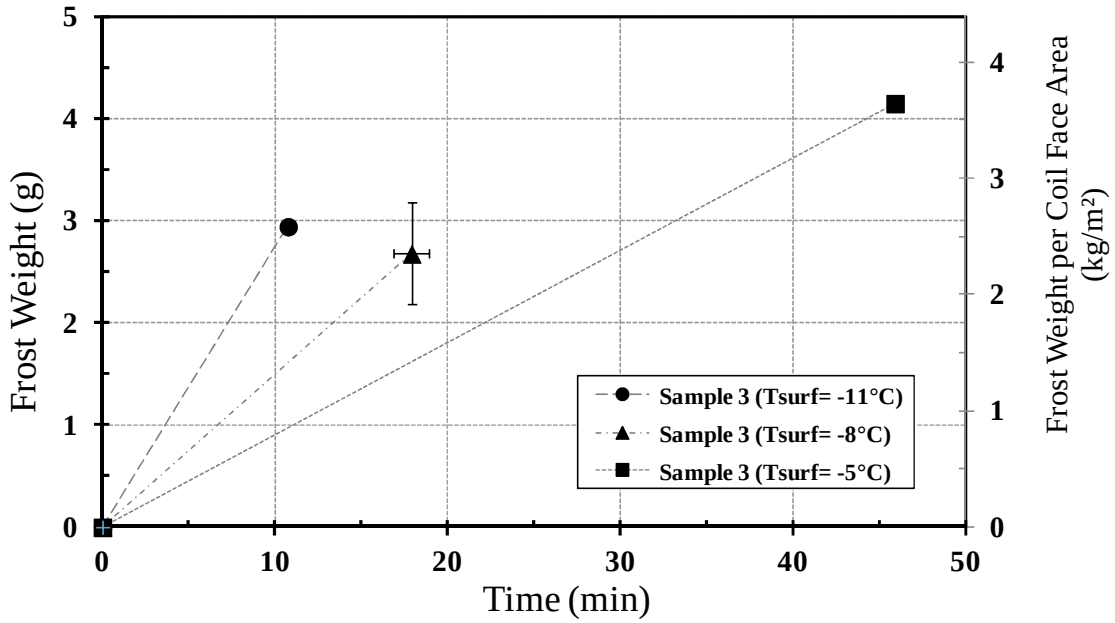

Figure 101: Frost weight measurements on microchannel sample 3 at different surface temperatures.

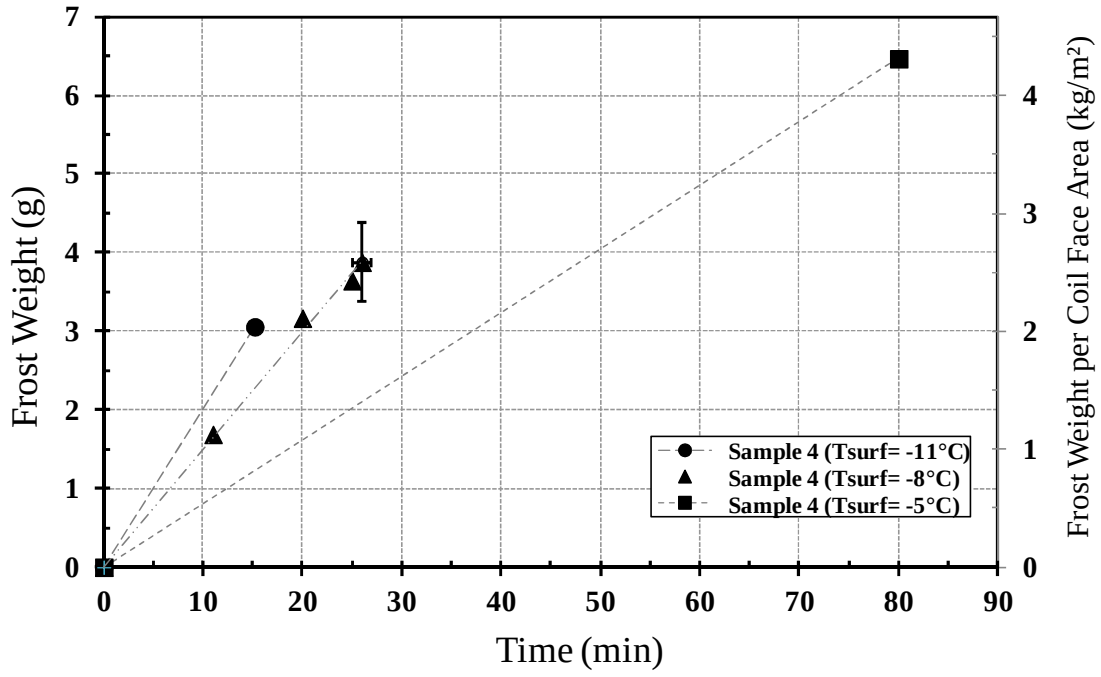

Figure 102: Frost weight measurements on microchannel sample 4 at different surface temperatures (The only -5°C frost test that took long more than 60 minutes among all samples was sample 4. Since sample 4 was not an extreme geometry, author suspected that this was a possible anomaly with the -5°C frost test on sample 4. The time was expected to be about 50 minutes like other samples).

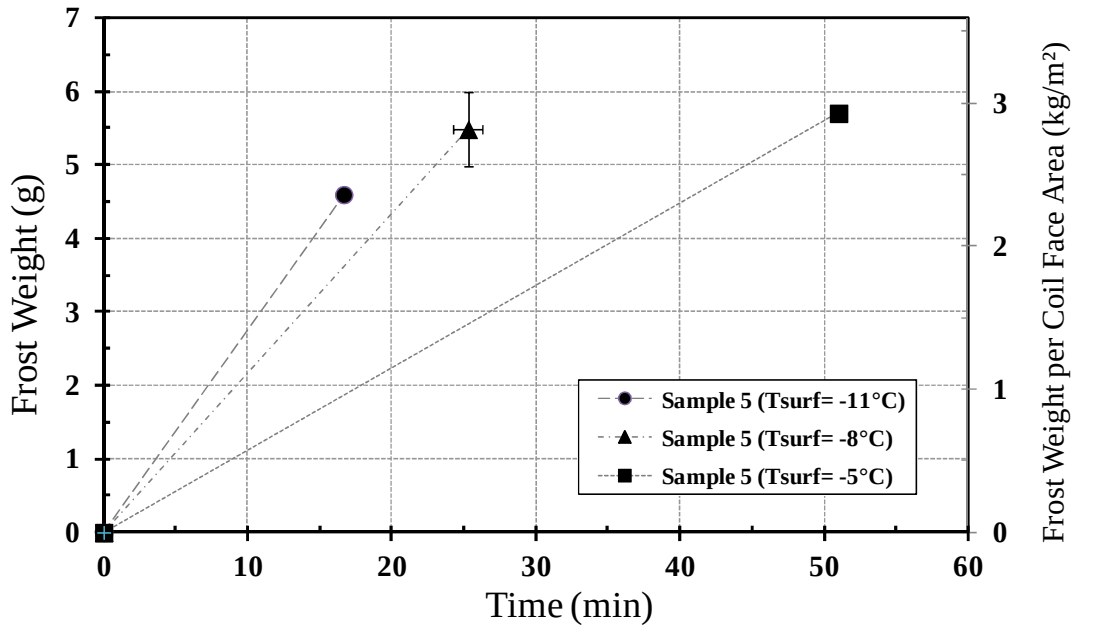

Figure 103: Frost weight measurements on microchannel sample 5 at different surface temperatures.

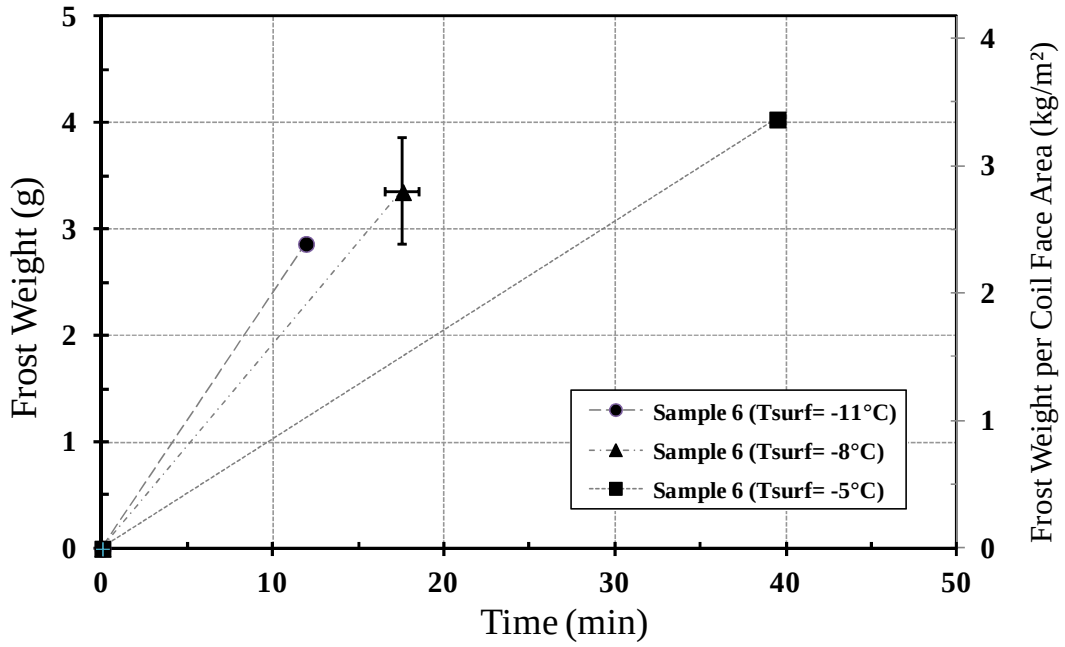

Figure 104: Frost weight measurements on microchannel sample 6 at different surface temperatures.

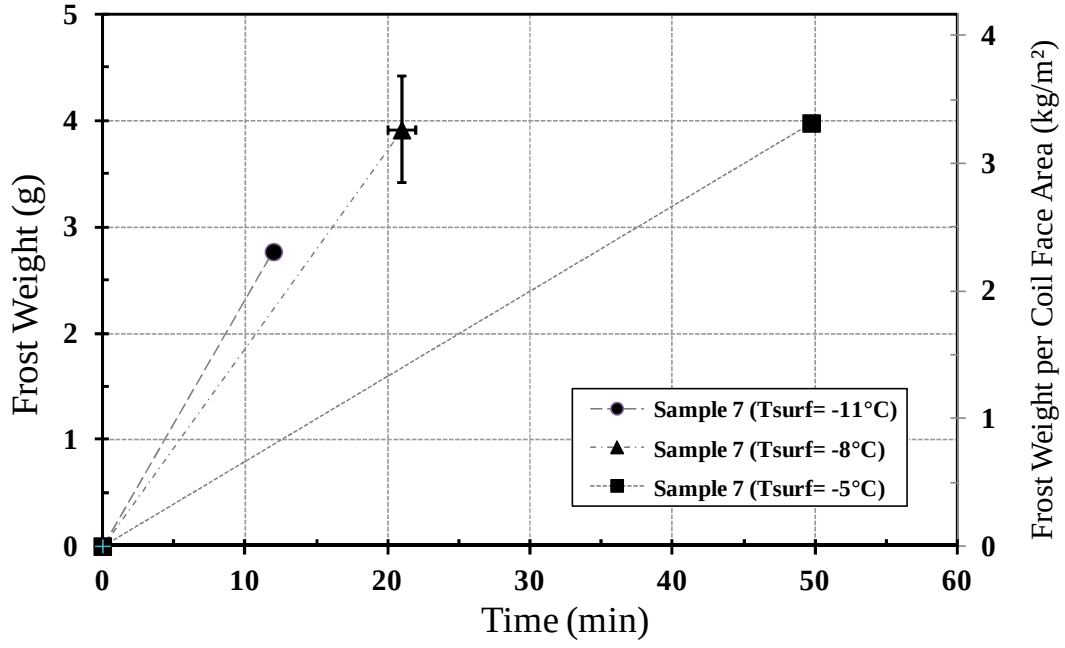

Figure 105: Frost weight measurements on microchannel sample 7 at different surface temperatures.

APPENDIX B: FROST THICKNESS MEASUREMENTS DATA AND DIMENSIONLESS FROST THICKNESS CORRELATION

In the present appendix, the detailed measurements of frost thickness for each frost test on each microchannel sample are presented. On each plot, result of developed frost thickness correlation is also shown.

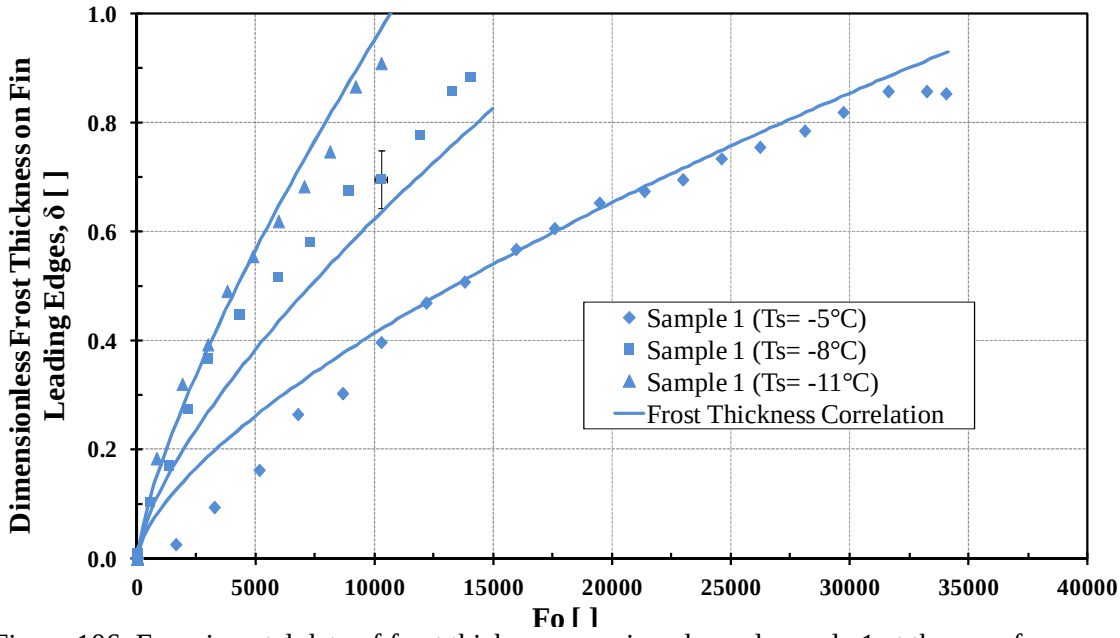

Figure 106: Experimental data of frost thickness on microchannel sample 1 at three surface temperatures. The developed frost thickness correaltion is also shown in the figure. Air temperature = 1.7°C/0.6°C db/wb

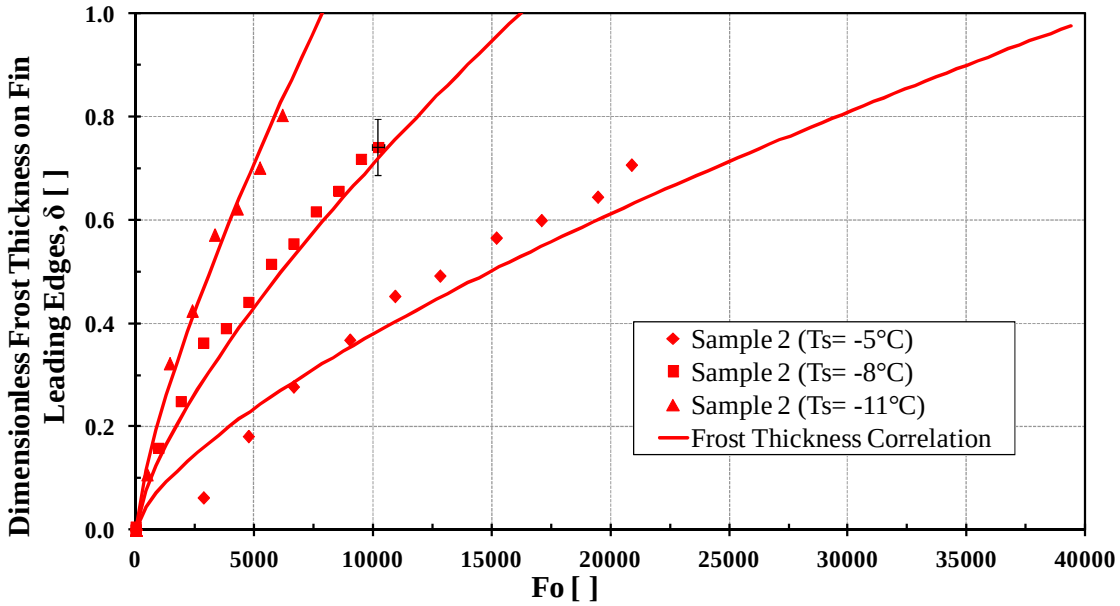

Figure 107: Experimental data of frost thickness on microchannel sample 2 at three surface temperatures. The developed frost thickness correaltion is also shown in the figure. Air temperature = 1.7°C/0.6°C db/wb

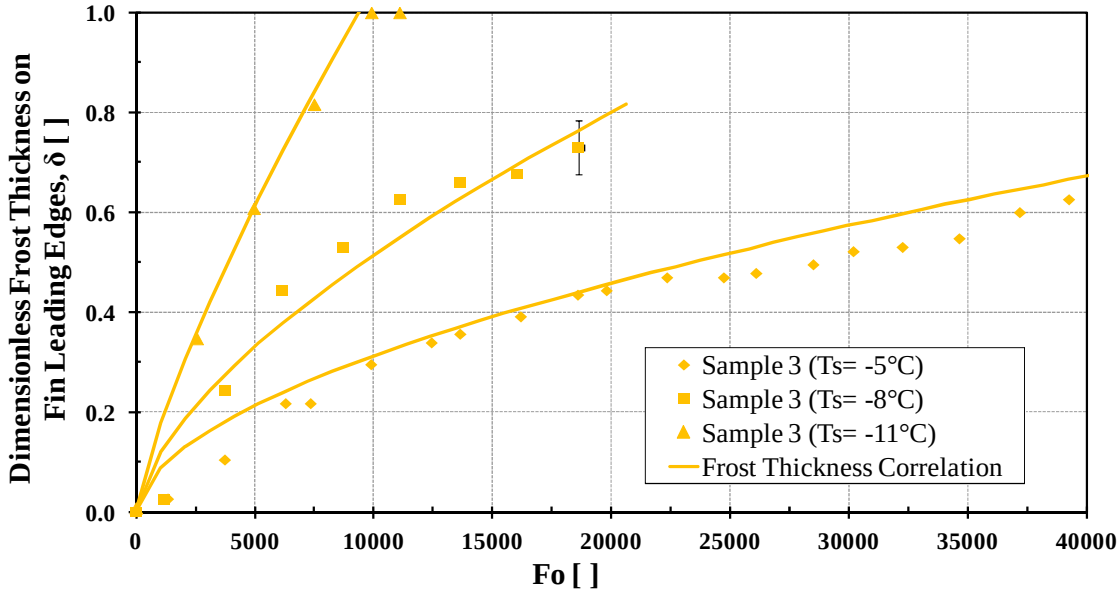

Figure 108: Experimental data of frost thickness on microchannel sample 3 at three surface temperatures. The developed frost thickness correaltion is also shown in the figure. Air temperature = 1.7°C/0.6°C db/wb

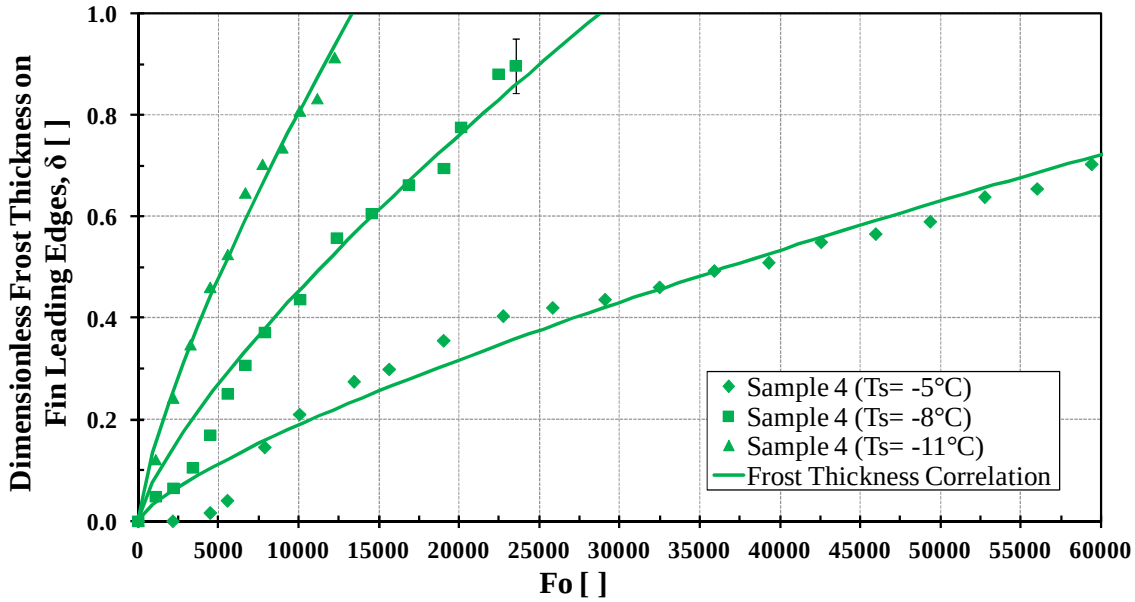

Figure 109: Experimental data of frost thickness on microchannel sample 4 at three surface temperatures. The developed frost thickness correaltion is also shown in the figure. Air temperature = 1.7°C/0.6°C db/wb.

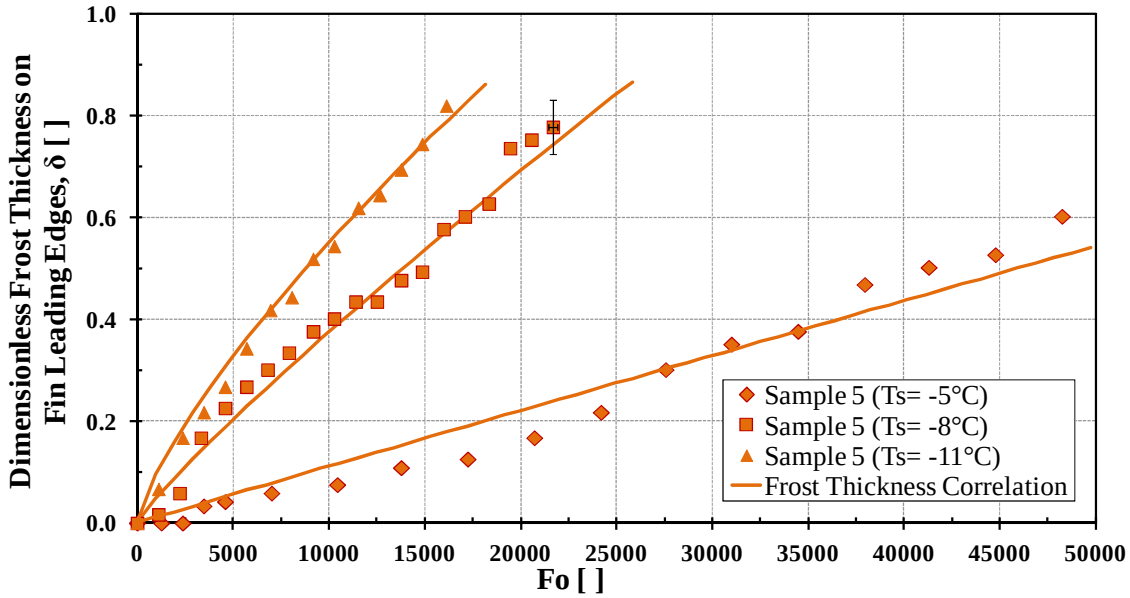

Figure 110: Experimental data of frost thickness on microchannel sample 5 at three surface temperatures. The developed frost thickness correaltion is also shown in the figure. Air temperature = 1.7°C/0.6°C db/wb.

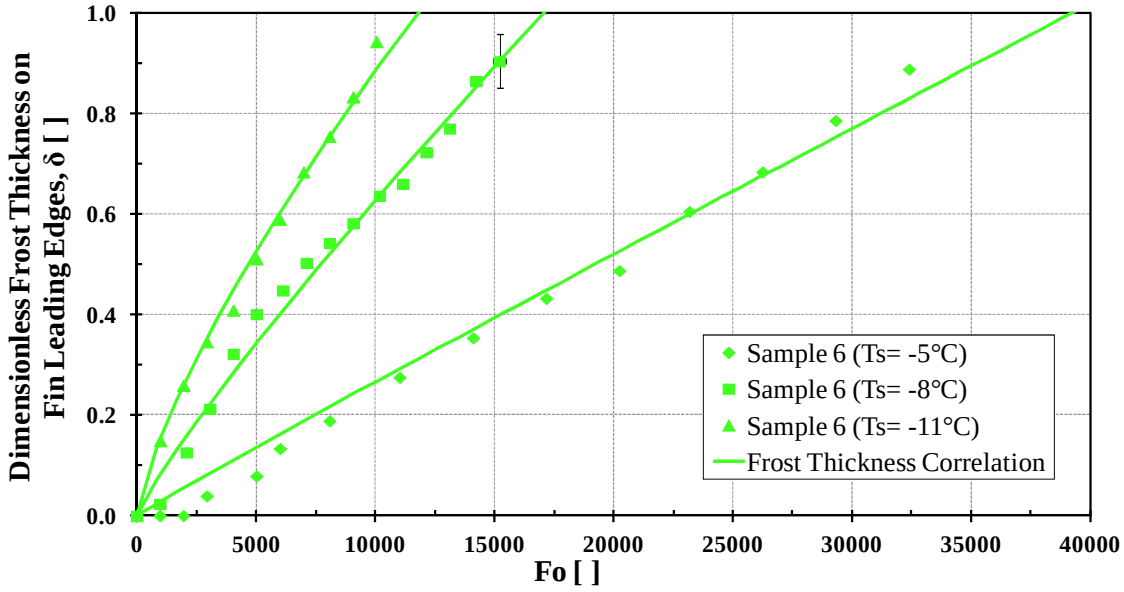

Figure 111: Experimental data of frost thickness on microchannel sample 6 at three surface temperatures. The developed frost thickness correaltion is also shown in the figure. Air temperature = 1.7°C/0.6°C db/wb.

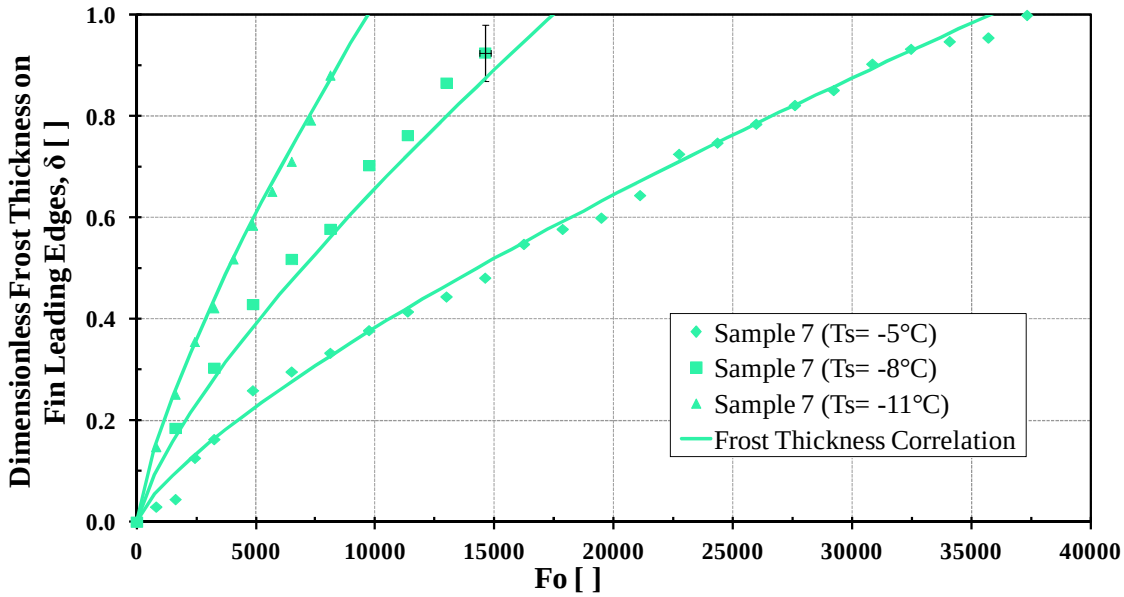

Figure 112: Experimental data of frost thickness on microchannel sample 7 at three surface temperatures. The developed frost thickness correaltion is also shown in the figure. Air temperature = 1.7°C/0.6°C db/wb.

APPENDIX C: FROST THICKNESS MEASUREMENTS DATA AND DIMENSIONAL FROST THICKNESS CORRELATION

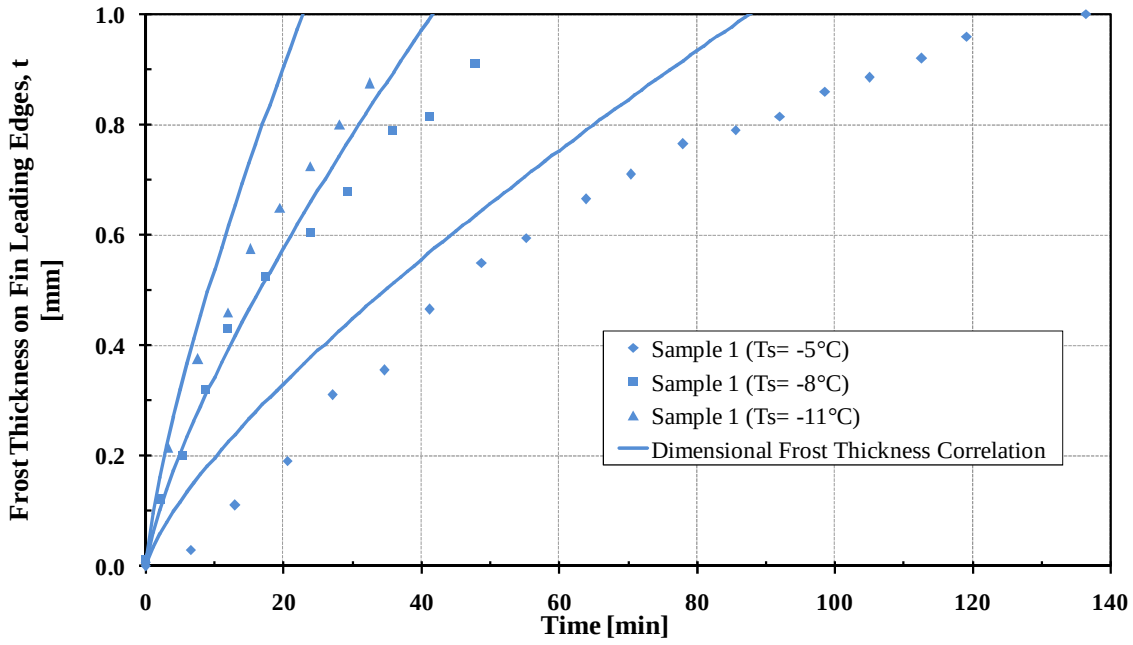

Figure 113: Dimensional form of frost thickness correlation vs experimental data of frost thickness on microchannel sample 1 at three surface temperatures. Air temperature = 1.7°C/0.6°C db/wb.

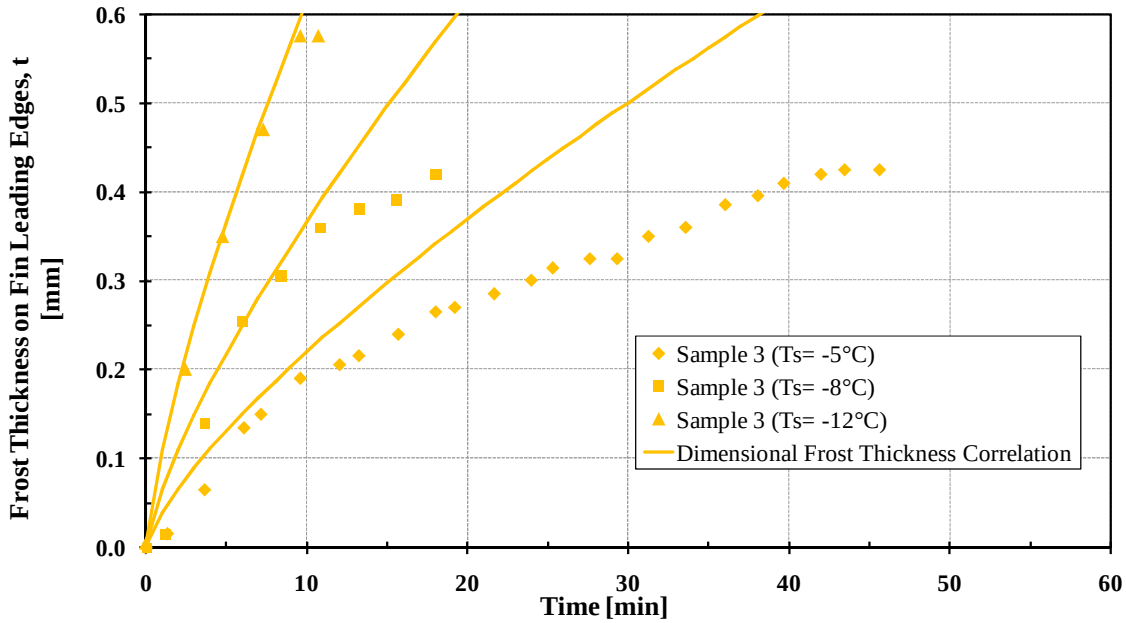

Figure 114: Dimensional form of frost thickness correlation vs experimental data of frost thickness on microchannel sample 3 at three surface temperatures. Air temperature = 1.7°C/0.6°C db/wb.

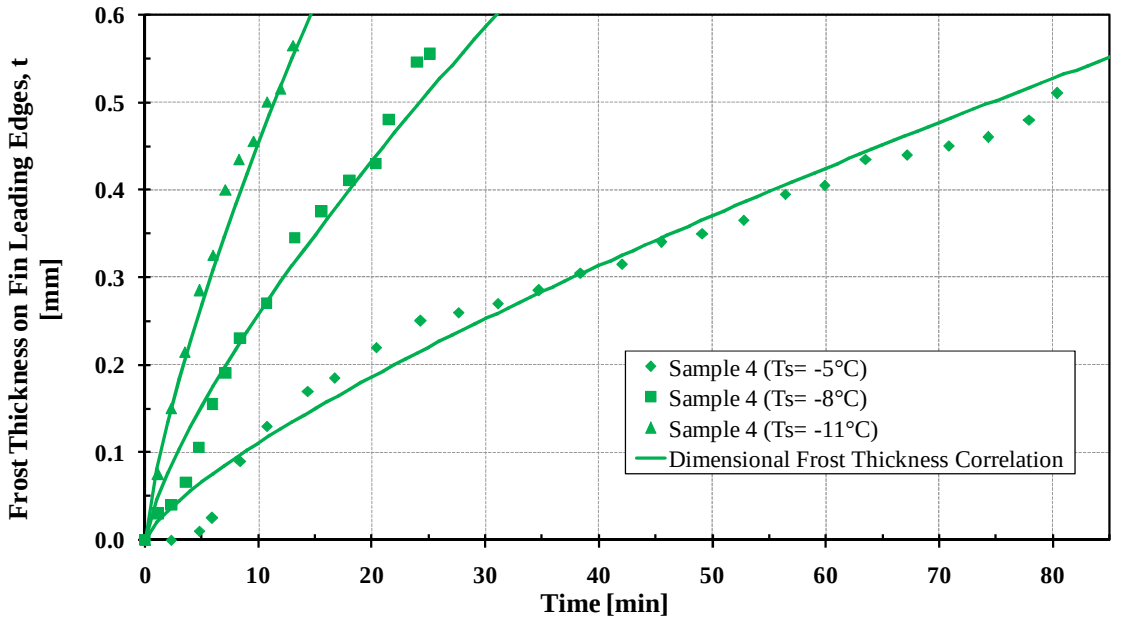

Figure 115: Dimensional form of frost thickness correlation vs experimental data of frost thickness on microchannel sample 4 at three surface temperatures. Air temperature = 1.7°C/0.6°C db/wb.

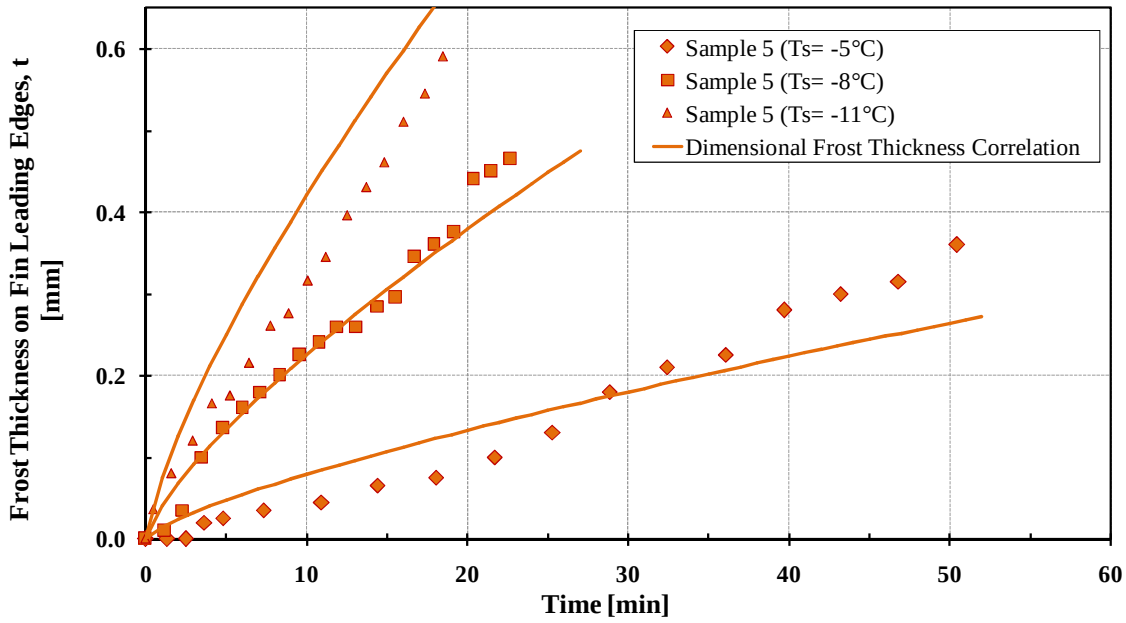

Figure 116: Dimensional form of frost thickness correlation vs experimental data of frost thickness on microchannel sample 5 at three surface temperatures. Air temperature = 1.7°C/0.6°C db/wb.

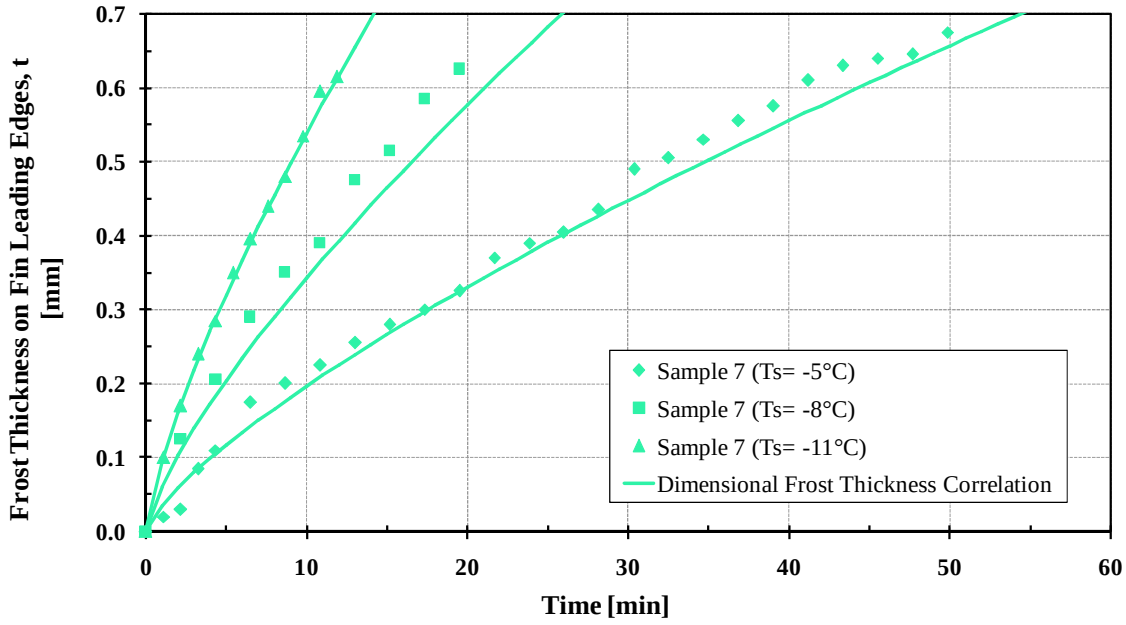

Figure 117: Dimensional form of frost thickness correlation vs experimental data of frost thickness on microchannel sample 7 at three surface temperatures. Air temperature = 1.7°C/0.6°C db/wb.

APPENDIX D: AIR PRESSURE DROP MEASUREMENTS DATA

In the present appendix, the detailed measurements of air side pressure drop during frost tests for each microchannel sample are presented.

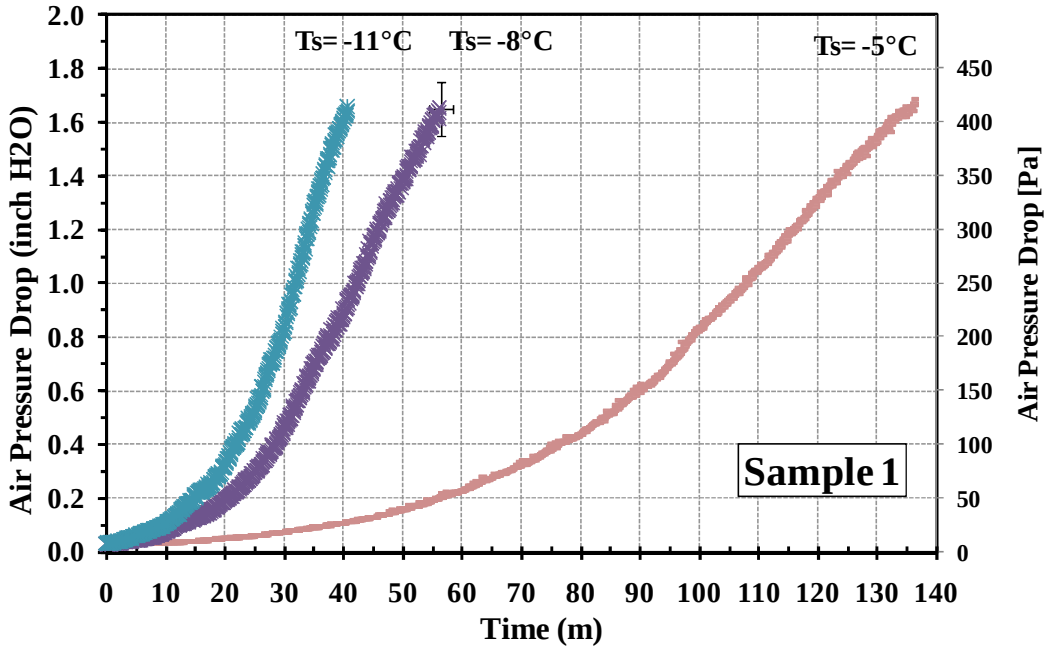

Figure 118: Experimental data of air side pressure drop on microchannel sample 1 under frosting condition at three surface temperatures. Air temperature = 1.7°C/0.6°C db/wb.

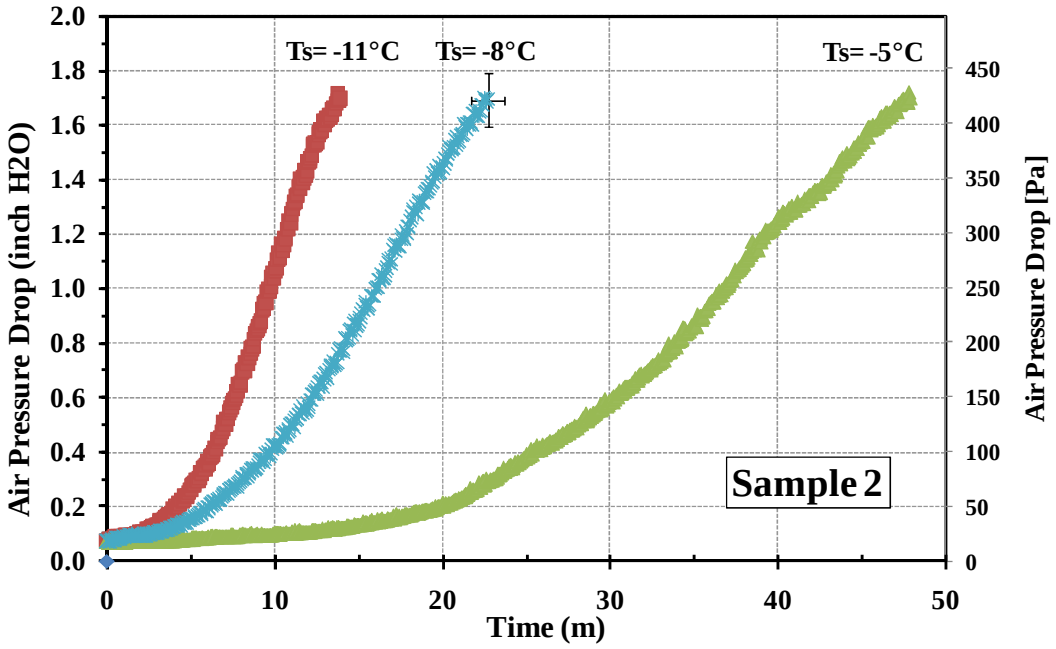

Figure 119: Experimental data of air side pressure drop on microchannel sample 2 under frosting condition at three surface temperatures. Air temperature = 1.7°C/0.6°C db/wb.

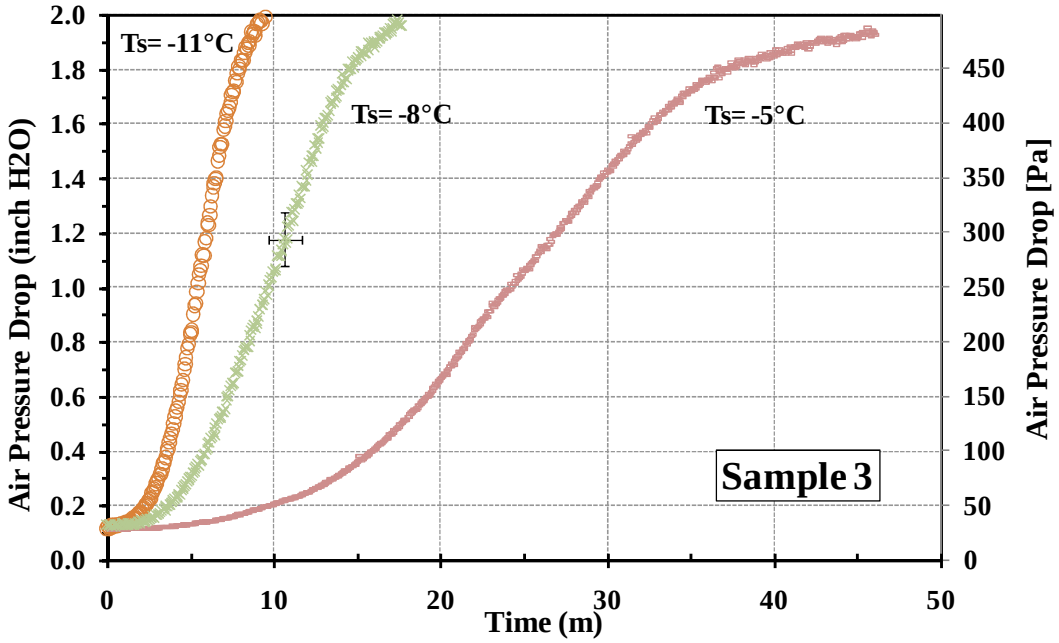

Figure 120: Experimental data of air side pressure drop on microchannel sample 3 under frosting condition at three surface temperatures. Air temperature = 1.7°C/0.6°C db/wb.

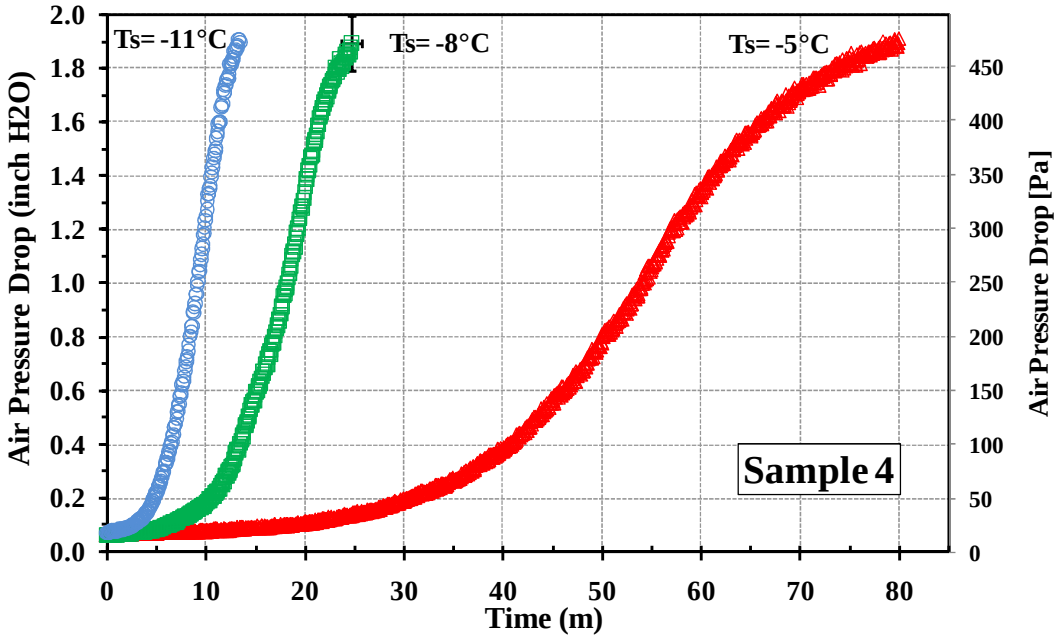

Figure 121: Experimental data of air side pressure drop on microchannel sample 4 under frosting condition at three surface temperatures. Air temperature = 1.7°C/0.6°C db/wb.

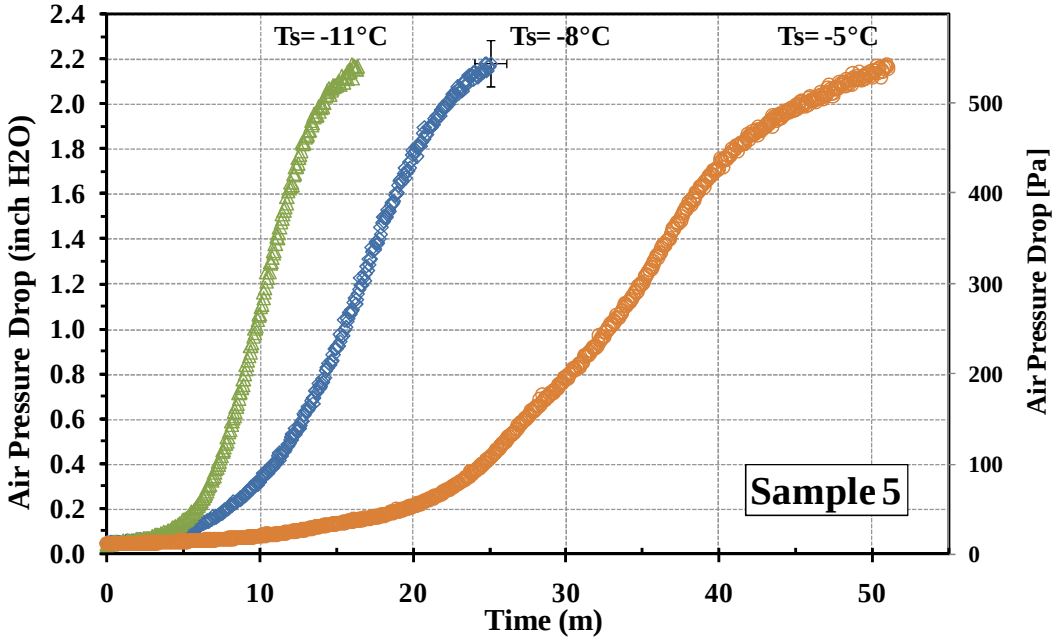

Figure 122: Experimental data of air side pressure drop on microchannel sample 5 under frosting condition at three surface temperatures. Air temperature = 1.7°C/0.6°C db/wb.

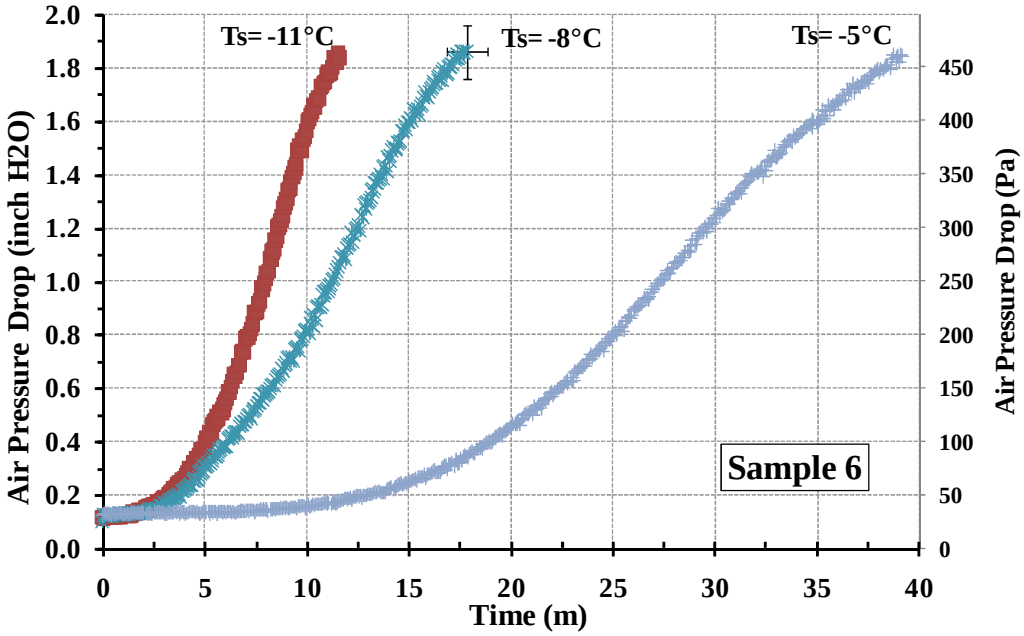

Figure 123: Experimental data of air side pressure drop on microchannel sample 6 under frosting condition at three surface temperatures. Air temperature = 1.7°C/0.6°C db/wb.

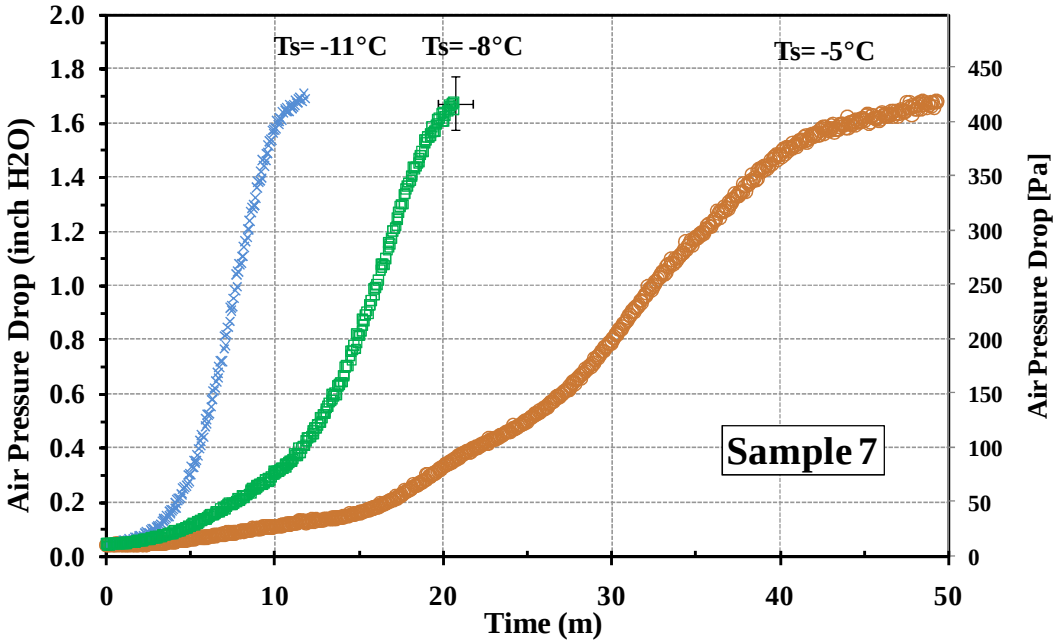

Figure 124: Experimental data of air side pressure drop on microchannel sample 7 under frosting condition at three surface temperatures. Air temperature = 1.7°C/0.6°C db/wb.

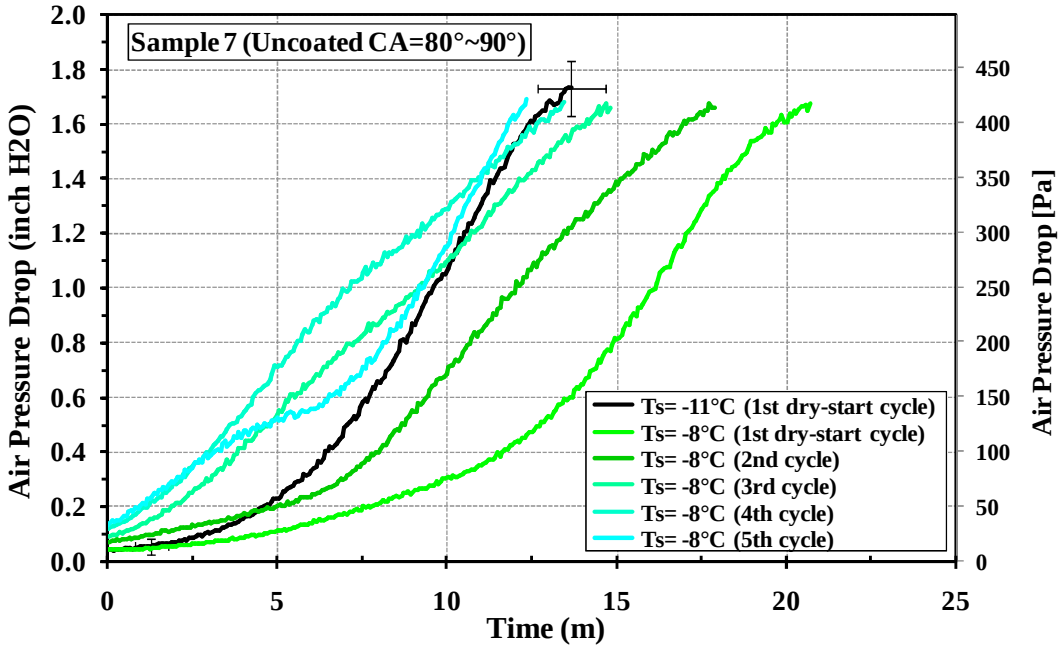

Figure 125: Experimental data of air side pressure drop on microchannel sample 7 under frost/defrost and refrost. Air temperature = 1.7°C/0.6°C db/wb.

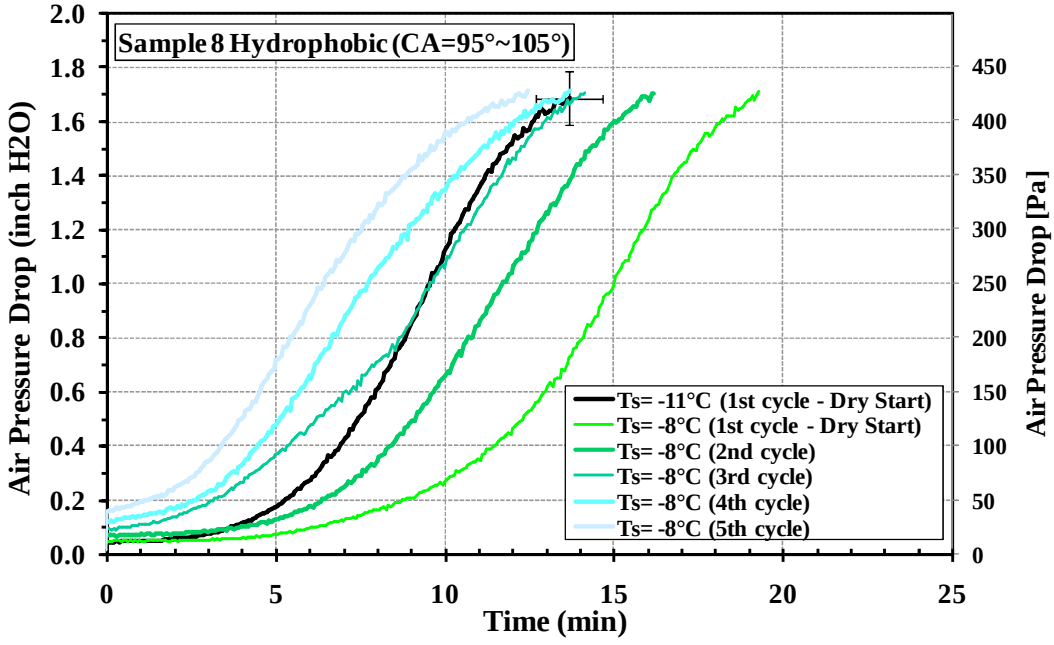

Figure 126: Experimental data of air side pressure drop on hydrophobic microchannel sample 8 under frost/defrost and refrost conditions. Air temperature = 1.7°C/0.6°C db/wb.

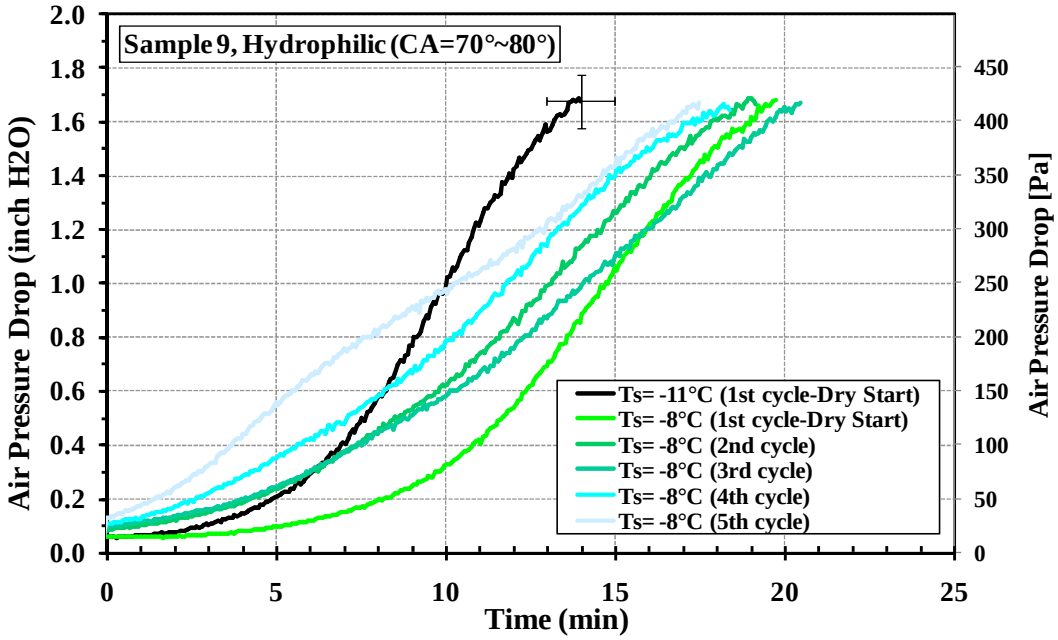

Figure 127: Experimental data of air side pressure drop on hydrophilic microchannel sample 9 under frost/defrost and refrost conditions. Air temperature = 1.7°C/0.6°C db/wb.

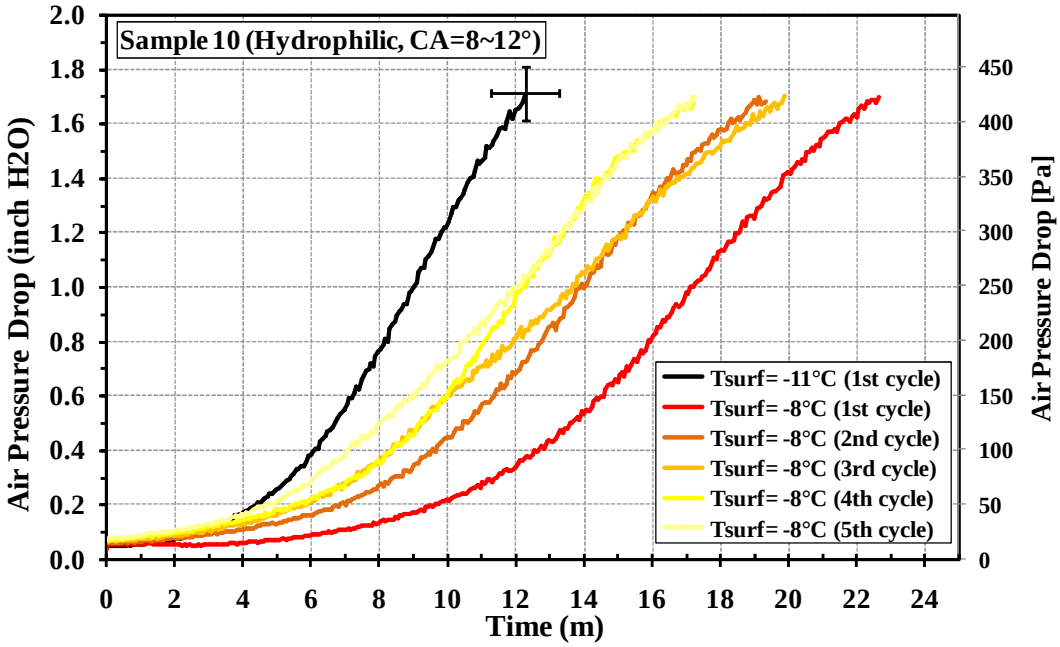

Figure 128: Experimental data of air side pressure drop on hydrophilic microchannel sample 10 under frost/defrost and refrost conditions. Air temperature = 1.7°C/0.6°C db/wb.

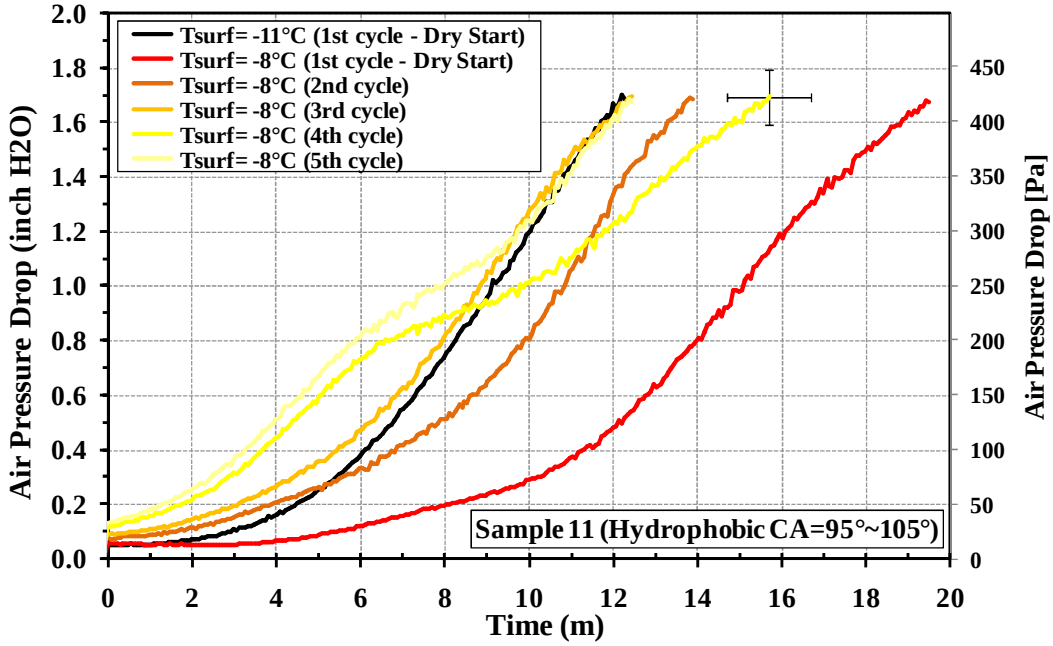

Figure 129: Experimental data of air side pressure drop on hydrophobic microchannel sample 11 under frost/defrost and refrost conditions. Air temperature = 1.7°C/0.6°C db/wb.

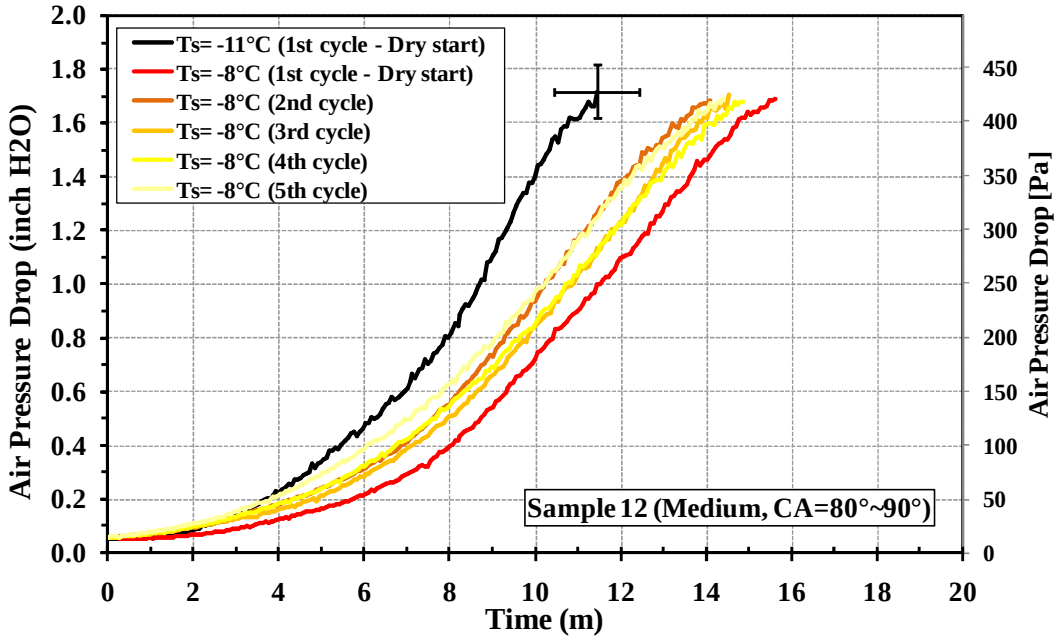

Figure 130: Experimental data of air side pressure drop on medium coated microchannel sample 12 under frost/defrost and refrost conditions. Air temperature = 1.7°C/0.6°C db/wb.

APPENDIX E: CAPACITY DEGRADATION MEASUREMENTS DATA

In the present appendix, the detailed measurements of capacity measurements during frost tests for each microchannel sample are presented. The capacity of the samples are measured form the air side while refrigerant side was showing similar results within the uncertainty of measurements and heat balance (10 to 15%).

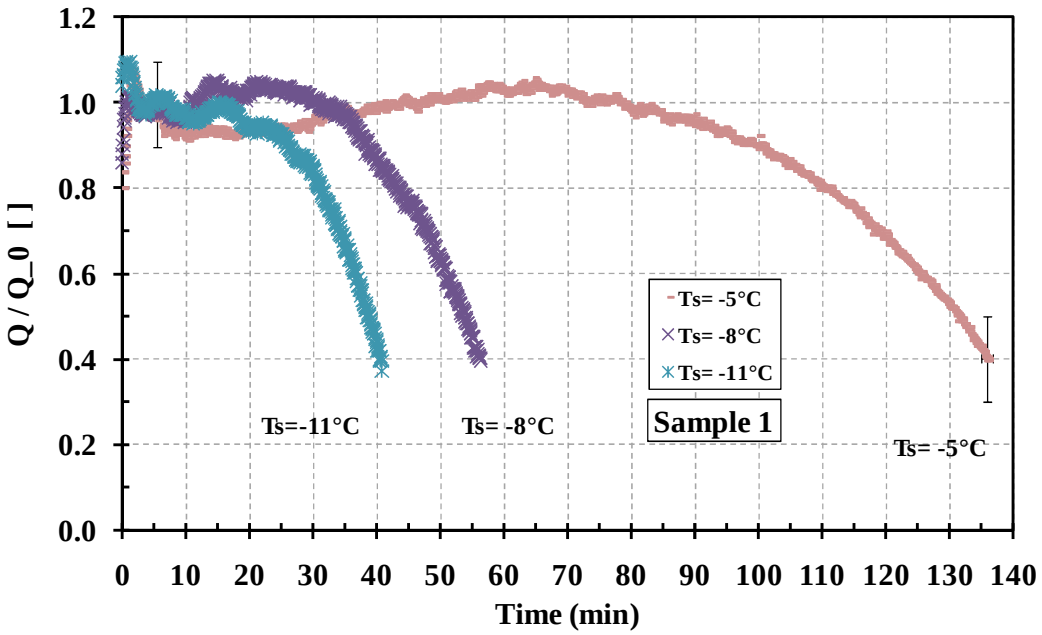

Figure 131: Experimental data of capacity degradation during the frost tests for microchannel Sample 1 with different surface temperatures. The Q_0 for the surface temperature of -5, -8 and -11°C is 11.6, 16.5 and 22.3W respectively (capacity per face area: 9.7, 13.8 and 18.6 kW/m^2). Air temperature = 1.7°C/0.6°C db/wb.

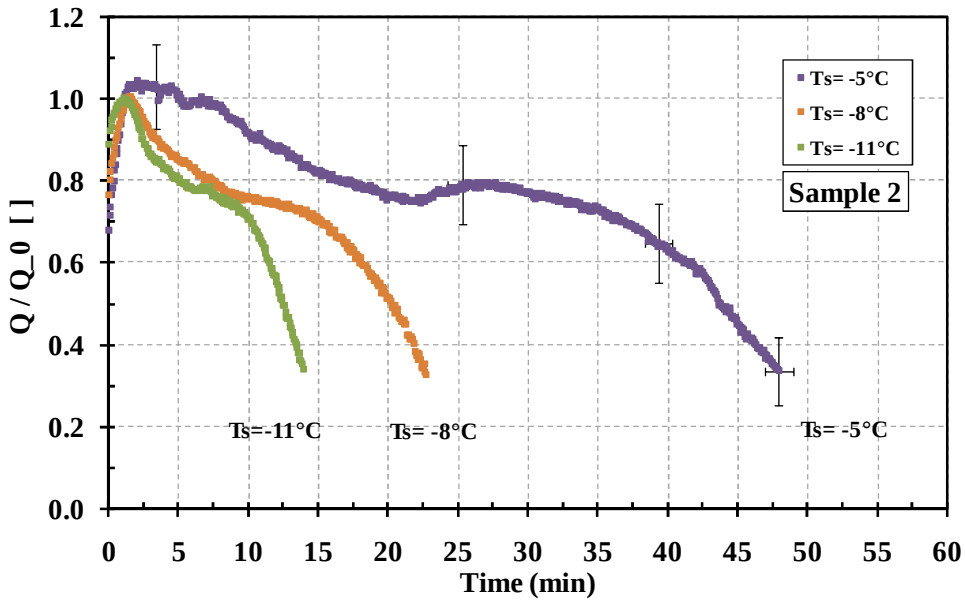

Figure 132: Experimental data of capacity degradation during the frost tests for microchannel Sample 2 with different surface temperatures. The Q_0 for the surface temperature of -5, -8 and -11°C is 18.0, 27.1 and 34.0W respectively (capacity per face area: 15.0, 22.6 and 28.4 kW/m^2). Air temperature = 1.7°C/0.6°C db/wb.

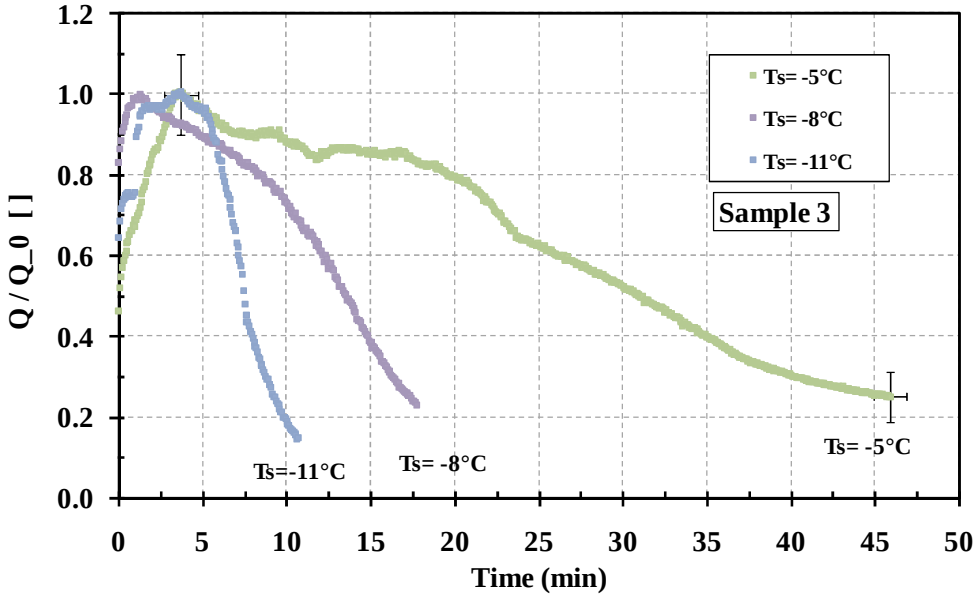

Figure 133: Experimental data of capacity degradation during the frost tests for microchannel Sample 3 with different surface temperatures. The Q_0 for the surface temperature of -5, -8 and -11°C is 18.0, 28.2 and 31.2W respectively (capacity per face area: 15.8, 24.8 and 27.4 kW/m^2). Air temperature = 1.7°C/0.6°C db/wb.

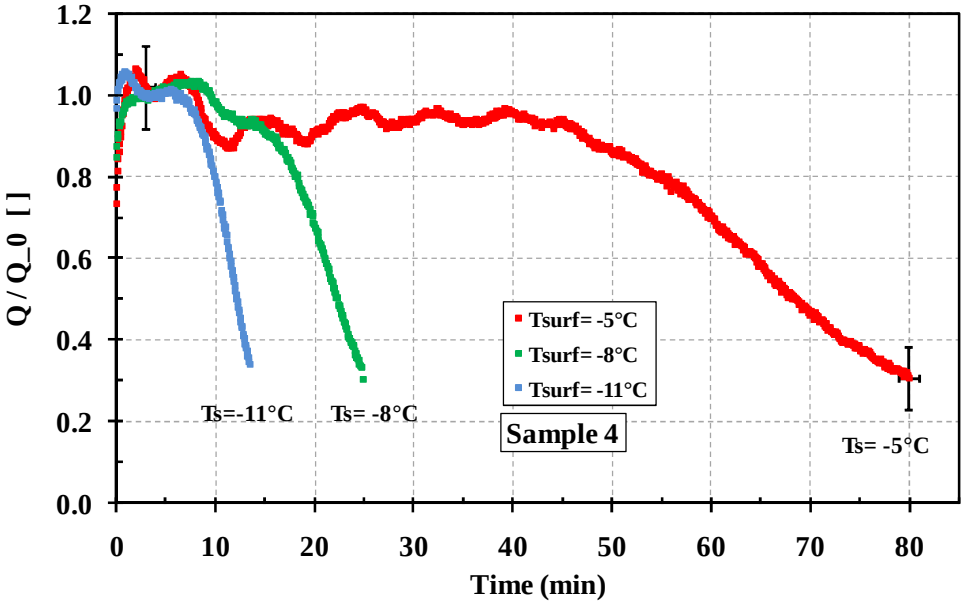

Figure 134: Experimental data of capacity degradation during the frost tests for microchannel Sample 4 with different surface temperatures. The Q_0 for the surface temperature of -5, -8 and -11°C is 17.6, 26.8 and 30.8W respectively (capacity per face area: 10.5, 17.9 and 20.6 kW/m2). Air temperature = 1.7°C/0.6°C db/wb (The only -5°C frost test that took long more than 60 minutes among all samples was sample 4. Since sample 4 was not an extreme geometry, author suspect that this was an anomaly with the -5°C frost test on sample 4. The time was expected to be around 50 minutes like other samples).

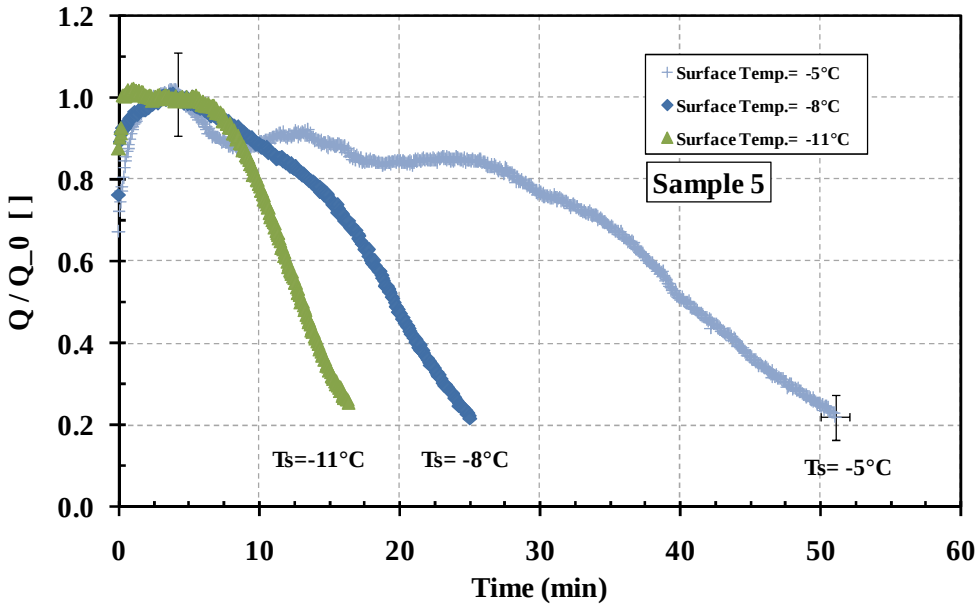

Figure 135: Experimental data of capacity degradation during the frost tests for microchannel Sample 5 with different surface temperatures. The Q_0 for the surface temperature of -5, -8 and -11°C is 23.5, 32.9 and 40.2W respectively (capacity per face area: 12.1, 16.9 and 21.7 kW/m^2). Air temperature = 1.7°C/0.6°C db/wb.

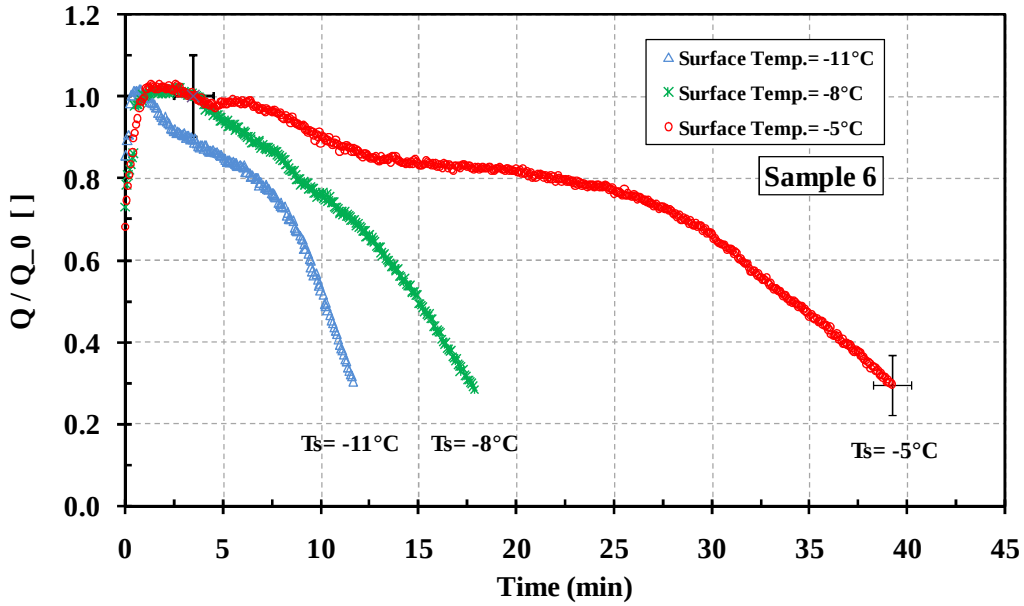

Figure 136: Experimental data of capacity degradation during the frost tests for microchannel Sample 6 with different surface temperatures. The Q_0 for the surface temperature of -5, -8 and -11°C is 19.5, 30.6 and 39.0W respectively (capacity per face area: 16.3, 25.5 and 32.5 kW/m^2). Air temperature = 1.7°C/0.6°C db/wb.

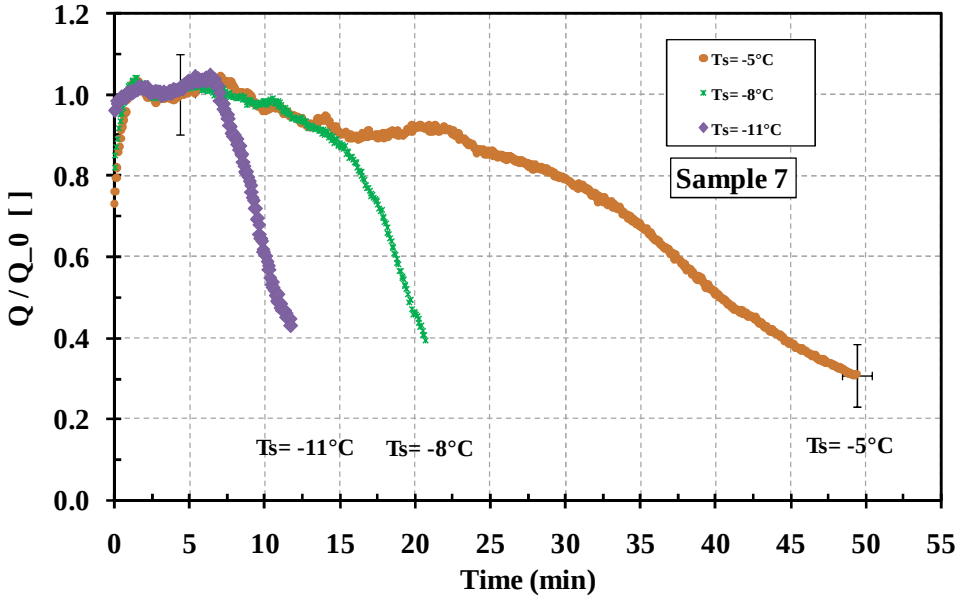

Figure 137: Experimental data of capacity degradation during the frost tests for microchannel Sample 7 with different surface temperatures. The Q_0 for the surface temperature of -5, -8 and -11°C is 16.9, 22.5 and 27.6W respectively (capacity per face area: 14.1, 18.8 and 23.0 kW/m^2). Air temperature = 1.7°C/0.6°C db/wb.

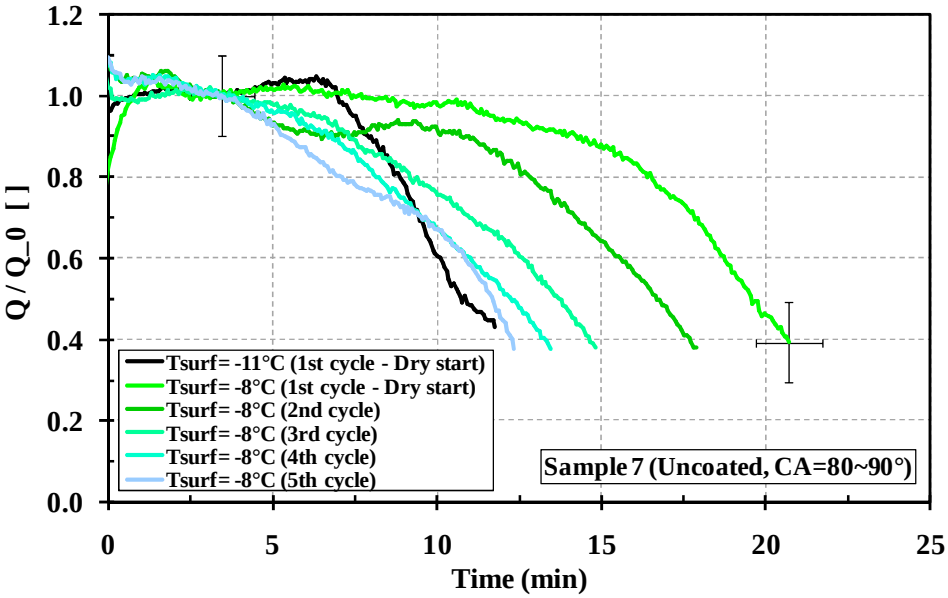

Figure 138: Experimental data of capacity degradation for uncoated microchannel sample 7 during five consequent frost/defrost tests. The Q_0 for the surface temperature of -8 and -11°C is 22.5 and 27.6W respectively (capacity per face area: 18.8 and 23.0 kW/m^2). Air temperature = 1.7°C/0.6°C db/wb.

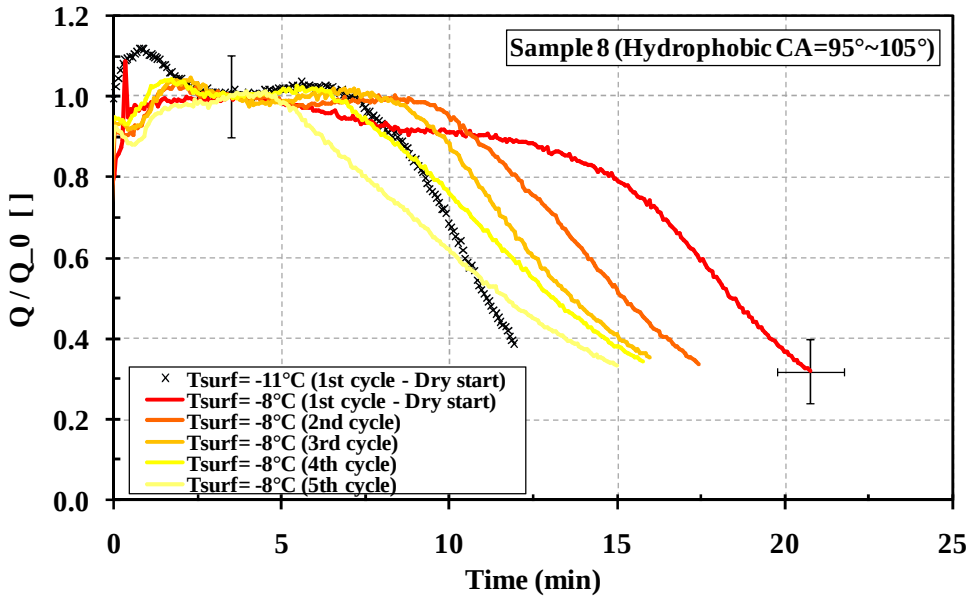

Figure 139: Experimental data of capacity degradation for hydrophobic microchannel sample 8 during five consequent frost/defrost tests. The Q_0 for the surface temperature of -8 and -11°C is 25.8 and 29.5W respectively (capacity per face area: 21.5 and 24.6 kW/m^2). Air temperature = 1.7°C/0.6°C db/wb.

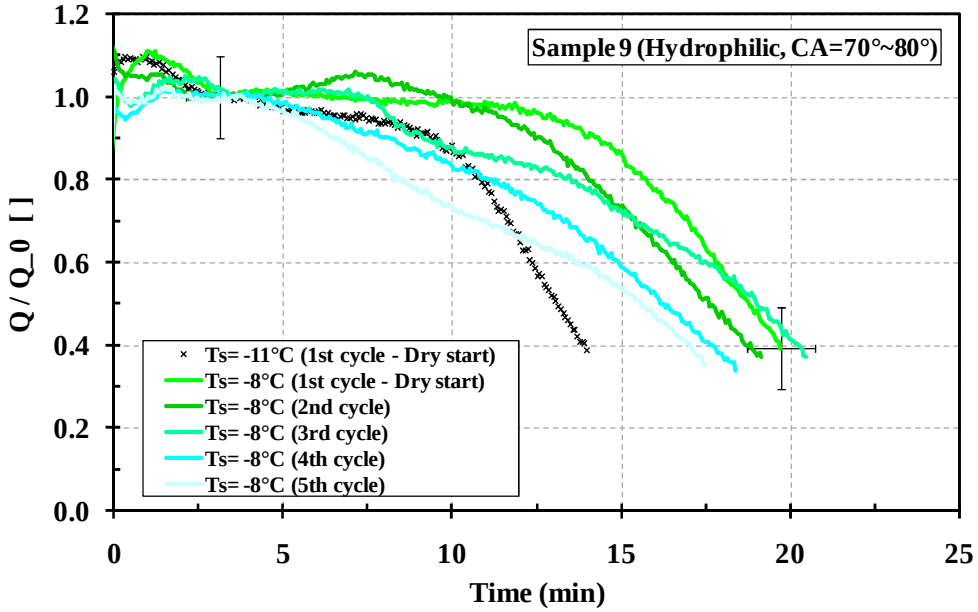

Figure 140: Experimental data of capacity degradation for hydrophilic microchannel sample 9 during five consequent frost/defrost tests. The Q_0 for the surface temperature of -8 and -11°C is 23.8 and 28.3W respectively (capacity per face area: 19.9 and 23.6 kW/m^2). Air temperature = 1.7°C/0.6°C db/wb.

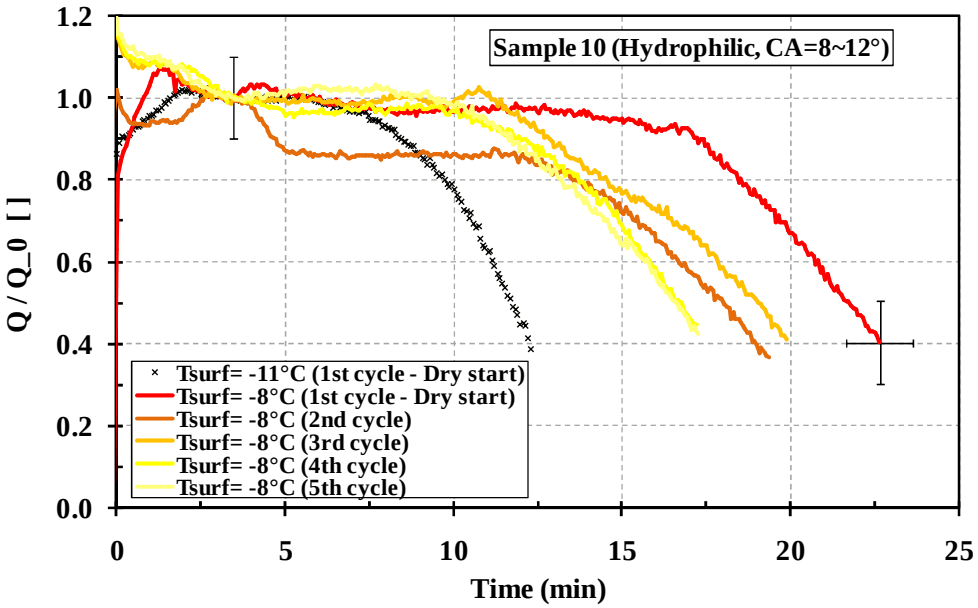

Figure 141: Experimental data of capacity degradation for hydrophilic microchannel sample 10 during five consequent frost/defrost tests. The Q_0 for the surface temperature of -8 and -11°C is 22.5 and 28.4W respectively (capacity per face area: 18.8 and 23.7 kW/m^2). Air temperature = 1.7°C/0.6°C db/wb.

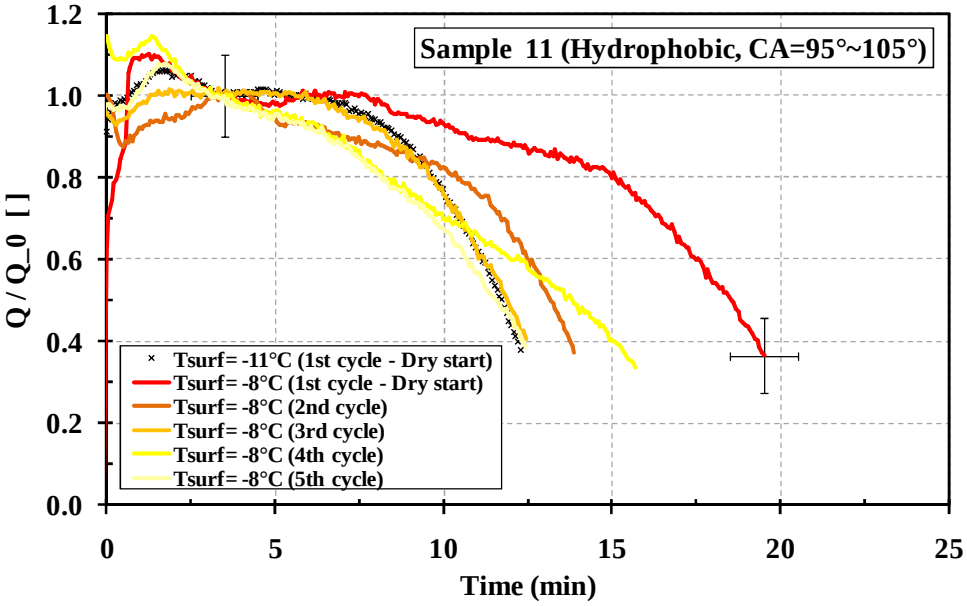

Figure 142: Experimental data of capacity degradation for hydrophobic microchannel sample 11 during five consequent frost/defrost tests. The Q_0 for the surface temperature of -8 and -11°C is 24.7 and 28.8W respectively (capacity per face area: 20.6 and 24.0 kW/m^2). Air temperature = 1.7°C/0.6°C db/wb.

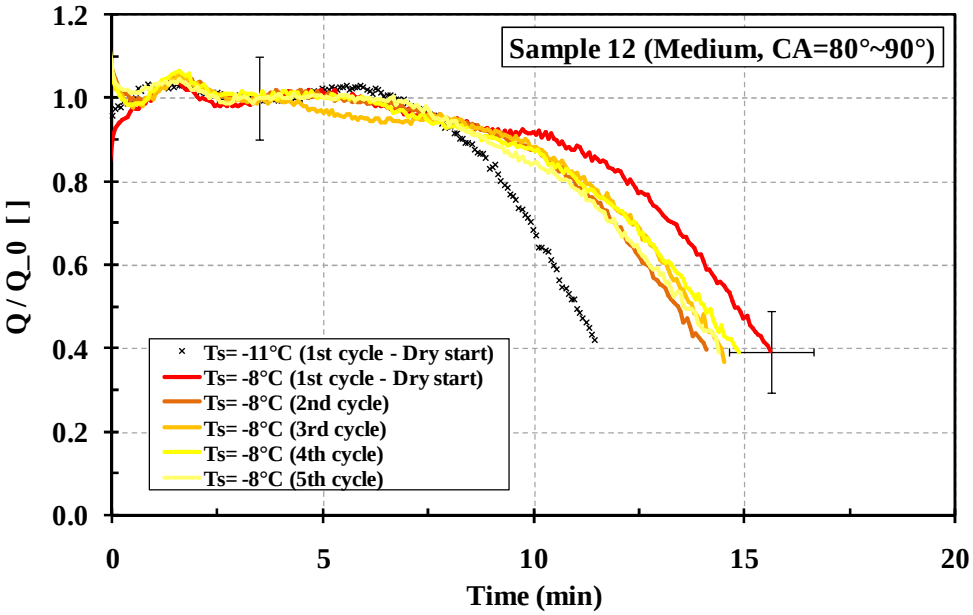

Figure 143: Experimental data of capacity degradation for medium coated microchannel sample 12 during five consequent frost/defrost tests. The Q_0 for the surface temperature of -8 and -11°C is 22.1 and 27.5W respectively (capacity per face area: 18.4 and 22.9 kW/m^2). Air temperature = 1.7°C/0.6°C db/wb.

APPENDIX F: HEAT TRANSFER COEFFICIENT (J-FACTOR) MEASUREMENTS DATA AND CORRELATION

In the present appendix, the detailed measurements of heat transfer coefficient in form of j-factor during the frost tests for each microchannel samples are presented. The results obtained from the present empirical frost correlation and previous dry microchannel correlations are also shown in the plots. The results of the present appendix are showing the frosting j-factor starting from dry-start condition.

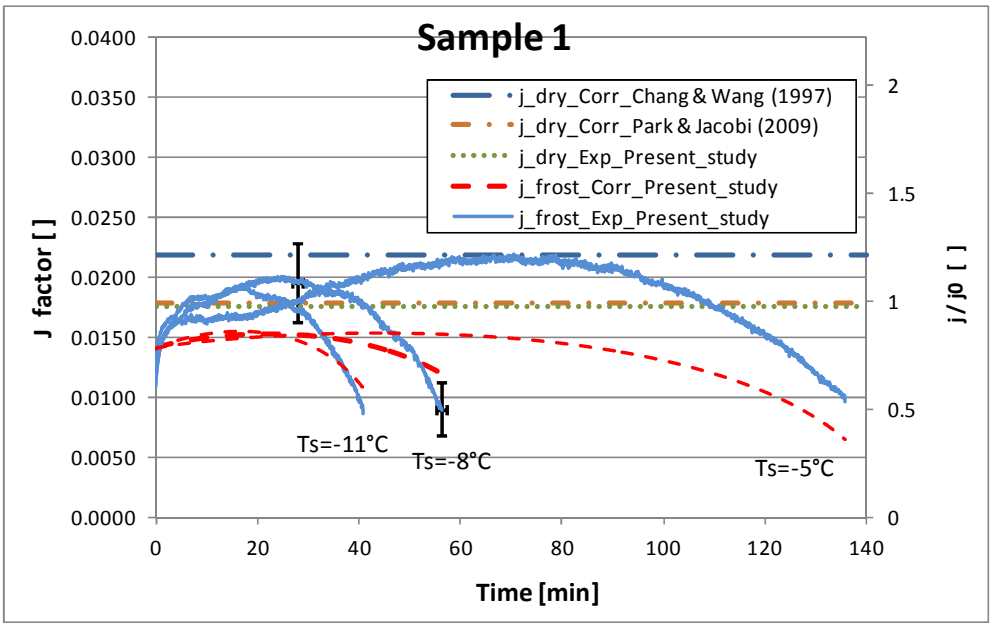

Figure 144: Experimental data of heat transfer coefficient in the form of j-factor for sample 1 at three surface temperatures. The result of developed frost j-factor correlation in the present study is also shown in the plot with dashed line plus a couple of previous dry j-factor correlations.

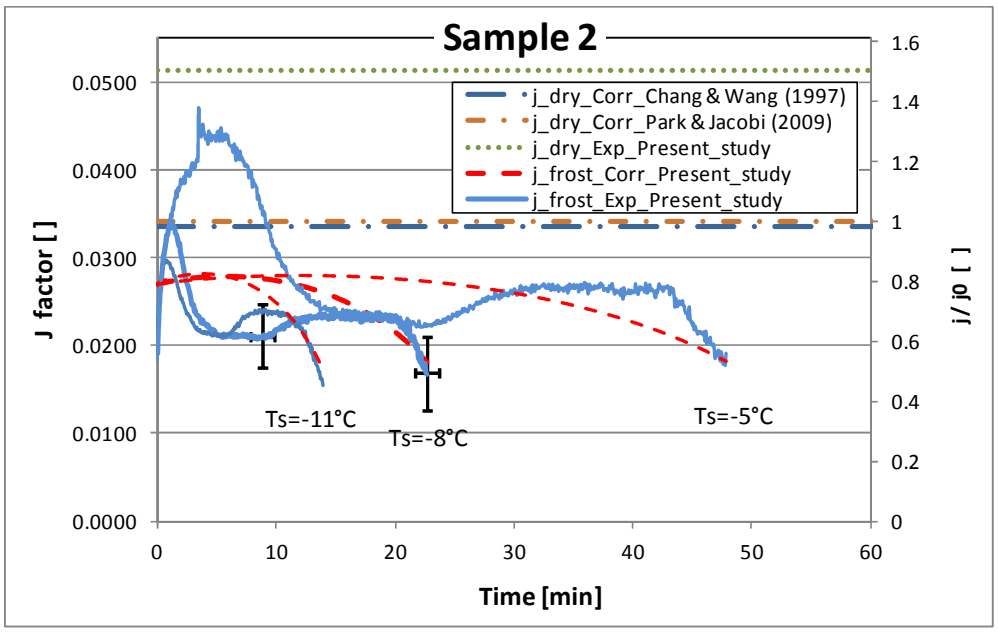

Figure 145: Experimental data of heat transfer coefficient in the form of j-factor for sample 2 at three surface temperatures. The result of developed frost j-factor correlation in the present study is also shown in the plot with dashed line plus a couple of previous dry j-factor correlations.

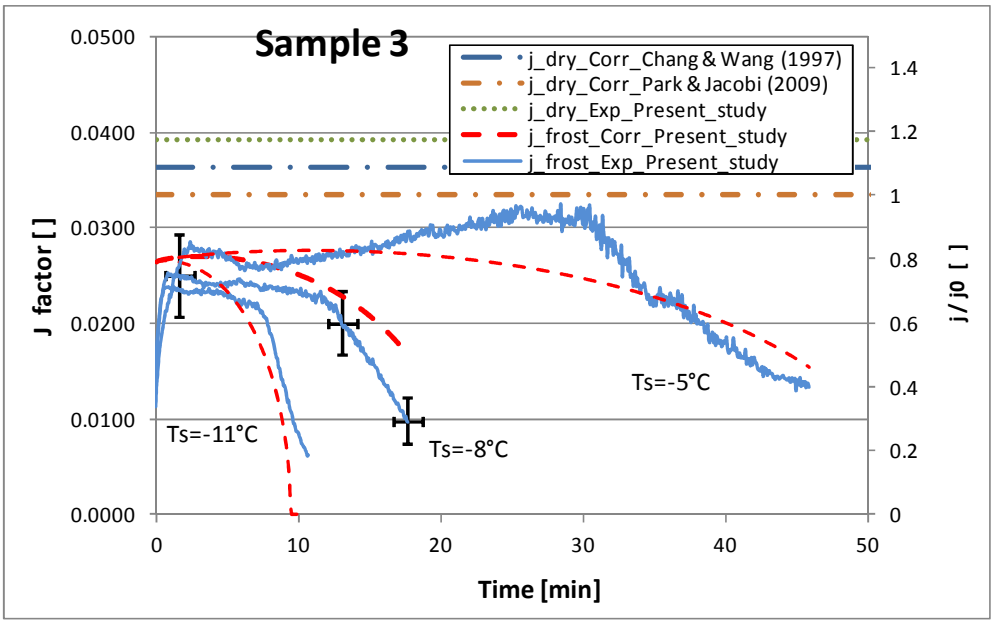

Figure 146: Experimental data of heat transfer coefficient in the form of j-factor for sample 3 at three surface temperatures. The result of developed frost j-factor correlation in the present study is also shown in the plot with dashed line plus a couple of previous dry j-factor correlations.

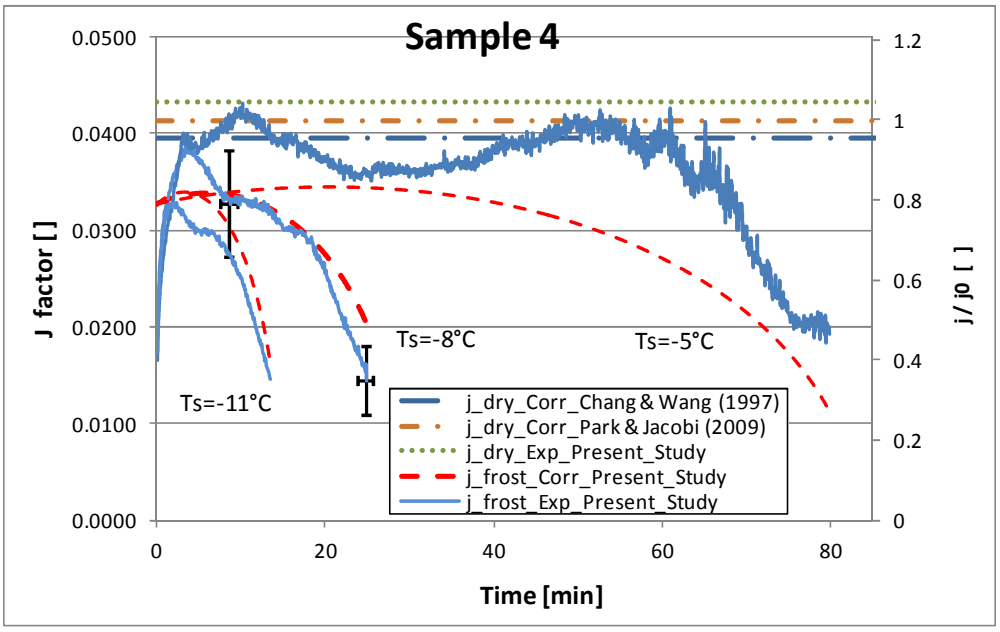

Figure 147: Experimental data of heat transfer coefficient in the form of j-factor for sample 4 at three surface temperatures. The result of developed frost j-factor correlation in the present study is also shown in the plot with dashed line plus a couple of previous dry j-factor correlations.

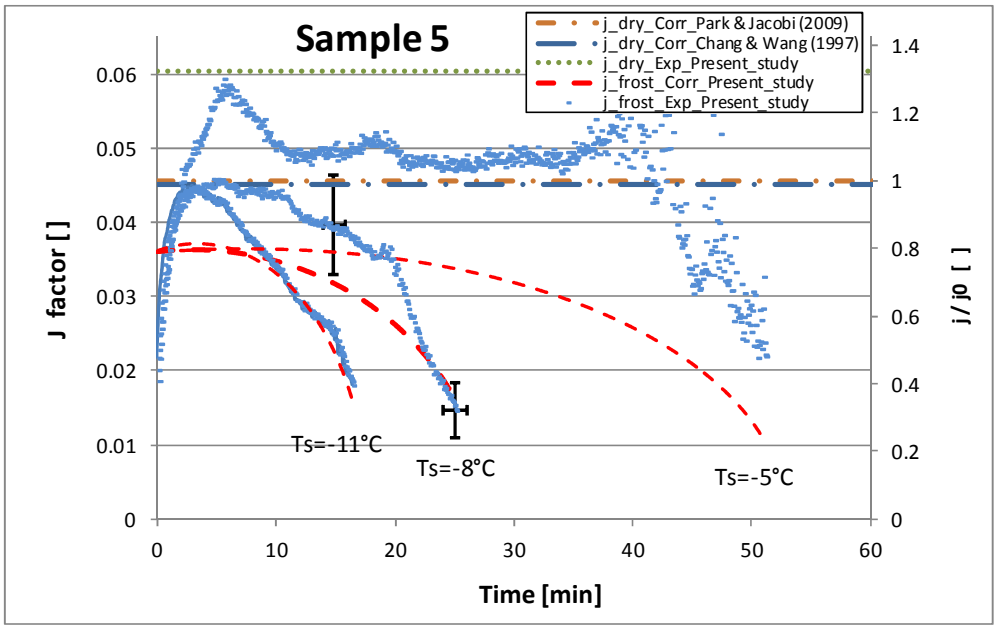

Figure 148: Experimental data of heat transfer coefficient in the form of j-factor for sample 5 at three surface temperatures. The result of developed frost j-factor correlation in the present study is also shown in the plot with dashed line plus a couple of previous dry j-factor correlations.

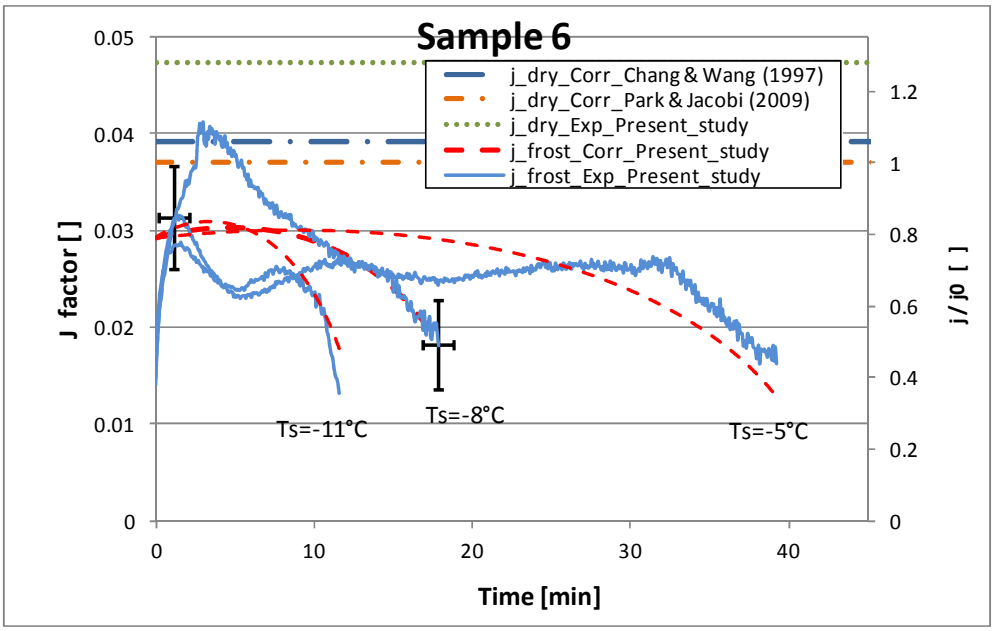

Figure 149: Experimental data of heat transfer coefficient in the form of j-factor for sample 6 at three surface temperatures. The result of developed frost j-factor correlation in the present study is also shown in the plot with dashed line plus a couple of previous dry j-factor correlations.

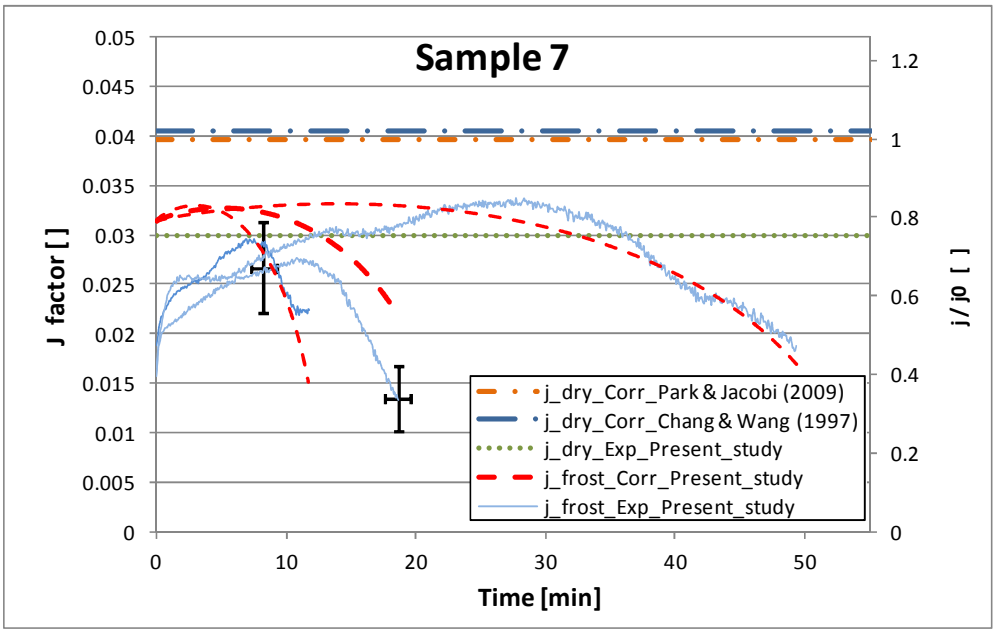

Figure 150: Experimental data of heat transfer coefficient in the form of j-factor for sample 7 at three surface temperatures. The result of developed frost j-factor correlation in the present study is also shown in the plot with dashed line plus a couple of previous dry j-factor correlations.

VITA

Ehsan Moallem

Candidate for the Degree of

Doctor of Philosophy

Thesis: EXPERIMENTAL AND THEORETICAL INVESTIGATION OF EFFECT OF FIN GEOMETRY ON FROST FORMATION ON MICROCHANNEL HEAT EXCHANGERS

Major Field: Mechanical Engineering

Biographical:

Ehsan Moallem is a graduate research assistant at Oklahoma State University. He has 6 years of industrial experience in heating, ventilation and air conditioning in manufacturing plants as a design and product engineer. He also has 5 years of experimental experience in designing and building laboratory test set ups and lab supervising in universities. He has years of experience with heat exchanger design and particularly he has worked during his PhD studies on compact heat exchangers and microchannels. He is expert in performing the tests, data analysis/reduction, lab programming and instrumentation, troubleshooting and assisting engineers working in the lab environment. He has experience in designing HVAC equipments such as chiller, air handlers, fan coils etc. and he is proficient to use ASHRAE, AHRI and other standards. He also has experiences in numerical simulation of the flow and CFD.

Education:

Completed the requirements for the Doctor of Philosophy in Mechanical Engineering at Oklahoma State University, Stillwater, Oklahoma in July, 2012.

Completed the requirements for the Master of Science in Mechanical Engineering at University of Tehran, Tehran, Iran in 2007.

Completed the requirements for the Bachelor of Science in your Mechanical Engineering at University of Tehran, Tehran, Iran in 2004.

Experience:
Head of R&D division Saravel Corp. Tehran, Iran (2002 – 2008)
Lab supervisor at Oklahoma State University (2008-2012)

Professional Memberships:
ASHRAE student member

Name: Ehsan Moallem Date of Degree: July, 2012

Institution: Oklahoma State University Location: Stillwater, Oklahoma

Title of Study: EXPERIMENTAL AND THEORETICAL INVESTIGATION OF EFFECT OF FIN GEOMETRY ON FROST FORMATION ON MICROCHANNEL HEAT EXCHANGERS

Pages in Study: 319 Candidate for the Degree of Doctor of Philosophy

Major Field: Mechanical Engineering

Scope and Method of Study:

The present work focused on different aspects of frost formation on louvered folded fins in microchannel heat exchangers used in air source heat pump systems. The approach taken was to perform laboratory experiments on small scale coils and sample fins that were cut out from commercially available heat exchangers and replicated their operating conditions in laboratory. More than 150 tests with different surface temperature, air velocity and air humidity were performed on 12 different microchannel fin samples; 7 fin samples had different geometry and 5 fin sample had identical geometry but with various surface coatings. The effects of surface temperature, fin geometries, surface coatings and environmental parameters were studied. Frost thickness and frost mass were measured. Air pressure drop across the coil, heat transfer rate and coefficients in form of Colburn j-factor during the frosting periods were measured.

Findings and Conclusions:

It was found that non-louvered low fin density sample had longer frost time (3.2 times) but lower capacity (-1.6 times) in comparison to louvered samples. Other geometrical parameters such as fin length (height) and fin depth had minor effect on frosting time and capacity per face area. Surface temperature had the highest impact on frosting time and capacity of all fin samples so that 6 degrees Celsius higher surface temperature resulted in around 1.8 times decrease in initial capacity but 3.3 times longer frost time. The tested hydrophilic coated sample resulted in slightly increased frost time (15%) in comparison to hydrophobic sample. This study broke new ground on developing a set of three correlations for frost thickness, air face velocity drop, and heat transfer coefficient of 7 fin geometries for microchannel heat exchangers. The developed correlations were able to predict the frost thickness, air face velocity degradation and dimensionless heat transfer Colburn j-factor within ±17.6% and ±7.7% and ±16.7%.

ADVISER'S APPROVAL: Dr. Lorenzo Cremaschi